ResearchGate

See discussions, stats, and author profiles for this publication at: https://www.researchgate.net/publication/342916469

Realistic Modeling of Power Lines for Transient Electromagnetic Interference Studies

Thesis · July 2020

CITATIONS
0

READS
63

1 author:

Amauri Martins-Britto
University of Brasília
4 PUBLICATIONS **2** CITATIONS

SEE PROFILE

Some of the authors of this publication are also working on these related projects:

Transmission Line Modeling & EMI View project

All content following this page was uploaded by Amauri Martins-Britto on 14 July 2020.

The user has requested enhancement of the downloaded file.

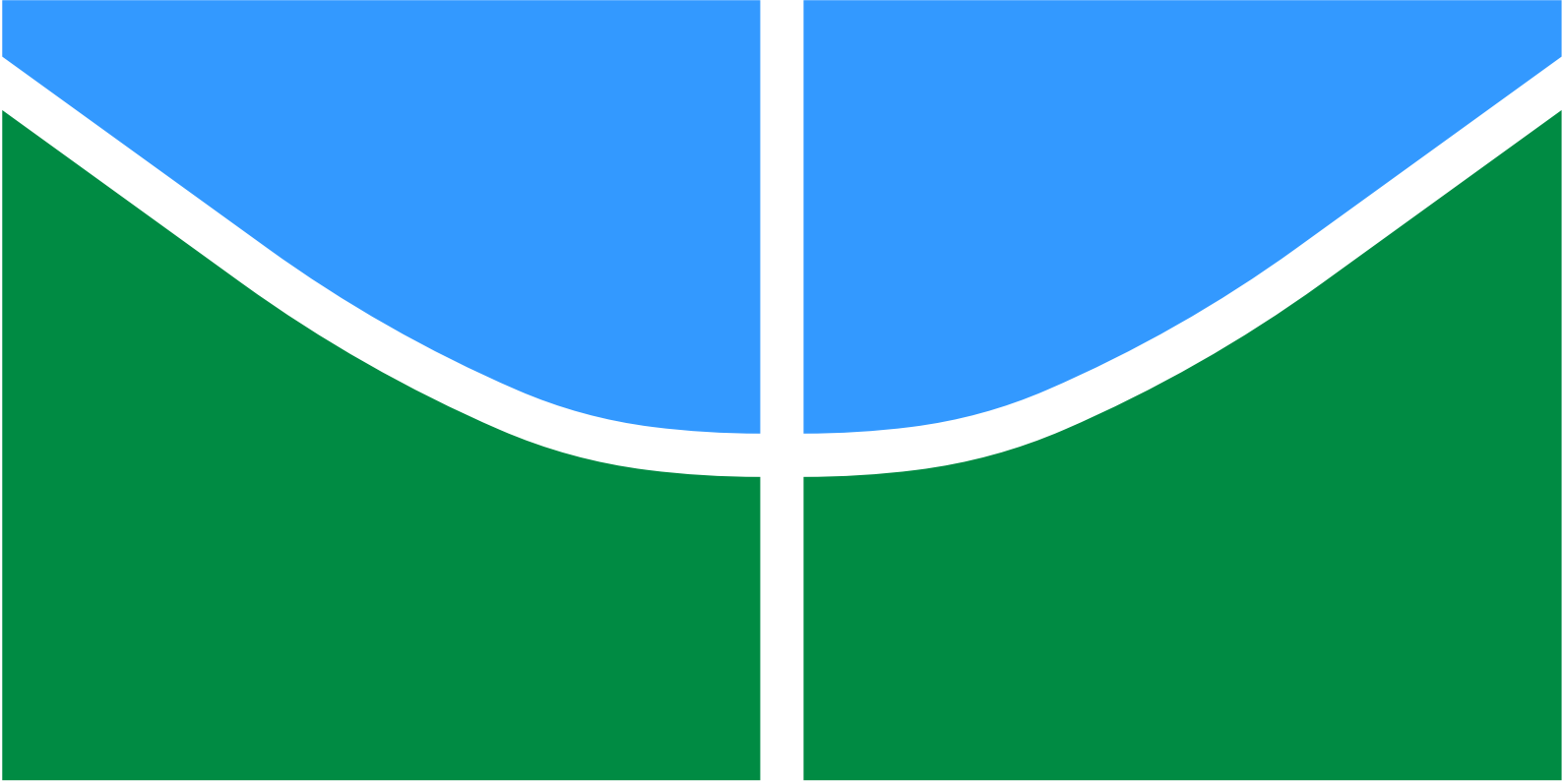

REALISTIC MODELING OF POWER LINES FOR TRANSIENT ELECTROMAGNETIC INTERFERENCE STUDIES

AMAURI GUTIERREZ MARTINS BRITTO

TESE DE DOUTORADO
EM ENGENHARIA ELÉTRICA

DEPARTAMENTO DE ENGENHARIA ELÉTRICA

FACULDADE DE TECNOLOGIA

UNIVERSIDADE DE BRASÍLIA

Universidade de Brasília
Faculdade de Tecnologia
Departamento de Engenharia Elétrica

Realistic Modeling of Power Lines for Transient Electromagnetic Interference Studies

Amauri Gutierrez Martins Britto

TESE DE DOUTORADO SUBMETIDA AO PROGRAMA DE PÓS-GRADUAÇÃO EM ENGENHARIA ELÉTRICA DA UNIVERSIDADE DE BRASÍLIA COMO PARTE DOS REQUISITOS NECESSÁRIOS PARA A OBTENÇÃO DO GRAU DE DOUTOR.

APROVADA POR:

Prof. Felipe Vigolvino Lopes, D.Sc. (ENE-UnB)
(Orientador)

Prof. Sébastien Roland Marie Joseph Rondineau, Ph.D. (ENE-UnB)
(Co-orientador)

Prof. Washington Luiz Araújo Neves, Ph.D. (UFCG)
(Examinador Externo)

Prof. Sérgio Kurokawa, D.Sc. (UNESP / Ilha Solteira)
(Examinador Externo)

Prof. Fernando Cardoso Melo, D.Sc. (ENE-UnB)
(Examinador Interno)

Brasília/DF, julho de 2020.

FICHA CATALOGRÁFICA

MARTINS-BRITTO, AMAURI GUTIERREZ

Realistic Modeling of Power Lines for Transient Electromagnetic Interference Studies. [Distrito Federal] 2020.

xxiii, 157p., 210 x 297 mm (ENE/FT/UnB, Doutor, Tese de Doutorado, 2020).

Universidade de Brasília, Faculdade de Tecnologia, Departamento de Engenharia Elétrica.

Departamento de Engenharia Elétrica

1. ATP/EMTP
2. Electric grounding
3. Electromagnetic interferences
4. FDTD
5. Line parameters
6. Pipelines
7. Soil resistivity
8. Transmission lines

I. ENE/FT/UnB
II. Título (série)

REFERÊNCIA BIBLIOGRÁFICA

MARTINS-BRITTO, A. G. (2020). Realistic Modeling of Power Lines for Transient Electromagnetic Interference Studies. Tese de Doutorado em Engenharia Elétrica, Publicação PPGENE.TD-166A/2020, Departamento de Engenharia Elétrica, Universidade de Brasília, Brasília, DF, 157p.

CESSÃO DE DIREITOS

AUTOR: Amauri Gutierrez Martins Britto

TÍTULO: Realistic Modeling of Power Lines for Transient Electromagnetic Interference Studies.

GRAU: Doutor ANO: 2020

É concedida à Universidade de Brasília permissão para reproduzir cópias desta tese de doutorado e para emprestar ou vender tais cópias somente para propósitos acadêmicos e científicos. O autor reserva outros direitos de publicação e nenhuma parte desta tese de doutorado pode ser reproduzida sem autorização por escrito do autor.

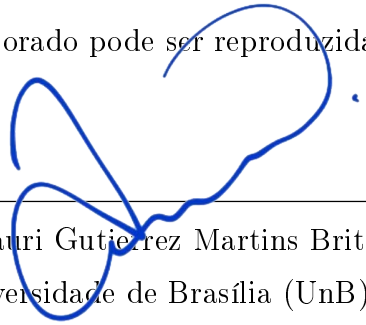

Amauri Gutierrez Martins Britto

Universidade de Brasília (UnB)

Campus Darcy Ribeiro

Faculdade de Tecnologia - FT

Departamento de Eng. Elétrica (ENE)

Brasília - DF CEP 70919-970

To my beloved sons, Lucas, Caio and Tiago.

ACKNOWLEDGEMENTS

I wish to express my gratitude...

...to Professor Felipe, Professor Sébastien and Professor Kleber, for their time, direction and, above all, for the encouragement, from the beginning to the end of this work.

...to my dear wife Bárbara, for her support, patience with my stubbornness, and for bringing to this world our precious gift, Tiago.

...to my baby boys Lucas, Caio and Tiago, my daily source of joy and pride.

...to grannies Ângela and Zélia, for their invaluable assistance during the challenging times while this work was being concluded.

I will always be indebted with you.

ABSTRACT

This work describes the problem of electromagnetic interferences between high voltage power lines and neighboring metallic installations, in steady-state and transient conditions, and the main risks to which people and facilities are exposed to. Computational tools are developed to carry out realistic simulations of electromagnetic interferences, under two different approaches: an FDTD implementation and a circuit-based model using the Alternative Transients Program (ATP). A new formula, fully compatible with the native ATP routines, is proposed to model multilayered soil structures in ground return impedance calculations. All programs are validated through case studies and comparisons with results obtained by using industry-standard software. Of practical interest to the industries of energy, oil & gas, ore and water distribution/sanitation, this work is expected to contribute with advanced techniques to predict and mitigate risks to which people and installations are subjected, thus assisting in the design of safer facilities, with technically feasible and economical solutions.

Keywords: ATP/EMTP, electric grounding, electromagnetic interferences, FDTD, line parameters, pipelines, soil resistivity, transmission lines.

RESUMO

Este trabalho descreve o problema das interferências eletromagnéticas entre linhas de transmissão de energia elétrica em alta tensão e instalações metálicas vizinhas, em condições de regimes permanente e transitório, bem como os principais riscos a que se sujeitam pessoas e as instalações envolvidas. São desenvolvidas ferramentas computacionais com o propósito de realizar simulações realistas de casos de interferências eletromagnéticas, por meio de duas abordagens distintas: o método FDTD e um modelo baseado em teoria de circuitos utilizando o programa ATP (Alternative Transients Program). Uma nova fórmula é proposta para modelar solos multiestratificados em cálculos de impedâncias com caminho de retorno pela terra utilizando as rotinas nativas do ATP. Os códigos são validados por meio de estudos de casos e comparações com resultados obtidos utilizando programas considerados padrão de mercado. Este trabalho é de interesse prático para as indústrias de energia elétrica, óleo, gás, minérios, abastecimento de água e saneamento, por meio do qual se espera contribuir com o desenvolvimento de técnicas avançadas para prever e mitigar riscos às pessoas e ao patrimônio, auxiliando no projeto de instalações mais seguras, com soluções técnica e economicamente viáveis.

Palavras-chave: aterramento elétrico, ATP/EMTP, FDTD, interferências eletromagnéticas, linhas de transmissão, parâmetros de linha, resistividade do solo, tubulações.

TABLE OF CONTENTS

Table of contents i

List of figures iv

List of tables xiii

List of symbols xv

Glossary xxii

Chapter 1 – Introduction 1

1.1 Preface 1
1.2 Objectives and scope of work 3
1.3 Contributions 4
1.4 Thesis structure 6

Chapter 2 – Fundamental concepts 8

2.1 Soil resistivity analysis 8
2.1.1 Wenner method 10
2.1.2 Multilayered soil models 12
2.2 Inductive coupling mechanism 14
2.2.1 Electromagnetic interference zone 15
2.2.2 Calculation of mutual impedances over uniform soil 16
2.2.3 Calculation of mutual impedances over multilayered soil 18
2.2.4 Calculation of self impedances with ground return path 20
2.2.4.1 Parameters of a cylindrical tubular conductor 22
2.2.4.2 Parameters of a buried insulated conductor 22
2.3 Capacitive coupling mechanism 23
2.4 Conductive coupling mechanism 25
2.4.1 Current distribution under fault conditions 26
2.4.2 Potentials produced by a point current source in soil 27

2.4.2.1 Green's functions for uniform soil . . . 29
2.4.2.2 Green's functions for two-layered soil . . . 30
2.4.2.3 Green's functions for multilayered soil . . . 32
2.4.3 Computation of grounding electrode parameters . . . 33
2.5 Risks and safety limits . . . 36
2.5.1 Touch voltages . . . 36
2.5.2 Step voltages . . . 39
2.5.3 Damage to structures and equipment . . . 39
2.6 Transmission line parameters under interference conditions . . . 40
2.6.1 Series impedance and shunt admittance matrices . . . 42
2.6.2 Sequence parameters for continuously transposed lines . . . 43
2.6.3 Modal parameters for untransposed lines . . . 45
2.7 Review of the specialized literature . . . 46
2.8 Chapter summary . . . 48

Chapter 3 – Electromagnetic theory approach 49

3.1 Basics of lightning discharges and protection . . . 49
3.2 Proposed FDTD implementation . . . 52
3.2.1 Flowchart of the proposed program . . . 52
3.2.2 Model of the lightning channel . . . 53
3.3 Case studies . . . 54
3.3.1 Simple test case . . . 54
3.3.2 Grounding electrode of a transmission line tower . . . 56
3.3.3 Transient interferences on a nearby pipeline . . . 63
3.4 Chapter summary . . . 67

Chapter 4 – Proposed circuit theory approach 69

4.1 Classic circuit model . . . 69
4.2 Proposed time-domain circuit implementation . . . 72
4.3 Proposed multilayer earth structure approximation . . . 76
4.3.1 Earth return conduction effects . . . 78
4.3.2 Derivation of the equivalence formula for two layers . . . 80
4.3.3 Equivalent model of a multilayered soil structure . . . 81
4.3.4 Numerical results . . . 83
4.3.5 Validity of the new expression . . . 92
4.4 Case studies . . . 93
4.4.1 Applications of the equivalent resistivity formula . . . 93

4.4.1.1 Line-to-ground fault response of a transmission line 94
4.4.1.2 Inductive interference between a power line and a pipeline . . . 95
4.4.2 Validation of the ATP circuit implementation 98
4.4.2.1 Inductive interference between a traction system and a pipeline 99
4.4.2.2 Total interference between an 88 kV distribution system and a pipeline 106
4.5 Chapter summary 119

Chapter 5 – Conclusions and future work 120

References 123

Appendix A – Calculation of Green's functions for multilayered soils 133

Appendix B – Description of the FDTD method 140

B.1 Yee algorithm 141
B.2 Stability condition 144
B.3 Lumped components 145
B.3.1 Voltage source 145
B.3.2 Current source 146
B.3.3 Resistor 147
B.3.4 Inductor 148
B.3.5 Capacitor 148
B.4 Thin-wire model 149
B.5 Absorbing boundary conditions 151

Appendix C – Brief description of the calculation methods used in ATP 153

C.1 Resistance model 153
C.2 Inductance model 154
C.3 Capacitance model 154
C.4 Distributed-parameter transmission line model 155
C.5 Fundamental nodal equations 156

LIST OF FIGURES

2.1 Typical Wenner array for measurement of soil apparent resistivity. The electrode spacing a is numerically equal to depth at which the reading is taken. 10

2.2 Apparent resistivity profile for measurements in Table 2.2. 11

2.3 Real soil (a); and horizontally layered model described by parameters $[\rho_1, \rho_2, \rho_3, \rho_4]$ and $[h_1, h_2, h_3, h_4]$ (b). 12

2.4 N-layered horizontal soil model with finite resistivities $[\rho_1, \rho_2, \rho_3, ..., \rho_N]$ and thicknesses $[h_1, h_2, h_3, ..., h_{N-1}]$. 12

2.5 Electromagnetic interference zone, with distances in meters. The exposure length corresponds to the line segment $AA' + A'B$. 15

2.6 Two overhead conductors above a semi-infinite uniform ground and its images arranged symmetrically with respect to the plane $z = 0$, with distances H, D and D$'$ given in meters. Soil structure is described by permeability μ, permittivity ε and resistivity ρ. 17

2.7 Two overhead conductors above N layers of soil, with distances H, D, D$'$ and h_n given in meters. Each soil layer is described by permeability μ_n, permittivity ε_n, resistivity ρ_n and thickness h_n. Thickness of layer N extends to infinity. 19

2.8 Phase composed of four bundled conductors symmetrically arranged on a circumference with radius r_b. 21

2.9 Cross-section of a coated cylindrical tubular conductor with internal radius r_{int}, external radius r_{ext} and coating thickness δ_c. 22

2.10 Transmission line subject to a phase-to-ground fault, injecting a current I into the soil through the tower grounding electrode, causing a potential rise (GPR) of the adjacent earth. 25

2.11 Fault current distribution on a transmission line with n and m sections between, respectively, terminals A and B and the fault point F. $I_{F,A}$ and $I_{F,B}$ are the fault current contributions coming from the substations. $[I_{R,A1}, ..., I_{R,An}, I_{R,B1}, ..., I_{R,Bm}]$ are the shield wire return currents. $[I_{G,A1}, ..., I_{G,An}, I_{G,F}, I_{G,B1}, ..., I_{G,Bm}]$ are the currents flowing into the ground. 27

2.12 Equivalent circuit of the system shown in Figure 2.11. 28

2.13 Point source located at the ground surface ($z = 0$) over uniform soil and equipotential hemispherical surface with radius a. 30

2.14 Point source at depth d in uniform soil and its image, distances in meters. . . . 30

2.15 Point source at depth d in a two-layered soil, distances in meters. 31

2.16 Point source at depth d in a multilayered soil, distances in meters. 32

2.17 Linear conductor with length L_j, radius r_{ext} and micro-segment with infinitesimal length du buried in soil. 34

2.18 Illustration of V_S, E_T and U_E in a hypothetical pipeline under interference conditions. Z_C and Z_E represent, respectively, coating and earth impedances. 37

2.19 Concept of touch voltage and equivalent circuit. 38

2.20 Concept of step voltage and equivalent circuit. 39

2.21 Nominal-π model of a transmission line, described by a series impedance Z and a shunt admittance Y. Subscripts S and R denote, respectively, the source and remote terminals. 41

2.22 Overhead phase conductors, shield wires and interfered conductors. 43

3.1 Shield wires on the top of a power line, parallel to the phase conductors, made of bare wires with a direct connection to the tower structure, designed to intercept lightning discharges and conduct surge currents to the ground. Shield wires provide a protection cone, under which structures, such as the phase conductors, are shielded against lightning strokes. 50

3.2 Lightning discharge waveforms, with peak magnitude 30 kA, time constants: 8/20 μs, 1/50 μs, 0.25/100 μs and 10/350 μs. 51

3.3 Flowchart of the proposed FDTD implementation. 53

3.4 Lightning equivalent current source connected to a grounding grid. The circuit is completed through a remote electrode, with ground return path. 54

3.5 A simple grounding grid with horizontal and vertical conductors subject to a lightning discharge. 54

3.6 Current distribution along vertical rods in Figure 3.5 (reference values). 55

3.7 Current distribution along vertical rods in Figure 3.5, for the proposed implementation. Results agree with the reference values of Figure 3.6. 55

3.8 Perspective view of the system under study. The pipeline is parallel to the transmission line, with a distance of 10 m. A lightning discharge is assumed to hit the top of tower, being conducted to the ground through the tower structure, counterpoises and tower foundations. 56

3.9 Transient grounding impedance of the earthing grid. Values oscillate over time until a stable value of 8 Ω is reached. 58

3.10 Currents injected into the soil by the counterpoises. Curves follow the trend of the lightning discharge, with a maximum value of 6.6 kA being injected by counterpoise 3. 59

3.11 Currents injected into the soil by the tower foundations. Values are of the order of 32% of the amount discharged by the counterpoises, even though the dry concrete is a poor conductor. Maximum value is 2.1 kA. 60

3.12 Touch voltage at the tower vicinity. Maximum value of 171.4 kV exceeds the tolerable limits given in Table 3.3. Covering the soil with a layer of crushed rock 10 cm thick increases the safe limit to 242 kV, according to Table 3.4, thus mitigating risks of electrocution. 60

3.13 Top view of the electric field magnitude at the soil surface (step voltage), logarithmic color scale. The maximum value is 94 kV, exceeding the maximum step voltage limit. Highest magnitudes occur at the extremities of the conductors, which agrees with previous works where a similar grounding grid was simulated using the method of moments (MARTINS-BRITTO, 2017b). 61

3.14 Side view of the electric field magnitude around the tower, logarithmic color scale. The shielding effect is visible close to the phase conductors and inside the tower structure (Faraday cage). 62

3.15 Side view showing the pipeline, counterpoises, burial depths, tower structure, concrete foundations and steel-frames. Tower height is 30 m from the soil surface. Pipeline and counterpoises are buried, respectively, at 3.5 m and 0.5 m. Foundations are 10 m long with steel-frames of 3 m. 63

3.16 Top view showing counterpoises lengths, horizontal spacing, foundations and observation points. Currents injected into the ground are sampled at points 1 to 4. Ground potential rise is sampled at points $L = -30$ to $L = 30$. 64

3.17 GPR at observation points over the first 10 μs. Maximum value is of the order of 226 kV at point $L = 0$, $t = 1$ μs, which agrees with the fact that this observation point is the closest to the current source. Values are consistent with the simplified analytical expression (2.37). 65

3.18 Pipeline coating stress voltages at observation points for the first 10 μs. Maximum absolute value is 2.1 kV, which exceeds the tolerable limit of the pipeline coating (2 kV) and equipment connected to the pipeline, such as rectifiers (1.5 kV) and insulating flanges (1 kV). 66

4.1 Representation of a complex electromagnetic interference zone in terms of equivalent parallel sections. 69

4.2 Oblique approximation between a transmission line and an interfered system. . . 70

4.3 Equivalent circuit composed of n parallel sections, representing the general interfered (target) system in Figure 4.1. 70

4.4 ATPDraw representation of one section of a three-phase line with one shield wire and one interfered conductor. Resistance R_G represents the tower grounding. Admittance Y_C accounts for the coating of the target line. 73

4.5 ATPDraw representation of one section of a three-phase line with one shield wire and one interfered conductor, accounting for conductive coupling effects. Resistance R_G represents the tower grounding. Admittance Y_C accounts for the coating of the target line. Voltage source U_S is the ground potential rise of the soil adjacent to the target line. 74

4.6 ATPDraw representation of a large transmission system composed of three phases, one shield wire and one interfered line, where each transmission line span is modeled individually using LCC components. 75

4.7 Flowchart of the proposed ATP implementation. 76

4.8 Skin depth as a function of frequency and resistivity. For common earth materials and frequencies between 60 Hz and 1 kHz, values range from 5.03 m to 6.49 km. 79

4.9 Soil model composed of N equally spaced layers whose alternating resistivities differ proportionally to the contrast ratio R. On the left, $\rho_N > \rho_1$ as R increases. On the right, $\rho_N < \rho_1$ with increasing R. 87

4.10 Approximation error as function of the resistivity contrast ratio R. Relative error is kept below 1% for $R < 3$ and below 5% for $R < 10$. 87

4.11 Approximation error as function of the layer thickness and contrast ratio, for top layer resistivities equal to, respectively, 10000, 1000, 100 and 10 Ω.m. Thickness axis is normalized with respect to the skin depth δ. Maximum error is less than 5.45% for depths shallower than 5% of the skin depth δ. 88

4.12 Frequency response of two-layered soil models 1, 2 and 3. Errors are under 2% from the 1 Hz range up to the 10 kHz band. 90

4.13 Frequency response of three-layered soil models 4, 7, 8 and 9. Models 4 and 9 perform under 2% error from 1 Hz up to the 10 kHz band. 90

4.14 Frequency response of four-layered soil models 10, 11, 12 and 13. Errors are below 2% in the range from 1 Hz to 100 Hz. 91

4.15 Frequency response of five-layered soil models 15, 16 and 17. Errors are below 2% in the range from 1 Hz up to the 10 kHz band. 91

4.16 Frequency response of six-layered soil models 18, 19 and 20. Errors are below 3% from 1 Hz up to 100 Hz. 92

4.17 Single-circuit 150 kV transmission system. 94

4.18 Transmission line cross-section. Dimensions in meters. 94

4.19 Phase b open-end voltages. Peak value is 172.7 kV for the four-layered earth and 163.3 kV for the homogeneous soil model. Difference between both models is 9.4 kV. 96

4.20 Single phase line and pipeline cross-section. Dimensions in meters. Parallel length is 5 km. 97

4.21 Pipeline induced voltages due to magnetic coupling with the phase conductor. Maximum error between FEMM and the proposed technique is 2%. Maximum error between the four-layered model and homogeneous earth is 50%. 98

4.22 Geometry of the approximation between an electric traction system (railway) and a pipeline. Coordinates given in meters with reference to the railway axis. . 99

4.23 ATPDraw representation of the equivalent circuit of the electric traction system and the pipeline. 100

4.24 Steady-state induced voltages due to inductive coupling with the electric traction system conductor. Errors between the proposed ATP model and SESTLC are below 1%. 101

4.25 Pipeline induced voltages versus time at distance: 0 m. 101

4.26 Pipeline induced voltages versus time at distance: 260 m. 102

4.27 Pipeline induced voltages versus time at distance: 620 m. 102

4.28 Pipeline induced voltages versus time at distance: 900 m. 103

4.29 Pipeline induced voltages versus time at distance: 1230 m. 103

4.30 Pipeline induced voltages versus time at distance: 1500 m. 104

4.31 Currents at the receiving end of the transmission line in the presence of the target pipeline and neglecting the interference, in the period between $t = 0.01$ s and $t = 0.02$ s. Source current waveform is included to establish a baseline. . . 105

4.32 Single-line diagram of the power system. 106

4.33 Cross-section of a 88 kV distribution line tower. Dimensions in meters. 107

4.34 Geometry of the approximation between a 88 kV distribution line and a pipeline. Coordinates given in meters with respect to the transmission line axis. 107

4.35 ATPDraw representation of the equivalent circuit of the 88 kV distribution system and the pipeline. 109

4.36 Pipeline voltages due to inductive coupling with the 88 kV distribution line under nominal load conditions. Error between the proposed ATP model and SESTLC is below 5% in the worst point. 110

4.37 Phase currents flowing from the grid connection (Terminal A). Maximum transient current in the faulted phase is 13.64 kA and decays to 8.98 kA in steady-state. 112

4.38 Currents through the fault branch and the grounding system of the faulted tower. Maximum values are, respectively, 13.64 kA and 4.61 kA. Steady-state values are 8.99 kA and 3.03 kA. 112

4.39 Currents returning from the fault branch through the shield wires to Terminals A and B. Maximum absolute values are, respectively, 5.1 kA and 3.93 kA. Steady-state values are 3.41 kA and 2.56 kA. 113

4.40 Currents discharged into the soil through the grounding conductors. Terminal substations are represented by A and B. Towers inside the EMI zone are numbered from 1 to 7. 113

4.41 Pipeline potentials, GPR and stress voltages along the interfered pipeline. Maximum stress voltages of 1671 V (transient) and 1015 V (steady-state) occur at the crossing point (811 m along the target pipeline). 114

4.42 Pipeline potentials, GPR and stress voltages at the crossing point (811 m along the target pipeline). 115

4.43 Pipeline potentials, GPR and stress voltages along the interfered pipeline for a double-phase-to-ground (ABG) fault. 116

4.44 Pipeline potentials, GPR and stress voltages along the interfered pipeline for a thee-phase-to-ground (ABCG) fault. 116

4.45 Fault currents flowing from Terminal A comparing the realistic model with the case where interferences and soil resistivity variations are ignored. Maximum discrepancy between results is 898 A. 117

4.46 Fault currents through the faulted tower grounding comparing the realistic model with the case where interferences and soil resistivity variations are ignored. Maximum discrepancy between both models is 2836 A. 118

A.1 Source and observation points in a five-layered soil. All dimensions are in meters and not in scale. 138

B.1 Representation of the three-dimensional FDTD domain and of the electromagnetic fields on a Yee cell with modified node numbering. 142

B.2 Voltage source with magnitude V_S and internal resistance R_S placed between nodes (i, j, k) and $(i, j, k + 1)$. 145

B.3 Current source with magnitude I_S and internal resistance R_S placed between nodes (i, j, k) and $(i, j, k + 1)$. 146

B.4 Resistor with resistance R placed between nodes (i, j, k) and $(i, j, k + 1)$. 147

B.5 Inductor with inductance L placed between nodes (i, j, k) and $(i, j, k + 1)$. 148

B.6 Capacitor with capacitance C placed between nodes (i, j, k) and $(i, j, k + 1)$. . . 149

B.7 Thin wire with radius a, oriented towards the z direction, placed between nodes (i, j, k) and $(i+1, j+1, k+1)$, and the surrounding magnetic field components H_x and H_y. 150

C.1 Resistance R connecting nodes k and m (a); and time-domain ATP equivalent circuit (b). 154

C.2 Inductance L connecting nodes k and m (a); and time-domain ATP equivalent circuit (b). 155

C.3 Capacitance C connecting nodes k and m (a); and time-domain ATP equivalent circuit (b). 156

C.4 Distributed-parameter transmission line connecting nodes k and m (a); and time-domain ATP equivalent circuit (b). 157

LIST OF TABLES

2.1 Relative permittivity (ε_r) and electrical resistivity (ρ) of soils and common materials. 9

2.2 Soil apparent resistance samples and corresponding apparent resistivities. Calculations are valid for an electrode insertion depth c of 20 cm. 11

2.3 Electromagnetic properties and voltage limits of common coatings. 40

3.1 Properties of materials represented in Figure 3.8. 57

3.2 Dimensions of conductors in Figure 3.8. 57

3.3 Tolerable voltage limits for bare soil and exposure times of 20 μs, 60 μs and 100 μs. 65

3.4 Tolerable voltage limits for soil covered with insulating material and exposure times of 20 μs, 60 μs and 100 μs. 66

4.1 Skin depth in meters for different soil resistivities. 78

4.2 Two-layered soil models. 84

4.3 Three-layered soil models. 84

4.4 Four-layered soil models. 84

4.5 Five-layered soil models. 85

4.6 Six-layered soil models. 85

4.7 Soil equivalent resistivities and approximation errors. 86

4.8 Maximum errors, contrast ratios and frequencies. 89

4.9 Average computational load. 89

4.10 Specifications of transmission line conductors in Figure 4.18. 95

4.11 Pipeline characteristics for the system shown in Figure 4.20. 96

4.12 Parameters of the electric traction system and pipeline conductors. 99

4.13 Parameters of the 88 kV distribution system and pipeline conductors. 106

4.14 Apparent resistivity measurements along the 88 kV transmission line. 108

4.15 Soil stratification data along the 88 kV transmission line. 108

4.16 Soil resistivity equivalent and uniform models along the 88 kV transmission line. 110

4.17 Grounding resistances along the 88 kV transmission line. 111

A.1 Green's function values calculated in volts using the proposed program. 139

A.2 Green's function values calculated in volts using software CDEGS. 139

LIST OF SYMBOLS

ε_r	Relative electric permittivity	[p.u.]
ρ	Electrical resistivity	[Ω.m]
ρ_a	Apparent electrical resistivity	[Ω.m]
R_a	Apparent resistance	[Ω]
I_{AB}	Test current between terminals A and B in the Wenner array	[A]
V_{CD}	Voltage drop between terminals C and D in the Wenner array	[V]
ρ_a^m	Measured apparent resistivity	[Ω.m]
a	Electrode spacing in the Wenner array	[m]
c	Electrode insertion depth in the Wenner array	[m]
N	Number of elements (layers, measurements, conductors etc.)	
ρ_i	Resistivity of the i^{th} soil layer in the stratified model	[Ω.m]
h_i	Thickness of the i^{th} soil layer in the stratified model	[m]
$\widehat{J}_0$	Bessel function of first kind and order zero	
k_S	Reflection coefficient between layers S and $S+1$	
Ψ_e	Stratification normalized quadratic error	[p.u.]
d_{zi}	Distance from the transmission line in the EMI zone	[m]
ε	Electric permittivity	[F/m]
μ	Magnetic permeability	[H/m]
I, I_j	Electric current	[A]

E	Induced electromotive force	[V/m]
$Z_{i,j}$	Mutual impedance between conductors i and j	[Ω/m]
ω	System angular frequency	[rad/s]
ε_0	Vacuum electric permittivity ($\approx 8.85 \times 10^{-12}$)	[F/m]
μ_0	Free space magnetic permeability ($= 4\pi \times 10^{-7}$)	[H/m]
$\widehat{\boldsymbol{H_1}}$	Struve function of the first kind	
$\widehat{Y_1}$	Neumann function	
$Z_{i,i}$	Self impedance of conductor i	[Ω/m]
$Z_{s,int}$	Internal part of conductor self impedance	[Ω/m]
$Z_{s,ext}$	External part of conductor self impedance	[Ω/m]
R_{AC}	Conductor ohmic AC resistance	[Ω/m]
r_{ext}	Conductor external radius	[m]
r_{ef}	Effective radius of conductor or bundle	[m]
r_b	Radius of the circumference that contains the conductor bundle	[m]
r_{int}	Conductor internal radius	[m]
ρ_p	Tubular conductor resistivity	[Ω.m]
μ_p	Tubular conductor relative magnetic permeability	[p.u.]
Y_c	Coating shunt admittance	[S/m]
ρ_c	Coating specific resistivity	[Ω.m]
δ_c	Insulation layer thickness	[m]
ε_c	Insulation layer relative permittivity	[p.u.]
Q_i	Charge per unit length of the i^{th} conductor	[C/m]
V	Voltage relative to the earth	[V]
$P_{i,j}$	Mutual potential coefficient between conductors i and j	[m/F]

$P_{i,i}$	Self potential coefficient of conductor i	[m/F]
L, L_j	Length of conductor	[m]
O_j	Center coordinates (x,y,z) of conductor j	[m]
U_P	Potential rise at point P	[V]
$\widehat{G}(P, O_j)$	Green's function for a unit point current source	[Ω]
$\delta(ij)$	Kronecker delta	
d	Depth of point source	[m]
t_i	Depth of the i^{th} soil layer in the stratified model	[m]
δ_j	Leakage current linear density of conductor j	[A/m]
V_G	Potential rise of the grounding electrode	[V]
ξ_j	Normalized leakage current linear density of conductor j	[S/m]
$R_{j,k}$	Mutual resistance between conductors j and k	[Ω]
$\boldsymbol{R}$	Resistance matrix of the grounding system	[Ω]
R_G	Grounding resistance	[Ω]
V_S	Stress voltage in the target conductor	[V]
E_T	Potential rise in the target conductor	[V]
U_E	Local earth potential rise	[V]
V_t	Touch voltage	[V]
I_B	Maximum tolerable current through the human body	[A]
t_s	Exposure time to the shock current	[s]
$V_{t,max}$	Maximum tolerable touch voltage	[V]
R_B	Resistance of the human body	[Ω]
R_{2Fp}	Resistance of two feet in parallel	[Ω]
C_s	Correction factor of the soil covering layer	

ρ_s	Cover material resistivity	[Ω.m]
h_s	Cover layer thickness	[m]
$V_{p,max}$	Maximum tolerable step voltage	[V]
R_{2Fs}	Resistance of two feet in series	[Ω]
Z	Series impedance	[Ω]
Y	Shunt admittance	[S]
Z_C	Characteristic (or surge) impedance	[Ω]
γ	Propagation constant	[m^{-1}]
$\Re$	Real part of a complex number	
$\Im$	Imaginary part of a complex number	
α	Attenuation constant	[Np/m]
β	Phase constant	[rad/m]
v_p	Phase velocity	[m/s]
λ	Wavelength	[m]
$\boldsymbol{Z}$	Series impedance matrix of the transmission line	[Ω/m]
$\boldsymbol{P}$	Matrix of potentials of the transmission line	[m/F]
$\boldsymbol{Y}$	Shunt admittance matrix of the transmission line	[S/m]
$\boldsymbol{T}$	Fortescue transformation matrix	
$\boldsymbol{Z_{012}}$	Sequence domain impedance matrix of the transmission line	[Ω/m]
$\boldsymbol{Y_{012}}$	Sequence domain admittance matrix of the transmission line	[S/m]
$\boldsymbol{T_V}$	Modal matrix associated to the matrix product $\boldsymbol{Z} \cdot \boldsymbol{Y}$	
Λ_k	k^{th} eigenvalue of $\boldsymbol{Z} \cdot \boldsymbol{Y}$	
$\boldsymbol{T_{V,k}}$	k^{th} column of modal matrix $\boldsymbol{T_V}$	
$\boldsymbol{Z_M}$	Modal series impedance matrix of the transmission line	[Ω/m]
$\boldsymbol{Y_M}$	Modal shunt admittance matrix of the transmission line	[S/m]

D_{eq}	Distance of the equivalent parallel section	[m]
L_{eq}, L^{eq}	Length of the equivalent parallel section	[m]
$\boldsymbol{Z_T}$	Impedance matrix of the target line	[Ω]
$\bar{\boldsymbol{I}}_{\boldsymbol{T}}$	Vector of longitudinally induced current phasors	[A]
$\bar{\boldsymbol{E}}$	Vector of induced voltage phasors	[V]
Δt	Simulation time-step	[s]
T_{max}	Maximum simulation time	[s]
L'	Transmission line inductance per unit length	[H/m]
C'	Transmission line capacitance per unit length	[F/m]
τ	Transmission line travel time	[s]
$\boldsymbol{G}$	Circuit conductance matrix	[S]
$\boldsymbol{v(t)}$	Vector of n node voltages	[V]
$\boldsymbol{i(t)}$	Vector of n current sources	[A]
$\boldsymbol{I_H}$	Vector of past current terms	[A]
σ	Electrical conductivity	[S/m]
δ	Skin depth	[m]
ρ_{eq}	Equivalent resistivity of the multilayered soil	[Ω.m]
I_s	Lightning current pulse	[A]
I_0	Current amplitude at the base of the lightning channel	[A]
τ_1	Lightning rise time constant	[s]
τ_2	Lightning half-value time constant	[s]
η	Current amplitude correction factor	
$\vec{H}$	Magnetic field vector	[A/m]
$\vec{E}$	Electric field vector	[V/m]

$\vec{J_i}$	Impressed current density vector	[A/m^2]
$\vec{M_i}$	Impressed magnetic current density vector	[V/m^2]
σ^e	Electric conductivity	[S/m]
σ^m	Magnetic conductivity	[Ω/m]
$\Delta x, \Delta y, \Delta z$	Space discretization steps along directions x, y and z	[m]
N_x, N_y, N_z	Number of Yee cells along directions x, y and z	
c_{max}	Maximum wave propagation velocity	[m/s]
E_x, E_y, E_z	Electric field components along directions x, y and z	[V/m]
H_x, H_y, H_z	Magnetic field components along directions x, y and z	[A/m]
$\varepsilon_x, \varepsilon_y, \varepsilon_z$	Electric permittivity along directions x, y and z	[F/m]
μ_x, μ_y, μ_z	Magnetic permeability along directions x, y and z	[H/m]
$\sigma_x^e, \sigma_y^e, \sigma_z^e$	Electric conductivity along directions x, y and z	[S/m]
$\sigma_x^m, \sigma_y^m, \sigma_z^m$	Magnetic conductivity along directions x, y and z	[Ω/m]
J_{ix}, J_{iy}, J_{iz}	Impressed current densities along x, y and z	[A/m^2]
M_{ix}, M_{iy}, M_{iz}	Impressed magnetic current densities along x, y and z	[V/m^2]
E_x^n, E_y^n, E_z^n	Electric field components along x, y and z at $n\Delta t$	[V/m]
$E_x^{n+1}, E_y^{n+1}, E_z^{n+1}$	Electric field components along x, y and z at $(n+1)\Delta t$	[V/m]
$H_x^{n+\frac{1}{2}}, H_y^{n+\frac{1}{2}}, H_z^{n+\frac{1}{2}}$	Magnetic field components along x, y and z at $(n+\frac{1}{2})\Delta t$	[A/m]
$H_x^{n-\frac{1}{2}}, H_y^{n-\frac{1}{2}}, H_z^{n-\frac{1}{2}}$	Magnetic field components along x, y and z at $(n-\frac{1}{2})\Delta t$	[A/m]
C_{exe}	FDTD update coefficient for E_x^{n+1} associated to E_x^n	
C_{exhz}	FDTD update coefficient for E_x^{n+1} associated to $H_z^{n+\frac{1}{2}}$	
C_{exhy}	FDTD update coefficient for E_x^{n+1} associated to $H_y^{n+\frac{1}{2}}$	
C_{exj}	FDTD update coefficient for E_x^{n+1} associated to $J_{ix}^{n+\frac{1}{2}}$	

C_{eye}	FDTD update coefficient for E_y^{n+1} associated to E_y^n
C_{eyhx}	FDTD update coefficient for E_y^{n+1} associated to $H_x^{n+\frac{1}{2}}$
C_{eyhz}	FDTD update coefficient for E_y^{n+1} associated to $H_z^{n+\frac{1}{2}}$
C_{eyj}	FDTD update coefficient for E_y^{n+1} associated to $J_{iy}^{n+\frac{1}{2}}$
C_{eze}	FDTD update coefficient for E_z^{n+1} associated to E_z^n
C_{ezhy}	FDTD update coefficient for E_z^{n+1} associated to $H_y^{n+\frac{1}{2}}$
C_{ezhx}	FDTD update coefficient for E_z^{n+1} associated to $H_x^{n+\frac{1}{2}}$
C_{ezj}	FDTD update coefficient for E_z^{n+1} associated to $J_{iz}^{n+\frac{1}{2}}$
C_{hxh}	FDTD update coefficient for $H_x^{n+\frac{1}{2}}$ associated to $H_x^{n-\frac{1}{2}}$
C_{hxey}	FDTD update coefficient for $H_x^{n+\frac{1}{2}}$ associated to E_y^n
C_{hxez}	FDTD update coefficient for $H_x^{n+\frac{1}{2}}$ associated to E_z^n
C_{hxm}	FDTD update coefficient for $H_x^{n+\frac{1}{2}}$ associated to M_{ix}^n
C_{hyh}	FDTD update coefficient for $H_y^{n+\frac{1}{2}}$ associated to $H_y^{n-\frac{1}{2}}$
C_{hyez}	FDTD update coefficient for $H_y^{n+\frac{1}{2}}$ associated to E_z^n
C_{hyex}	FDTD update coefficient for $H_y^{n+\frac{1}{2}}$ associated to E_x^n
C_{hym}	FDTD update coefficient for $H_y^{n+\frac{1}{2}}$ associated to M_{iy}^n
C_{hzh}	FDTD update coefficient for $H_z^{n+\frac{1}{2}}$ associated to $H_z^{n-\frac{1}{2}}$
C_{hzex}	FDTD update coefficient for $H_z^{n+\frac{1}{2}}$ associated to E_x^n
C_{hzey}	FDTD update coefficient for $H_z^{n+\frac{1}{2}}$ associated to E_y^n
C_{hzm}	FDTD update coefficient for $H_z^{n+\frac{1}{2}}$ associated to M_{iz}^n

GLOSSARY

AGA	American Gas Association
3LPE	Three-layer polyethylene
ABC	Absorbing boundary condition
ABNT	Associação Brasileira de Normas Técnicas
ATP	Alternative Transients Program
CEM	Computational electromagnetics
CENELEC	European Committee for Electrotechnical Standardization
CIGRÉ	Conseil International des Grands Rèseaux Èlectriques
CFL	Courant-Friedrichs-Lewy condition
CPML	Convolutional perfectly matching layer
ECCAPP	Electromagnetic and Conductive Coupling Analysis of Powerlines and Pipelines
EMF	Electromotive force
EMI	Electromagnetic interference
EMTP	Electromagnetic Transients Program
EN	European standard
EPRI	Electrical Power Research Institute
FBE	Fiber bonded epoxy
FDTD	Finite difference time domain
FEM	Finite element method
FLOPS	Floating-point operations per second

GMR	Geometric mean radius
GPR	Ground potential rise
IE	Integral equation
IEC	International Electrotechnical Commission
IEEE	Institute of Electrical and Electronics Engineers
LCC	Line/Cable Constants
LPS	Lightning protection system
MoM	Method of moments
NACE	National Association of Corrosion Engineers
NBR	Norma Técnica Brasileira
ONS	Operador Nacional do Sistema Elétrico
PDE	Partial differential equation
SP	Standard practice

CHAPTER 1

INTRODUCTION

1.1 PREFACE

The problem of mutual electromagnetic influences between transmission lines and other metallic structures, such as gas and oil pipelines, fences, railroads etc., remains current and still poses challenges to the scientific community. Due to the increasingly restrictive environmental regulations regarding the use of space, cases of interference in right-of-ways shared with power lines have become common and progressively more complex, which has motivated various researches in this area (CIGRÉ WG-36.02, 1995; PEABODY; VERHIEL, 1971; DACONTI; BRASIL, 1986; CHRISTOFORIDIS *et al.*, 2003a; QI *et al.*, 2013).

A metallic structure, when exposed to the energized conductors of a transmission line, is subjected to a variety of phenomena, which results in the rise of metal potential along its path due to inductive, capacitive and conductive coupling mechanisms between the two installations, in both steady-state and transient regimes (CIGRÉ WG-36.02, 1995; CHRISTOFORIDIS *et al.*, 2003a). These coupling mechanisms depend on the geometry of the structures, type and arrangement of conductors, voltage and current levels, presence and type of coating, soil electrical resistivity, among other factors. As a consequence, risks to the integrity of assets and people arise, such as: electrical shock caused by touch or step voltages, breakdown of the dielectric coating, metal electrochemical corrosion and damage to equipment caused by current imposition (CIGRÉ WG-36.02, 1995).

Conversely, the presence of a metallic structure in the vicinity of the transmission line, especially for long extensions of parallelism, also imposes the aforementioned coupling mechanisms to the energized power line conductors, which directly influences the calculation of its impedances. In applications that rely on the knowledge of transmission line parameters, such as short-circuit studies, protection design and fault location algorithms, the presence of an

interfering metallic structure can greatly affect the system response and may result in mislead adjustments of protection or fault location devices in situations where the interference is not properly taken into account (MARTINS-BRITTO, 2017b).

Due to the nature of the facilities and hazards involved, the problem of interferences is often addressed during the project design phase, by means of numerical simulations to predict induced currents and voltages (CIGRÉ WG-36.02, 1995; DABKOWSKI; TAFLOVE, 1978a). If violations to established safety criteria are detected, mitigation solutions are designed accordingly (DABKOWSKI; TAFLOVE, 1978b). Professionals in charge of such designs and studies are subject both to great technical and ethical liability, since they are responsible for ensuring conformity to safety standards while maintaining installation costs under budget constraints. Building realistic simulation models is of substantial value for this task, as it enables the user to work with less conservative assumptions and safety coefficients, by accounting for more variables and providing greater control over uncertainties.

Soil resistivity is a key parameter which is present in a variety of phenomena relevant to power system analysis, including transient simulations, low-frequency electromagnetic interferences, transmission line parameters, short-circuit computations and shield-wire current distribution (STEVENSON; GRAINGER, 1994; MARTINS-BRITTO, 2017b; CIGRÉ WG-36.02, 1995). At the same time, soil parameters are a widely recognized source of error in such problems (DAS *et al.*, 2014), due to the complexity of actual structures, which are highly variable in their properties and rarely homogeneous. Soils are composed of solid, liquid and gaseous elements, whose electrical resistivity depends on the presence of water, particle porosity, type of electrolyte and temperature (HE *et al.*, 2013). Therefore, field measurements are necessary and processing the so-called apparent resistivities to build an accurate soil model requires complex calculations (TAKAHASHI; KAWASE, 1990).

In a previous publication (MARTINS-BRITTO, 2017b), the author proposed a set of tools to compute steady-state low-frequency induced voltages and currents by an overhead power line into a target underground pipeline, accounting for arbitrary cross-sections, any number of phases, shield/neutral and pipeline conductors. Inductive and conductive coupling effects were evaluated in terms of a two-layered horizontal soil structure, to which N-layered soil models were reduced using a simple average formula. Capacitive coupling mechanisms were neglected,

because simulations were focused on underground interfered structures.

As the natural continuity, it is desired to develop the necessary tools to handle general target structures and arbitrary soil models, including finite volumes with different constitutive parameters and variations along the transmission line axis, as well as the effects of transients commonly observed in power systems. By addressing the limitations of the previous work, it is sought to contribute with the construction of more accurate electromagnetic interference (EMI) simulation models, which may be useful in a wide range of problems relevant to the industry.

1.2 OBJECTIVES AND SCOPE OF WORK

The main objective of this work is to develop new efficient techniques to simulate the mutual electromagnetic interferences involving transmission lines and metallic structures, both in steady-state and transient conditions. This goal can be broken down into the following specific objectives:

1. Review of the fundamental theoretical concepts related to the electromagnetic coupling phenomena;
2. Development of techniques to effectively model the multilayered and/or heterogeneous characteristic of real soils in calculations of ground return impedances and potentials produced by conductive coupling;
3. Development of techniques to determine the return current distribution along neutral/shield wires in transmission lines under fault conditions;
4. Development of a full wave electromagnetic approach to carry out high-frequency interference simulations in realistic domain models using the finite difference time domain (FDTD) method;
5. Development of time-domain circuit models of the inductive, capacitive and conductive interference mechanisms using the Alternative Transients Program (ATP).

The tools and routines described throughout this work are developed to be as general as possible, i.e., capable of handling arbitrary geometries composed of any number of phases,

neutral/shield wires and target structures, aboveground or underground, over soil models made of N-layers or finite volumes with different properties, without the need to modify the program codes and models. Results are validated by means of comparisons with analytical expressions, industry-standard software and/or case studies reported in the literature.

1.3 CONTRIBUTIONS

The main contributions of this thesis are the following innovations:

- A systematic multipurpose approach to address EMI problems involving power lines is developed, with a set of integrated methods based on modern techniques to model, simultaneously, the inductive, conductive and capacitive coupling mechanisms. Most documents in the literature provide individual contributions to the study of specific phenomena or variables of interest, such as soil resistivity analysis, electromagnetic induction or grounding system response, with scarce reports where all relevant effects are superposed in order to obtain a meaningful response in the EMI context;

- A technique to model soil structures composed of N horizontal layers in ground return impedances is proposed, differently from current approaches that regard the earth as a homogeneous medium. A novel formula which enables multilayered soils to be introduced into industry-standard software and classic formulations, such as ATP and Carson equation, is proposed and validated;

- A detailed transmission line circuit model is developed for simulations, where line spans, grounding structures, phase conductors, shield wires and interfered installation are modeled and analyzed individually, allowing the construction of complex designs of long transmission lines, accounting for variations along its course (geometry and conductor changes, transpositions, soil heterogeneities) and providing direct access to current and voltage responses for all conductors at every line section. A variety of supporting routines is developed to build the circuit model from the actual transmission line geometry and configuration, making it viable to simulate arbitrary systems. This has the potential to greatly benefit current analysis practices, since components that are usually implicit into

line impedances (shield wires and grounding structures) may be analyzed explicitly, and well-known sources of uncertainties (soil resistivity and topography) may be modeled with higher precision;

- All methods are developed in the time-domain, allowing the determination of steady-state and transient responses of structures subject to interferences. This is an important enhancement to current simulation models, since the majority of EMI studies discussed in the specialized literature, as well as commercial software widely employed in the industry, are concerned with the phasor response of the target system, even in fault conditions. With the proposed techniques, it is possible to simulate a broad range of electromagnetic transients, from power system frequencies to very fast transients, such as lightning discharges.

With the products of this thesis, it is possible to carry out a variety of relevant tasks related to EMI studies, with improved accuracy, involving realistic models of complex systems, such as:

- Computation of steady-state and transient voltages and currents induced by electromagnetic interferences between power lines and metallic structures, such as pipelines, fences, rails etc., in complex right-of-way layouts, multilayered soils and accounting for variations along the transmission line course;
- Simulation of power grounding systems, including transient behavior, in arbitrary soil models (horizontal and vertical layers, finite volumes), different materials, such as tower foundations concrete, steel frames, bentonite etc., with computations of grid resistance, ground potential rise, touch voltages and step voltages;
- Calculation of transmission line parameters under interference conditions, accounting for stratified soil models and variations along the right-of-way, allowing for accurately conducting parametric studies related to short-circuits, shield wire design, fault location algorithms and protection relays;
- Construction of realistic lightning discharge simulation models, accounting for actual tower structures and geometry of shield wires, lightning discharge paths and multiple strokes;

- Evaluation of electromagnetic fields distribution around transmission line conductors with arbitrary configurations, for emission studies, such as radio-noise and visual corona;
- Design and simulation of mitigation solutions: surge protection devices, grounding electrodes, shielding cages and/or conductors, gradient control wires etc.

With respect to peer-review and publication of results related to this thesis research, the following papers are selected and listed in chronological order and of importance:

1. A. G. MARTINS-BRITTO; F. V. LOPES; S. R. M. J. RONDINEAU, "Multilayer Earth Structure Approximation by a Homogeneous Conductivity Soil for Ground Return Impedance Calculations", *IEEE Transactions on Power Delivery*, v. 35, n. 2, p. 881-891, ISSN 1937-4208, DOI 10.1109/TPWRD.2019.2930406;
2. A. G. MARTINS-BRITTO; F. V. LOPES; S. R. M. J. RONDINEAU, "Power Line Transient Interferences on a Nearby Pipeline Due to a Lightning Discharge", in *International Conference on Power Systems Transients (IPST 2019)*. Perpignan, France: IPST, 2019;
3. A. G. MARTINS-BRITTO; F. V. LOPES; S. R. M. J. RONDINEAU, "Transient Response of the Grounding Grid of a Power Line Tower Subject to a Lightning Discharge", in *WCNPS 2018: 3rd Workshop on Communication Networks and Power Systems*. Brasília, Brazil: IEEE Xplore, 2018.

1.4 THESIS STRUCTURE

The current chapter highlights the context under which the research is inserted and its relevance and describes the objectives, scope of work and main contributions of this thesis.

Chapter 2 provides the theoretical basis related to electromagnetic interference mechanisms and fundamental equations, soil resistivity analysis, electrical safety criteria and transmission line models. A review of the specialized literature regarding EMI studies involving power lines is performed, with a brief history of the main contributions and description of the state-of-the-art.

Chapter 3 presents an FDTD implementation devised to conduct high-frequency transients simulations, in special of lightning discharges, on realistic domain representations made of

arbitrary materials. The FDTD method is leveraged with the construction of accurate models, in which the actual tower structure, concrete foundations and steel-frames are fully accounted. Case studies are performed to investigate the transient behavior of grounding electrodes and potentials transferred to the interfered system due to conductive coupling, as well as the mechanisms of lightning protection and shielding effects.

Chapter 4 describes the implementation of a circuit-theory based model on ATP, designed to simulate time-domain responses due to inductive, conductive and capacitive coupling mechanisms in large systems. An innovative method to model multilayered soil structures in ground return problems is proposed and validated, with a discussion about its validity domain and limitations with respect to frequency. A variety of case studies are presented and discussed, including steady-state analysis and transients commonly verified in power systems.

Chapter 5 exposes the final considerations and points directions for future continuity of this work.

CHAPTER 2

FUNDAMENTAL CONCEPTS

The study of electromagnetic interferences involving power lines and metallic facilities employs concepts from several fields of research, including geophysics, electromagnetism, electrical safety theory and power systems analysis. This chapter describes the main topics of relevance for the understanding of EMI phenomena and exposes the fundamental equations and methods intended to be used and/or enhanced in the subsequent chapters of this thesis.

2.1 SOIL RESISTIVITY ANALYSIS

Soil resistivity is a variable present in the three main coupling mechanisms to which installations under interference conditions are subjected: inductive, capacitive and conductive. Resistivity affects the response of grounding grids, earth return impedances and, consequently, transmission line parameters and induced potentials. It also determines the extension of the electromagnetic interference zone and is associated with electrochemical corrosion of metals (CIGRÉ WG-36.02, 1995; NACE, 2007). High resistivity soils are a recognized challenge in power grounding design and studies report that, in interference situations, the induced voltage response tends to be aggravated by high resistivity values, with frequent violations of safety criteria (MARTINS-BRITTO, 2017b).

Soils are complex structures, composed of solid, liquid and gaseous phases. The solid phase is usually made of minerals and organic matter; the liquid phase is the water solution in the form of moisture content; and the gas phase is represented by the air in between solid particles (HE *et al.*, 2013). The predominant conduction mechanism in soils is the electrolytic conduction in the solutions of water-bearing materials (HE *et al.*, 2013). Under certain conditions, metallic conduction, electronic semiconduction and solid electrolytic conduction may also occur (HADDAD; WARNE, 2009). Moist soils at low frequencies (below 100 kHz) behave primarily

as conductors with nonmagnetic properties (STEINBERG; LEVITSKAYA, 2001). Table 2.1 contains typical electromagnetic parameters (dielectric constant and electrical resistivity) of soils and common materials, compiled from several sources.

Table 2.1. Relative permittivity (ε_r) and electrical resistivity (ρ) of soils and common materials.

Dry materials	ε_r	ρ **[Ω.m]**	**Saturated materials**	ε_r	ρ **[Ω.m]**
Air	1	10^9–10^{15}	Distilled water	81	10^5
Sand and gravel	2–6	10^5	Fresh water	81	2000
Clay	5	300–5000	Sea water	81	<10
Shale and dry silt	5	1000	Sand	20–30	1000–10^4
Limestone gravel	4	7×10^6	Silt	10	100–1000
Sandy soil	2.6	1000–8000	Clay	40	<10
Loamy soil	2.4	300–5000	Sandy soil	25	<150
Granite	5	1500–10^4	Granite	7	1000
Limestone	4	500–5000	Limestone	8	500
Salt	5–6	1000–10^5	Loamy soil	15	20
Granite gravel	5	1.5×10^6–4.5×10^6	Granite gravel	7	5000–10^4
Basalt	6	1000	Silt	30	10
Diabase	7	100	Shale	7	10
Iron	1	9.70×10^{-8}	Limestone gravel	8	2000–3000
Carbon steel	1	1.43×10^{-7}	Diabase	8	10
PVC	8	15×10^{17}	Basalt	8	100
Asphalt	3–5	2×10^6–30×10^6	Asphalt	3–5	10^4–6×10^6
Dry concrete	5.5	10^6–10^9	Wet concrete	12.5	21–100

Source: (PORSANI; MALAGUTTI, 1999; ABNT, 2012; SERAN *et al.*, 2017; PAWAR *et al.*, 2009; IEEE, 2000).

Almost all natural soils are heterogeneous and anisotropic (MUALEM, 1984). Heterogeneity is related to lithology (thin soft/stiff layers embedded in a stiffer/softer media) and the inherent spatial soil variability, which is the variation of soil properties from one point to another in space due to different deposition conditions and different geotechnical histories (ELKATEB *et al.*, 2003). Anisotropy is related to differences between particles sizes and shapes (TODD, 2006). Due to these characteristics, appropriate field surveys and specific modeling methods should be employed in order to accurately describe the soil structure for the purposes of EMI studies.

There are several techniques available for measuring the soil resistivity from the earth surface, among which the Wenner method is widely employed in practical situations, due to its simplicity. The method consists of measuring the so-called apparent resistivity (ρ_a) for a configuration of test electrodes that corresponds to the soil depth where the reading is taken (WENNER, 1915). The process of deriving a soil model structured in layers with finite thicknesses and resistivities is known as stratification (HE *et al.*, 2013; ZHANG *et al.*, 2005; ABNT, 2012).

2.1.1 Wenner method

Figure 2.1 illustrates the Wenner method for measuring soil apparent resistivity. Four electrodes are placed collinearly and equally spaced of a meters, with an insertion depth into the soil of c meters. A known test current I_{AB} is injected through terminal A and collected at terminal B, resulting in a voltage drop of V_{CD} between terminals C and D and, therefore, an apparent resistance $R_a = V_{CD}/I_{AB}$, corresponding to the soil equivalent resistance in the electrical path at depth a (MOMBELLO *et al.*, 1996; WENNER, 1915).

Figure 2.1. Typical Wenner array for measurement of soil apparent resistivity. The electrode spacing a is numerically equal to depth at which the reading is taken.

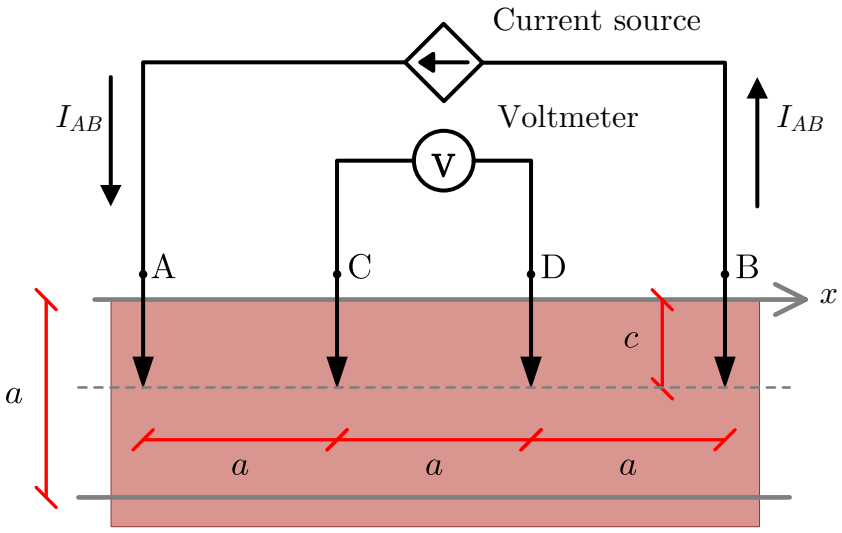

Source: own authorship.

The apparent resistivity relates to the apparent resistance R_a according to the following

expression (WENNER, 1915; ABNT, 2012):

$$\rho_a^m = \frac{4\pi a R_a}{1 + \frac{2a}{\sqrt{a^2+4c^2}} - \frac{a}{\sqrt{a^2+c^2}}}, \tag{2.1}$$

in which ρ_a^m is the measured apparent resistivity at depth a, in Ω.m; R_a is the apparent resistance, in Ω; a is the electrode spacing, in meters; and c is the electrode insertion depth, in meters. For a proper interpretation of the soil geophysics, it is necessary to collect a sufficient amount of samples of R_a, for several depths and at different directions, in order to establish a meaningful profile $\rho_a^m \times a$.

Table 2.2 exemplifies the application of (2.1) using field measurements data provided in (ABNT, 2012). Figure 2.2 illustrates the corresponding apparent resistivity profile.

Table 2.2. Soil apparent resistance samples and corresponding apparent resistivities. Calculations are valid for an electrode insertion depth c of 20 cm.

a [m]	R_a [Ω]	ρ_a^m [Ω.m]
2	53.20	680
4	33.28	840
8	18.48	930
16	6.86	690
32	1.64	330

Source: adapted from (ABNT, 2012).

Figure 2.2. Apparent resistivity profile for measurements in Table 2.2.

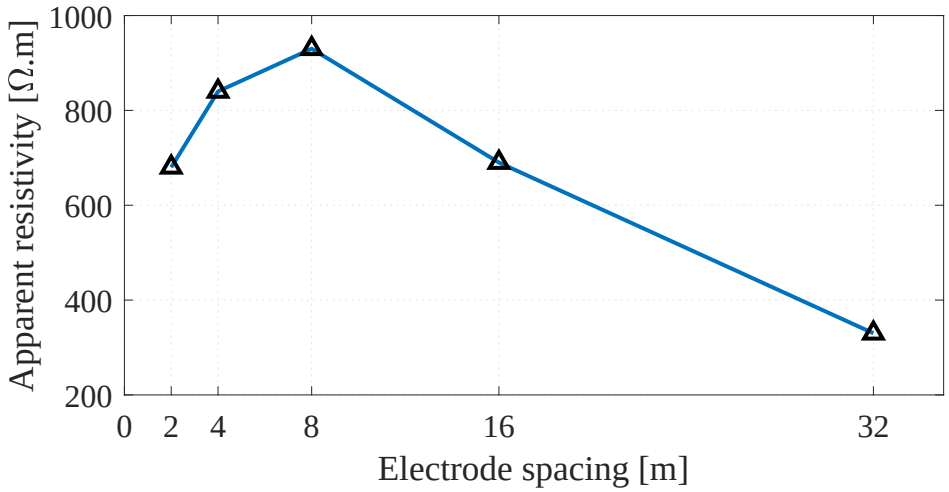

Source: adapted from (ABNT, 2012).

2.1.2 Multilayered soil models

Extracting information from apparent resistivity data is often the most complex step of the soil modeling process. The objective is to determine a set of parameters that accurately describe the actual soil structure. Usually it is reasonable to approximate the earth by a horizontally stratified multilayer structure, as resistivity tends to change more steeply with depth than with lateral distance (ZHANG *et al.*, 2005; IEEE, 2000). This procedure is illustrated in Figure 2.3.

Figure 2.3. Real soil (a); and horizontally layered model described by parameters $[\rho_1, \rho_2, \rho_3, \rho_4]$ and $[h_1, h_2, h_3, h_4]$ (b).

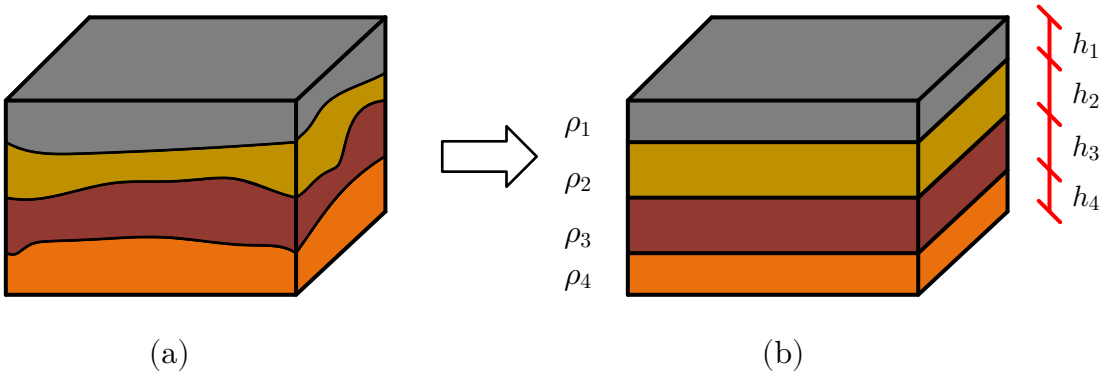

Source: adapted from (ABNT, 2012).

In the general case, represented in Figure 2.4, the multilayered soil structure is described by $(N-1)$ layers with resistivities $[\rho_1, \rho_2, \rho_3, ..., \rho_{N-1}]$ and thicknesses $[h_1, h_2, h_3, ..., h_{N-1}]$, on top of a N^{th} layer, known as deep layer, with resistivity ρ_N, whose thickness is considered to extend to infinity.

Figure 2.4. N-layered horizontal soil model with finite resistivities $[\rho_1, \rho_2, \rho_3, ..., \rho_N]$ and thicknesses $[h_1, h_2, h_3, ..., h_{N-1}]$.

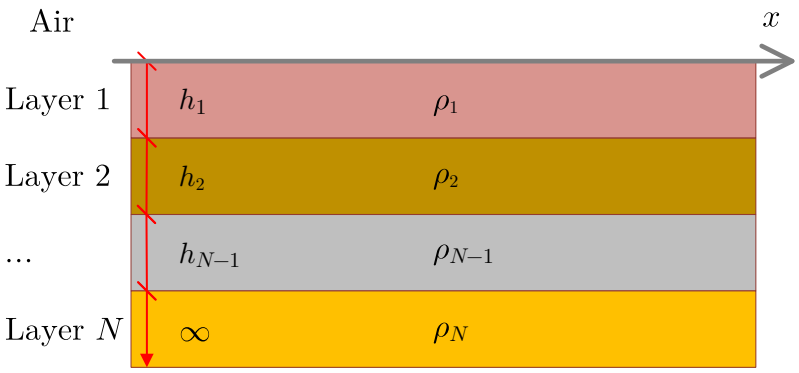

Source: own authorship.

The particular case $N = 1$ describes a homogeneous, or uniform, soil model, in which the electrical resistivity is simply the arithmetic mean of the measured apparent resistivities (IEEE, 2000). The uniform model holds theoretical value and is useful for quick simplified estimations, but it represents few practical cases, since real soil structures present in nature are reported to be composed of three to five layers (WHELAN *et al.*, 2010).

For $N \geq 2$, the soil apparent resistivity behavior is determined by solving Laplace equation for the scalar electric potential and setting boundary conditions at layer interfaces (HE *et al.*, 2013).

For a soil structure composed by N layers and parameters $[\rho_1, \rho_2, \rho_3, ..., \rho_N]$ and $[h_1, h_2, h_3, ..., h_{N-1}]$, the analytical expression for the apparent resistivity is (TAKAHASHI; KAWASE, 1990; ZHANG *et al.*, 2005):

$$\rho_a = \rho_1 \left[1 + 2F_N(a) - F_N(2a)\right], \tag{2.2}$$

$$F_N(x) = 2x \int_0^\infty \frac{K_{N,1} e^{-2\lambda h_1}}{1 - K_{N,1} e^{-2\lambda h_1}} \widehat{J}_0(\lambda x) d\lambda, \tag{2.3}$$

in which $\widehat{J}_0$ is the Bessel function of the first kind and order zero; λ is an auxiliary integration variable that represents the spatial frequency of the Fourier spectrum and can be physically associated to the energy attenuation throughout the layers (TSIAMITROS *et al.*, 2007); and $K_{N,1}$ is the soil structure kernel function, defined recursively as:

$$K_{N,s} = \frac{k_s + K_{N,s+1} e^{-2\lambda h_{s+1}}}{1 + k_s K_{N,s+1} e^{-2\lambda h_{s+1}}}, \tag{2.4}$$

$$K_{N,N-1} = k_{N-1}, \tag{2.5}$$

$$k_S = \frac{\rho_{\mathrm{S}+1} - \rho_{\mathrm{S}}}{\rho_{\mathrm{S}+1} + \rho_{\mathrm{S}}}, \tag{2.6}$$

$$k_{N-1} = \frac{\rho_{\mathrm{N}} - \rho_{\mathrm{N}-1}}{\rho_{\mathrm{N}} + \rho_{\mathrm{N}-1}}, \tag{2.7}$$

in which k_S is known as the reflection coefficient between layers S and $S + 1$, ranging between values -1 and $+1$. The improper integral in (2.3) quickly decays to zero, such that the upper limit may be truncated to a convenient choice. Normally, integration within the interval $[0, \frac{4}{h_1}]$ is enough to produce accurate results (HE *et al.*, 2013).

Inversion of soil parameters consists of determining $[\rho_1, \rho_2, \rho_3, ..., \rho_N]$ and $[h_1, h_2, h_3, ..., h_{N-1}]$ from the measured values of $\rho_a^m \times a$. Since the theoretical value of ρ_a is known from (2.2)-(2.7),

the following error function can be defined:

$$\Psi_e\left(\rho_1, \rho_2, \ldots, \rho_N, h_1, h_2, \ldots, h_{N-1}\right) = \sum_{j=1}^{M} \left[\frac{\rho_{a,j}^m - \rho_{a,j}}{\rho_{a,j}^m}\right]^2, \tag{2.8}$$

in which Ψ_e is the stratification normalized quadratic error; and M is the number of apparent resistivity measurements. Soil parameters are then determined by setting an initial estimate and employing an appropriate minimization technique using (2.8), which has an explicit and differentiable form, as objective function. For this purpose, methods such as those based on steepest descent, Levenberg-Marquardt and/or evolutionary algorithms are reported to provide satisfactory results (ALAMO, 1993; MARTINS-BRITTO, 2017b; DAWALIBI; BLATTNER, 1984).

2.2 INDUCTIVE COUPLING MECHANISM

Inductive coupling, also referred as magnetic coupling, occurs between transmission lines and aboveground or underground metallic installations with a parallel approximation between conductors. The installation exposed to interferences is often known as target, or victim circuit, and is subjected to induced voltages caused by the time varying magnetic fields around the energized transmission line conductors. When there is magnetic flux through the target conductor, electromotive forces (EMF) arise, causing current flow in the interfered structure.

Electromagnetic interferences caused by inductive coupling mechanisms depend essentially on the following parameters (CIGRÉ WG-36.02, 1995):

- **Current magnitude:** in steady-state conditions, induced EMF increases with the transmission line current load. During transients, EMF depends on the phase and shield wire current magnitudes;
- **Distance between structures:** induced EMF decreases with distance between the power line and the target structure;
- **Length of exposure:** induced EMF increases linearly with the exposure length within the EMI zone;

- **Soil resistivity:** soil resistivity determines system's self and mutual impedances, which, on their turn, define the magnitude of the induced EMF. Resulting voltages increase with the soil resistivity;
- **Transmission line characteristics:** installation (overhead or underground), circuit type (single or double), cross-section layout (vertical or horizontal configuration and phase arrangement), transposition and presence of shield wires determine the induced coupling response;
- **Target system characteristics:** material type, cross-section, presence of coating and its parameters affect the inductive coupling response.

2.2.1 Electromagnetic interference zone

The electromagnetic interference zone, represented in Figure 2.5, corresponds to the linear extension along the target route where the induced EMF produced by a current with ground return path exceeds 10 V/km.kA, i.e., the region where a ground return current of 1000 A produces an induced EMF greater than 10 V per kilometer of exposure (CIGRÉ WG-36.02, 1995).

Figure 2.5. Electromagnetic interference zone, with distances in meters. The exposure length corresponds to the line segment $AA' + A'B$.

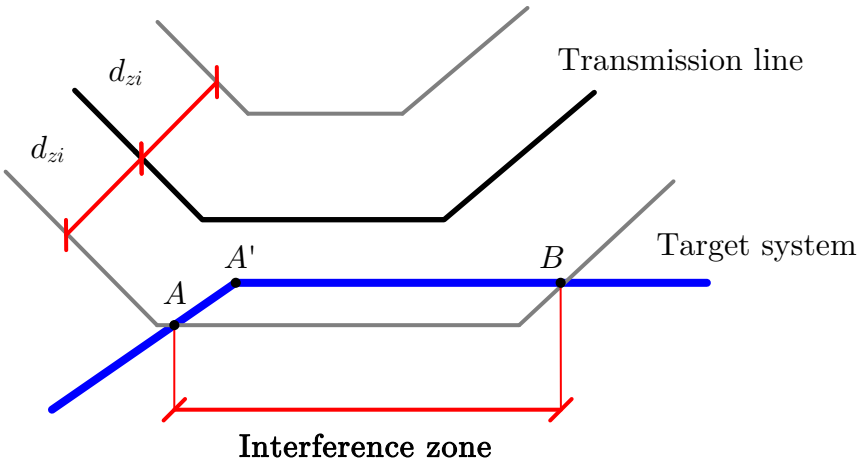

Source: adapted from (CIGRÉ WG-36.02, 1995).

The EMI zone is determined numerically, in meters, by the distance d_{zi} from the transmission line axis, as a function of the soil resistivity ρ expressed in (2.9):

$$d_{zi} = 200\sqrt{\rho}, \tag{2.9}$$

in which ρ is the soil resistivity, given in Ω.m.

2.2.2 Calculation of mutual impedances over uniform soil

Figure 2.6 describes a system composed of two parallel conductors i and j over uniform soil, described by resistivity ρ, permittivity ε and permeability μ. As most soil types are nonmagnetic, permeability μ is assumed to be equal to the free space value μ_0 (TSIAMITROS *et al.*, 2007). This situation may be regarded, without loss of generality, as the basic block for building interference models composed of crossings and/or oblique approximations, including combinations of overhead and underground conductors, as complex geometries can be split into several cells expressed in terms of equivalent parallelisms (CIGRÉ WG-36.02, 1995; MARTINS-BRITTO, 2017b; FURLAN, 2015).

If conductor i is energized with a current I, the resulting magnetic field in the vicinities of conductor j induces electromotive forces in the exposed conductor expressed by:

$$E = Z_{i,j} \times I, \tag{2.10}$$

in which E is the induced EMF, in volts per unit length; I is the source current, in ampères; and $Z_{i,j}$ is the mutual impedance between conductors i and j with ground return path, given in ohms per unit length according to the following general equation:

$$Z_{i,j} = \frac{j\omega\mu_0}{2\pi} \ln\left(\frac{D'_{i,j}}{D_{i,j}}\right) + \Delta Z_{i,j}, \tag{2.11}$$

$$\Delta Z_{i,j} = \frac{j\omega\mu_0}{\pi} \int_0^\infty e^{-H\lambda} \cos(\lambda D) \hat{F}(\lambda) d\lambda, \tag{2.12}$$

in which ω is the angular frequency, in rad/s; $\mu_0 = 4\pi \times 10^{-7}$ H/m is the free space magnetic permeability constant; H, D, $D_{i,j}$ and $D'_{i,j}$ are the relative distances represented in Figure 2.6, in meters, with: $H = |y_i - y_j|$, $D = |x_i - x_j|$, $D_{i,j} = \sqrt{(x_i - x_j)^2 + (y_i - y_j)^2}$ and $D'_{i,j} = \sqrt{(x_i - x'_j)^2 + (y_i - y'_j)^2}$; and $\hat{F}(\lambda)$ is a function determined by the problem boundary conditions (PAPAGIANNIS *et al.*, 2005; CARSON, 1926). Although Figure 2.6 explicitly

Figure 2.6. Two overhead conductors above a semi-infinite uniform ground and its images arranged symmetrically with respect to the plane $z = 0$, with distances H, D and D′ given in meters. Soil structure is described by permeability μ, permittivity ε and resistivity ρ.

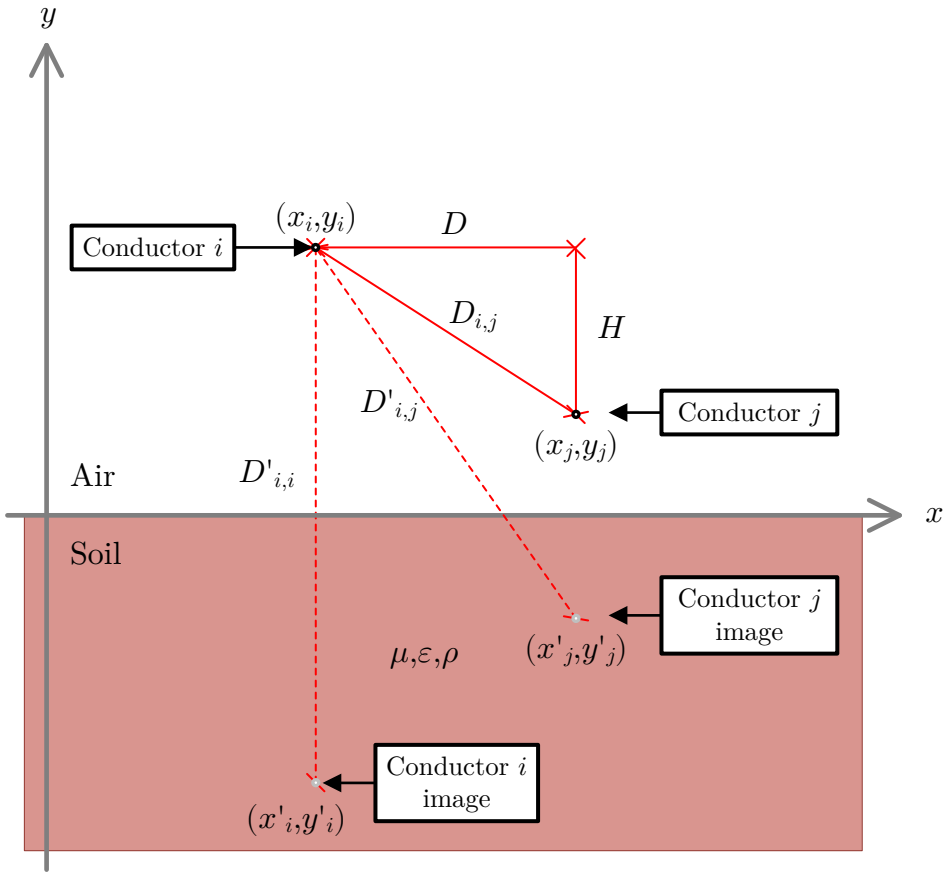

Source: own authorship.

shows the case of two overhead conductors, expressions (2.11)-(2.12) hold valid for calculations involving underground structures as well, with the appropriate adjustments in conductor coordinates (MARTINS-BRITTO, 2017b).

The first term of (2.11) may be regarded as the ground return impedance for a perfectly conductive soil (CARSON, 1926). The term $\Delta Z_{i,j}$ represents the effects of the soil with finite resistivity, including losses in the earth return path (CARSON, 1926; NAKAGAWA *et al.*, 1973; PAPAGIANNIS *et al.*, 2005; MARTINS-BRITTO, 2017b).

Function $\hat{F}(\lambda)$ depends on the soil structure. Assuming a semi-infinite uniform ground, Carson equation has $\hat{F}(\lambda)$ with the form:

$$\hat{F}(\lambda) = \frac{1}{\lambda + \sqrt{\lambda^2 + \frac{j\omega\mu_0}{\rho} - \omega^2\mu_0\varepsilon}}, \tag{2.13}$$

in which ρ is the local soil electrical resistivity, in Ω.m; and ε is the local soil electric permittivity,

in F/m (CARSON, 1926).

Carson equation has been studied by several researchers over the years, with approaches that range from power series expansions to derivation of simplified formulas (CARSON, 1926; CIGRÉ WG-36.02, 1995; DERI *et al.*, 1981; AMETANI *et al.*, 2009). A closed-form solution has been provided by Carson himself and further studied by Theodoulidis, who provided an exact solution in terms of a Struve function of first kind with complex argument (CARSON, 1926; THEODOULIDIS, 2015; AARTS; JANSSEN, 2003). It can be shown that the improper integral of (2.13) in (2.12) can be computed analytically, with 14 significant digits precision and without convergence problems, by using the variable transformation:

$$u_1 = \sqrt{\left(\frac{j\omega\mu_0}{\rho} - \omega^2\mu_0\varepsilon\right)}\,(H - jD), \tag{2.14}$$

$$u_2 = \sqrt{\left(\frac{j\omega\mu_0}{\rho} - \omega^2\mu_0\varepsilon\right)}\,(H + jD), \tag{2.15}$$

which leads to:

$$\begin{aligned}&\int_0^\infty \frac{2e^{-H\lambda}}{\lambda + \sqrt{\lambda^2 + \frac{j\omega\mu_0}{\rho} - \omega^2\mu_0\varepsilon}}\cos(\lambda D)\,d\lambda = \\ &\frac{\pi}{2u_1}[\widehat{\boldsymbol{H}_1}(u_1) - \widehat{Y}_1(u_1)] - \frac{1}{u_1^2} + \frac{\pi}{2u_2}[\widehat{\boldsymbol{H}_1}(u_2) - \widehat{Y}_1(u_2)] - \frac{1}{u_2^2},\end{aligned} \tag{2.16}$$

in which $\widehat{\boldsymbol{H}_1}$ is the Struve function of the first kind and $\widehat{Y}_1$ is the Neumann function (THEODOULIDIS, 2015; BOYCE; DIPRIMA, 2012; AARTS; JANSSEN, 2003; ABRAMOWITZ; STEGUN, 1965).

Approaches deriving from the original Carson contribution, which account for the soil as a uniform structure, have been widely employed in the industry and are present in well-known professional software, among which a remarkable example is the Line/Cable Constants ATP routine.

2.2.3 Calculation of mutual impedances over multilayered soil

Figure 2.7 describes a system composed of two overhead conductors above a soil structure with N layers, which are defined by permeability μ_n, permittivity ε_n and resistivity ρ_n, with $1 \leq n \leq N$, in which n represents the n^{th} soil layer.

Figure 2.7. Two overhead conductors above N layers of soil, with distances H, D, D′ and h_n given in meters. Each soil layer is described by permeability μ_n, permittivity ε_n, resistivity ρ_n and thickness h_n. Thickness of layer N extends to infinity.

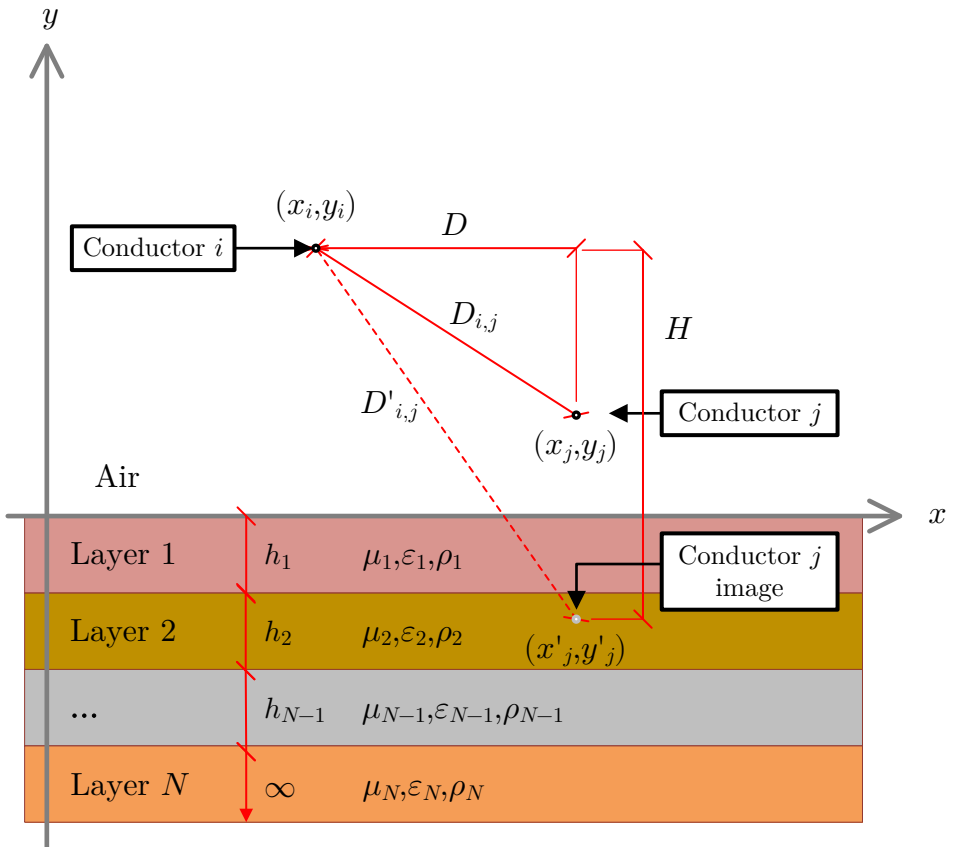

Source: own authorship.

The analytical expression for the N-layered case has been developed by Nakagawa *et al.* (1973) from the Helmholtz equation of the Hertzian vector. The recursive solution is (2.11)-(2.12) with $\hat{F}(\lambda)$ on the form of:

$$\hat{F}(\lambda) = \frac{\hat{F}_1(\lambda) + \hat{G}_1(\lambda)}{(\lambda + \mu_0 b_1)\hat{F}_1(\lambda) + (\lambda - \mu_0 b_1)\hat{G}_1(\lambda)}, \tag{2.17}$$

$$\begin{aligned} \hat{F}_{N-1}(\lambda) &= b_{N-1} + b_N, \\ \hat{G}_{N-1}(\lambda) &= (b_{N-1} - b_N)e^{-2\alpha_{N-1}t_{N-1}}, \end{aligned} \tag{2.18}$$

$$\vdots$$

$$\begin{aligned} \hat{F}_m(\lambda) &= (b_m + b_{m+1})\hat{F}_{m+1}(\lambda) + (b_m - b_{m+1})\hat{G}_{m+1}(\lambda)e^{2\alpha_{m+1}t_m}, \\ \hat{G}_m(\lambda) &= [(b_m - b_{m+1})\hat{F}_{m+1}(\lambda) + (b_m + b_{m+1})\hat{G}_{m+1}(\lambda)e^{2\alpha_{m+1}t_m}]e^{-2\alpha_m t_m}, \end{aligned} \tag{2.19}$$

$$t_1 = h_1, t_m = \sum_{1}^{m} h_i, (1 \leq m \leq N-2), \tag{2.20}$$

$$\alpha_i = \sqrt{\lambda^2 + k_0^2 - k_i^2}, b_i = \alpha_i/\mu_i, \tag{2.21}$$

$$k_i^2 = -j\omega\mu_i\left(\frac{1}{\rho_i} + j\omega\varepsilon_i\right), k_0^2 = \omega^2\mu_0\varepsilon_0, \quad (i = 1,2,...,N), \tag{2.22}$$

in which h_i is the thickness of the i^{th} layer, in meters; $\varepsilon_0 \approx 8.85 \times 10^{-12}$ F/m is the vacuum electric permittivity; μ_0 is the free space magnetic permeability, in H/m; μ_i is the magnetic permeability of the i^{th} layer, in H/m; ε_i is the electric permittivity of the i^{th} layer, in F/m; ρ_i is the resistivity of the i^{th} layer, in Ω.m; and ω is the angular frequency, in rad/s.

Derived directly from Maxwell's equations, the model proposed by Nakagawa *et al.* (1973) provides an exact solution to the mutual impedance problem over multilayered soils. Applications of this model have been reported in the literature for soils composed of two and three layers (NAKAGAWA *et al.*, 1973; PAPAGIANNIS *et al.*, 2005), despite the fact that the model is natively capable of handling the general N-layered case.

2.2.4 Calculation of self impedances with ground return path

Mutual impedances discussed in the preceding section define EMF sources, whose effect is to induce interference voltages and currents in the target structure. Although inspection of (2.10) shows that the EMF has unit of volts, it is relevant to highlight that the EMF itself is not the actual structure-to-ground voltage induced in the interfered conductor. Interference voltages and currents arise from the interaction between the EMF source and the conductor's self impedance.

Self impedance $Z_{i,i}$ of conductor i, expressed in ohms per unit length in (2.23), is composed by an internal part $Z_{s,int}$, which depends on the metal characteristics and geometry, and an external part $Z_{s,ext}$, related to the ground return path impedance.

$$Z_{i,i} = Z_{s,int} + Z_{s,ext}. \tag{2.23}$$

For solid or stranded conductors, the internal component $Z_{s,int}$ is simply the ohmic resistance R_{AC} at the operation temperature, supplied by the cable manufacturer or calculated from the DC resistance with the appropriate corrections, due to temperature, skin and proximity effects (MORGAN, 2013).

The external impedance component $Z_{s,ext}$ is determined by setting $j = i$, $D_{i,i} = r_{ef}$, $D'_{i,i} = 2|y_i|$ and $D = 0$ in (2.11)-(2.12), with the appropriate choice of $\hat{F}(\lambda)$, according to the soil model, resulting in (2.24):

$$Z_{s,ext} = \frac{j\omega\mu_0}{2\pi} \ln\left(\frac{2|y_i|}{r_{ef}}\right) + \frac{j\omega\mu_0}{\pi} \int_0^\infty e^{-2|y_i|\lambda} \hat{F}(\lambda) d\lambda, \tag{2.24}$$

in which ω is the angular frequency, in rad/s; μ_0 is the free space magnetic permeability, in H/m; $|y_i|$ is the height of the i^{th} conductor, in meters; and r_{ef} is the effective radius, in meters. For solid and stranded conductors, r_{ef} is the geometric mean radius (GMR), supplied by the manufacturer or calculated according to the geometry of conductor strands (STEVENSON; GRAINGER, 1994).

If the transmission line phases are arranged in bundles, i.e., a phase is composed by N conductors connected in parallel, as exemplified in Figure 2.8, effective radius r_{ef} is calculated as:

$$r_{ef} = \sqrt[N]{r_{ext} N r_b^{N-1}}, \tag{2.25}$$

in which N is the number of bundled conductors; r_{ext} is the conductor external radius, in meters; and r_b is the radius of the circumference that contains the symmetrically arranged conductors, in meters, as shown in Figure 2.8 (CIGRÉ WG-36.02, 1995).

Figure 2.8. Phase composed of four bundled conductors symmetrically arranged on a circumference with radius r_b.

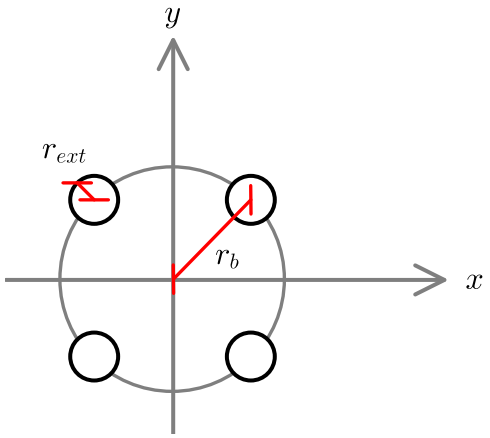

Source: own authorship.

2.2.4.1 Parameters of a cylindrical tubular conductor

A case of particular interest is a cylindrical tubular conductor (a pipe), exemplified in Figure 2.9. The internal impedance component in (2.23) is (CIGRÉ WG-36.02, 1995):

$$Z_{s,int} = \frac{\sqrt{\rho_p \mu_0 \mu_p \omega}}{2\pi r_{ext}\sqrt{2}}(1+j), \tag{2.26}$$

in which ρ_p is the conductor resistivity, in Ω.m; μ_p is the conductor relative permeability; and r_{ext} is the conductor outer radius, in meters.

Figure 2.9. Cross-section of a coated cylindrical tubular conductor with internal radius r_{int}, external radius r_{ext} and coating thickness δ_c.

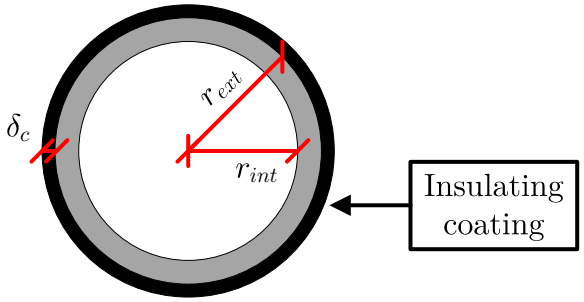

Source: own authorship.

The external impedance component in (2.24) is calculated by setting the effective radius according to the following relation (SENEFF, 1947):

$$\ln(r_{ef}) = \ln(r_{ext}) - \frac{\frac{r_{ext}^4}{4} - r_{ext}^2 r_{int}^2 + r_{int}^4\left[\frac{3}{4} + \ln\left(\frac{r_{ext}}{r_{int}}\right)\right]}{\left(r_{ext}^2 - r_{int}^2\right)^2}, \tag{2.27}$$

in which r_{ext} and r_{int} are, respectively, the conductor external and internal radius, in meters, as shown in Figure 2.9.

2.2.4.2 Parameters of a buried insulated conductor

If the target conductor is coated with an insulation layer and buried into the ground, part of the induced currents by magnetic coupling will leak to the adjacent soil through the imperfect insulation, thus affecting induced voltages. This effect is expressed in terms of a coating shunt admittance Y_c, defined in S/m as:

$$Y_c = \frac{2\pi r_{ext}}{\rho_c \delta_c} + j\omega \frac{\varepsilon_0 \varepsilon_c 2\pi r_{ext}}{\delta_c}, \tag{2.28}$$

in which r_{ext} is the conductor external radius, in meters; ρ_c is the coating specific resistivity, in Ω.m; δ_c is the coating thickness, in meters, as illustrated in Figure 2.9; ε_0 is the vacuum electric permittivity, in F/m; and ε_c is the coating relative electric permittivity (CIGRÉ WG-36.02, 1995).

2.3 CAPACITIVE COUPLING MECHANISM

Capacitive, or electrostatic coupling, occurs between overhead transmission lines and above-ground installations. The electric field produced by the energized phases, in the vicinities of an ungrounded target conductor immersed in a dielectric medium (air), forms a capacitor between both structures, with accumulation of charges on the surface of the interfered conductor, which may give cause to electrostatic discharge currents.

Capacitive coupling response is influenced by (CIGRÉ WG-36.02, 1995):

- **Voltage magnitude:** capacitive effect increases linearly with the power system voltage;
- **Distance between structures:** induced electrostatic voltages decrease with distance between the power line and the target installation;
- **Length of exposure:** capacitive voltages are unaffected, but electrostatic discharge currents increase with exposure length;
- **Transmission line characteristics:** cross-section layout, phase arrangement and transposition may cause partial cancellation of capacitive coupling components. In transient conditions, temporary overvoltages may increase interference levels.

Capacitive coupling effects are evaluated in terms of the Maxwell potential coefficients (DABKOWSKI; TAFLOVE, 1978a). Conductors are assumed to be long in comparison with distances between them and parallel to the earth surface and to each other. The effect of the earth is considered by using the method of images, which is a reasonable approximation for frequencies up to 1 MHz (CIGRÉ WG-36.02, 1995).

Referring to the system of two conductors represented in Figure 2.6, denoted by i and j,

with charges per unit length Q_i and Q_j, voltages relative to earth can be written as:

$$V_i = P_{i,i}Q_i + P_{i,j}Q_j, \tag{2.29}$$

$$V_j = P_{j,i}Q_i + P_{j,j}Q_j, \tag{2.30}$$

in which Q_i and Q_j are given in C/m; $P_{i,j} = P_{j,i}$ is the mutual potential coefficient between conductors i and j, expressed in m/F; $P_{i,i}$ and $P_{j,j}$ are, respectively, the self potential coefficients of conductors i and j, also in m/F.

Mutual potential coefficients $P_{i,j}$ are determined according to the following expression:

$$P_{i,j} = \frac{1}{2\pi\varepsilon_0\varepsilon_r} \ln\left(\frac{D'_{i,j}}{D_{i,j}}\right), \tag{2.31}$$

in which ε_0 is the vacuum electric permittivity, in F/m; ε_r is the medium relative electric permittivity; $D'_{i,j}$ is the distance between conductor i and the image of conductor j, in meters; and $D_{i,j}$ is the distance between conductors i and j, in meters.

For transmission line conductors where heights are greater than respective radii, self potentials $P_{i,i}$ are given by:

$$P_{i,i} = \frac{1}{2\pi\varepsilon_0\varepsilon_r} \ln\left(\frac{2|y_i|}{r_{ext}}\right), \tag{2.32}$$

in which $|y_i|$ is the height of conductor i, in meters; and r_{ext} is the conductor external radius, in meters. If conductors are bundled, r_{ext} is replaced by the effective radius r_{ef} described in (2.25).

If conductor radius cannot be neglected in relation to height, which is the case of a tubular conductor close to the ground surface, self potential coefficient assumes the form of (CIGRÉ WG-36.02, 1995):

$$P_{i,i} = \frac{1}{2\pi\varepsilon_0\varepsilon_r} \ln\left[\frac{|y_i|}{r_{ext}} + \sqrt{\left(\frac{|y_i|}{r_{ext}}\right)^2 - 1}\right]. \tag{2.33}$$

If conductor i is the interference source, term V_i in (2.29) is known and corresponds to the phase energization voltage. In order to determine the response of the target conductor j, corresponding conditions are applied to the system of equations (2.29)-(2.30): (a) if the target structure is insulated from ground, $Q_j = 0$ and V_j is determined as the no-load target-to-ground voltage; or (b) if the target structure is grounded, directly or through a low impedance, $V_j = 0$ and Q_j determines the charging current in the target conductor (CIGRÉ WG-36.02, 1995).

2.4 CONDUCTIVE COUPLING MECHANISM

Conductive, or resistive coupling, is caused by the injection of current into the soil by a transmission line or substation during phase-to-ground fault conditions, as illustrated in Figure 2.10. Under such circumstances, the current I flowing into the earth through the grounding electrode produces a ground potential rise, commonly referred as GPR, which appears in the form of a voltage gradient around the grounding conductors. If a person or a target structure is inside the region affected by the GPR, potentially hazardous voltages may occur.

Figure 2.10. Transmission line subject to a phase-to-ground fault, injecting a current I into the soil through the tower grounding electrode, causing a potential rise (GPR) of the adjacent earth.

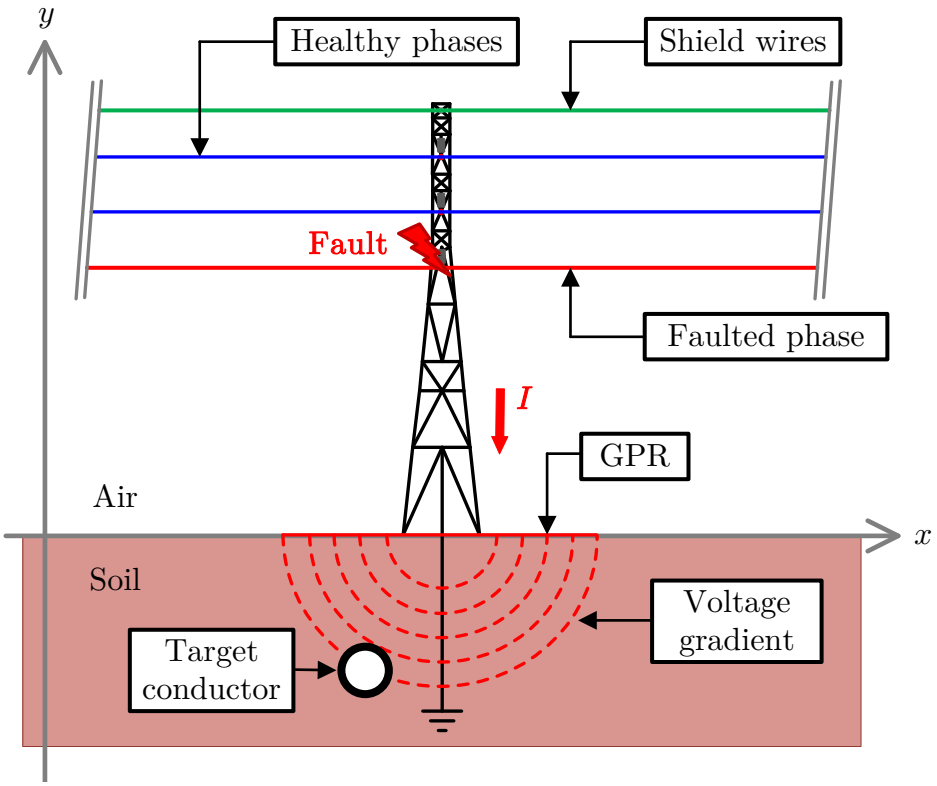

Source: own authorship.

Electromagnetic influence due to conductive coupling is determined by the following variables:

- **Short-circuit levels:** short-circuit levels at substations directly determine the fault current injected by the grounding electrode and, therefore, the GPR and voltages transferred to the target structure;

- **Quantity and type of shield wires:** during a short-circuit, part of the fault currents supplied by the phases return to the substations through the shield wires, reducing the net current injected into the soil;

- **Distance between structures:** soil potentials decrease with the distance between the source electrode and the observation point;

- **Grounding electrode geometry:** characteristics and layout of grounding conductors determine the grid resistance and the leakage current distribution;

- **Soil resistivity:** soil resistivity and stratification, in special the values of the deep layer, affect ground resistance and GPR magnitude. Voltages increase with resistivity.

2.4.1 Current distribution under fault conditions

Figure 2.11 represents a transmission line fed from terminals A and B, where a phase-to-ground fault occurs at point F. The faulted site is located n sections apart from terminal A and m sections apart from terminal B.

During a short-circuit, current contributions $I_{F,A}$ and $I_{F,B}$, coming from terminals A and B, flow through the faulted phase. Part of the fault contributions returns to the substations through the shield wires, expressed as $[I_{R,A1}, ..., I_{R,An}, I_{R,B1}, ..., I_{R,Bm}]$, and the other part is discharged into the soil through the tower grounding electrodes, expressed as $[I_{G,A1}, ..., I_{G,An}$, $I_{G,F}, I_{G,B1}, ..., I_{G,Bm}]$.

Currents flowing into the earth disturb neighboring soil potentials, not only due to the effects of the faulted site, but of the adjacent towers as well. Therefore, in order to evaluate the interference effects on a target system, it is necessary to determine the current distribution on the shield wires and grounding electrodes.

Figure 2.12 contains the equivalent circuit model of the faulted transmission line under study. It consists of a shield wire described by self impedances $[Z_{S,A1}, ..., Z_{S,An}, Z_{S,B1}, ..., Z_{S,Bm}]$, grounded at every section through impedances $[Z_{G,A0}, ..., Z_{G,An}, Z_{G,F}, Z_{G,B0}, ..., Z_{G,Bm}]$, and mutually coupled with the phase conductors, which is accounted by means of the virtual EMF sources $[E_{A1}, ..., E_{An}, E_{B1}, ..., E_{Bm}]$. System is fed by the equivalent short-circuit current sources $I_{F,A}$

Figure 2.11. Fault current distribution on a transmission line with n and m sections between, respectively, terminals A and B and the fault point F. $I_{F,A}$ and $I_{F,B}$ are the fault current contributions coming from the substations. $[I_{R,A1}, ..., I_{R,An}, I_{R,B1}, ..., I_{R,Bm}]$ are the shield wire return currents. $[I_{G,A1}, ..., I_{G,An}, I_{G,F}, I_{G,B1}, ..., I_{G,Bm}]$ are the currents flowing into the ground.

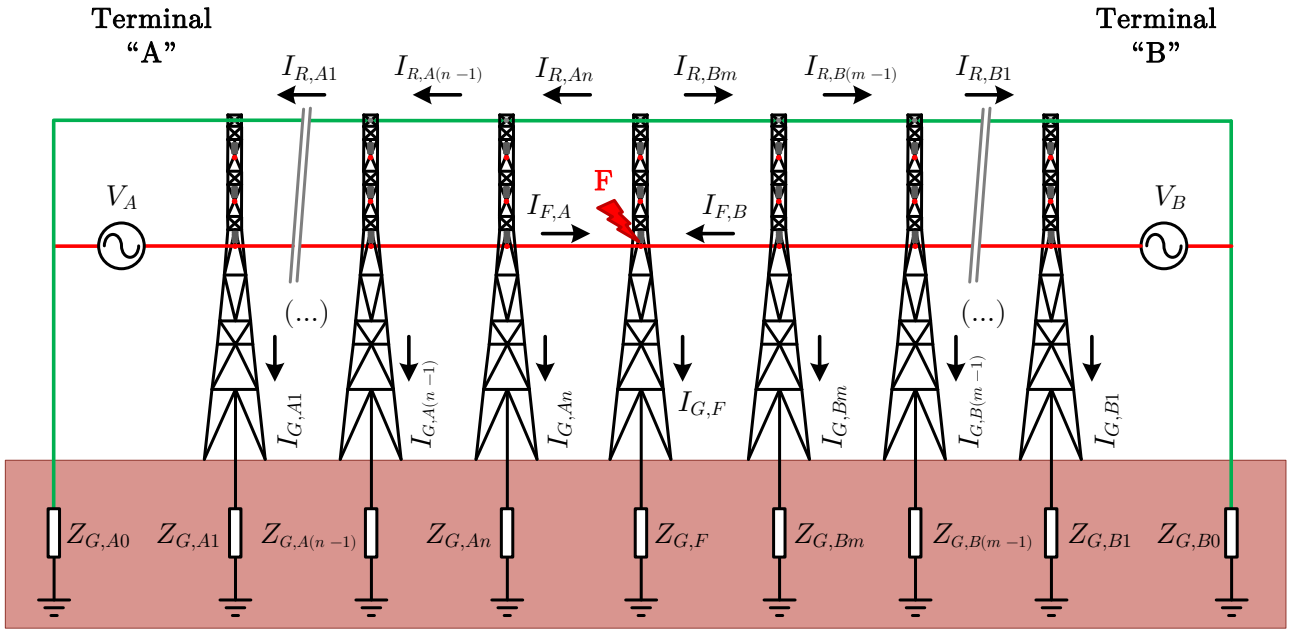

Source: own authorship.

and $I_{F,B}$. Impedances $[Z_{S,A1}, ..., Z_{S,An}, Z_{S,B1}, ..., Z_{S,Bm}]$ are calculated using (2.23). EMF sources $[E_{A1}, ..., E_{An}, E_{B1}, ..., E_{Bm}]$ are defined according to (2.10). Once the grounding impedances are known, voltages and currents in the equivalent circuit are determined by simple nodal analysis (FURLAN, 2015).

It is relevant to notice that although this section describes specifically a case of a single phase-to-ground fault in a transmission line with one shield wire, the method is general and holds valid for other types of faults and configurations, with the appropriate modifications in the equivalent circuit. If the transmission line is fitted with more than one shield wire, the same technique can be employed by firstly reducing the N shield wires to an equivalent conductor (YANG *et al.*, 2002).

2.4.2 Potentials produced by a point current source in soil

Determination of the potentials produced by a grounding system is the fundamental step for obtaining its electrical parameters. A grounding electrode is first subdivided into many small

Figure 2.12. Equivalent circuit of the system shown in Figure 2.11.

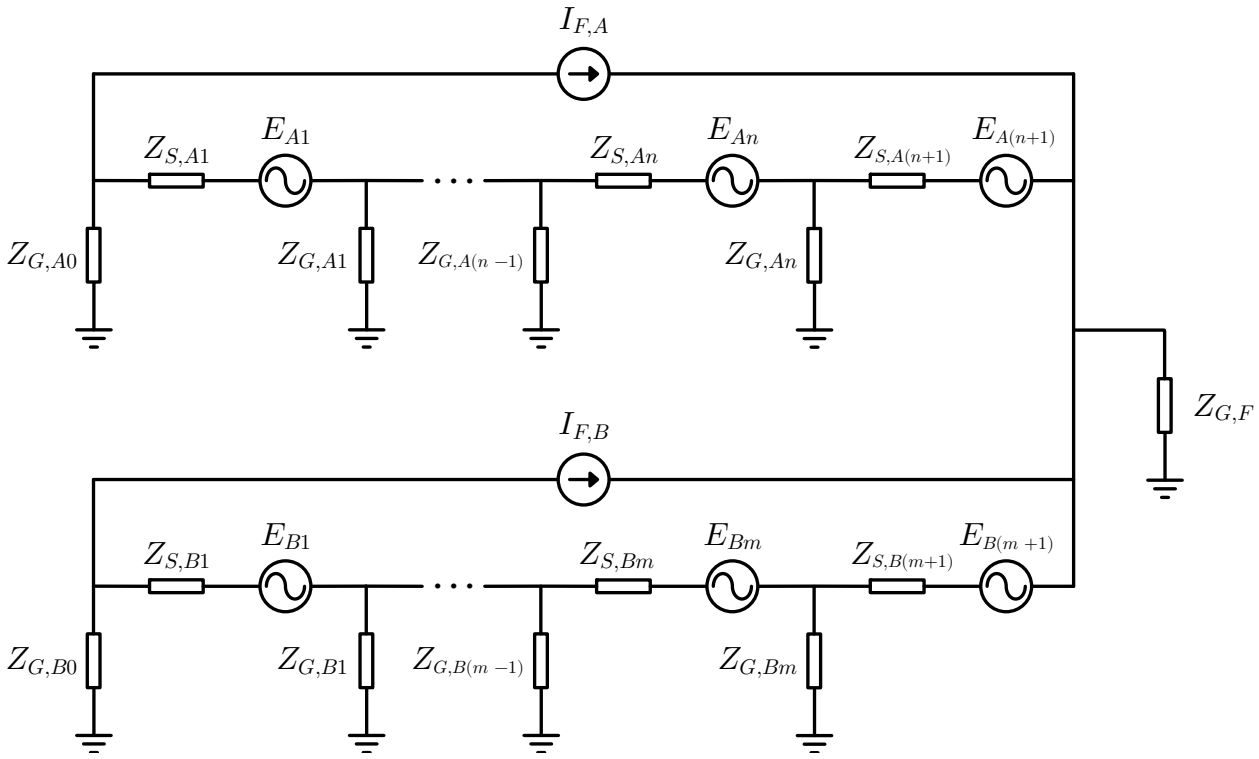

Source: adapted from (FURLAN, 2015).

segments, where each segment is regarded as a point source when a current is injected into the grounding system (HE *et al.*, 2013). The contribution of each segment is evaluated individually and the complex system response is determined by the principle of superposition.

Assuming the total length of the grounding grid is L and the total current discharging through L is I, L is divided into N segments. Then the length, center coordinates and leakage current of the j^{th} segment are L_j, O_j and I_j, respectively, and:

$$L = \sum_{j=1}^{N} L_j, \tag{2.34}$$

$$I = \sum_{j=1}^{N} I_j. \tag{2.35}$$

According to the principle of superposition, the potential rise at point P produced by the current I flowing through L is:

$$U_P = \sum_{j=1}^{N} \widehat{G}\left(P, O_j\right) I_j, \tag{2.36}$$

in which U_P is the potential at point P, in volts; O_j are the spatial coordinates of the j^{th} observation point O; and $\widehat{G}\left(P, O_j\right)$ is a special function that describes the potential produced

at point P by a unit point current source located at point O_j, known as Green's function (SADIKU, 2000; HE *et al.*, 2013).

In advanced mathematics, a Green's function provides a technique to write a partial differential equation (PDE) which may be unsolvable by other methods in the form of an integral equation (IE). It forms the basis of the method of moments (MoM), which is a numerical approach widely employed in electromagnetism, underlying to commonly adopted power grounding analysis techniques (SADIKU, 2000; HE *et al.*, 2013).

A Green's function is the impulse response (Dirac delta function) of an inhomogeneous linear differential operator defined on a domain with specified initial or boundary conditions. In other words, it describes the response of an arbitrary PDE to a source, or driving term, under a set of boundary conditions (ARFKEN; WEBER, 2005). To obtain the overall response caused by a distributed source by the Green's function technique, the effects of each elementary portion of source are evaluated and integrated over the domain occupied by the source (SADIKU, 2000). Therefore, the task is to determine a suitable form of a Green's function, which is highly dependent on the domain shape and characteristics. For the purposes of power grounding analysis, Green's functions are essentially defined by the soil structure (ZOU *et al.*, 2004).

2.4.2.1 Green's functions for uniform soil

First it is examined the simple case of a point source located at the surface of a uniform soil with resistivity ρ, as shown in Figure 2.13. Orientation of z-axis is arbitrarily set as pointing downwards. Green's function at observation point P is (CIGRÉ WG-36.02, 1995; HE *et al.*, 2013):

$$\widehat{G}(P,O) = \frac{\rho}{2\pi r}, \tag{2.37}$$

with:

$$r = \sqrt{(x - x_O)^2 + (y - y_O)^2 + z^2}. \tag{2.38}$$

If the point source is below the soil surface, Green's function at point P is determined by using the method of electrostatic images (HE *et al.*, 2013):

$$\widehat{G}\,(P,O) = \frac{\rho}{4\pi}\left(\frac{1}{r} - \frac{1}{r'}\right), \tag{2.39}$$

Figure 2.13. Point source located at the ground surface ($z = 0$) over uniform soil and equipotential hemispherical surface with radius a.

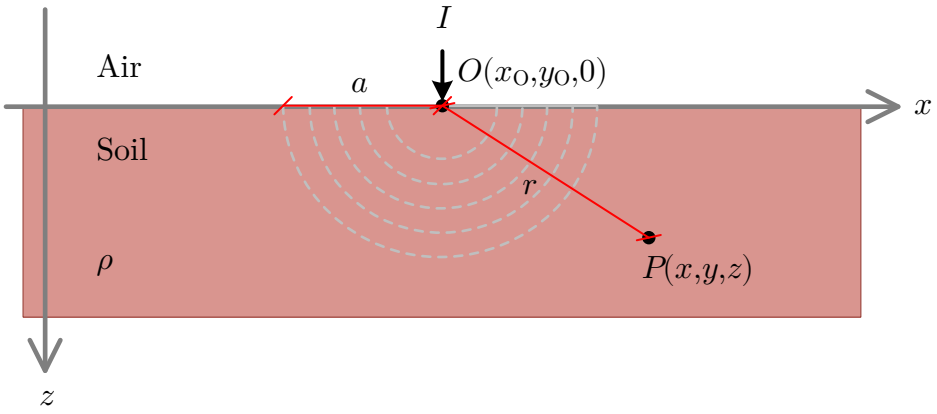

Source: own authorship.

with:

$$r = \sqrt{(x - x_O)^2 + (y - y_O)^2 + (z - d)^2}, \tag{2.40}$$

$$r' = \sqrt{(x - x_O)^2 + (y - y_O)^2 + (z + d)^2}. \tag{2.41}$$

Figure 2.14. Point source at depth d in uniform soil and its image, distances in meters.

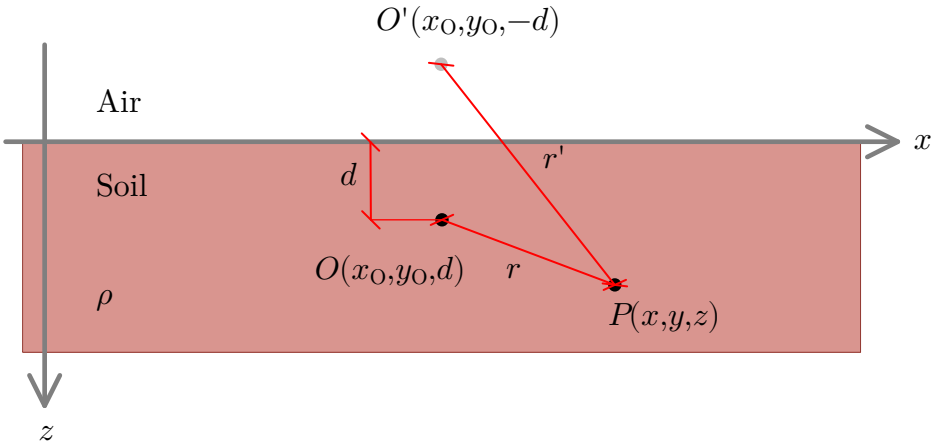

Source: own authorship.

2.4.2.2 Green's functions for two-layered soil

Figure 2.15 shows a point electrode buried in a two-layered soil, described by parameters $[\rho_1, \rho_2]$, with a top layer thickness h_1. Green's functions are obtained by using the method of complex images, expressed in (2.42)-(2.45), and depend on which layer the source and the observation point are inserted (DAWALIBI; MUKHEDKAR, 1975b).

Figure 2.15. Point source at depth d in a two-layered soil, distances in meters.

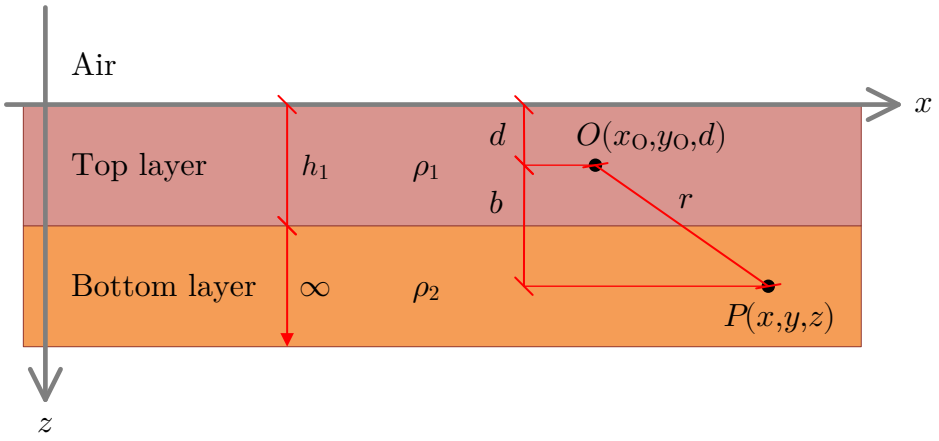

Source: own authorship.

If source and observation points are in the top soil layer, then Green's function is written as:

$$\widehat{G}_{1,1}(P,O) = \frac{\rho_1}{4\pi}\left\{\psi_0 + \sum_{n=1}^{\infty} k^n \left[\psi(nh_1) + \psi(nh_1 + d) + \psi(-nh_1) + \psi(-nh_1 + d)\right]\right\}. \tag{2.42}$$

If the point source is in the top layer and the observation point in the bottom layer, Green's function has the form:

$$\widehat{G}_{1,2}(P,O) = \frac{\rho_1(1+k)}{4\pi}\left\{\psi_0 + \sum_{n=1}^{\infty} k^n \left[\psi(nh_1) + \psi(nh_1 + d)\right]\right\}. \tag{2.43}$$

If the point source is in the bottom layer and the observation point is in the top layer, Green's function is described as:

$$\widehat{G}_{2,1}(P,O) = \frac{\rho_2}{4\pi}\left\{\psi_0 + \sum_{n=1}^{\infty} k^n \left\{\psi(-nh_1) + \psi(nh_1 + d) - \psi[(-n-1)h_1] - \psi[(n-1)h_1 + d]\right\}\right\}. \tag{2.44}$$

Finally, if source and observation points are both in the bottom layer, Green's function is given as:

$$\widehat{G}_{2,2}(P,O) = \frac{\rho_2}{4\pi}\left\{\psi_0 + \sum_{n=1}^{\infty} k^n \left\{\psi(nh_1 + d) - \psi[(n-2)h_1 + d]\right\}\right\}. \tag{2.45}$$

In equations above, k is the reflection coefficient, defined as in (2.46). Term ψ is an auxiliary function defined according to (2.47)-(2.48).

$$k = \frac{\rho_2 - \rho_1}{\rho_2 + \rho_1}, \tag{2.46}$$

$$\psi(\alpha) = \frac{1}{\sqrt{r^2 + (2\alpha + b)^2}}, \tag{2.47}$$

$$\psi_0 = \psi(0) + \psi(d), \tag{2.48}$$

in which r, d and b are the distances shown in Figure 2.15.

2.4.2.3 Green's functions for multilayered soil

Figure 2.16 depicts the general case of a soil composed by N layers, described by resistivities $[\rho_1, \rho_2, \rho_3, ..., \rho_N]$ and thicknesses $[h_1, h_2, h_3, ..., h_{N-1}]$. The point source is represented in the first layer and the observation point in the second, for illustration purposes, without loss of generality.

Figure 2.16. Point source at depth d in a multilayered soil, distances in meters.

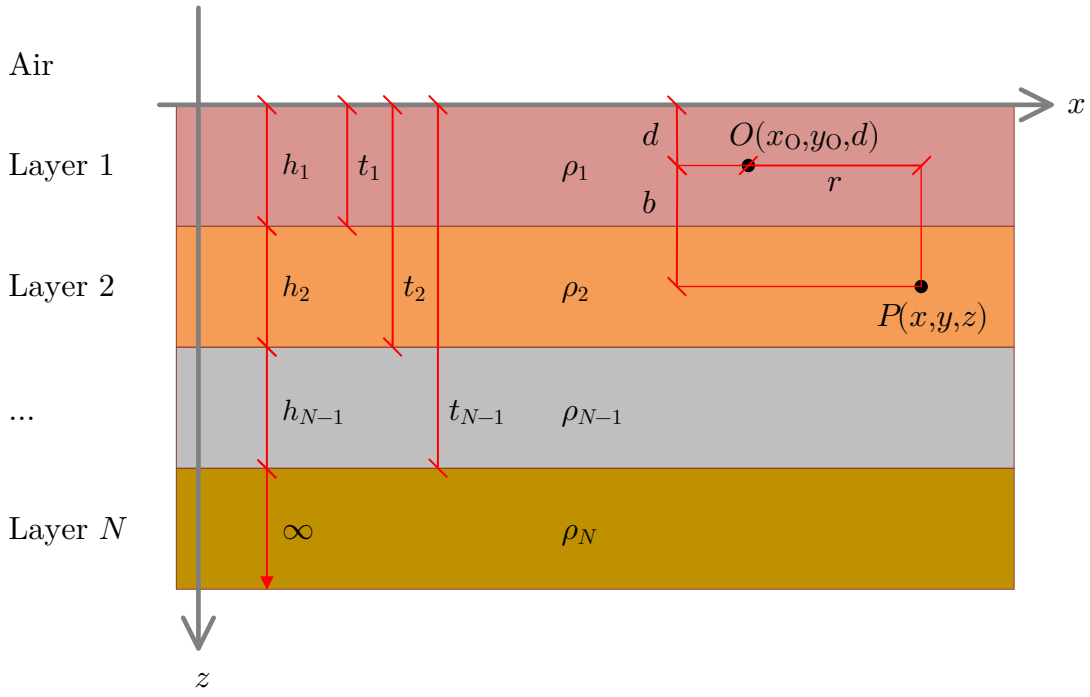

Source: own authorship.

Systematic approaches for obtaining expressions of Green's functions to model the N-layered case have been described by Zou *et al.* (2004), Li *et al.* (2007) and He *et al.* (2013). If the point source is located in the i^{th} layer and the observation point is in the j^{th} layer, Green's function general form is written as:

$$\widehat{G}_{i,j}(P,O) = \frac{\rho_i}{4\pi}\left(\int_0^\infty A_{i,j}(\lambda)\widehat{J}_0(\lambda r)e^{-\lambda z}d\lambda + \int_0^\infty B_{i,j}(\lambda)\widehat{J}_0(\lambda r)e^{\lambda z}d\lambda + \int_0^\infty \delta(ij)\widehat{J}_0(\lambda r)e^{-\lambda|z|}d\lambda\right), \tag{2.49}$$

in which ρ_i is the resistivity of the i^{th} (source) layer, in Ω.m; $\widehat{J}_0$ is the Bessel function of the first kind and order zero; r and d are the distances shown in Figure 2.16; $\delta(ij)$ is the Kronecker delta, defined as equal to 1 if $i = j$, and equal to 0 otherwise (LOVELOCK; RUND, 1989).

Green's function coefficients $A_{i,j}$ and $B_{i,j}$ are determined by enforcing the boundary conditions described in (2.50)-(2.53):

$$\widehat{G}_{i,j}(r,z)\Big|_{z=H_j-d} = \widehat{G}_{i,j+1}(r,z)\Big|_{z=H_j-d}, \tag{2.50}$$

$$\frac{1}{\rho_j}\frac{\partial\widehat{G}_{i,j}(r,z)}{\partial z}\bigg|_{z=H_j-d} = \frac{1}{\rho_{j+1}}\frac{\partial\widehat{G}_{i,j+1}(r,z)}{\partial z}\bigg|_{z=H_j-d}, \tag{2.51}$$

$$\widehat{G}_{i,N}(r,z)\Big|_{z\to\infty} = 0, \tag{2.52}$$

$$\frac{\partial\widehat{G}_{i,1}(r,z)}{\partial z}\bigg|_{z=-d} = 0. \tag{2.53}$$

One particularly challenging aspect of working with multilayered soils is the fact that potentials distribution throughout space cannot be described by one single equation. Indeed, (2.49) expresses a family of Green's functions that considers all relative positions between the source point O and the observation point P, whose coefficients grow in complexity as the number of layers N increases.

Explicit forms of Green's functions are given by He *et al.* (2013) for soil models composed of three, four and five layers, showing that it is impractical to manually write such equations for arbitrary soil structures. An example is discussed in Appendix A, in which is provided a computer routine devised by the author to overcome this difficulty, by symbolically calculating (2.50)-(2.53) for any number of layers specified by the user and solving the resulting system of linear equations.

2.4.3 Computation of grounding electrode parameters

Grounding electrodes can be of any shape and size and are commonly comprised of buried linear conductors, horizontally or vertically laid close to the ground surface. Figure 2.17 shows

a line conductor with length L_j and radius r_{ext} below the soil surface, which may be uniform or stratified. Regardless of the conductor orientation, an auxiliary coordinate system uvw is chosen, with origin at the left extremity of the conductor and with the u-axis directed towards its length.

Figure 2.17. Linear conductor with length L_j, radius r_{ext} and micro-segment with infinitesimal length du buried in soil.

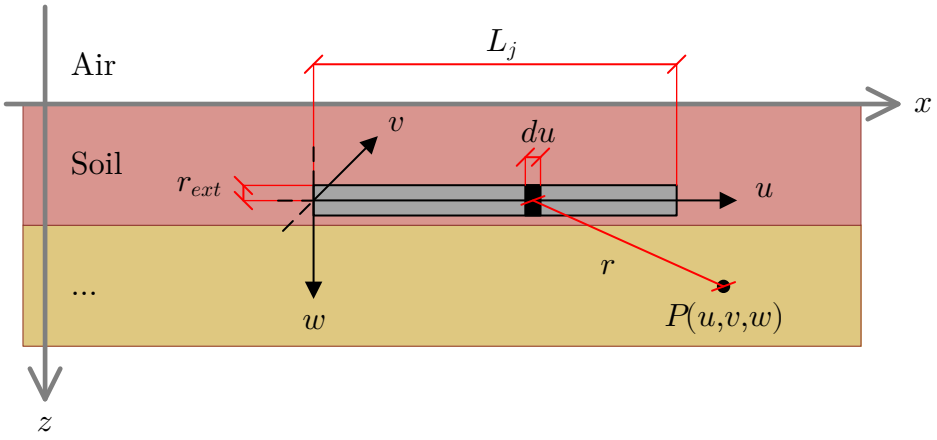

Source: own authorship.

Such grounding device may be treated as a succession of point electrodes, or micro-segments, with infinitesimal length du, as shown, leaking a total current I_j into the soil. If the conductor diameter $2r_{ext}$ is small if compared to its length L_j, then the leakage current linear density δ_j, defined in (2.54), may be considered uniform along the conductor surface (BENSTED *et al.*, 1981).

$$\delta_j = \frac{I_j}{L_j}. \tag{2.54}$$

The incremental current injected into the soil by each micro-segment is:

$$dI_j = \delta_j du, \tag{2.55}$$

and the contribution to the ground potential rise at point $P(u,v,w)$ caused by the micro-segment at point $O_j(u_O,v_O,w_O)$ is:

$$dU_j = \widehat{G}\,(P, O_j)\,\delta_j du. \tag{2.56}$$

The potential at point $P(u,v,w)$ is determined by integrating along the conductor length (NAGAR *et al.*, 1985; DAWALIBI; MUKHEDKAR, 1975b):

$$U_j = \delta_j \int_0^{L_j} \widehat{G}\,(P, O_j)\,du. \tag{2.57}$$

A complex grounding system composed of several linear conductors is subdivided in a suitable number of segments N and modeled according to the preceding equations. Then, according to the principle of superposition, the total ground potential rise at the observation point P is:

$$U_P = \sum_{j=1}^{N} U_j. \tag{2.58}$$

It happens, however, that for complex geometries, leakage current densities δ_j distribute nonuniformly throughout the grounding electrode and are not initially known, as in practical situations, the available parameters are the fault current or energization voltage (BARIC; NIKOLOVSKI, 2004; DAWALIBI *et al.*, 1981; MARTINS-BRITTO, 2017b). Therefore, it is necessary to determine the leakage current distribution along the grounding conductors, which is accomplished by employing the matrix method described in (2.59)-(2.62) (NAGAR *et al.*, 1985; HE *et al.*, 2013; MUKHEDKAR; DAWALIBI, 1976).

It is assumed that the grounding system is an equipotential structure, which is acceptable for most cases at power system frequencies and for small to medium size grounding grids (HE *et al.*, 2013). If the potential rise of the grounding electrode is V_G, any point S located at the surface of any conductor of the grounding grid must satisfy the following boundary condition:

$$V_G = \sum_{j=1}^{N} U_j \Bigg|_{S(r=r_{ext})}, \tag{2.59}$$

which allows the normalized leakage current linear density ξ_j to be defined as:

$$\xi_j = \frac{\delta_j}{V_G}. \tag{2.60}$$

Combining (2.60) and (2.59), the following matrix relation may be written:

$$\boldsymbol{\xi} = \boldsymbol{R}^{-1} \begin{bmatrix} 1 & 1 & \cdots & 1 \end{bmatrix}^T, \tag{2.61}$$

or, in expanded form:

$$\begin{bmatrix} \xi_1 \\ \xi_2 \\ \vdots \\ \xi_N \end{bmatrix} = \begin{bmatrix} R_{1,1} & R_{1,2} & \cdots & R_{1,N} \\ R_{2,1} & R_{2,2} & \cdots & R_{2,N} \\ \vdots & \vdots & \ddots & \vdots \\ R_{N,1} & R_{N,2} & \cdots & R_{NN} \end{bmatrix}^{-1} \begin{bmatrix} 1 \\ 1 \\ \vdots \\ 1 \end{bmatrix}. \tag{2.62}$$

Elements $R_{j,k}$ in matrix $\boldsymbol{R}$ are determined by setting $\delta_j = 1$ in (2.57), placing the source point at the center of conductor j and computing the potential rise $U_{j,k}$ at the center of conductor k. For $j = k$, the potential rise is calculated at the conductor surface $w = r_{ext}$.

Relations between the current I imposed to the grounding system, leakage currents on each segment and electrode ground potential rise are given below:

$$I_j = \delta_j L_j, \tag{2.63}$$

$$I = \sum_{j=1}^{N} I_j = \sum_{j=1}^{N} \delta_j L_j = V_G \sum_{j=1}^{N} \xi_j L_j, \tag{2.64}$$

$$V_G = \frac{I}{\sum_{j=1}^{N} \xi_j L_j}. \tag{2.65}$$

Finally, the grounding grid equivalent resistance is:

$$R_G = \frac{V_G}{I}. \tag{2.66}$$

2.5 RISKS AND SAFETY LIMITS

Electromagnetic interference mechanisms affect a target installation under two distinct forms, which may or may not occur simultaneously. Inductive and capacitive coupling effects cause a voltage rise of the interfered conductor, e.g. the metal itself. Under fault conditions, conductive coupling produces a voltage gradient on the soil adjacent to the target structure.

The total voltage transferred to the interfered installation is the potential difference between the conductor and the local earth, or:

$$V_S = E_T - U_E, \tag{2.67}$$

in which V_S is the total stress voltage, in volts; E_T is the potential of the target structure resulting from inductive/capacitive coupling mechanisms, in volts; and U_E is the local earth potential rise, in volts. Relation 2.67 remains valid in the time-domain, as well as with the phasor forms of the involved quantities: $\bar{V}_S$, $\bar{E}_T$ and $\bar{U}_E$. Figure 2.18 illustrates resulting voltages, which may subject people and facilities to hazards, such as: electrocution caused by touch and step voltages and damage to structures and equipment.

2.5.1 Touch voltages

According to standard ABNT NBR 15751, touch voltage is defined as the potential difference between a metallic object, grounded or not, and a point at the earth surface with a horizontal

Figure 2.18. Illustration of V_S, E_T and U_E in a hypothetical pipeline under interference conditions. Z_C and Z_E represent, respectively, coating and earth impedances.

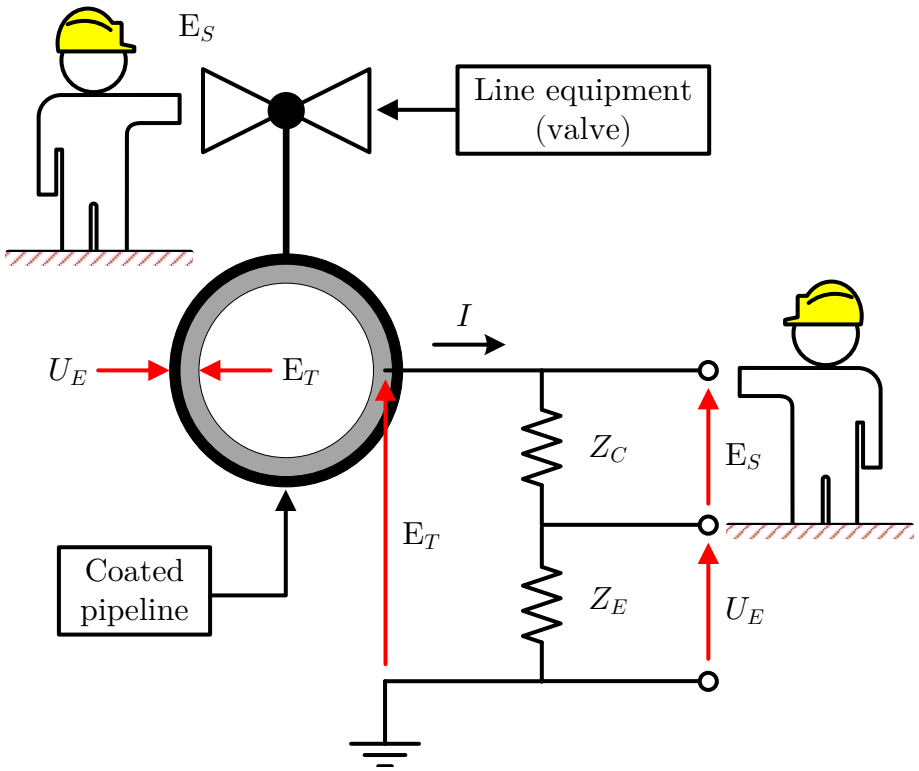

Source: own authorship.

separation of 1 m, equivalent to the normal reach of a person's arm (ABNT, 2009).

The touch voltage V_t is numerically equal to the stress voltage V_S, determined in (2.67) and represented in Figure 2.18.

The tolerable touch voltage value for human beings is such that the current flowing through the body in contact with the energized metal is inferior to the ventricular fibrillation threshold, which is determined as a function of current intensity and exposure time, according to the characteristic curves given in IEC 60479-1 (IEC, 1984).

IEEE Std. 80 establishes that for exposure times between 30 ms and 3 s and individuals with a body weight of approximately 50 kg, the maximum tolerable current through the body I_B in 99.5% of the cases is calculated as:

$$I_B = \frac{0.116}{\sqrt{t_s}}, \tag{2.68}$$

in which t_s is the exposure time to the shock current, in seconds (IEEE, 2000). Then, the safety

limit for touch voltages is:

$$V_{t,max} = (R_B + R_{2Fp}) \times I_B, \tag{2.69}$$

in which $V_{t,max}$ is the maximum tolerable touch voltage, in volts; R_B is the resistance representative of the human body, in Ω; and R_{2Fp} is the resistance, given in Ω, representing the two feet of an individual in parallel, as illustrated in Figure 2.19.

For power system frequencies, the human body presents resistive behavior with $R_B = 1000$ Ω (DALZIEL; LEE, 1968). Resistance R_{2Fp} is related to the electric contact with earth and is calculated according to (2.70).

$$R_{2Fp} = 1.5 \times C_s \times \rho_s, \tag{2.70}$$

$$C_s \cong 1 - 0.106 \times \left[\frac{1 - \frac{\rho_1}{\rho_s}}{2 \times h_s + 0.106} \right], \tag{2.71}$$

in which ρ_s is the resistivity of the material covering the soil surface, if any, in Ω.m; h_s is the thickness of the cover layer, in meters; and ρ_1 is the local soil resistivity, in Ω.m (IEEE, 2000). For bare soil conditions, $C_s = 1$ and $\rho_s = \rho_1$.

Figure 2.19. Concept of touch voltage and equivalent circuit.

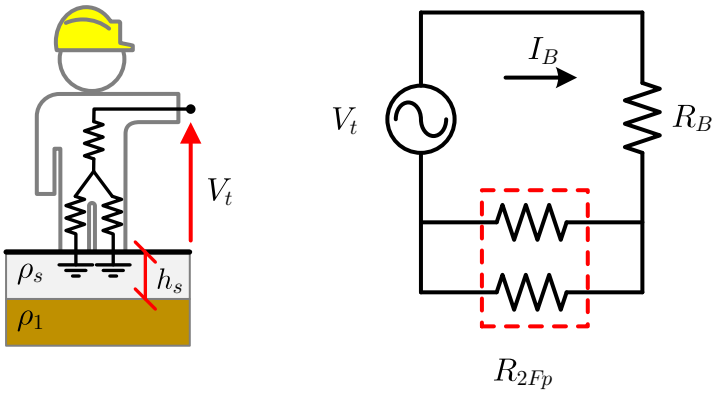

Source: own authorship.

For continuous exposures to steady-state interferences, standard NACE SP0177-2007 recommends the touch voltage to be limited to 15 V, whereas British standard CENELEC EN 50443 recommends a maximum value of 60 V (NACE, 2007; CENELEC, 2011).

2.5.2 Step voltages

Step voltage is defined as the potential difference between two points on the earth surface separated by 1 m, equivalent to the normal length of a person's step (ABNT, 2009).

If the distribution of potentials on the soil surface $U_E(x,y)$ is known, then the step voltage at an observation point $P(x,y)$ is determined by calculating the absolute value of the gradient, or:

$$V_p = |\nabla U_E(P)|. \tag{2.72}$$

According to IEEE Std. 80, the maximum allowable step voltage value is:

$$V_{p,max} = (R_B + R_{2Fs}) \times I_B, \tag{2.73}$$

in which I_B is the tolerable current through the human body, defined in (2.68); and R_{2Fs} is the resistance, given in Ω, representative of the two feet of an individual in series, as illustrated in Figure 2.20 and defined in (2.74) (IEEE, 2000).

$$R_{2Fs} = 6 \times C_s \times \rho_s, \tag{2.74}$$

with C_s calculated as in (2.71).

Figure 2.20. Concept of step voltage and equivalent circuit.

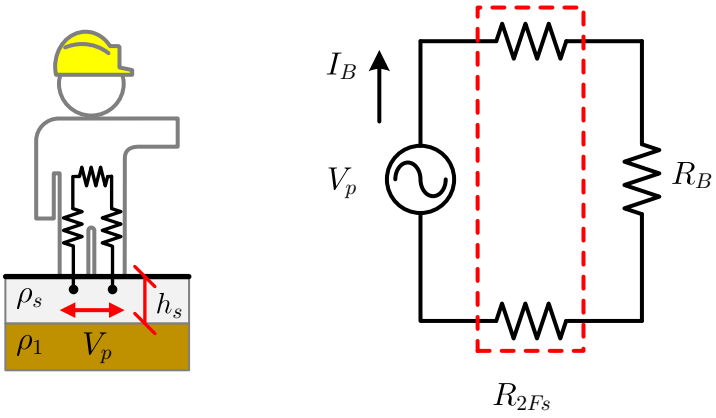

Source: own authorship.

2.5.3 Damage to structures and equipment

The risk of damage is intrinsically related to the nature of the target installation and equipment physically connected to it, and it usually follows specific recommendations and criteria

provided by the manufacturers or from recognized standards.

Stress voltages are a recognized source of concern when the affected installation is a buried coated conductor, case exemplified in Figure 2.18. The difference of potentials between the inner metal (inductive/capacitive coupling) and the external earth (conductive coupling) may reach considerable values, of the order of kilovolts, especially under fault conditions, which may cause breakdown of the dielectric of the coating layer, exposing the metal to electrochemical corrosion (NACE, 2007). Table 2.3 contains the electromagnetic parameters and nominal voltage limits of some coating materials commonly employed in industry.

Table 2.3. Electromagnetic properties and voltage limits of common coatings.

Coating type	ε_r	ρ [Ω.m]	**Voltage limit [kV]**
Plastic tapes	2–9	0.917×10^{13}–18×10^{13}	2
Coal-tar	2–3	0.2×10^{6}–2×10^{6}	5
Fiber bonded epoxy (FBE)	3.77	8.48×10^{16}	3–5
Extruded polyethylene	2.25	2×10^{7}–1×10^{12}	3–5

Source: (NACE, 2007; LI, 2015).

2.6 TRANSMISSION LINE PARAMETERS UNDER INTERFERENCE CONDITIONS

As discussed in the preceding sections, electromagnetic interference mechanisms affect a target installation in the form of induced voltages in metallic parts that would not be energized otherwise. On the other hand, inspection of (2.11) and (2.31) shows that the source transmission line and the interfered system interact mutually while inductive and capacitive coupling phenomena take place. Therefore, it is expected that, under interference conditions, the transmission line is also affected by the same coupling mechanisms with the neighboring interfered conductor.

Recent studies support the idea that transmission line parameters, in special the zero sequence impedance, are sensitive to the presence of interferences, which should be properly accounted in applications that rely on line parameters, such as short-circuit analysis, protection and fault location algorithms (MARTINS-BRITTO, 2017a; MARTINS-BRITTO, 2017b).

In order to introduce the concept of interference into the classical transmission line model,

first the nominal-π model, represented in Figure 2.21, is considered. The methods proposed in this section remain valid, without loss of generality, for the long line model (equivalent-π model), by using the appropriate correction factors in terms of the propagation constant and line length, according to the procedure extensively documented in the literature (SAADAT, 1999; STEVENSON; GRAINGER, 1994).

Figure 2.21. Nominal-π model of a transmission line, described by a series impedance Z and a shunt admittance Y. Subscripts S and R denote, respectively, the source and remote terminals.

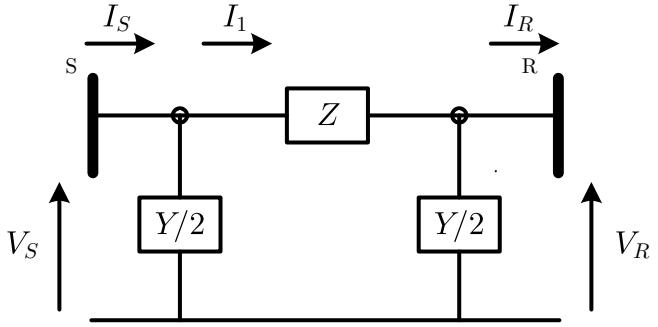

Source: own authorship.

The sought transmission line parameters are the series impedances Z and shunt admittances Y shown in Figure 2.21. Then, the following transmission line related quantities are defined (STEVENSON; GRAINGER, 1994):

$$Z_C = \sqrt{\frac{Z}{Y}}, \tag{2.75}$$

$$\gamma = \sqrt{ZY}, \tag{2.76}$$

$$\alpha = \Re\{\gamma\}, \tag{2.77}$$

$$\beta = \Im\{\gamma\}, \tag{2.78}$$

$$v_p = \frac{\omega}{\beta}, \tag{2.79}$$

$$\lambda = \frac{2\pi}{|\gamma|}, \tag{2.80}$$

in which: Z_C is the characteristic impedance, in [Ω]; γ is the propagation constant, in [m^{-1}]; α is the attenuation constant, given in [Np/m]; β is the phase constant, in [rad/m]; v_p is the phase velocity, in [m/s]; and λ is the wavelength, expressed in [m]. Operators $\Re$ and $\Im$ refer, respectively, to the real and imaginary parts of the quantities in brackets.

2.6.1 Series impedance and shunt admittance matrices

Figure 2.22 shows a system comprised of three phase conductors, designated by the subscripts a, b and c, N shield/neutral wires, identified by the subscripts $n1...nN$ and M interfered (target) conductors, followed by the subscripts $t1...tM$, above uniform or stratified earth. The series impedance matrix representing this system assumes the general form expressed in (2.81) (STEVENSON; GRAINGER, 1994).

$$\boldsymbol{Z} = \begin{bmatrix} Z_{a,a} & Z_{a,b} & Z_{a,c} & Z_{a,n1} & \cdots & Z_{a,nN} & Z_{a,t1} & \cdots & Z_{a,tM} \\ Z_{b,a} & Z_{b,b} & Z_{b,c} & Z_{b,n1} & \cdots & Z_{b,nN} & Z_{b,t1} & \cdots & Z_{b,tM} \\ Z_{c,a} & Z_{c,b} & Z_{c,c} & Z_{c,n1} & \cdots & Z_{c,nN} & Z_{c,t1} & \cdots & Z_{c,tM} \\ Z_{n1,a} & Z_{n1,b} & Z_{n1,c} & Z_{n1,n1} & \cdots & Z_{n1,nN} & Z_{n1,t1} & \cdots & Z_{n1,tM} \\ \vdots & \vdots & \vdots & \vdots & \ddots & \vdots & \vdots & \ddots & \vdots \\ Z_{nN,a} & Z_{nN,b} & Z_{nN,c} & Z_{nN,n1} & \cdots & Z_{nN,nN} & Z_{nN,t1} & \cdots & Z_{nN,tM} \\ Z_{t1,a} & Z_{t1,b} & Z_{t1,c} & Z_{t1,n1} & \cdots & Z_{t1,nN} & Z_{t1,t1} & \cdots & Z_{t1,tM} \\ \vdots & \vdots & \vdots & \vdots & \ddots & \vdots & \vdots & \ddots & \vdots \\ Z_{tM,a} & Z_{tM,b} & Z_{tM,c} & Z_{tM,n1} & \cdots & Z_{tM,nN} & Z_{tM,t1} & \cdots & Z_{tM,tM} \end{bmatrix}. \tag{2.81}$$

Elements $Z_{i,j}$ outside the main diagonal of the matrix $\boldsymbol{Z}$ correspond to the mutual impedances between conductors i and j with ground return path, computed in ohms per unit length using (2.11). Elements $Z_{i,i}$ in the main diagonal are the conductor self impedances, calculated as in (2.23).

A similar procedure is performed to determine the transmission line admittances. Referring again to Figure 2.22, and using the same notation as above, the matrix of potentials $\boldsymbol{P}$ is constructed with the mutual and self Maxwell coefficients of the overhead conductors, defined in (2.31) and (2.32). Underground conductors are immersed in a conductive medium (the earth) and outside the electrostatic coupling region. Therefore, influences are not expected in the results and underground conductors are not considered when building matrix $\boldsymbol{P}$.

$$\boldsymbol{P} = \begin{bmatrix} P_{a,a} & P_{a,b} & P_{a,c} & P_{a,n1} & \cdots & P_{a,nN} & P_{a,t1} & \cdots & P_{a,tM} \\ P_{b,a} & P_{b,b} & P_{b,c} & P_{b,n1} & \cdots & P_{b,nN} & P_{b,t1} & \cdots & P_{b,tM} \\ P_{c,a} & P_{c,b} & P_{c,c} & P_{c,n1} & \cdots & P_{c,nN} & P_{c,t1} & \cdots & P_{c,tM} \\ P_{n1,a} & P_{n1,b} & P_{n1,c} & P_{n1,n1} & \cdots & P_{n1,nN} & P_{n1,t1} & \cdots & P_{n1,tM} \\ \vdots & \vdots & \vdots & \vdots & \ddots & \vdots & \vdots & \ddots & \vdots \\ P_{nN,a} & P_{nN,b} & P_{nN,c} & P_{nN,n1} & \cdots & P_{nN,nN} & P_{nN,t1} & \cdots & P_{nN,tM} \\ P_{t1,a} & P_{t1,b} & P_{t1,c} & P_{t1,n1} & \cdots & P_{t1,nN} & P_{t1,t1} & \cdots & P_{t1,tM} \\ \vdots & \vdots & \vdots & \vdots & \ddots & \vdots & \vdots & \ddots & \vdots \\ P_{tM,a} & P_{tM,b} & P_{tM,c} & P_{tM,n1} & \cdots & P_{tM,nN} & P_{tM,t1} & \cdots & P_{tM,tM} \end{bmatrix}. \tag{2.82}$$

Figure 2.22. Overhead phase conductors, shield wires and interfered conductors.

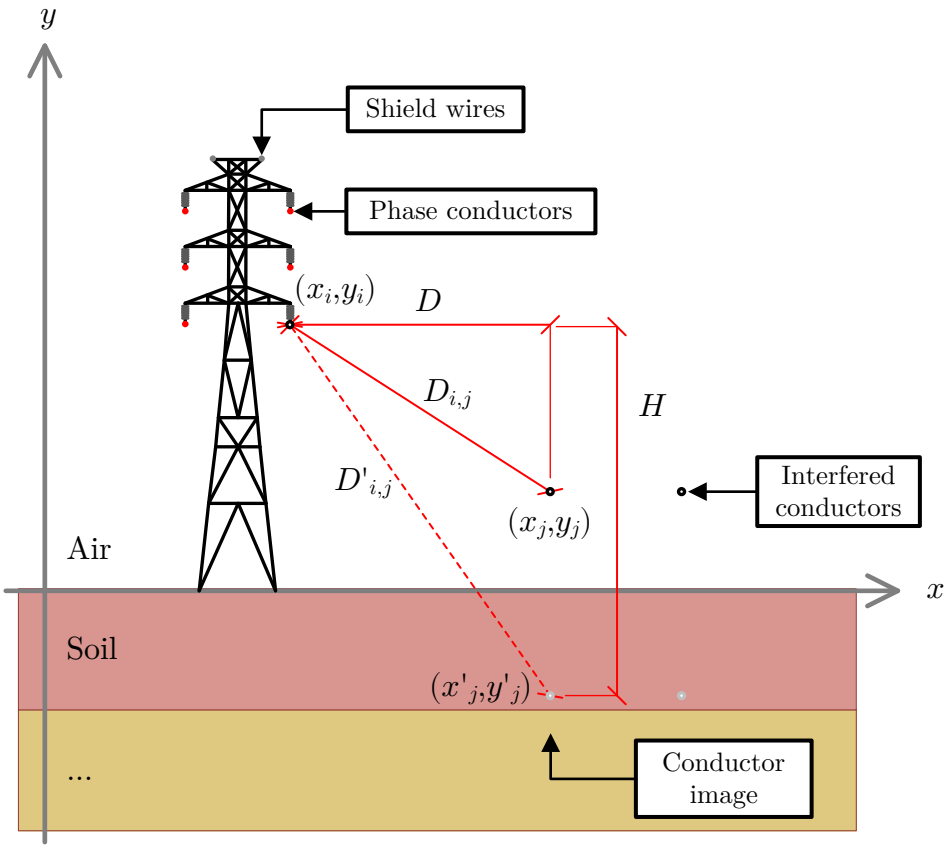

Source: own authorship.

Then, the shunt admittance matrix $\boldsymbol{Y}$ is determined as follows:

$$\boldsymbol{Y} = j\omega \boldsymbol{P}^{-1}, \tag{2.83}$$

in which $j = \sqrt{-1} = 1\underline{/90°}$; and ω is the power system angular frequency, in rad/s.

2.6.2 Sequence parameters for continuously transposed lines

If a three-phase transmission line is continuously transposed, matrices (2.81) and (2.83) can be decoupled into three single-phase equivalents using the theory of symmetrical components (STEVENSON; GRAINGER, 1994; DOMMEL, 1996).

Since the interfered conductors are not energized by the power system and often grounded at their extremities, they can be treated in the same way as the shield conductors in the calculation model. Therefore, nodes related to the shield conductors and the interfered system can be eliminated from (2.81) using Kron reduction, yielding a lower order equivalent matrix. For a

three-phase system, considering shield and interfered conductors grounded on both extremities, one can write the following equivalent series impedance 3×3 matrix:

$$\boldsymbol{Z_{EQ}} = \boldsymbol{Z_{FF}} - \boldsymbol{Z_{FG}} \cdot \boldsymbol{Z_{GG}}^{-1} \cdot \boldsymbol{Z_{GF}}, \tag{2.84}$$

with:

$$\boldsymbol{Z_{FF}} = \begin{bmatrix} Z_{a,a} & Z_{a,b} & Z_{a,c} \\ Z_{b,a} & Z_{b,b} & Z_{b,c} \\ Z_{c,a} & Z_{c,b} & Z_{c,c} \end{bmatrix}, \tag{2.85}$$

$$\boldsymbol{Z_{FG}} = \begin{bmatrix} Z_{a,n1} & \dots & Z_{a,nN} & Z_{a,t1} & \dots & Z_{a,tM} \\ Z_{b,n1} & \dots & Z_{b,nN} & Z_{b,t1} & \dots & Z_{b,tM} \\ Z_{c,n1} & \dots & Z_{c,nN} & Z_{c,t1} & \dots & Z_{c,tM} \end{bmatrix}, \tag{2.86}$$

$$\boldsymbol{Z_{GG}} = \begin{bmatrix} Z_{n1,n1} & \dots & Z_{n1,nN} & Z_{n1,t1} & \dots & Z_{n1,tM} \\ \vdots & \ddots & \vdots & \vdots & \ddots & \vdots \\ Z_{nN,n1} & \dots & Z_{nN,nN} & Z_{nN,t1} & \dots & Z_{nN,tM} \\ Z_{t1,n1} & \dots & Z_{t1,nN} & Z_{t1,t1} & \dots & Z_{t1,tM} \\ \vdots & \ddots & \vdots & \vdots & \ddots & \vdots \\ Z_{tM,n1} & \dots & Z_{tM,nN} & Z_{tM,t1} & \dots & Z_{tM,tM} \end{bmatrix}, \tag{2.87}$$

$$\boldsymbol{Z_{GF}} = \begin{bmatrix} Z_{n1,a} & \dots & Z_{nN,a} & Z_{t1,a} & \dots & Z_{tM,a} \\ Z_{n1,b} & \dots & Z_{nN,b} & Z_{t1,b} & \dots & Z_{tM,b} \\ Z_{n1,c} & \dots & Z_{nN,c} & Z_{t1,c} & \dots & Z_{tM,c} \end{bmatrix}. \tag{2.88}$$

Assuming the transmission line to be transposed, the matrix (2.84) is rewritten in an ideal scenario as:

$$\boldsymbol{Z_{EQ,T}} = \begin{bmatrix} Z_P & Z_M & Z_M \\ Z_M & Z_P & Z_M \\ Z_P & Z_M & Z_P \end{bmatrix}, \tag{2.89}$$

where scalars Z_P and Z_M are:

$$Z_P = \frac{Z_{EQ}(1,1) + Z_{EQ}(2,2) + Z_{EQ}(3,3)}{3}, \tag{2.90}$$

$$Z_M = \frac{Z_{EQ}(1,2) + Z_{EQ}(2,3) + Z_{EQ}(3,1)}{3}. \tag{2.91}$$

Finally, considering an ABC[1] phase sequence, the symmetrical component transform is applied using Fortescue matrix $\boldsymbol{T}$, resulting in matrix $\boldsymbol{Z_{012}}$:

$$\boldsymbol{T} = \frac{1}{3} \begin{bmatrix} 1 & 1 & 1 \\ 1 & a & a^2 \\ 1 & a^2 & a \end{bmatrix}, a = e^{j\frac{2\pi}{3}}, \tag{2.92}$$

[1]The same results would be obtained for a system with reverse phase sequence CBA.

$$\boldsymbol{Z_{012}} = \boldsymbol{T}^{-1} \cdot \boldsymbol{Z_{EQ,T}} \cdot \boldsymbol{T} = \begin{bmatrix} Z_0 & 0 & 0 \\ 0 & Z_1 & 0 \\ 0 & 0 & Z_2 \end{bmatrix}, \tag{2.93}$$

in which Z_0 and $Z_1 = Z_2$ are, respectively, the zero, positive and negative sequence impedances of the transmission line, in ohms per unit length.

The procedure for obtaining the sequence domain admittance matrix $\boldsymbol{Y_{012}}$ is rigorously the same as (2.84)-(2.93) and further calculation steps are omitted.

2.6.3 Modal parameters for untransposed lines

Although the symmetrical components approach provides a convenient method to handle multiphase systems, it results in average values for surge impedances and propagation constants, which may mask important effects produced by asymmetry of conductors (WEDEPOHL, 1963). Besides, when the phenomenon of interest is the conductive coupling, shield wire currents have to be determined explicitly, as represented in Figure 2.11, which cannot be performed in the sequence domain model due to Kron elimination (2.84). It is possible to overcome these issues by building a modal domain representation of the transmission line, where the N coupled line conductors are represented by their respective decoupled propagation modes (WEDEPOHL; NGUYEN, 1996).

Differently from the preceding section, where the transformation matrix $\boldsymbol{T}$ is known, the transformation parameters for untransposed lines have to be calculated from each pair of phase-domain matrices $\boldsymbol{Z}$ and $\boldsymbol{Y}$. Using eigenvalue/eigenvector theory, one can convert the coupled matrices (2.81) and (2.83) into diagonal matrices (DOMMEL, 1996; WEDEPOHL; NGUYEN, 1996):

$$\boldsymbol{\Lambda} = \boldsymbol{T_V}^{-1} \cdot \boldsymbol{Z} \cdot \boldsymbol{Y} \cdot \boldsymbol{T_V}, \tag{2.94}$$

in which $\boldsymbol{\Lambda}$ is the diagonal matrix composed by the eigenvalues of the matrix product $\boldsymbol{Z} \cdot \boldsymbol{Y}$; and $\boldsymbol{T_V}$ is the matrix of eigenvectors, or modal matrix, associated to $\boldsymbol{Z} \cdot \boldsymbol{Y}$. Matrices $\boldsymbol{\Lambda}$ and $\boldsymbol{T_V}$ are determined by solving the following system of linear equations:

$$\{\boldsymbol{Z} \cdot \boldsymbol{Y} - \Lambda_k \boldsymbol{I}\} \cdot \boldsymbol{T_{V,k}} = 0, \tag{2.95}$$

in which $\boldsymbol{I}$ is the identity matrix; Λ_k is the k^{th} eigenvalue of matrix product $\boldsymbol{Z} \cdot \boldsymbol{Y}$; and $\boldsymbol{T_{V,k}}$ denotes the k^{th} column of modal matrix $\boldsymbol{T_V}$. Classically, solutions to the linear system (2.95)

are obtained by using the Newton-Raphson algorithm (WEDEPOHL; NGUYEN, 1996). A convenient approach involves the use of similarity transformations to convert matrix products $\boldsymbol{Z} \cdot \boldsymbol{Y}$ and $\boldsymbol{Y} \cdot \boldsymbol{Z}$ into diagonal matrices (KUROKAWA *et al.*, 2007).

Modal parameters are the diagonal elements of matrices $\boldsymbol{Z_M}$ and $\boldsymbol{Y_M}$, calculated according to (2.96) and (2.97) (DOMMEL, 1996).

$$\boldsymbol{Z_M} = \boldsymbol{T_V}^{-1} \cdot \boldsymbol{Z} \cdot \boldsymbol{T_V}^{-T}, \tag{2.96}$$

$$\boldsymbol{Y_M} = \boldsymbol{T_V}^{T} \cdot \boldsymbol{Y} \cdot \boldsymbol{T_V}, \tag{2.97}$$

where superscript $^{-T}$ denotes the inverse of the transposed matrix.

2.7 REVIEW OF THE SPECIALIZED LITERATURE

Historically, the safety issues to which metallic installations are exposed under interference conditions have been identified as a special concern by the oil & gas and telecommunications sectors, motivating numerous studies aiming at prediction and mitigation techniques.

In 1978, in the United States, a joint research program between the Electrical Power Research Institute (EPRI) and the American Gas Association (AGA) culminated in the technical report EL-904 (DABKOWSKI; TAFLOVE, 1978a; DABKOWSKI; TAFLOVE, 1978b), which provides design guidelines to mitigate the impacts of AC interferences produced by overhead transmission lines on gas pipelines. This work proposes several empirical equations, based on electric circuits theory, to estimate the induced potentials in an interfered pipeline, which are intended to be implemented on a computer or programmable calculator.

This work has been further enhanced by Dawalibi *et al.* (1987), who developed a generalized approach to analyze the effects of transmission line faults on natural gas pipelines, documented in the technical report EPRI-EL-5472, and implemented in the computer program ECCAPP (Electromagnetic and Conductive Coupling Analysis of Powerlines and Pipelines). Models employed in ECCAPP are mainly based on the contributions provided by Carson (1926), Pollaczek (1926), Sunde (1968) and Heppe (1979), and form the basis of what has become the industry standard up to date.

In Europe, CIGRÉ working group 36.02 issued a report in 1995, named “Guide on the Influ-

ence of High Voltage AC Power Systems on Metallic Pipelines - Electromagnetic Compatibility with Telecommunication Circuits, Low Voltage Networks and Metallic structures" (CIGRÉ WG-36.02, 1995). This document provides comprehensible information on the electromagnetic coupling mechanisms and exposes computational methods also based in the works by Carson (1926), Pollaczek (1926) and Sunde (1968).

All the aforementioned publications rely on expressing the system composed by the power line and the interfered installation as an equivalent electric circuit, in which inductive coupling effects are represented by means of fictitious voltage sources that depend on the values of the mutual impedances between conductors. Therefore, a considerable amount of research efforts has been dedicated to finding suitable forms of Carson equation (2.13), being relevant to mention the approximations derived by Deri *et al.* (1981), Lucca (1994) and Ametani *et al.* (2009), which are reported to provide satisfactory accuracy for uniform soil models in a variety of applications.

Conductive coupling mechanisms are a complete self-contained research subject which have been extensively studied in the context of substation grounding (IEEE, 2000). Common approaches have been the use of simplified formulas and analytical expressions for uniform and two-layered soil models (SUNDE, 1968; DAWALIBI; MUKHEDKAR, 1975; DAWALIBI; MUKHEDKAR, 1975a; DAWALIBI; MUKHEDKAR, 1975b; DWIGHT, 1983; SEEDHER; THAPAR, 1987).

With the increasing computational power, multilayered soil models have become a topic of interest among researchers, in inductive coupling studies (NAKAGAWA *et al.*, 1973; PAPAGIANNIS *et al.*, 2005; TSIAMITROS *et al.*, 2008; LEE *et al.*, 2013), as well as electrical grounding applications (DAWALIBI; BARBEITO, 1991; DAWALIBI *et al.*, 1994; ZOU *et al.*, 2004; ZHANG *et al.*, 2005; LI *et al.*, 2007). Modern professional software for EMI studies integrate tools for soil stratification analysis, calculations of faults in transmission lines, simulations of inductive interferences and of grounding grids (DAWALIBI; DONOSO, 1993).

Currently, the state-of-the-art in EMI research involves the study of the transient behavior of complex geometries and convoluted soil heterogeneities, including the effects of soil ionization and frequency-dependent parameters (HE *et al.*, 2013). Techniques based in computational electromagnetics (CEM) have gained popularity recently, due to the fact that the difficulties

intrinsic to EMI modeling, in special the complex formulations of (2.17) and (2.49), are handled in a systematic and relatively simple form by directly solving Maxwell equations. There are successful reports of applications using the FDTD method (CHEN *et al.*, 2010; AMETANI *et al.*, 2015), as well as finite element analysis (CHRISTOFORIDIS *et al.*, 2003b; GÜEMES; HERNANDO, 2004; PAPAGIANNIS *et al.*, 2005; FURLAN, 2015).

2.8 CHAPTER SUMMARY

This chapter provided a straightforward exposition of the main concepts necessary to build accurate models of transmission lines under interference conditions.

Starting with the fundamentals of soil resistivity analysis, mechanisms of inductive, capacitive and conductive coupling were described, along with the relevant variables determinant to each phenomena and the equations necessary to consider the multilayered nature of soils in the simulation models.

A review of the basics of electrical safety was performed in order to establish a clear understanding of how interference mechanisms affect a target installation and which criteria should be adopted in order to determine safe limits and whether or not corrective actions and/or mitigations should be carried out.

Since a significant part of this thesis relies on the use of circuit models to simulate EMI phenomena, it was found pertinent to recall what transmission line parameters are relevant to the discussion, how to determine them from the fundamental equations, how they are affected by the interference mechanisms and how to express line parameters both in the sequence and in the modal domains.

Finally, a review of the specialized EMI literature was provided, in order to familiarize the reader with the background, evolution and state-of-the-art of the methods currently available.

In the next chapter, the FDTD method is applied to an EMI case involving a power line and a pipeline. In the discussion, the benefits of using CEM-based tools to handle power systems problems are highlighted, as well as its drawbacks, which are presented as the reason to develop the improved techniques proposed in this thesis, described in the subsequent chapters.

CHAPTER 3

ELECTROMAGNETIC THEORY APPROACH

The study of transients caused by lightning discharges is presented as the context and motivation to develop techniques based on the electromagnetic theory to carry out EMI analysis.

Lightning discharges are a well-known cause of failure of transmission lines and external installations, such as pipelines (DAS *et al.*, 2014; NACE, 2007). A direct discharge on a power line or induced voltages caused by a lightning strike on its vicinities may provoke line flashover or insulation failure of transformers, arresters or other equipment, ultimately leading to power outage, what justifies the adoption of measures such as installation of shield wires.

In case of interferences between a transmission line and a target installation, lightning discharge currents flowing through the shield wires and being discharged into the soil through the grounding conductors may induce substantial transient voltages in the interfered system, due to the inductive and conductive coupling mechanisms described in Sections 2.2 and 2.4. Induced voltages resulting from lightning discharges may subject the target installation to the same hazards described in Section 2.5, i.e., equipment damage, as well as potentially harmful voltages for living beings.

A review of basic lightning discharge and protection mechanisms is provided, after which the FDTD method is employed to investigate the transient voltages induced on a target installation by the lightning discharge currents flowing through the conductors of a power line.

3.1 BASICS OF LIGHTNING DISCHARGES AND PROTECTION

Lightning is a sudden electrostatic discharge that occurs typically during a thunderstorm. An electrically active thundercloud may be regarded as an electrostatic generator suspended in an atmosphere of low electrical conductivity (RAKOV; UMAN, 2003).

As a thundercloud moves over the surface of the Earth, an equal electric charge, but of

opposite polarity, is induced on the soil surface underneath the cloud. The oppositely charged regions create an electric field within the air between them – the greater the accumulated charge, the higher the electric field. If the electric field intensity reaches the air breakdown field strength, which magnitude is of the order of 3 MV/m, the discharge occurs. Lightning discharges may reach up to 30 million volts at 100 thousand ampères, during a time period of the order of microseconds (RAKOV; UMAN, 2003).

Lightning protection systems (LPS) are used to prevent or mitigate lightning strike damage to structures by intercepting such strikes and safely conducting discharge currents to the ground. A lightning protection system often includes a network of air terminals, bonding conductors and ground electrodes designed to provide a low impedance path to the ground, from which follows that the grounding grid is the critical component of an LPS.

Overhead power lines are commonly equipped with a shield or earth wire, as depicted in Figure 3.1, which is a bare conductor grounded at the top of each tower structure, in order to reduce the probability of direct lightning strikes on the phase conductors.

Figure 3.1. Shield wires on the top of a power line, parallel to the phase conductors, made of bare wires with a direct connection to the tower structure, designed to intercept lightning discharges and conduct surge currents to the ground. Shield wires provide a protection cone, under which structures, such as the phase conductors, are shielded against lightning strokes.

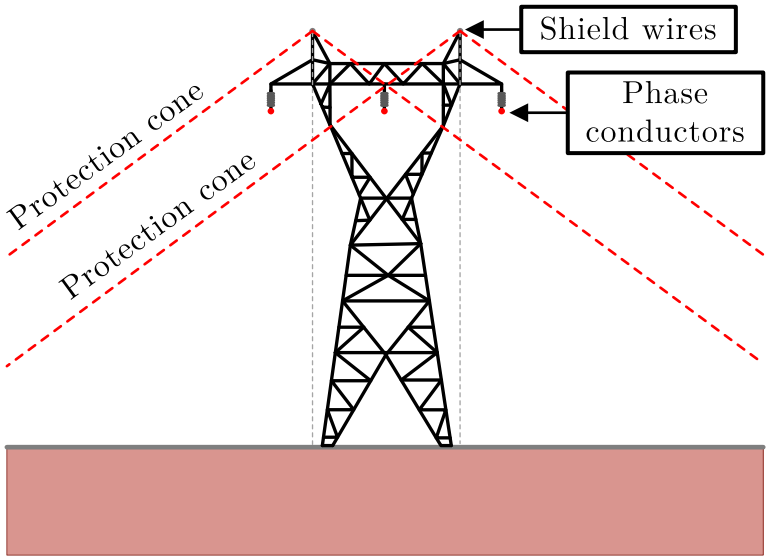

Source: own authorship.

The lightning current pulse is characterized by a peak value, rise time and half-value time and is approximated by the Heidler function (3.1), which accounts for the concave behavior of

the rising portion of a typical lightning stroke (IEC, 1995):

$$I_s(t) = \frac{I_0}{\eta} \frac{(t/\tau_1)^n}{1 + (t/\tau_1)^n} e^{(-t/\tau_2)}, \tag{3.1}$$

in which I_0 is the current amplitude at the base of the lightning channel, in A; τ_1 is the rise time constant, in s; τ_2 is the half-value time constant, in s; n is an integer [1, 2,...,10]; and η is the current amplitude correction factor, given by:

$$\eta = e^{\left[\left(\frac{\tau_1}{\tau_2}\right)\left(n\frac{\tau_1}{\tau_2}\right)\right]^{-1/n}}. \tag{3.2}$$

Lightning strokes with moderate amplitudes are reported to reach a peak value of the order of 30 kA, with a rise time $\tau_1 = 1$ μs and half-value time $\tau_2 = 50$ μs (ZIPSE, 1994). Other time constants are also considered common in the literature, such as: 8/20 μs, 0.25/100 μs and 10/350 μs (RAKOV; UMAN, 2003). Figure 3.2 shows the waveforms of lightning pulses with such characteristics.

Figure 3.2. Lightning discharge waveforms, with peak magnitude 30 kA, time constants: 8/20 μs, 1/50 μs, 0.25/100 μs and 10/350 μs.

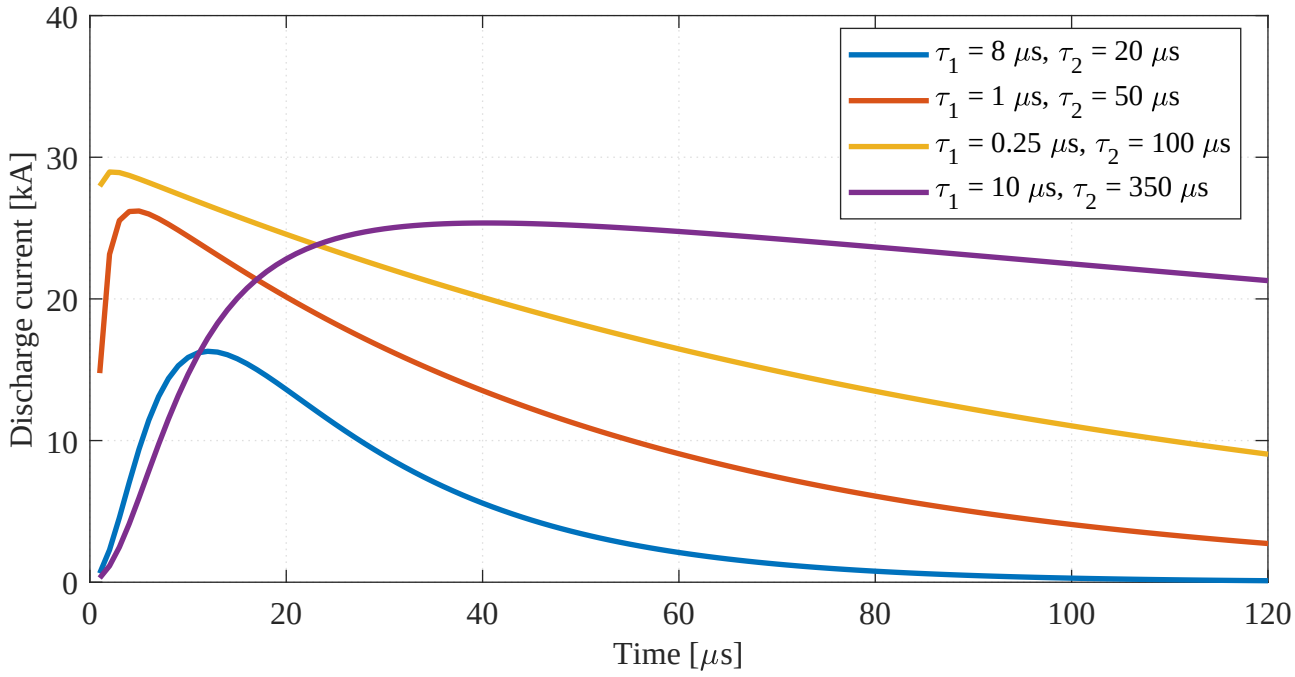

Source: own authorship.

3.2 PROPOSED FDTD IMPLEMENTATION

The FDTD method is chosen due to the relative simplicity with which electromagnetic transient simulations can be performed directly in the time-domain on complex, highly-realistic 3D models, with composite geometries consisting of different types of materials including dielectric, magnetic, frequency-dependent, nonlinear, and anisotropic materials (ELSHERBENI; DEMIR, 2015).

In the FDTD method, the electromagnetic coupling phenomena relevant to interference analysis, i.e., inductive, capacitive and conductive coupling mechanisms, are implicit and flow naturally from the time-domain solution of Maxwell equations. Besides, the method can easily handle structures that are difficult to represent using electric circuit components, such as mitigation devices based on shielding effects.

A general-purpose FDTD code is fully developed in this work, enabling the user to perform the necessary tasks for a professional EMI study under applicable standards (IEEE, 2000; NACE, 2007), with the following enhancements: (a) simulations are carried out on three-dimensional domains; (b) arbitrary soil structures and material heterogeneities are consistently accounted; and (c) high-frequency transients, in special lightning discharge currents, are accurately modeled.

The decision of building custom programs instead of using readily-available software is justified by two main reasons: 1) most commercial FDTD software are designed to work with frequencies typical of scattering problems, and often limited to standard waveforms, such as sinusoidal, Gaussian pulse etc., and do not feature implementations of the Heidler function (3.1); and 2) having access to the FDTD routines provides improved run-time control over calculations, which makes possible the integration with large-scale circuit models based on the tools described in the subsequent chapter, resulting in very sophisticated simulation models.

3.2.1 Flowchart of the proposed program

The FDTD method provides a direct approximation of Maxwell equations by means of central finite differences, which are evaluated in the time-domain for electrically small discrete

subdomains (YEE, 1966).

With all the necessary FDTD equations, which are thoroughly discussed in Appendix B, a time-marching algorithm is constructed according to the flowchart shown in Figure 3.3.

Figure 3.3. Flowchart of the proposed FDTD implementation.

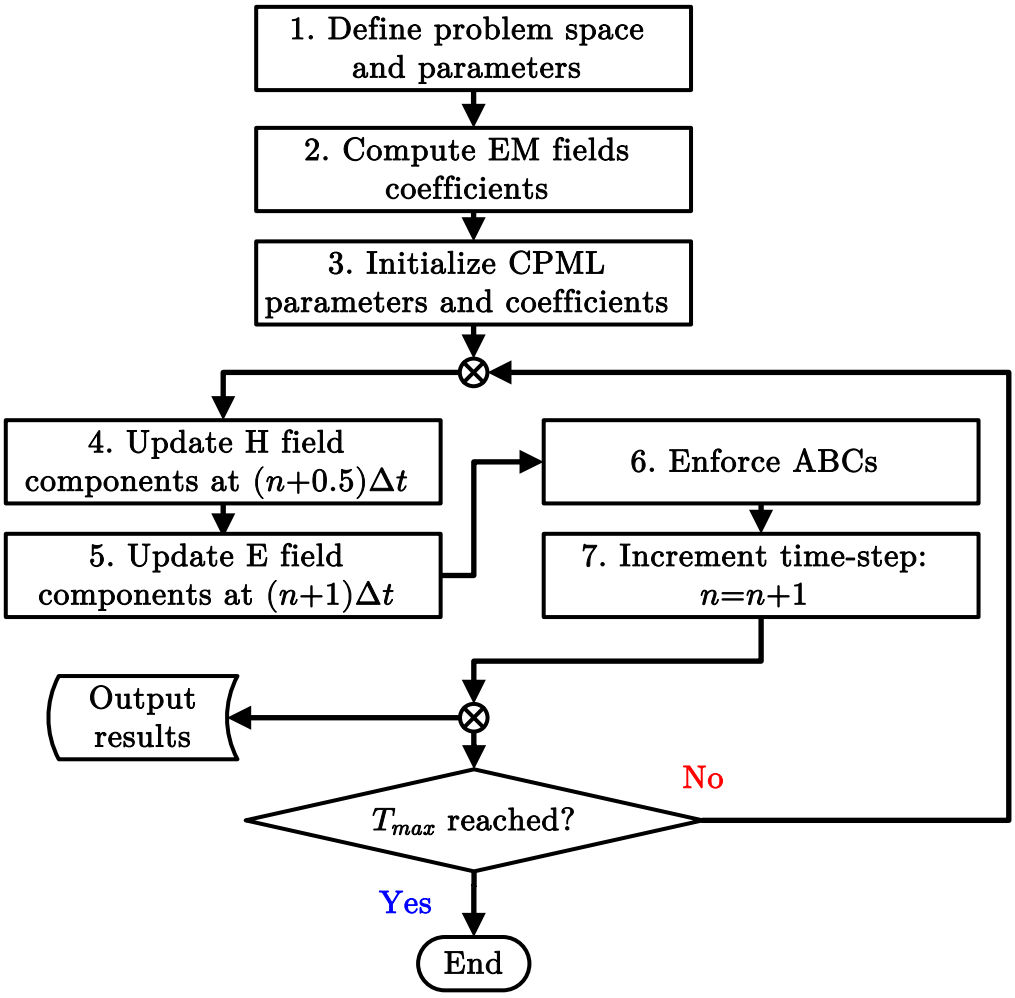

Source: own authorship.

3.2.2 Model of the lightning channel

In order to introduce the lightning stroke channel into the FDTD model, a current source given by (3.1), whose waveform is shown in Figure 3.2, and a loop electrode with ground return path are employed (CHEN *et al.*, 2010). The loop electrode is positioned at a remote location from the system under study (e.g. distance $>$ 100 m) to simulate the discharge current in a practical situation, as illustrated in Figure 3.4.

Figure 3.4. Lightning equivalent current source connected to a grounding grid. The circuit is completed through a remote electrode, with ground return path.

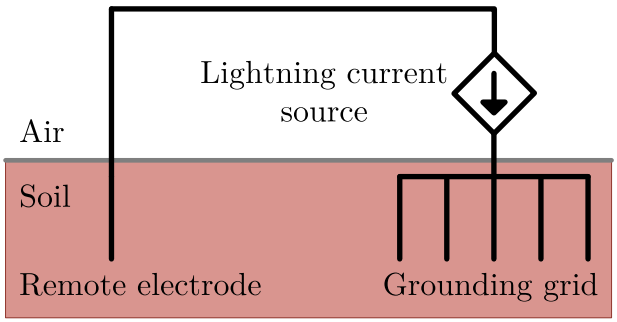

Source: own authorship.

3.3 CASE STUDIES

3.3.1 Simple test case

Figure 3.5 shows a system studied by Chen *et al.* (2010), composed of one air terminal and a grounding grid with 12 peripheral rods and a mesh with size equal to 5 m.

Figure 3.5. A simple grounding grid with horizontal and vertical conductors subject to a lightning discharge.

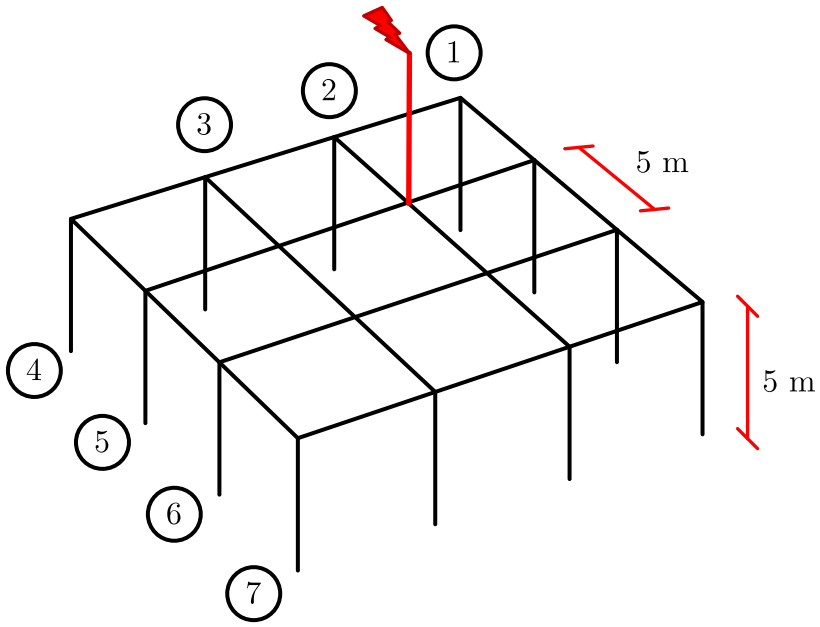

Source: adapted from (CHEN *et al.*, 2010).

Conductors are made of reinforced steel with conductivity $\sigma_{steel} = 7.96 \times 10^6$ S/m and diameter 10 mm. The grounding grid is buried 1 m below the surface of the soil, which is

assumed to be an uniform medium with conductivity $\sigma_{soil} = 0.002$ S/m and relative permittivity $\varepsilon_r = 10$. The lightning current is a pulse with peak value 10 kA, $\tau_1 = 2.6$ μs, $\tau_2 = 40$ μs, $n = 1$. Figure 3.6 shows the current distribution along vertical rods numbered from 1 to 7 obtained by Chen *et al.* (2010). Figure 3.7 contains the response of the proposed FDTD program.

Figure 3.6. Current distribution along vertical rods in Figure 3.5 (reference values).

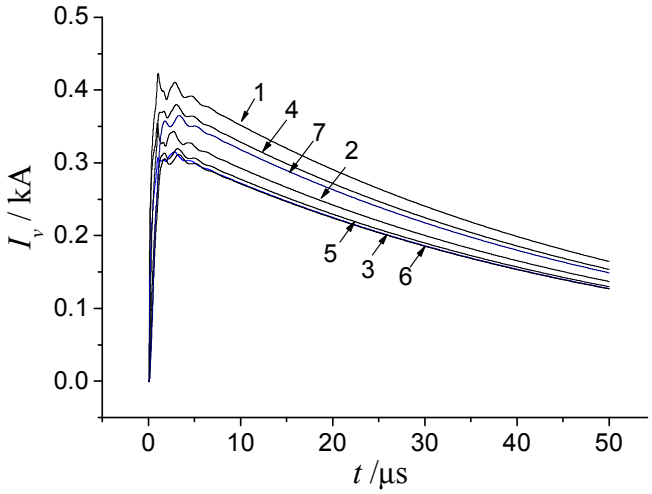

Source: reproduced from (CHEN *et al.*, 2010).

Figure 3.7. Current distribution along vertical rods in Figure 3.5, for the proposed implementation. Results agree with the reference values of Figure 3.6.

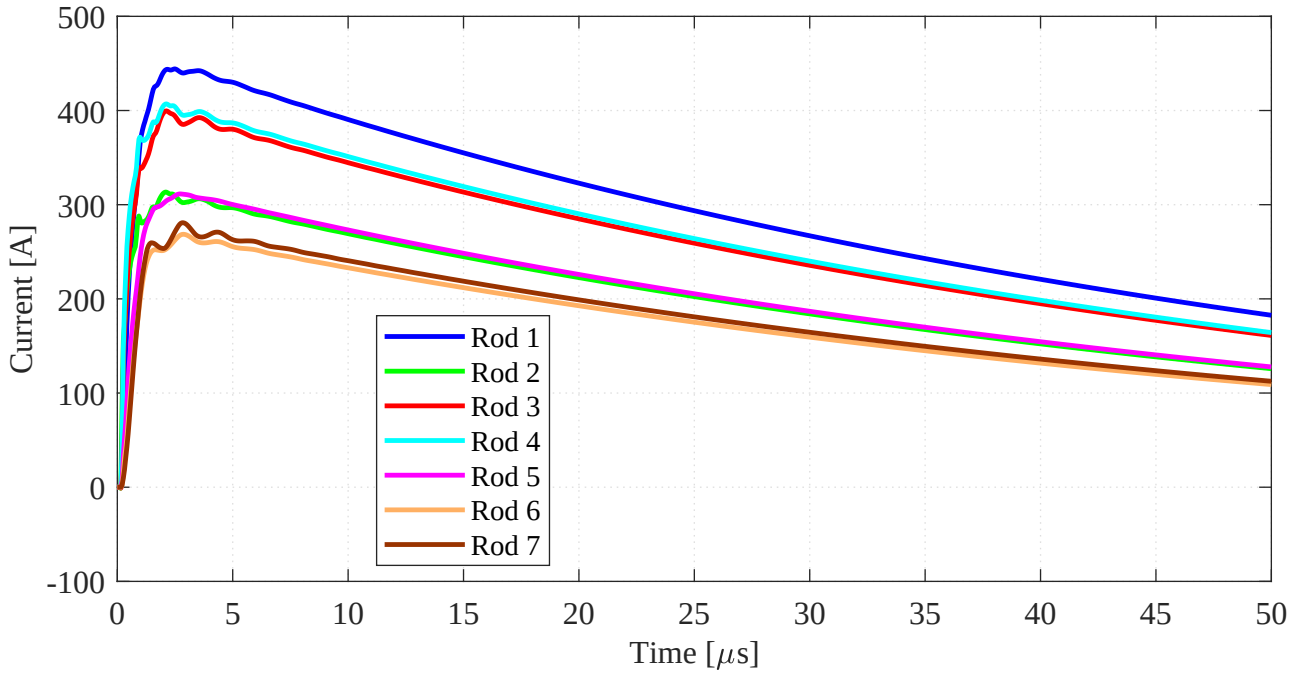

Source: own authorship.

As simulation results agree with the reference values, the implemented FDTD code is considered validated. The next sections follows with the simulation of a lightning strike on a power line tower and the interferences caused in a nearby pipeline.

3.3.2 Grounding electrode of a transmission line tower

The system under study, shown in Figure 3.8, is composed of the tower structure, phase conductors, shield wires, grounding conductors, also known as counterpoises, and the concrete foundations with the internal steel-frames.

Figure 3.8. Perspective view of the system under study. The pipeline is parallel to the transmission line, with a distance of 10 m. A lightning discharge is assumed to hit the top of tower, being conducted to the ground through the tower structure, counterpoises and tower foundations.

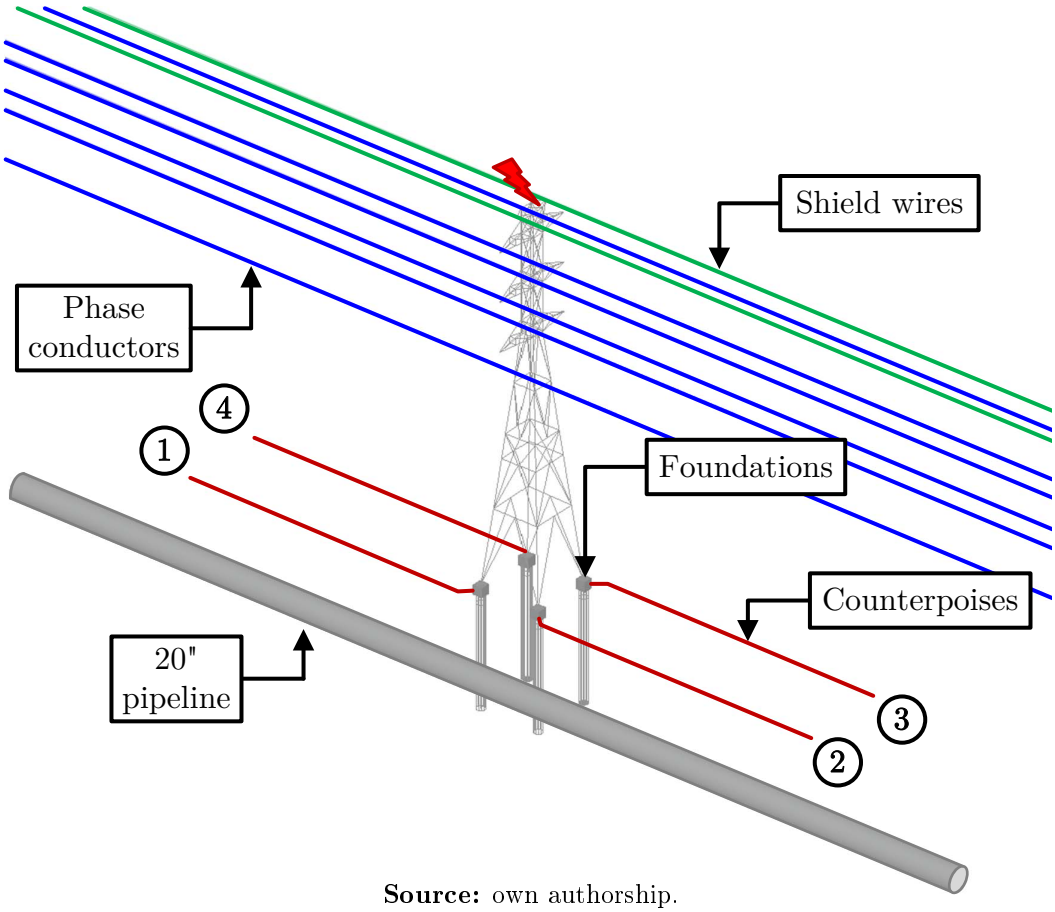

Source: own authorship.

The transmission line shares the right-of-way with a 20″ diameter underground carbon steel pipeline, coated with three-layer polyethylene (3LPE), installed at 3.5 m depth, which runs parallel to the transmission line axis, with a horizontal separation of 10 m.

Tables 3.1 and 3.2 summarize the constitutive properties and dimensions of the materials used. The concrete foundations are modeled as solid cylinders with diameter 70 cm, length 10 m, extending to the depth below the soil surface, which is assumed to be at z =0. The counterpoises are 25 m long in extension, buried at 50 cm depth. The total tower height is 30 m.

Table 3.1. Properties of materials represented in Figure 3.8.

Description	Material	σ [S/m]	ε_r	μ_r
Phase conductors	ACSR Grosbeak	2.5417×10^7	1	1.064
Shield wires	EHS Steel	4.0904×10^6	1	63.29
Tower structure	EHS Steel	4.0904×10^6	1	63.29
Counterpoises	Annealed copper	5.8001×10^7	1	1
Soil layer	Dry clay	2×10^{-3}	10	1
Foundations	Dry concrete	1×10^{-6}	4.5	1
Steel-frame	EHS Steel	4.0904×10^6	1	63.29
Pipeline wall	Carbon Steel	5.8001×10^6	1	300
Pipeline coating	Polyethylene	1×10^{-12}	2.25	1

Source: (IEEE, 2000; CHEN *et al.*, 2010; MARTINS-BRITTO *et al.*, 2019).

Table 3.2. Dimensions of conductors in Figure 3.8.

Description	Radius [m]
Phase conductors	1.2570×10^{-2}
Shield wires	0.4572×10^{-2}
Tower structure	0.05
Counterpoises	0.4572×10^{-2}
Pipeline	0.25

Source: own authorship.

The FDTD domain is a rectangular parallelepiped with dimensions $145 \times 105 \times 82.5$ m, with a discretization resolution of 50 cm. An air buffer of 5 m is added to each domain dimension, under 10 extra cells of fictitious absorbing materials, designed to prevent wave reflections at the domain boundaries, according to the techniques described in Section B.5. Simulation is carried out over 120 μs, with a time-step of 866 ps in order to comply with the stability criterion described in (B.15). A total computation time of approximately 121 h was required to run on an Intel® Core i9-7900X CPU @ 3.3 GHz with 64 GB RAM, which justifies the decision of

limiting the analysis to the effects of a single tower, since increasing the domain size to include more structures would make necessary a considerably higher computing time.

The lightning model, whose waveform is shown in Figure 3.2, is a pulse with peak value of 30 kA, $\tau_1 = 1$ μs, $\tau_2 = 50$ μs, $n = 1$. The lightning discharge is assumed to strike the top of the tower with an oblique incidence angle.

Figure 3.9 describes the grounding impedance, defined as the ratio of the electrode potential rise and the discharge current. It can be seen that the grounding impedance is not purely resistive, as it shows a transient behavior before it stabilizes in a value of the order of 8 Ω.

Figure 3.9. Transient grounding impedance of the earthing grid. Values oscillate over time until a stable value of 8 Ω is reached.

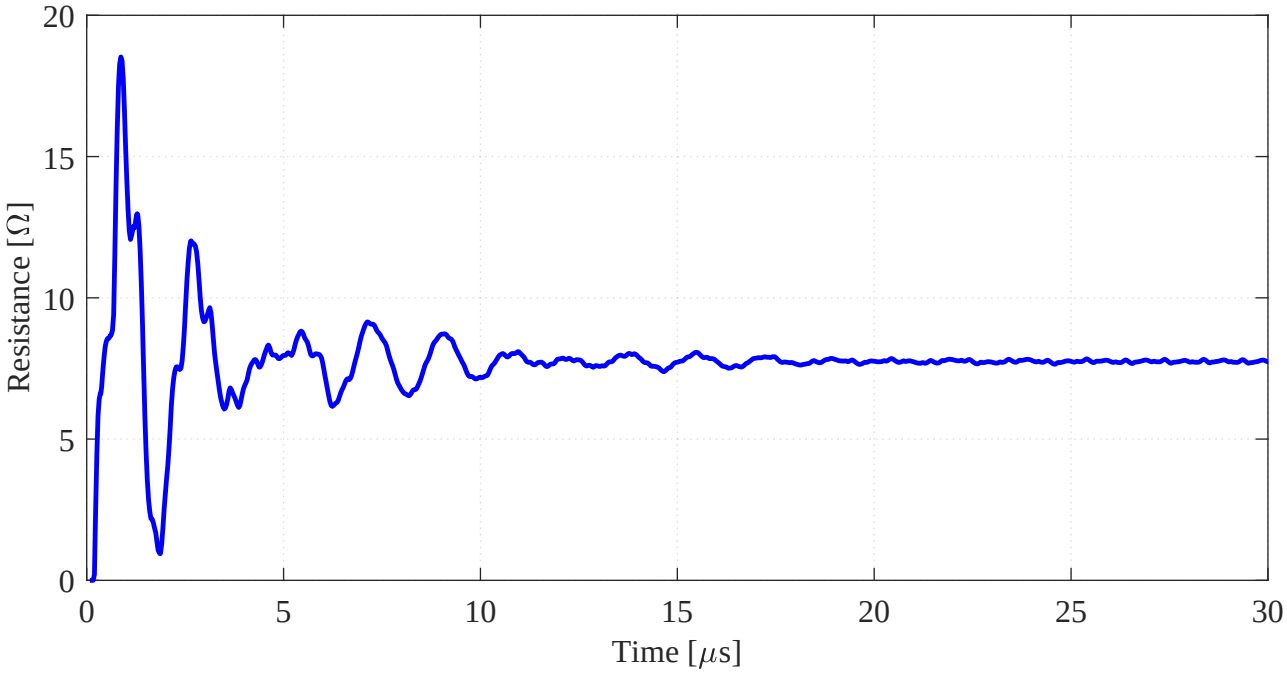

Source: own authorship.

Figures 3.10 and 3.11 present, respectively, the currents injected into the soil by the counterpoises and the tower foundations, which are numbered according to Figure 3.8. Figures are zoomed into the first 20 μs, which Figure 3.9 demonstrates to be the period where the transients reach the most considerable magnitudes. They indicate that the counterpoises play the most significant role in discharging the lightning current to the ground, as expected, since it is the controlled grounding device. However, the contribution of the tower foundations, of the order of 32% of the current flowing through the counterpoises, is not to be neglected, even though the concrete in dry conditions is a poor conductor. One interesting detail is that all the

curves follow the same trend, which is expected due to the grounding system symmetry. The differences in magnitudes are explained by the lightning path oblique incidence, which energizes the grounding conductors asymmetrically.

Figure 3.10. Currents injected into the soil by the counterpoises. Curves follow the trend of the lightning discharge, with a maximum value of 6.6 kA being injected by counterpoise 3.

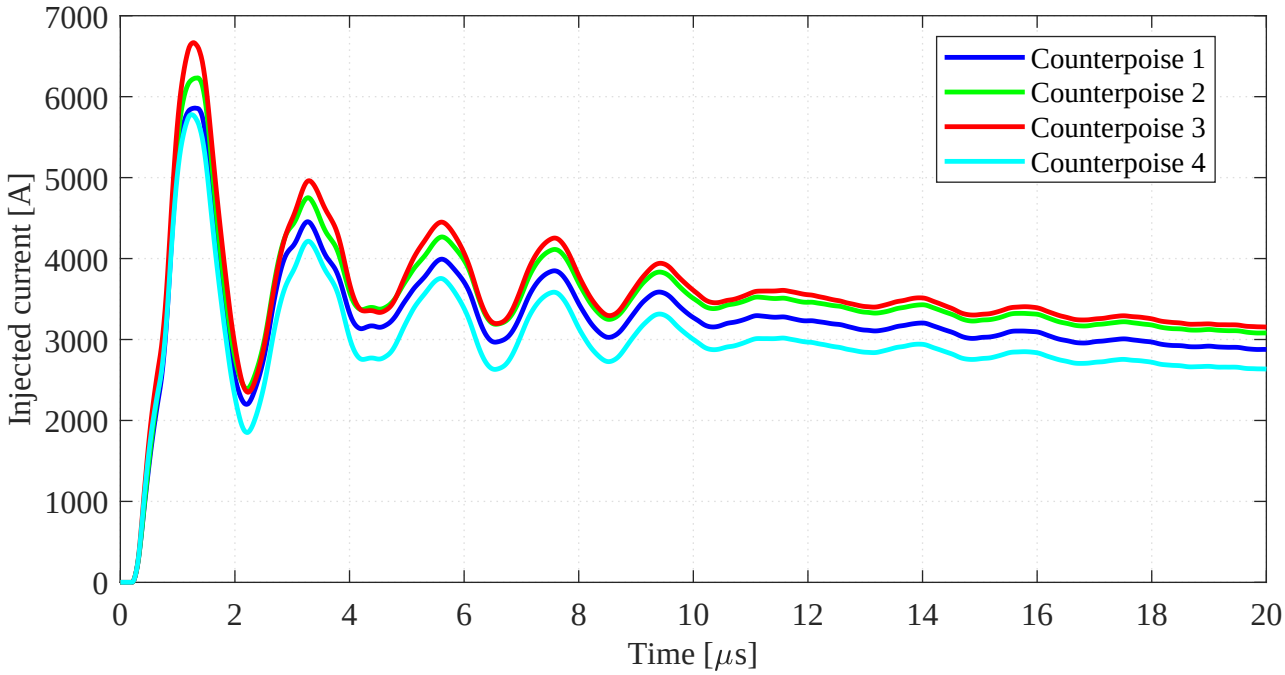

Source: own authorship.

As a consequence of the current injection into the ground, touch and step voltages arise at the tower vicinity. Figure 3.12 shows the touch voltage at 1 m apart from the tower. Figure 3.13 presents the electric field intensity at the soil surface (z =0) at time $t = 1$ μs, corresponding to the instant when the discharge current reaches its peak value. Since the electric field is the gradient of the scalar potential, the figure also happens to describe the step voltage distribution around the tower.

Finally, Figure 3.14 contains a side view of the electric field distribution around the tower. It can be seen that the energy flows throughout the external surface of the metallic tower, which works as a Faraday cage, as expected. Also, the shielding effect of the earth wires is evident, as the electric field intensities in the regions closer to the phase conductors are considerably low.

Electromagnetic field magnitudes are maximum at the top of the tower and symmetrically distributed throughout the geometry. As time progresses, values fade away. With enough simulation time, values are expected to vanish completely.

Figure 3.11. Currents injected into the soil by the tower foundations. Values are of the order of 32% of the amount discharged by the counterpoises, even though the dry concrete is a poor conductor. Maximum value is 2.1 kA.

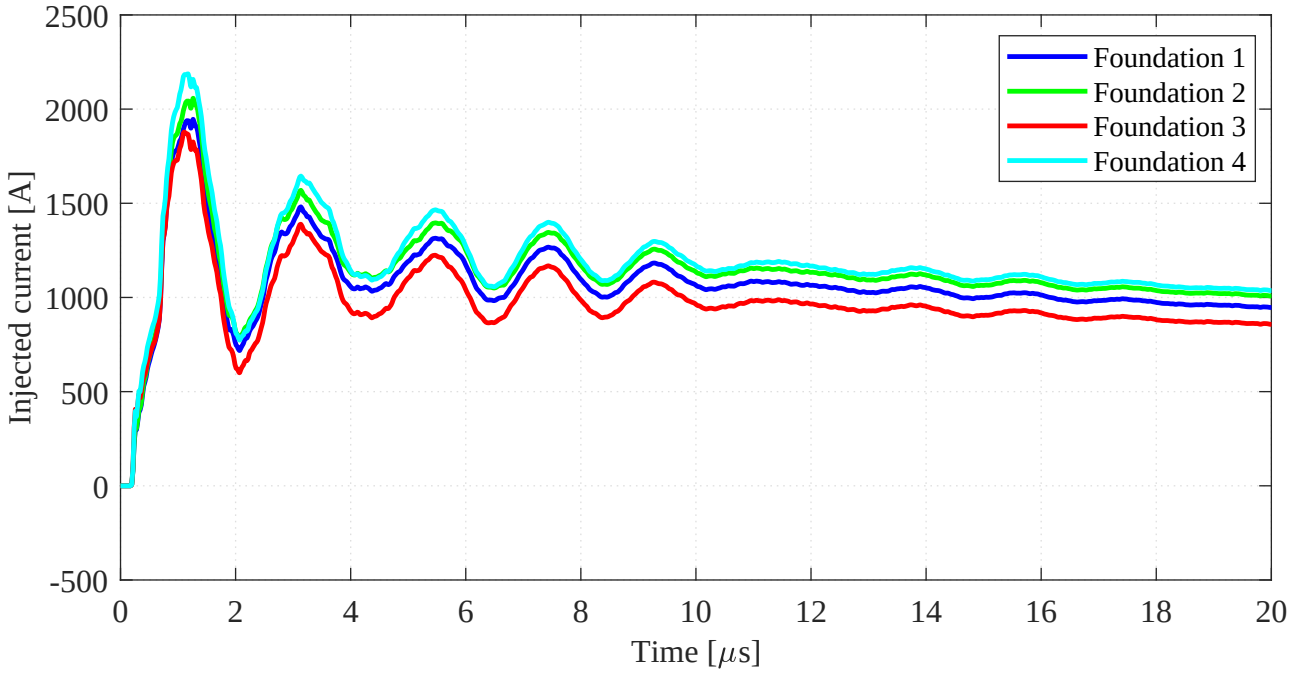

Source: own authorship.

Figure 3.12. Touch voltage at the tower vicinity. Maximum value of 171.4 kV exceeds the tolerable limits given in Table 3.3. Covering the soil with a layer of crushed rock 10 cm thick increases the safe limit to 242 kV, according to Table 3.4, thus mitigating risks of electrocution.

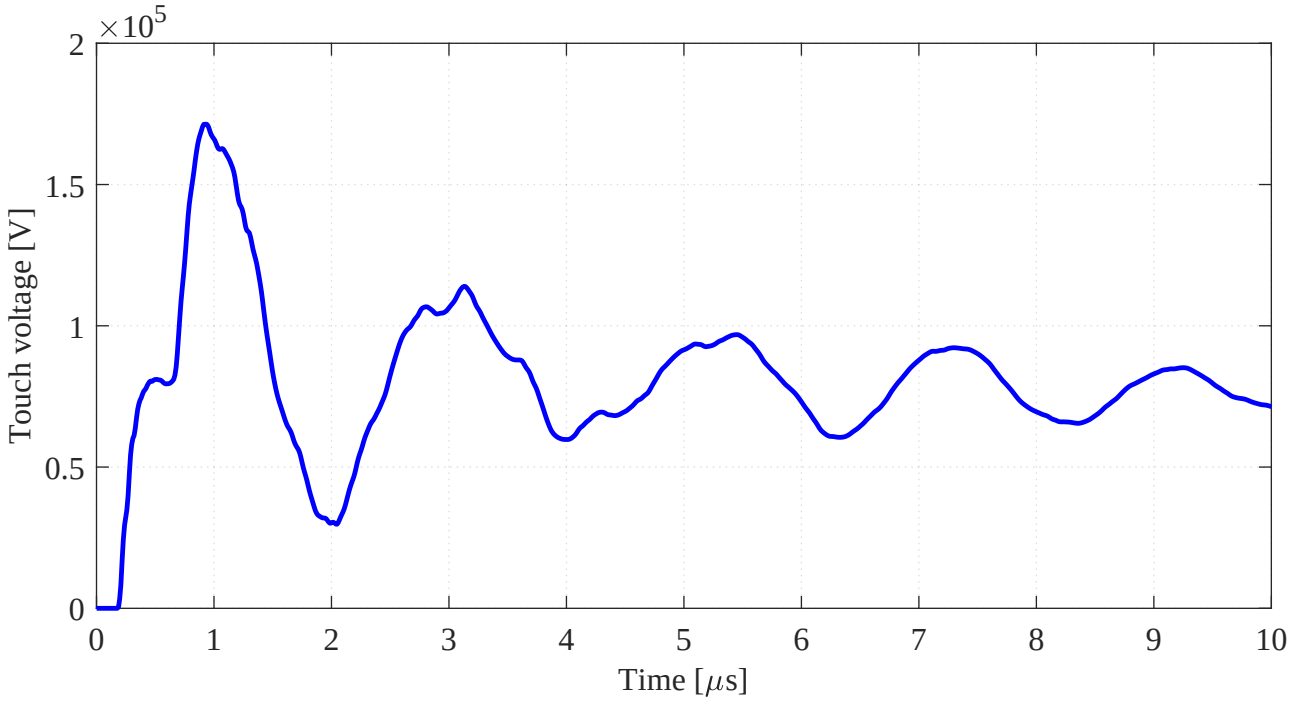

Source: own authorship.

Figure 3.13. Top view of the electric field magnitude at the soil surface (step voltage), logarithmic color scale. The maximum value is 94 kV, exceeding the maximum step voltage limit. Highest magnitudes occur at the extremities of the conductors, which agrees with previous works where a similar grounding grid was simulated using the method of moments (MARTINS-BRITTO, 2017b).

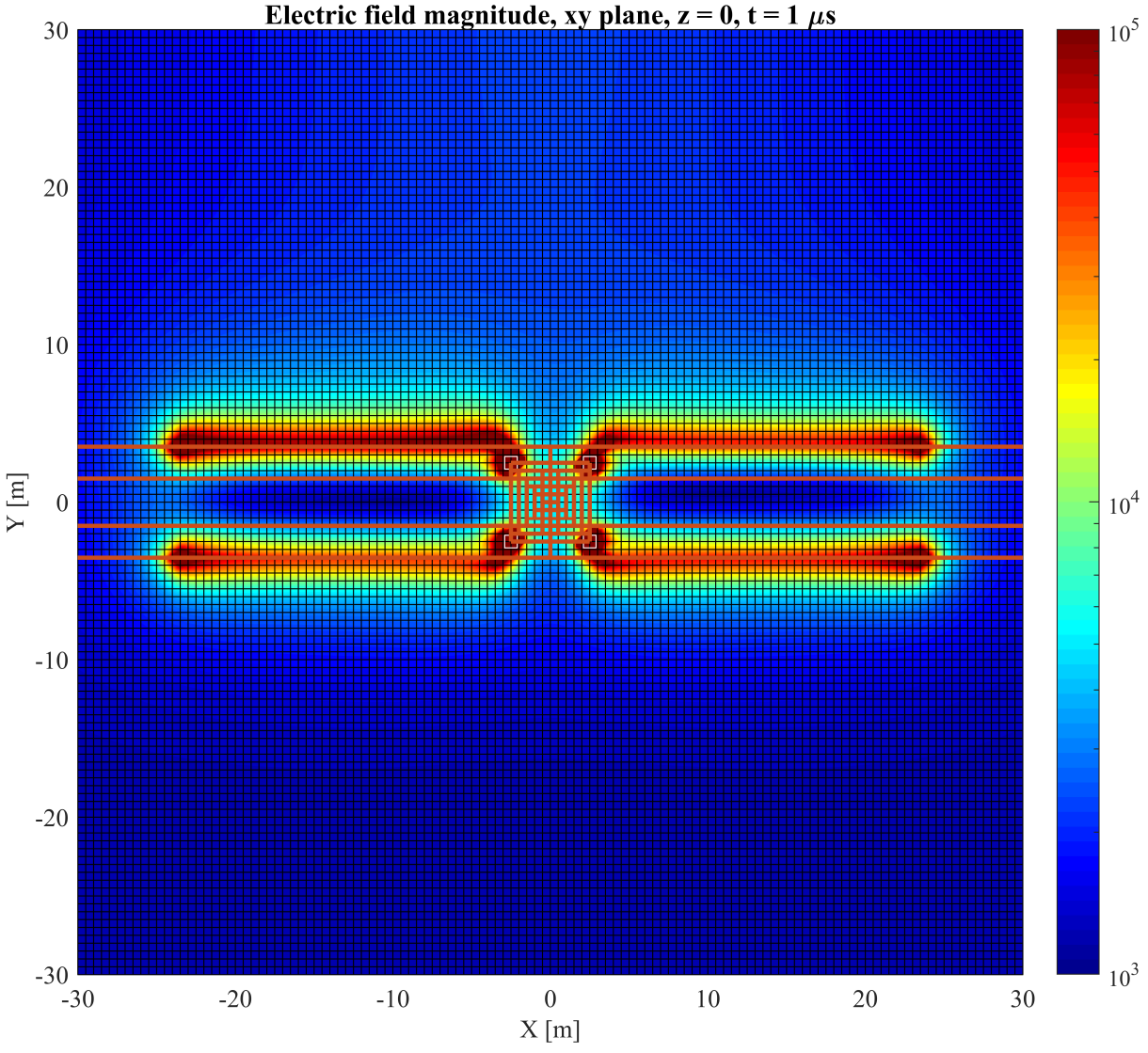

Source: own authorship.

Figure 3.14. Side view of the electric field magnitude around the tower, logarithmic color scale. The shielding effect is visible close to the phase conductors and inside the tower structure (Faraday cage).

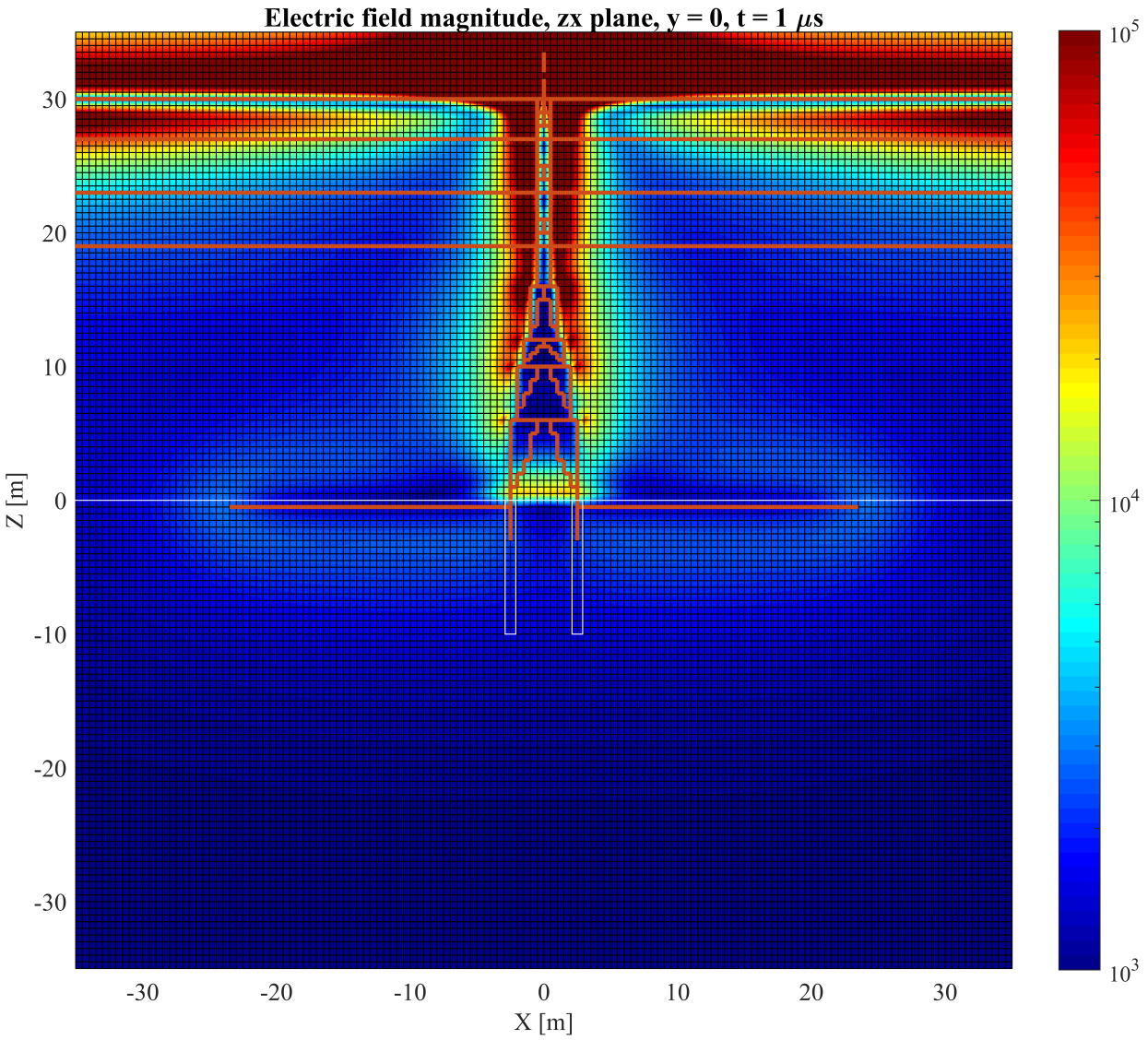

Source: own authorship.

3.3.3 Transient interferences on a nearby pipeline

In this section, the focus of the analysis are potentials transferred to the buried pipeline in the vicinities of the interfering transmission line, due to the lightning discharge studied in the preceding section. Figures 3.15 and 3.16 provide, respectively, the side and top views of the system shown in Figure 3.8, with the most relevant dimensions.

Figure 3.15. Side view showing the pipeline, counterpoises, burial depths, tower structure, concrete foundations and steel-frames. Tower height is 30 m from the soil surface. Pipeline and counterpoises are buried, respectively, at 3.5 m and 0.5 m. Foundations are 10 m long with steel-frames of 3 m.

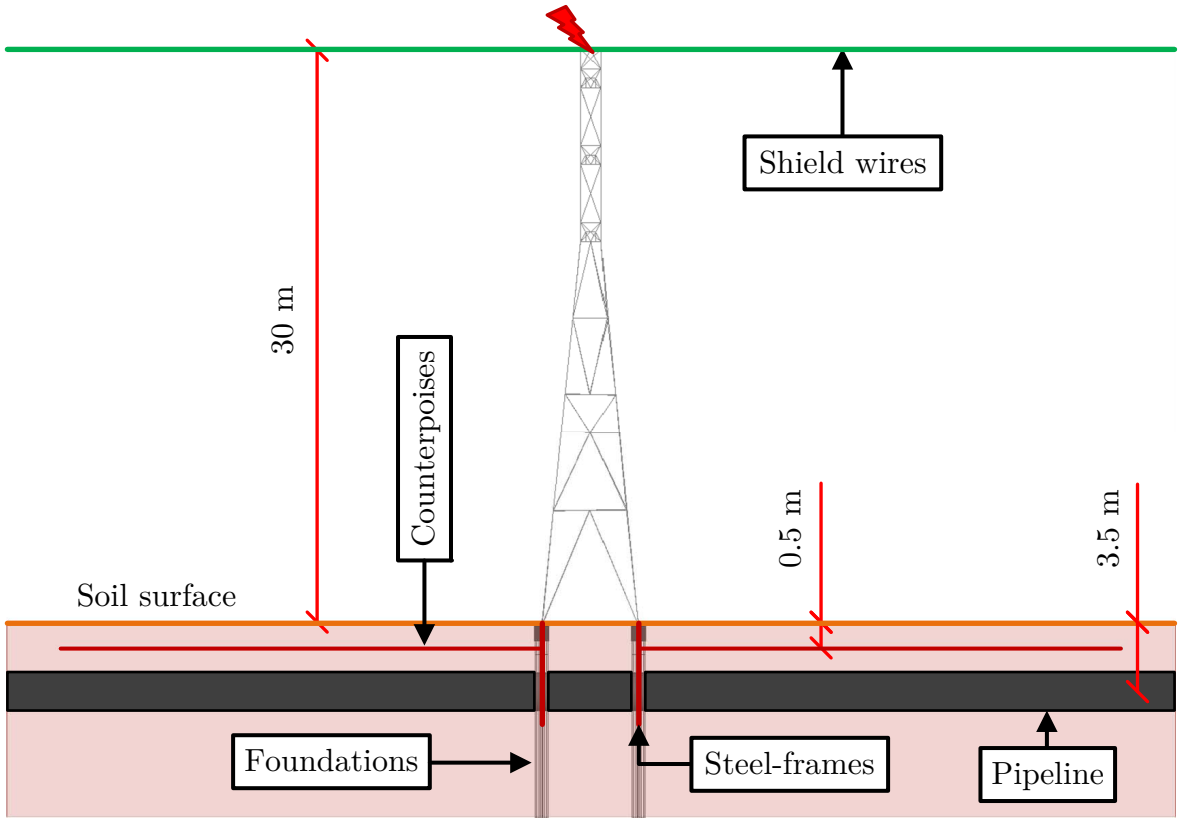

Source: own authorship.

The currents injected into the ground are shown in Figures 3.10 and 3.11. Transient ground potential rise and coating stress voltages are sampled at 7 observation points, labeled as $L = -30$ to $L = 30$ in Figure 3.16. Ground potentials are computed as the line integral of the electric field at the soil surface, from the observation point to the extremity of the domain, following the y-axis. Coating stress voltages are calculated as the line integral of the electric field along the z-direction, from the pipe wall cell to the soil cell immediately above the pipe. Therefore, a negative sign in a voltage value indicates that potentials decrease along the electric

Figure 3.16. Top view showing counterpoises lengths, horizontal spacing, foundations and observation points. Currents injected into the ground are sampled at points 1 to 4. Ground potential rise is sampled at points $L = -30$ to $L = 30$.

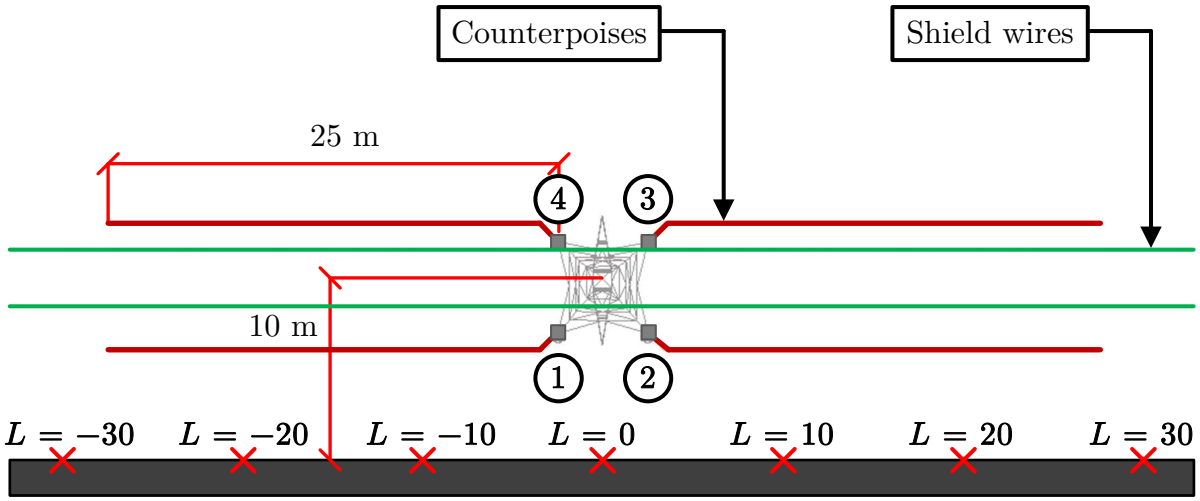

Source: own authorship.

field path.

Ground potentials due to the current injection into the earth are transferred to the pipeline as a result of the conductive coupling between the grounding conductors and the pipe metal. Figures 3.17 and 3.18 show, respectively, the ground potential rise and the pipeline coating stress voltages at the observation points. Figures are zoomed into the first 10 μs, period where discharged currents reach the highest magnitudes.

Figure 3.17 shows that the ground potential rise reaches a maximum value of 226 kV at observation point $L = 0$. In order to verify the coherence of this result, a simple verification can be made: a grounding electrode in uniform soil, sufficiently far from the observation point, behaves as a point source and produces a ground potential rise U_S calculated as in (2.37), in which $\rho = 500$ Ω.m is the soil resistivity for this case, $I = 30$ kA is the peak discharge current at $t = 1$ μs, and $r = 10$ m is the distance between the tower and the observation point $L = 0$, resulting in a GPR of 238 kV, which agrees with results above.

Figure 3.18 indicates that the maximum stress voltage is of the order of 2.1 kV, which is potentially damaging to the pipeline, depending on the type of coating (e.g. plastic tapes have an insulation limit of 2 kV, according to Table 2.3), as well as to equipment commonly associated to it, for instance: cathodic protection rectifiers are designed to withstand a maximum voltage of 1.5 kV between the negative terminal and the metallic enclosure, whereas insulating flanges

Figure 3.17. GPR at observation points over the first 10 μs. Maximum value is of the order of 226 kV at point $L = 0$, t =1 μs, which agrees with the fact that this observation point is the closest to the current source. Values are consistent with the simplified analytical expression (2.37).

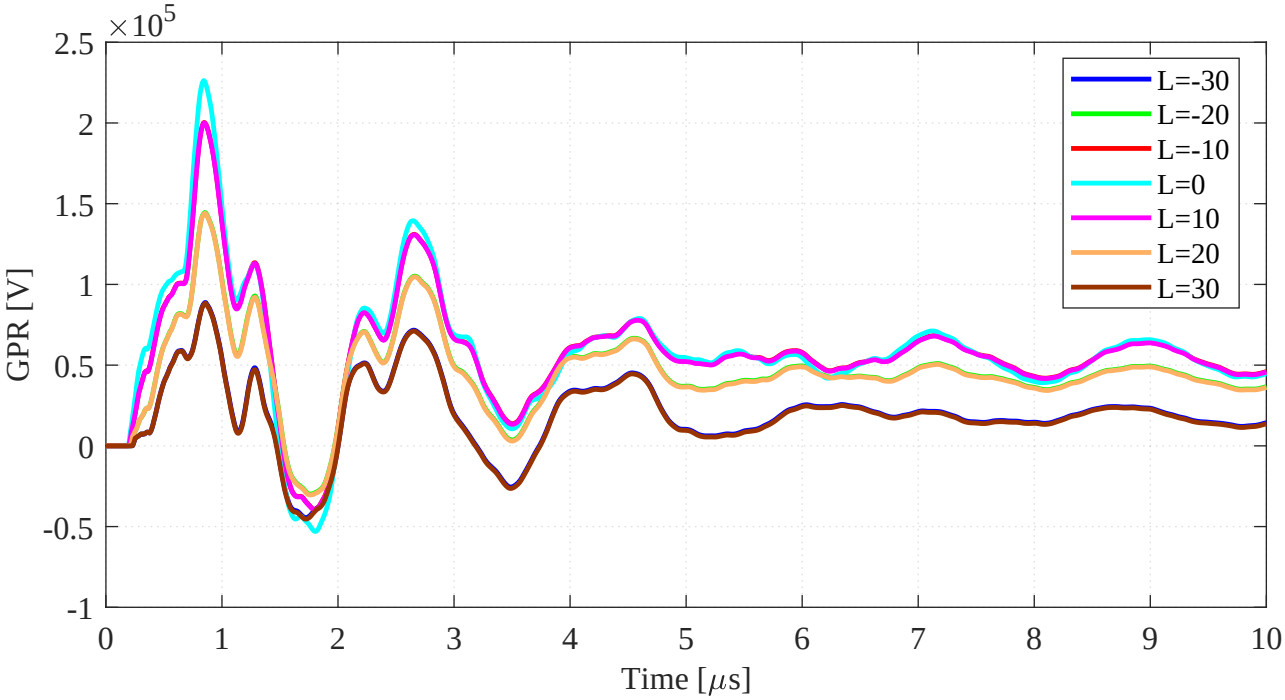

Source: own authorship.

endure a maximum voltage of 1 kV (NACE, 2007; MARTINS-BRITTO, 2017b).

As the stress voltage is defined as the difference of potential between the pipe metal and the adjacent ground, it happens to be numerically equal to the touch voltage a person would be subject to, in case of a worker in contact with an equipment connected to the pipeline within the interference zone. Therefore, it is convenient to analyze the safe voltage limits, as given in Section 2.5. Tables 3.3 and 3.4 summarize results for different exposure times and scenarios:

Table 3.3. Tolerable voltage limits for bare soil and exposure times of 20 μs, 60 μs and 100 μs.

Description	@ 20 μs [kV]	@ 60 μs [kV]	@ 100 μs [kV]
Touch voltage	45.39	26.20	20.3
Step voltage	103.75	59.90	46.4

Source: own authorship.

Tables above indicate that, although the potentials transferred to the pipeline are potentially damaging to the coating and equipment connected to the pipe, they range within the safe limits for humans, as long as very short exposure times occur. For comparison purposes, the reader

Figure 3.18. Pipeline coating stress voltages at observation points for the first 10 μs. Maximum absolute value is 2.1 kV, which exceeds the tolerable limit of the pipeline coating (2 kV) and equipment connected to the pipeline, such as rectifiers (1.5 kV) and insulating flanges (1 kV).

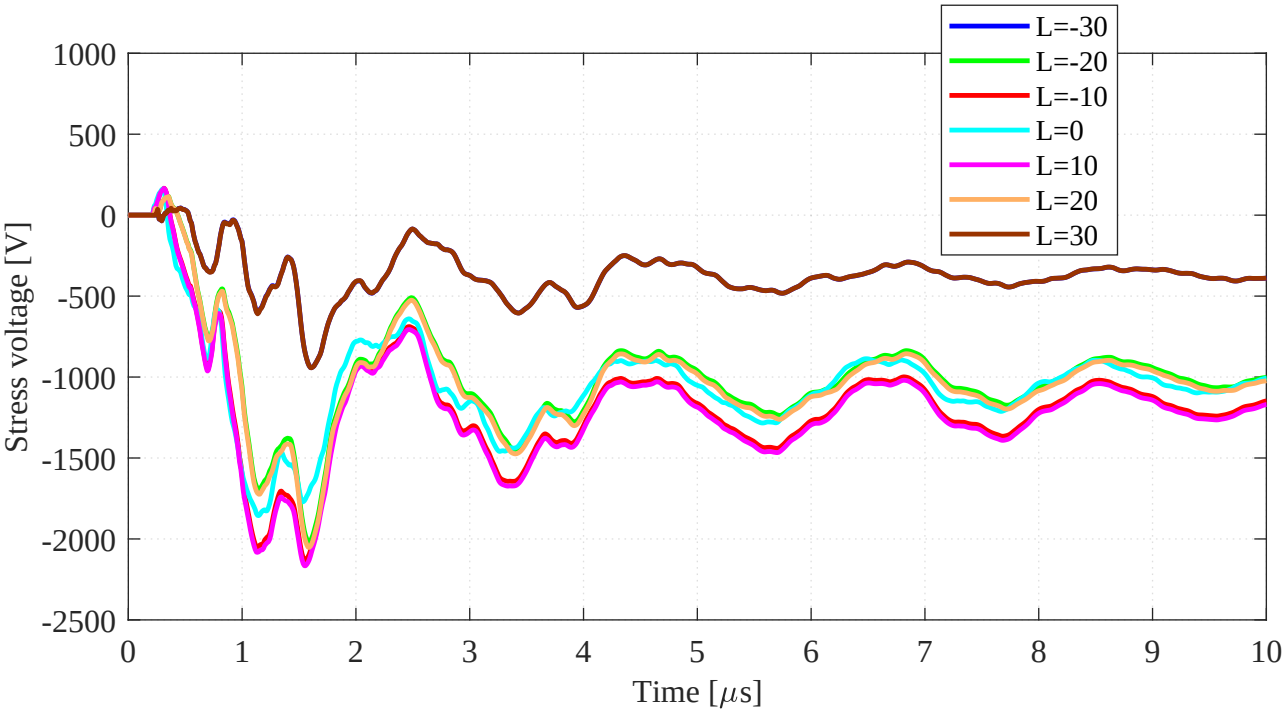

Source: own authorship.

Table 3.4. Tolerable voltage limits for soil covered with insulating material and exposure times of 20 μs, 60 μs and 100 μs.

Description	**@ 20 μs [kV]**	**@ 60 μs [kV]**	**@ 100 μs [kV]**
Touch voltage	541.27	312.50	242.06
Step voltage	2087	1205	933.45

Source: own authorship.

may recall Figures 3.12 and 3.13 from the preceding Section 3.3.2, which contain, respectively, the touch voltage between the tower and the ground and the step voltages near the grounding conductors. The tower touch voltage reaches a maximum value of 171.4 kV, which is far above the tolerable limit according to Table 3.3. The same happens with the step voltage near the counterpoises, of the order of 94 kV. One possible strategy to mitigate these hazards is to cover the soil surface with an insulating material, e.g. a layer with thickness 10 cm of crushed rock. If the material resistivity is 20000 Ω.m, the worst tolerable value increases to 242 kV, as can be verified from Table 3.4.

It is of relevance to observe that actual lightning surges may reach amplitudes as high as 200

kA (RAKOV; UMAN, 2003; ZIPSE, 1994). Therefore, considerably higher induced voltages may be expected in practical situations.

3.4 CHAPTER SUMMARY

This chapter provided a review of basic lightning discharge mechanisms, along with an FDTD implementation designed to simulate arbitrary geometries subject to high-frequency transients, especially those caused by lightning strikes.

The code was validated by comparison with results reported in the literature, then a realistic model of a transmission line parallel to a pipeline was constructed, accounting for phase conductors, shield wires, tower structure, counterpoises, concrete foundations and steel-frames, as well as the pipeline characteristics. The lightning discharge was modeled as a current source with ground return path, in terms of a Heidler function with peak magnitude of 30 kA, rise time of 1 μs and half-value time of 50 μs.

Transient grounding resistance, currents injected into the soil, touch and step voltages and electric field distribution around the tower were analyzed. It was shown how the lightning discharge is dissipated into the earth through the shield wires, grounding conductors and tower foundations, as well as the resulting impacts on the transmission line surroundings. Simulations indicated that the injection of current into the earth produces a GPR, a significant portion of which is transferred to the pipeline by means of conductive coupling between the grounding conductors and the pipe metal. Consequently, stress voltages arise throughout the pipeline course, with damaging potential to the pipeline and equipment connected to it. Also, potentially hazardous touch and step voltages appear at the tower vicinities. The shielding effect of the transmission line earth wires was also observed, as well as of the tower metallic structure.

The FDTD method proved to be a resourceful tool for determining the transient response of grounding grids and interfered structures subject to high-frequency phenomena. One strength of this method that is worth to highlight is the ability to seamlessly handle heterogeneities, such as layered structures and finite volumes of solids with different constitutive parameters. This became evident with the current distribution along the concrete foundations of the tower.

On the other hand, the computational burden imposed by mechanisms intrinsic to the FDTD

method may render its application impractical to the study of large-scale power systems, as well as of steady-state conditions at low frequencies, e.g. 60 Hz. The example discussed in this chapter involved a relatively small domain ($145 \times 105 \times 82.5$ m) and a simulation time of 120 μs, or 138570 time-steps, and required a computational time of 121 h, or 5 days, using a top tier machine.

Actual transmission systems and pipelines may span for several hundreds of kilometers. Besides, if one is concerned with steady-state phenomena involving power systems, simulation times should be of the order of milliseconds, i.e., 3 orders of magnitude greater than the discussed example. Clearly, other strategies should be pursued.

To address these issues, a modified version of the classic circuit theory approach is proposed in the following chapter.

CHAPTER 4

PROPOSED CIRCUIT THEORY APPROACH

4.1 CLASSIC CIRCUIT MODEL

Coupling equations described in Sections 2.2 and 2.3 are valid when conductors are disposed in parallel to each other. In real interference situations, however, crossings, parallelisms and oblique approximations may occur inside the EMI zone, as Figure 4.1 shows. The classic calculation model of a general geometry is constructed by subdividing the target installation into smaller segments that may be approximated by equivalent parallel sections (DAWALIBI *et al.*, 1987; CIGRÉ WG-36.02, 1995).

Figure 4.1. Representation of a complex electromagnetic interference zone in terms of equivalent parallel sections.

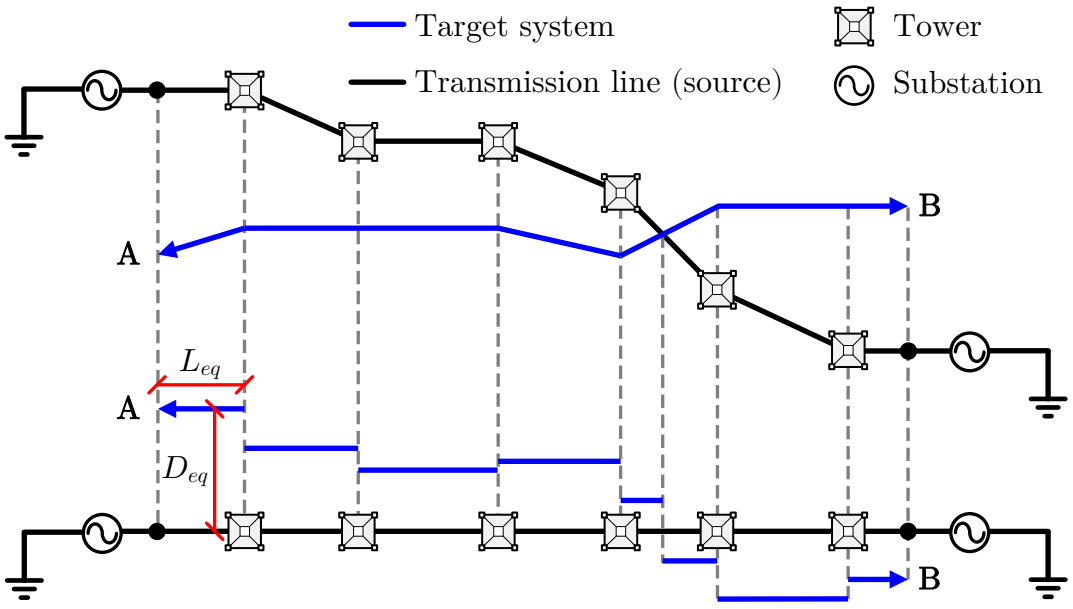

Source: own authorship.

The distance of the equivalent parallel section D_{eq} is determined as (4.1), referring to Figure 4.2:

$$D_{eq} = \sqrt{d_1 \cdot d_2}, \tag{4.1}$$

given the condition (CIGRÉ WG-36.02, 1995):

$$\frac{1}{3} \leq \frac{d_1}{d_2} \leq 3. \tag{4.2}$$

Figure 4.2. Oblique approximation between a transmission line and an interfered system.

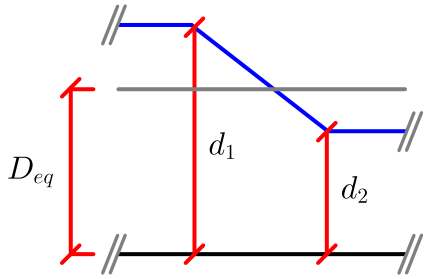

Source: own authorship.

Assuming the soil resistivity and the target conductor admittance to be constants along each subdivision, the interfered system in Figure 4.1, composed of n sections, is modeled by the equivalent circuit shown in Figure 4.3 (CIGRÉ WG-36.02, 1995; International Telecommunication Union, 1989). Once the interfered system parameters are known, which is accomplished by following the directives given in Section 2.2, induced voltages and currents are determined by employing nodal analysis techniques.

Figure 4.3. Equivalent circuit composed of n parallel sections, representing the general interfered (target) system in Figure 4.1.

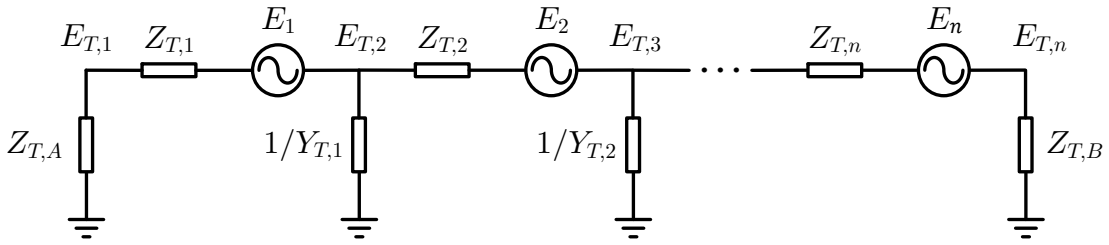

Source: own authorship.

In the circuit above, nodal voltages $[E_{T,1}, ..., E_{T,n}]$ are the unknown induced voltages. Impedances $Z_{T,A}$ and $Z_{T,B}$ depend on the presence and geometry of the grounding electrodes at the extremities A and B of the target line, and are calculated using (2.66). Sources $[E_1, ..., E_n]$ represent the mutual couplings with the transmission line conductors, including shield wires, and are determined using (2.10)-(2.11). Series impedances $[Z_{T,1}, ..., Z_{T,n}]$ are the target self impedances, expressed in (2.23). Finally, shunt admittances $[Y_{T,1}, ..., Y_{T,n}]$ depend on the coating characteristics (if any) and are computed using (2.28).

Under steady-state conditions, induced currents and voltages in the target line are determined in the phasor domain by solving the system of n linear equations cast in matrix form as:

$$\boldsymbol{Z_T} \cdot \bar{\boldsymbol{I}}_{\boldsymbol{T}} = \bar{\boldsymbol{E}}, \tag{4.3}$$

in which $\boldsymbol{Z_T}$ is the $(n \times n)$ impedance matrix of the target line; $\bar{\boldsymbol{I}}_{\boldsymbol{T}}$ is the $(n \times 1)$ vector of longitudinally induced currents; and $\bar{\boldsymbol{E}}$ is the $(n \times 1)$ vector of induced electromotive forces. The symbol $\bar{X}$ denotes the phasor form of $X(t)$.

Impedance matrix $\boldsymbol{Z_T}$ is constructed as:

$$\boldsymbol{Z_T} = \begin{bmatrix} T_1 & -Y_{T,1}^{-1}L_1^{eq} & 0 & \dots & 0 \\ -Y_{T,1}^{-1}L_1^{eq} & T_2 & -Y_{T,2}^{-1}L_2^{eq} & \dots & 0 \\ \vdots & \ddots & \ddots & \dots & \vdots \\ 0 & -Y_{T,i-1}^{-1}L_{i-1}^{eq} & T_i & -Y_{T,i}^{-1}L_i^{eq} & 0 \\ \vdots & \ddots & \ddots & \dots & \vdots \\ 0 & \dots & -Y_{T,n-2}^{-1}L_{n-2}^{eq} & T_{n-1} & -Y_{T,n-1}^{-1}L_{n-1}^{eq} \\ 0 & \dots & \dots & -Y_{T,n-1}^{-1}L_{n-1}^{eq} & T_n \end{bmatrix}, \tag{4.4}$$

with:

$$T_i = \begin{cases} Z_{T,A} + Z_{T,i}L_i^{eq} + Y_{T,i}^{-1}L_i^{eq}, \forall i = 1 \\ Y_{T,i-1}^{-1}L_{i-1}^{eq} + Z_{T,i}L_i^{eq} + Y_{T,i}^{-1}L_i^{eq}, \forall i \in [2, n-1] \\ Y_{T,n-1}^{-1}L_{n-1}^{eq} + Z_{T,n}L_{n-1}^{eq} + Z_{T,B}, \forall i = n \end{cases} . \tag{4.5}$$

Then, longitudinally induced currents are determined as:

$$\bar{\boldsymbol{I}}_{\boldsymbol{T}} = {\boldsymbol{Z_T}}^{-1} \cdot \bar{\boldsymbol{E}}, \tag{4.6}$$

and induced voltages are obtained by directly applying Ohm's law:

$$\bar{E}_{T,i} = \frac{\bar{I}_{T,i+1} - \bar{I}_{T,i}}{Y_{T,i}}, \tag{4.7}$$

in which $\bar{E}_{T,i}$ is the nodal voltage of the i^{th} section, in volts; $\bar{I}_{T,i}$ and $\bar{I}_{T,i+1}$ are the longitudinal currents flowing through sections i and $i+1$, respectively, given in ampères; and $Y_{T,i}$ is the total shunt admittance of the i^{th} section, in siemens.

This approach has been applied successfully in a variety of EMI studies reported in the literature (CIGRÉ WG-36.02, 1995; DAWALIBI *et al.*, 1987; MARTINS-BRITTO, 2017b; FURLAN, 2015), and is implemented in commercial software recognized by specialists as the

industry-standard (DAWALIBI *et al.*, 1987; DAWALIBI; DONOSO, 1993). However, it has to be observed that currently adopted practices for low-frequency EMI studies involving power lines came from the oil & gas and telecommunications industries, as thoroughly discussed in Section 2.7. Such practices are oriented towards the safety needs of the interfered systems (pipelines or telephone lines), with scarce reports related to the effects of EMI phenomena on the power system.

The classic circuit model is relatively easy to program using a computer and provides fast and reliable stress and touch voltage responses for large-scale target lines. Nevertheless, working with phasor quantities may hide important transient phenomena happening both in the interfered system and the source transmission line, which justifies the development of improved methods intended to be used in electromagnetic transients programs.

4.2 PROPOSED TIME-DOMAIN CIRCUIT IMPLEMENTATION

Although the idea of using EMTP-type tools to carry out EMI simulations is not exactly new, studies available in the literature are mostly limited to small systems, parallel approximations and uniform soil structures (FRAIJI; BASTOS, 2007; BARAÚNA; LIMA, 2007; CAULKER *et al.*, 2008; MILESEVIC *et al.*, 2011; PEPPAS *et al.*, 2014). In addition, these studies are concerned with the response of the target line caused by interferences, without mentioning the effects of the interfered conductor on the source transmission line.

In this thesis, it is developed a time-domain implementation of a realistic transmission line model under interference conditions, using the Alternative Transients Program (ATP). The term "realistic" in this context is understood as the capability to model the following characteristics commonly verified in practical situations: (a) multiphase systems with different energization sources, arbitrary number of phase conductors, shield wires and interfered structures; (b) complex interference geometries, composed of crossings, parallelisms and obliquities; (c) soil stratification with N layers; (d) soil resistivity, cross-section and conductor variations along the line routes (different soil conditions, transposition towers, underground/aboveground transitions etc.); (e) explicit representation of the shield wires and tower grounding electrodes; (f) simultaneous computation of voltages produced by inductive, capacitive and conductive

coupling mechanisms, allowing for an accurate representation of transient effects on the transmission line, as well as in the target conductors.

The basis of the proposed model lies in the fact that the equivalent circuit of the interfered system, illustrated in Figure 4.3, is a cascade of lossy transmission lines, each one described by the same nominal-π parameters that represent a power line, as a comparison with Figure 2.21 makes evident. Thus, with the appropriate adjustments, the classic circuit model described in Section 4.1 can be employed to simulate the source and the interfered conductors in the very same instance.

The first modification to the original circuit model is the segmentation criterion: prior to subdividing the target line to comply with the condition expressed in (4.2), the source line is subdivided at every tower, so that each span is represented by a transmission line section. Shield wires are connected to earth at every span section through a resistance R_G, determined as (2.66), to include the effects of the tower grounding. The target lines are included in every section where interference occurs and grounded through a shunt admittance Y_C, which is calculated using (2.28), to represent the effects of an imperfect dielectric coating. Figure 4.4 shows one section of a three-phase power line with one shield wire, interfering with one target line, modeled using the ATPDraw interface.

Figure 4.4. ATPDraw representation of one section of a three-phase line with one shield wire and one interfered conductor. Resistance R_G represents the tower grounding. Admittance Y_C accounts for the coating of the target line.

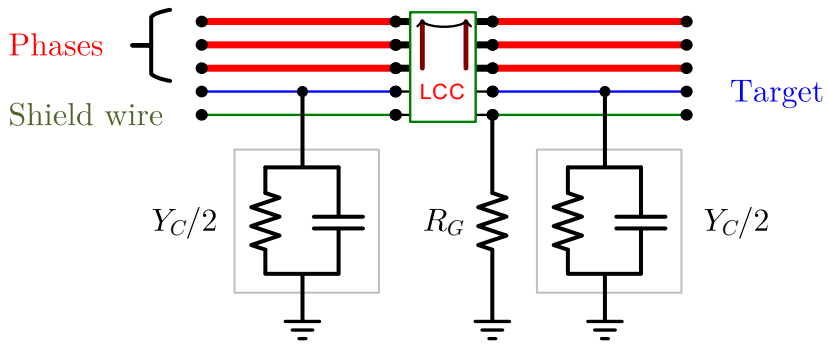

Source: own authorship.

The block labeled LCC represents the ATP routine Line/Cable Constants, which computes the transmission line matrices $\boldsymbol{Z}$ and $\boldsymbol{Y}$ from the system cross-section, conductor parameters, soil resistivity and operating frequency. The soil is represented in the LCC model as a uniform medium and Carson's correction term (2.12) is approximated by a power series expansion

(DOMMEL, 1996; WEDEHPOL; WILCOX, 1973).

A second modification is introduced into the classic model to consider interferences produced by conductive coupling. A controlled voltage source is connected to the target line extremity at the end of each section, representing the local ground potential rise in the case of a fault involving the earth, as shown in Figure 4.5. The controlled source voltage magnitude is given by the following equation:

$$U_S = I_{G,F} \times U_0, \tag{4.8}$$

in which $I_{G,F}$ is the fault current discharged into the soil through the tower grounding; and U_0 is the ground potential rise of the soil adjacent to the target line, caused by a current magnitude of 1 A being injected into the grounding grid. In other words, U_0 is the Green's function corresponding to the entire grounding electrode, and is determined according to the directives given in Section 2.4.3.

Figure 4.5. ATPDraw representation of one section of a three-phase line with one shield wire and one interfered conductor, accounting for conductive coupling effects. Resistance R_G represents the tower grounding. Admittance Y_C accounts for the coating of the target line. Voltage source U_S is the ground potential rise of the soil adjacent to the target line.

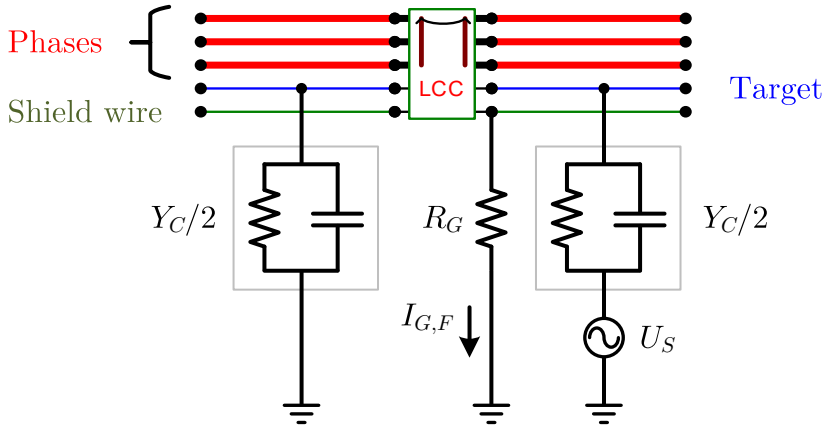

Source: own authorship.

By sequentially connecting individual sections shown in Figure 4.5, it is possible to build complex lines with or without interferences, such as the large transmission system exemplified in Figure 4.6. The fact that transmission line sections are modeled one by one intrinsically addresses the question of the variations along the route, as resistivities and cross-sections are set individually for each LCC block.

Figure 4.6. ATPDraw representation of a large transmission system composed of three phases, one shield wire and one interfered line, where each transmission line span is modeled individually using LCC components.

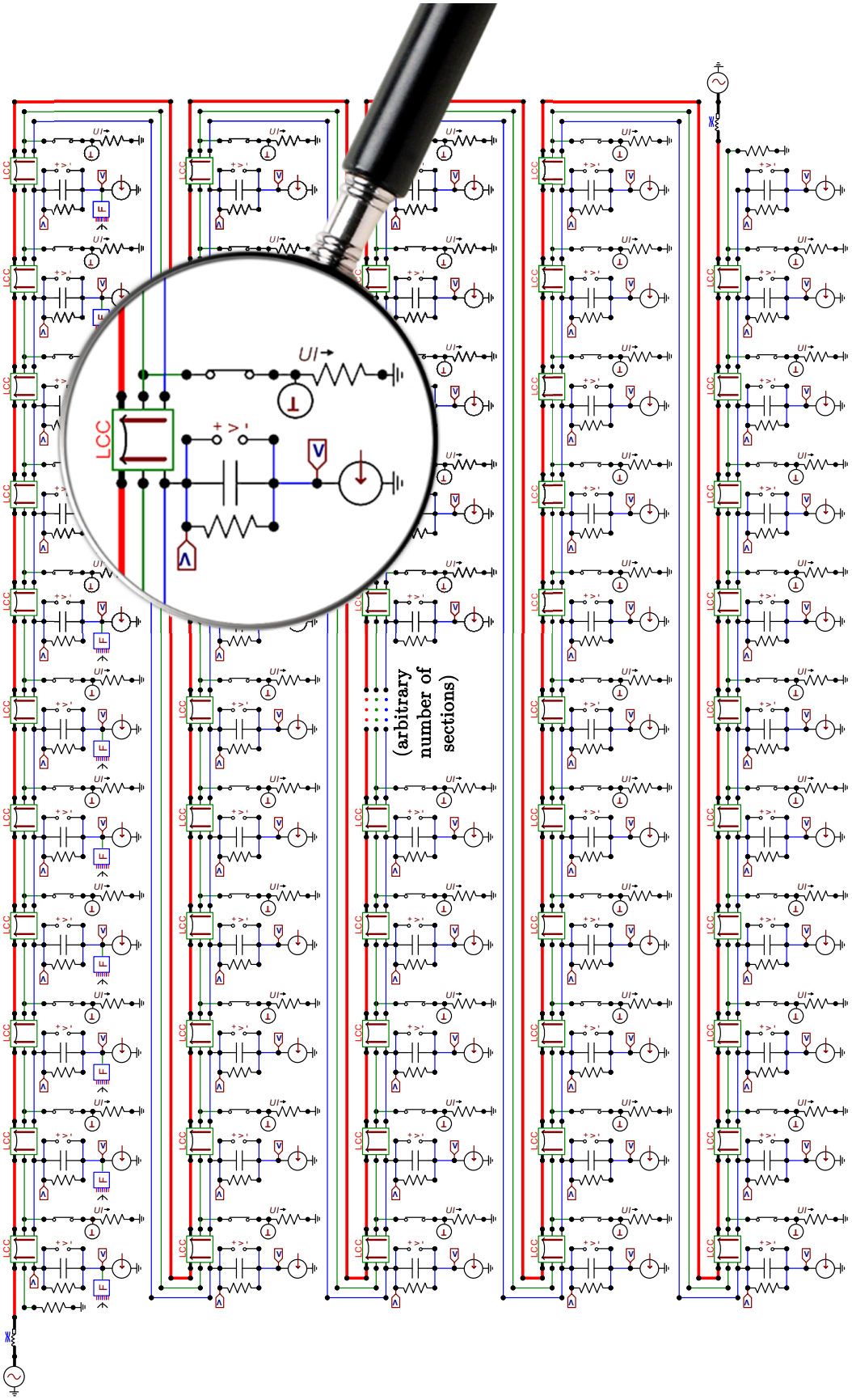

Source: own authorship.

Manually building complex models using the ATPDraw graphical interface is a time consuming process and subject to errors, due to the large number of variables and phenomena involved. To handle this issue, several auxiliary routines are developed and tested, so that the necessary ATP cards are written and processed automatically by the program, based on the system data. A basic flowchart of the proposed implementation is shown in Figure 4.7.

Figure 4.7. Flowchart of the proposed ATP implementation.

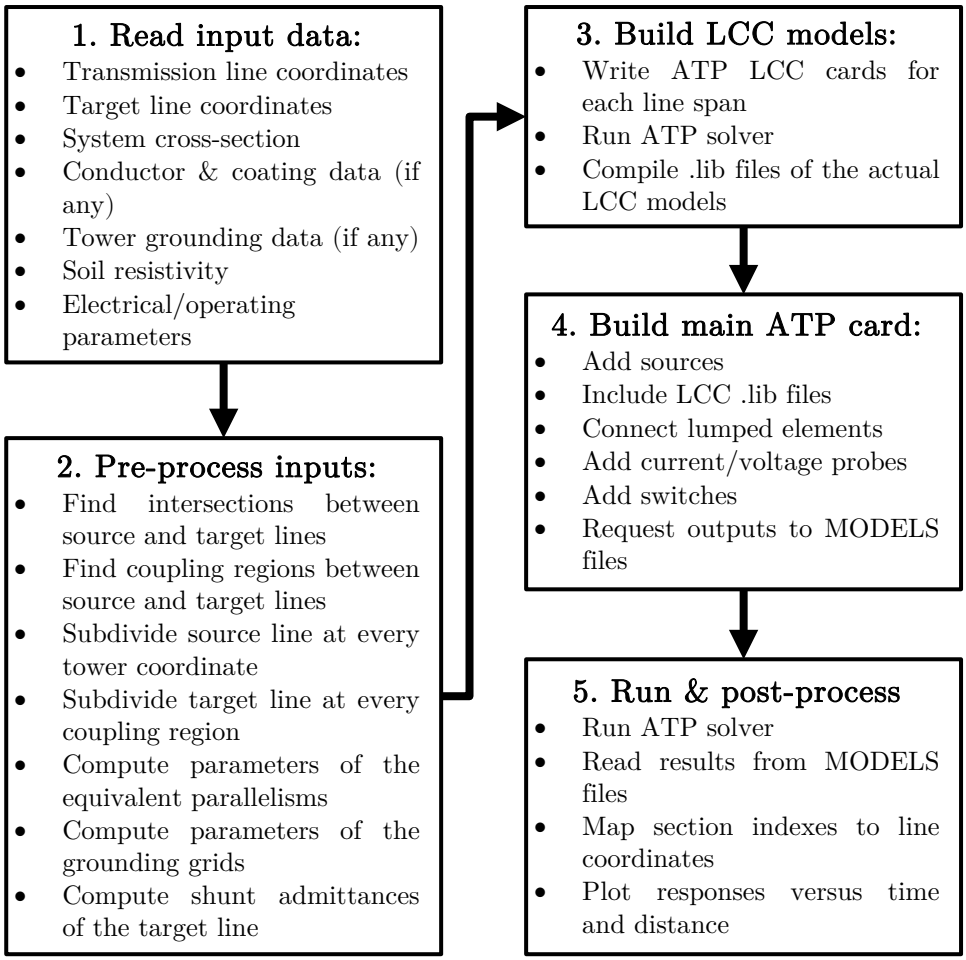

Source: own authorship.

4.3 PROPOSED MULTILAYER EARTH STRUCTURE APPROXIMATION

As previously outlined, by means of the Line/Cable Constants routine, ATP natively computes self and mutual impedances of transmission lines with the original Carson equation (2.13) by using the approximation derived by Wedehpol & Wilcox (1973). Thus, it models the soil as a uniform medium with resistivity ρ, which may lead to inaccuracies in real projects, as most natural soils are stratified structures (WHELAN *et al.*, 2010). The uncertainties related

to the soil electrical conductivity is a recognized source of error in applications that rely on ground return impedances, such as transmission line parameters and EMI (DAS *et al.*, 2014). Therefore, appropriate methods are required in order to model the multilayer nature of actual soils, introducing an important accuracy gain.

Equations for ground return impedances in uniform and multilayered soils are discussed in Sections 2.2.2 and 2.2.3. Inspection of (2.12) and (2.17) shows that as the number of soil layers increases, correction terms due to the finite resistivities become progressively more complex, with successive products of exponential functions on the integration variable λ. Solving a model with more than three layers is a cumbersome process that requires specific numerical integration techniques due to the oscillating form of (2.12), and is subject to numerical instabilities and convergence issues (PAPAGIANNIS *et al.*, 2005). Working with arbitrary soil structures requires methods which are not always readily available or easy to integrate to software commonly used in power systems analysis, in special the ATP. Therefore, it is convenient to seek an approach under which these issues are mitigated, preferably one that, for practical purposes, allows the use of the simpler uniform soil solution (2.13) with the same accuracy as the exact multilayer solution (2.17).

A paper published by Tsiamitros *et al.* (2007) proposed an expression valid for two-layered earth structures, based on deriving an equivalent homogeneous conductivity parameter to represent the stratified model. However, two-layered soils are not always suitable for real earth structure representation. To address this limitation, an extension of the original work is proposed in this section, in which an equivalent resistivity of the general N-layered case is obtained, by means of successively replacing pairs of layers, from bottom to top, by their homogeneous equivalent, calculated in function of the current penetration coefficient of each layer.

To validate the new formula, a configuration of two overhead conductors is given, and mutual impedances are computed using the uniform equivalent resistivity approach with the original Carson equation (2.13) and the general analytical expression for the N-layered soil model (2.17), and the relative errors are analyzed. A frequency-sweep is performed within the range from 1 Hz to 2 MHz, which is the domain of accuracy of the original solution derived by Nakagawa *et al.* (1973), to verify the limits of validity of the proposed method. Tests are carried out with 20 real soil models, with structures varying from 2 to 6 layers.

With the resulting equivalent resistivity value, a multilayered soil is easily introduced into the ATP model described in the preceding section, without structural modifications to the program routines.

4.3.1 Earth return conduction effects

Earth return conduction is closely associated with the induced eddy current in the soil surface (LEE *et al.*, 2013). In this context, soil surface means the depth range in which the energy of a propagating electromagnetic wave cannot be omitted, recalling that the wave decays with the distance along the propagation direction (LEE *et al.*, 2013). This region is determined analytically by the skin depth δ (STRATTON, 2007):

$$\delta = \sqrt{\frac{1}{\pi f \mu \sigma}\left(\sqrt{1+\left(\frac{2\pi f \varepsilon}{\sigma}\right)^2}+\frac{2\pi f \varepsilon}{\sigma}\right)}, \tag{4.9}$$

in which f is the frequency, in Hertz; μ is the magnetic permeability, in H/m; $\sigma = 1/\rho$ is the conductivity, in S/m; and ε is the electric permittivity, in F/m.

Table 4.1 contains skin depth values computed for various frequencies and resistivities. Figure 4.8 shows an intensity plot of the skin depth δ as a function of frequency and resistivity. Computations assume that permittivity and permeability constants are equal to, respectively, the vacuum and free space values. It can be seen that, for power system frequencies up to the kHz range, the skin depth, or the region regarded as the surface of earth for the sake of conduction phenomena, may reach the order of magnitude of kilometers, depending on the soil characteristics (COUSIN *et al.*, 2005).

Table 4.1. Skin depth in meters for different soil resistivities.

Resistivity ρ [Ω.m]	**60 Hz**	**1 kHz**	**10 kHz**	**100 kHz**
	Skin depth δ [m]			
10000	6497.6	1592	504.69	163.64
1000	2054.7	503.31	159.2	50.469
100	649.75	159.16	50.331	15.92
10	205.47	50.329	15.916	5.0331

Source: own authorship.

Figure 4.8. Skin depth as a function of frequency and resistivity. For common earth materials and frequencies between 60 Hz and 1 kHz, values range from 5.03 m to 6.49 km.

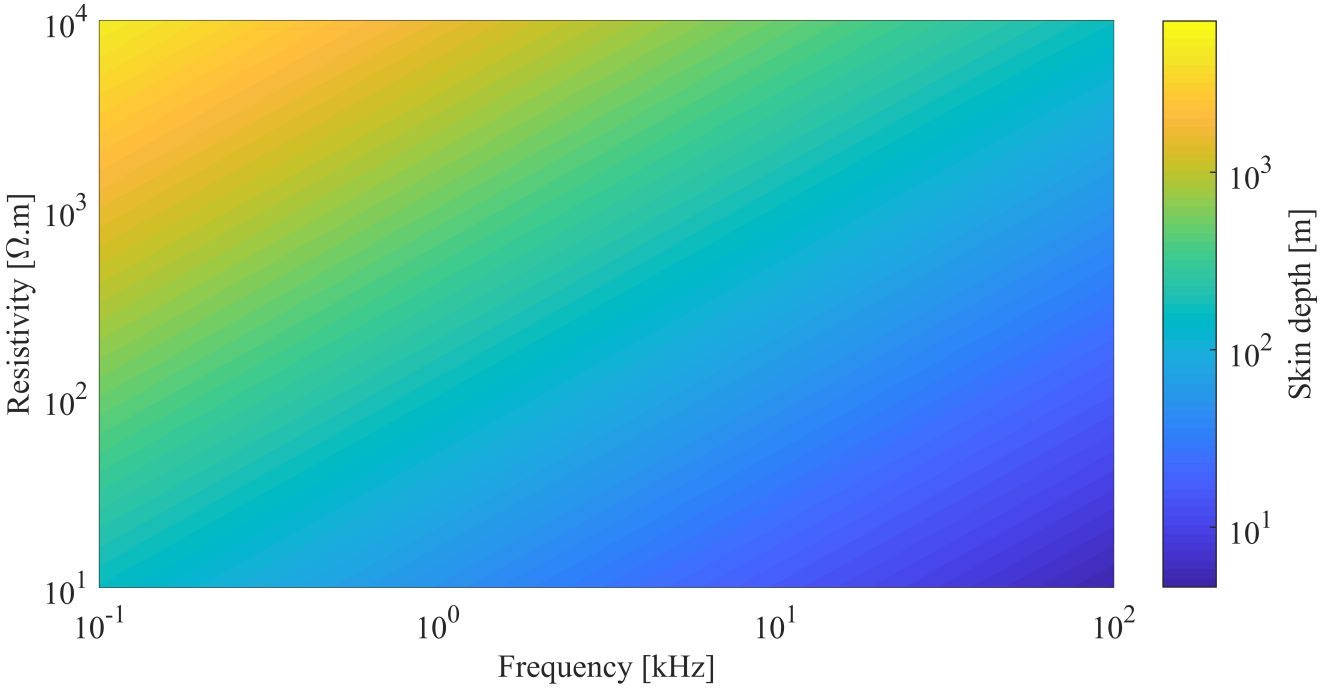

Source: own authorship.

Soil parameters are determined by employing survey techniques commonly performed from the soil surface (IEEE, 1984). Actual field measurements represent the equivalent, or apparent, electrical behavior of the nonuniform medium, from which physical models are derived (IEEE, 1984; STEINBERG; LEVITSKAYA, 2001; TSIAMITROS *et al.*, 2007). On the other hand, several authors agree that the multilayered nature of real soils has to be considered in order to accurately model ground return problems (LEE *et al.*, 2013; HE *et al.*, 2013; TSIAMITROS *et al.*, 2007; AMETANI *et al.*, 2009; DERI *et al.*, 1981; NAKAGAWA *et al.*, 1973; CHOW *et al.*, 1991; DAWALIBI; BARBEITO, 1991).

As discussed in Section 2.1.2, horizontally stratified models are characterized by $(N-1)$ layers with finite resistivities and thicknesses on top of the N^{th} layer whose depth extends to infinity, representing the apparent behavior of the deep soil (ZHANG *et al.*, 2005). Of course, an infinitely thick bottom layer is a mathematical abstraction that only holds meaning if the constraint imposed by the skin depth is observed. A horizontally stratified soil model is a good approximation of the local earth as long as its structure is contained within the conduction region, case in which resistivities of the deep layers influence ground conduction phenomena as

much as the values of the surface layers (SOUTHEY; DAWALIBI, 2005; NAKAGAWA *et al.*, 1973).

4.3.2 Derivation of the equivalence formula for two layers

Assuming a two-layered soil structure, where the top layer is described by the permeability μ_1, permittivity ε_1 and conductivity σ_1 and the bottom layer by the corresponding parameters μ_2, ε_2 and σ_2, Tsiamitros *et al.* (2007) derived an equivalent uniform model, suitable for working with earth return path problems within the frequency range from 60 Hz up to 1 MHz.

To obtain the equation, referring to Figure 2.7, let $N = 2$. Then, the kernel function $\hat{F}(\lambda)$ (2.17) of the multilayered soil model is expanded as:

$$\hat{F}(\lambda) = \frac{(\alpha_1 + \alpha_2) + (\alpha_1 - \alpha_2)\, e^{-2\alpha_1 h_1}}{(\alpha_1 + \alpha_2)\,(\alpha_1 + \lambda) + (\alpha_1 - \alpha_2)\,(\lambda - \alpha_1)\, e^{-2\alpha_1 h_1}}, \tag{4.10}$$

with:

$$\alpha_i = \sqrt{\lambda^2 + j\omega\mu_i\sigma_i}, \quad i = [1,2], \quad j = \sqrt{-1}. \tag{4.11}$$

Assuming a fictitious uniform soil model with equivalent resistivity ρ_{eq}, whose electrical behavior is the same as the N-layered soil, the kernel function is given by (2.13):

$$\hat{F}(\lambda) = \frac{1}{\lambda + \alpha_{eq}} = \frac{1}{\lambda + \sqrt{\lambda^2 + \frac{j\omega\mu_0}{\rho_{eq}} - \omega^2\mu_0\varepsilon}}, \tag{4.12}$$

Equating (4.10) and (4.12), the following expression is obtained:

$$\frac{1}{\lambda + \alpha_{eq}} = \frac{(\alpha_1 + \alpha_2) + (\alpha_1 - \alpha_2)\, e^{-2\alpha_1 h_1}}{(\alpha_1 + \alpha_2)\,(\alpha_1 + \lambda) + (\alpha_1 - \alpha_2)\,(\lambda - \alpha_1)\, e^{-2\alpha_1 h_1}}. \tag{4.13}$$

The variable λ results from the Fourier transform of the differential electromagnetic field equations and represents the spatial frequency of the Fourier spectrum (PERZ; RAGHUVEER, 1974). Equation (4.13) must remain valid for any value of λ within the domain $[0,\infty]$. Therefore, letting $\lambda = 0$ simplifies the equation above without loss of validity. Then, after some manipulations, the following equation is derived:

$$\rho_{eq} = \frac{1}{\sigma_1}\left[\frac{(\sqrt{\sigma_1} + \sqrt{\sigma_2}) + (\sqrt{\sigma_1} - \sqrt{\sigma_2})e^{-2h_1\sqrt{j\omega\mu_1\sigma_1}}}{(\sqrt{\sigma_1} + \sqrt{\sigma_2}) - (\sqrt{\sigma_1} - \sqrt{\sigma_2})e^{-2h_1\sqrt{j\omega\mu_1\sigma_1}}}\right]^2, \tag{4.14}$$

where resistivity ρ and conductivity σ are employed indistinctly for the sake of legibility. The exponential terms in the right-hand side of (4.14) are complex numbers, whereas the left-hand side term ρ_{eq} is a real value. To address this inconsistency, it is recalled that $\sqrt{j} = (\sqrt{2}/2) + j(\sqrt{2}/2)$, then (4.14) is further processed, resulting in:

$$\rho_{eq} = \frac{1}{\sigma_1}\left[\frac{(\sqrt{\sigma_1}+\sqrt{\sigma_2}) + (\sqrt{\sigma_1}-\sqrt{\sigma_2})e^{-2h_1\sqrt{\pi f\mu_1\sigma_1}}e^{-j2h_1\sqrt{\pi f\mu_1\sigma_1}}}{(\sqrt{\sigma_1}+\sqrt{\sigma_2}) - (\sqrt{\sigma_1}-\sqrt{\sigma_2})e^{-2h_1\sqrt{\pi f\mu_1\sigma_1}}e^{-j2h_1\sqrt{\pi f\mu_1\sigma_1}}}\right]^2. \tag{4.15}$$

Finally, by observing that the absolute value of $e^{-j2h_1\sqrt{\pi f\mu_1\sigma_1}}$ is always equal to 1, the equivalent real-valued resistivity approximation is:

$$\rho_{eq} = \frac{1}{\sigma_1}\left[\frac{(\sqrt{\sigma_1}+\sqrt{\sigma_2}) + (\sqrt{\sigma_1}-\sqrt{\sigma_2})e^{-2h_1\sqrt{\pi f\mu_1\sigma_1}}}{(\sqrt{\sigma_1}+\sqrt{\sigma_2}) - (\sqrt{\sigma_1}-\sqrt{\sigma_2})e^{-2h_1\sqrt{\pi f\mu_1\sigma_1}}}\right]^2. \tag{4.16}$$

This is a convenient method that has been successfully employed in transient analysis, line parameters calculations and interference studies between power lines and pipelines, including commercially available software that represents the soil as a homogeneous structure (TSIAMI-TROS *et al.*, 2007; PAPAGIANNIS *et al.*, 2005; FURLAN, 2015; MARTINS-BRITTO, 2017b). Although this is an useful formulation for a variety of cases of interest, its application range is limited, as most actual soil models are reported to be composed of more than two layers. For instance, He *et al.* (2013) and Whelan *et al.* (2010) report that most real soils are composed of three to five layers. Therefore, further enhancement and extension of (4.16) to the general N-layered case is desirable, as it makes possible to handle more complex structures with a relatively simple expression.

4.3.3 Equivalent model of a multilayered soil structure

The methodology proposed in this thesis consists of applying (4.16) recursively for each pair of layers, from bottom to top, in order to obtain an equivalent uniform soil model of any multilayer structure. Then, the mutual impedance with earth return path may be calculated using the closed-form solution of Carson equation (2.11)-(2.16) or directly used into the ATP routines.

First, it is analyzed the case where the soil is composed of three layers, with respective constitutive properties μ_n, ε_n, conductivity σ_n and thickness h_n, n = [1,2,3], as depicted in

Figure 2.7. The equivalent conductivity that represents the bottom and middle layers is:

$$\frac{1}{\sigma_{2,3}} = \frac{1}{\sigma_2}\left[\frac{(\sqrt{\sigma_2}+\sqrt{\sigma_3})+(\sqrt{\sigma_2}-\sqrt{\sigma_3})e^{-2h_2\sqrt{\pi f\mu_2\sigma_2}}}{(\sqrt{\sigma_2}+\sqrt{\sigma_3})-(\sqrt{\sigma_2}-\sqrt{\sigma_3})e^{-2h_2\sqrt{\pi f\mu_2\sigma_2}}}\right]^2, \tag{4.17}$$

and the overall equivalent uniform resistivity is:

$$\rho_{eq} = \frac{1}{\sigma_1}\left[\frac{(\sqrt{\sigma_1}+\sqrt{\sigma_{2,3}})+(\sqrt{\sigma_1}-\sqrt{\sigma_{2,3}})e^{-2h_1\sqrt{\pi f\mu_1\sigma_1}}}{(\sqrt{\sigma_1}+\sqrt{\sigma_{2,3}})-(\sqrt{\sigma_1}-\sqrt{\sigma_{2,3}})e^{-2h_1\sqrt{\pi f\mu_1\sigma_1}}}\right]^2. \tag{4.18}$$

As in the previous section, resistivity ρ and conductivity σ are used indistinctly to provide a better legibility of the equations.

Assuming a soil model with four layers, the equivalent conductivity representing the fourth and third layers is:

$$\frac{1}{\sigma_{3,4}} = \frac{1}{\sigma_3}\left[\frac{(\sqrt{\sigma_3}+\sqrt{\sigma_4})+(\sqrt{\sigma_3}-\sqrt{\sigma_4})e^{-2h_3\sqrt{\pi f\mu_3\sigma_3}}}{(\sqrt{\sigma_3}+\sqrt{\sigma_4})-(\sqrt{\sigma_3}-\sqrt{\sigma_4})e^{-2h_3\sqrt{\pi f\mu_3\sigma_3}}}\right]^2. \tag{4.19}$$

The equivalent conductivity corresponding to layers 4, 3 and 2 is:

$$\frac{1}{\sigma_{2,3}} = \frac{1}{\sigma_2}\left[\frac{(\sqrt{\sigma_2}+\sqrt{\sigma_{3,4}})+(\sqrt{\sigma_2}-\sqrt{\sigma_{3,4}})e^{-2h_2\sqrt{\pi f\mu_2\sigma_2}}}{(\sqrt{\sigma_2}+\sqrt{\sigma_{3,4}})-(\sqrt{\sigma_2}-\sqrt{\sigma_{3,4}})e^{-2h_2\sqrt{\pi f\mu_2\sigma_2}}}\right]^2. \tag{4.20}$$

Finally, the overall equivalent uniform resistivity of the four-layered soil is:

$$\rho_{eq} = \frac{1}{\sigma_1}\left[\frac{(\sqrt{\sigma_1}+\sqrt{\sigma_{2,3}})+(\sqrt{\sigma_1}-\sqrt{\sigma_{2,3}})e^{-2h_1\sqrt{\pi f\mu_1\sigma_1}}}{(\sqrt{\sigma_1}+\sqrt{\sigma_{2,3}})-(\sqrt{\sigma_1}-\sqrt{\sigma_{2,3}})e^{-2h_1\sqrt{\pi f\mu_1\sigma_1}}}\right]^2. \tag{4.21}$$

From inspection of equations (4.17)-(4.21), extracting the recursive pattern for a general structure composed of N layers is quite straightforward, as described in (4.22)-(4.24). Calculations are not only simpler and suitable for using with the original Carson equation, but also expressions have always the same form, regardless of the number of layers. The exponential terms show a familiar quantity, which is $\sqrt{\pi f\mu\sigma}$, the reciprocal of the material penetration skin depth. Therefore, the proposed uniformization technique can be understood as a correction of the earth return path impedance according to the effective current penetration in each soil layer, which holds more physical meaning than other approaches where the equivalent model is computed simply as the average of resistivities (IEEE, 2000; KINDERMANN; CAMPAGNOLO, 1995).

$$\frac{1}{\sigma_{N-1,N}} = \frac{1}{\sigma_{N-1}}\left[\frac{(\sqrt{\sigma_{N-1}}+\sqrt{\sigma_N})+(\sqrt{\sigma_{N-1}}-\sqrt{\sigma_N})e^{-2h_{N-1}\sqrt{\pi f\mu_{N-1}\sigma_{N-1}}}}{(\sqrt{\sigma_{N-1}}+\sqrt{\sigma_N})-(\sqrt{\sigma_{N-1}}-\sqrt{\sigma_N})e^{-2h_{N-1}\sqrt{\pi f\mu_{N-1}\sigma_{N-1}}}}\right]^2, \tag{4.22}$$

$$\vdots$$

$$\frac{1}{\sigma_{m-1,m}} = \frac{1}{\sigma_{m-1}} \left[\frac{(\sqrt{\sigma_{m-1}} + \sqrt{\sigma_{m-1,m}}) + (\sqrt{\sigma_{m-1}} - \sqrt{\sigma_{m-1,m}}) e^{-2h_{m-1}\sqrt{\pi f \mu_{m-1}\sigma_{m-1}}}}{(\sqrt{\sigma_{m-1}} + \sqrt{\sigma_{m-1,m}}) - (\sqrt{\sigma_{m-1}} - \sqrt{\sigma_{m-1,m}}) e^{-2h_{m-1}\sqrt{\pi f \mu_{m-1}\sigma_{m-1}}}} \right]^2, \quad (4.23)$$

$$\rho_{eq} = \frac{1}{\sigma_1} \left[\frac{(\sqrt{\sigma_1} + \sqrt{\sigma_{m-1,m}}) + (\sqrt{\sigma_1} - \sqrt{\sigma_{m-1,m}}) e^{-2h_1\sqrt{\pi f \mu_1 \sigma_1}}}{(\sqrt{\sigma_1} + \sqrt{\sigma_{m-1,m}}) - (\sqrt{\sigma_1} - \sqrt{\sigma_{m-1,m}}) e^{-2h_1\sqrt{\pi f \mu_1 \sigma_1}}} \right]^2, (1 \leq m \leq N-2). \quad (4.24)$$

4.3.4 Numerical results

To validate the proposed technique, several soil models reported in the literature, based on actual field measurements, have been tested. Tables 4.2 to 4.6 contain the soil parameters as in (PAPAGIANNIS *et al.*, 2005; TSIAMITROS *et al.*, 2007; ZHANG *et al.*, 2005; DAWALIBI; BARBEITO, 1991; ISERHIEN-EMEKEME, 2014), for models from 2 up to 6 layers. Referring to distances shown in Figure 2.7, two conductors are positioned at 15.24 m above the ground surface, with a horizontal separation of 21.34 m, which are the same values proposed in (PAPAGIANNIS *et al.*, 2005). Permittivity and permeability are assumed to be equal, respectively, to the vacuum and free space constants.

Computations are carried out over frequencies ranging from 1 Hz to 2 MHz, in order to check the validity of the proposed technique both for steady state and transient conditions. The analytical expression from Nakagawa *et al.* (1973) is assumed to be the reference due to the fact that it is an exact solution, derived directly from Maxwell equations. Mutual impedances are calculated using the analytical expression for the N-layered case (2.17) and Carson equation (2.13) with the uniform resistivity approximation (4.22)-(4.24). Then, the impedance relative error is calculated simply as:

$$\Delta = \left| \frac{Z_{\text{approximation}} - Z_{\text{analytical}}}{Z_{\text{analytical}}} \right|. \quad (4.25)$$

Table 4.7 contains the equivalent uniform resistivities and mutual impedance approximation relative errors, compared to the exact analytical solution, for each soil model analyzed, at frequencies of 50 and 60 Hz, along with respective top and bottom layer resistivities, ρ_1 and ρ_N.

For most analyzed soil models, the homogeneous approach is sufficiently accurate for practical purposes, with an average error of the order of 1%. One can notice that the lowest

Table 4.2. Two-layered soil models.

Model	ρ_1 [Ω.m]	ρ_2 [Ω.m]	h_1 [m]
1	373.13	145.35	2.69
2	246.91	1063.83	2.14
3	57.34	96.71	1.65

Source: own authorship.

Table 4.3. Three-layered soil models.

Model	ρ_1 [Ω.m]	ρ_2 [Ω.m]	ρ_3 [Ω.m]	h_1 [m]	h_2 [m]
4	128.04	1923.08	520.83	3.1	15
5	30.00	9.40	500.00	3.4	25.5
6	222.22	136.61	13.72	3.36	118.47
7	32.96	26.37	284.09	1.06	21.12
8	156.99	2325.58	300.30	0.7	35.3
9	210.97	724.64	253.81	3.3	25

Source: own authorship.

approximation errors occur when the equivalent resistivity results are closer to the bottom layer value, which agrees with reports in the literature that the deep soil resistivity plays a predominant role in problems involving ground return path (SOUTHEY; DAWALIBI, 2005).

Models 5, 6 and 14 show that significant errors arise when there are pairs of layers with large ratios between respective resistivities, which was also noted in (TSIAMITROS *et al.*, 2007). Maximum resistivity ratios for these models are, respectively, 53.19, 9.95 and 112. In such cases, the equivalent uniform resistivity diverges from the bottom layer value.

To further investigate this effect, let R be the contrast ratio in the hypothetical system

Table 4.4. Four-layered soil models.

Model	ρ_1 [Ω.m]	ρ_2 [Ω.m]	ρ_3 [Ω.m]	ρ_4 [Ω.m]	h_1 [m]	h_2 [m]	h_3 [m]
10	460.83	34.95	2.42	21.97	0.9	2.6	1.5
11	235.29	3571.43	205.34	1515.15	1.2	5.33	21.06
12	19.10	41.70	523.56	571.43	0.3	2.4	4.6
13	121.51	0.84	74.91	334.45	4.5	8.02	22.67
14	67.70	75.70	28.80	3225.81	1.2	17	61.9

Source: own authorship.

Table 4.5. Five-layered soil models.

Model	ρ_1 [Ω.m]	ρ_2 [Ω.m]	ρ_3 [Ω.m]	ρ_4 [Ω.m]	ρ_5 [Ω.m]	h_1 [m]	h_2 [m]	h_3 [m]	h_4 [m]
15	64.39	440.53	11.29	353.36	33.89	1.37	0.66	2.41	5.73
16	8333.33	20000.00	20000.00	4545.45	3125.00	0.64	0.29	3.47	7.4
17	251.26	2380.95	257.73	2439.02	952.38	3.64	4.74	9.75	128

Source: own authorship.

Table 4.6. Six-layered soil models.

Model	ρ_1 [Ω.m]	ρ_2 [Ω.m]	ρ_3 [Ω.m]	ρ_4 [Ω.m]	ρ_5 [Ω.m]	ρ_6 [Ω.m]	h_1 [m]	h_2 [m]	h_3 [m]	h_4 [m]	h_5 [m]
18	68.03	625.00	7.29	384.62	7.03	125.00	1.08	0.29	1.21	2.64	2.98
19	4545.45	277.78	769.23	1492.54	833.33	100.00	1.86	2.80	3.17	11.95	9.99
20	423.73	301.20	869.57	628.93	5882.35	150.38	0.44	5.31	5.63	82.23	31.17

Source: own authorship.

shown in Figure 4.9, composed of a top layer with resistivity ρ_1 and $(N-1)$ alternating layers whose resistivities differ proportionally to the factor R. Clearly two situations are possible: as R increases, (a) $\rho_N > \rho_1$; or (b) $\rho_N < \rho_1$. Figure 4.10 presents the uniform equivalent approximation error as a function of the contrast ratio R. If $R = 1$, the soil model is one single homogeneous medium with resistivity ρ_1 and there is no approximation error. For $3 < R < 10$, errors are kept within the range of 1% to 5% and tend to increase steeply for contrast ratios outside these boundaries, which explains the errors verified in soil models 5, 6, and 14. If better accuracy is desired in high contrast cases, the analytical solution provides more precise results. If problem constraints require the classic Carson equation (2.13) to be used, a technique based on nonlinear fitting can also be employed in such cases (FURLAN *et al.*, 2015). Due to the exposed in this paragraph, soils 5, 6, and 14 are omitted in subsequent discussions.

Layer thicknesses are also of relevance. To verify how they affect results, let $N = 2$ in the theoretical model presented in Figure 4.9. The impedance relative error as a function of the layer thickness h and the contrast ratio R is shown in Figure 4.11, assuming top layer conductivities equal to, respectively, 10000, 1000, 100 and 10 Ω.m. Thickness values are normalized with respect to the skin depth δ associated with the conductivity of the top layer ρ_1. In the worst case, the approximation error is smaller than 5.45% for depths shallower than 5% of the skin depth δ.

Figures 4.12 to 4.16 show the approximation error as a function of frequency, for all soil

Table 4.7. Soil equivalent resistivities and approximation errors.

Model	Top layer ρ_1 [Ω.m]	Bottom layer ρ_N [Ω.m]	@ 50 Hz		@ 60 Hz	
			ρ_{eq} [Ω.m]	Δ [%]	ρ_{eq} [Ω.m]	Δ [%]
1	373.13	145.35	145.8151	0.0586	145.8683	0.0652
2	246.91	1063.83	1052.41	0.0791	1051.7459	0.0879
3	57.34	96.71	96.4023	0.0513	96.3725	0.057
4	128.04	520.83	520.8605	0.0181	520.9419	0.0196
5	30.00	500.00	146.4429	13.2685	134.8054	14.1068
6	222.22	13.72	26.7191	8.0037	28.0924	8.4938
7	32.96	284.09	205.8715	4.3007	200.2603	4.7029
8	156.99	300.3	314.7128	0.6565	316.1256	0.7259
9	210.97	253.81	260.9195	0.3734	261.5747	0.4128
10	460.83	21.97	20.7098	1.0058	20.5989	1.1082
11	235.29	1515.15	1367.8019	1.1600	1355.9322	1.2801
12	19.10	571.43	547.2256	0.6278	544.87	0.6967
13	121.51	334.45	296.4984	1.5315	293.4272	1.6799
14	67.70	3225.81	406.5206	16.0025	363.1214	16.6225
15	64.39	33.89	34.1373	0.1112	34.1591	0.1216
16	8333.33	3125.00	3159.5577	0.0343	3160.5563	0.038
17	251.26	952.38	989.805	0.3555	992.7529	0.3818
18	68.03	125.00	106.4963	2.4191	104.9461	2.6653
19	4545.45	100.00	107.4818	1.0717	108.2064	1.1838
20	423.73	150.38	185.6355	2.5875	189.0395	2.8114

Source: own authorship.

models, except for 5, 6 and 14, whose issues related to the presence of large contrast ratios have already been discussed. Table 4.8 summarizes the maximum values of relative error and contrast ratio, as well as the frequency associated with the maximum error.

It is clear that the proposed approach is accurate for frequencies of 50 and 60 Hz, including transients with frequencies up to 100 kHz, which are typical of surges in electrical systems. For very fast transients, such as lightning discharges, whose spectrum is often within the megahertz band, the proposed approach precision depends on the soil structure. Similarly to the 50 and 60 Hz cases studied previously, there is a correlation between the approximation error and layer contrast ratios. However, it has to be noted that even though errors within the high-frequency

Figure 4.9. Soil model composed of N equally spaced layers whose alternating resistivities differ proportionally to the contrast ratio R. On the left, $\rho_N > \rho_1$ as R increases. On the right, $\rho_N < \rho_1$ with increasing R.

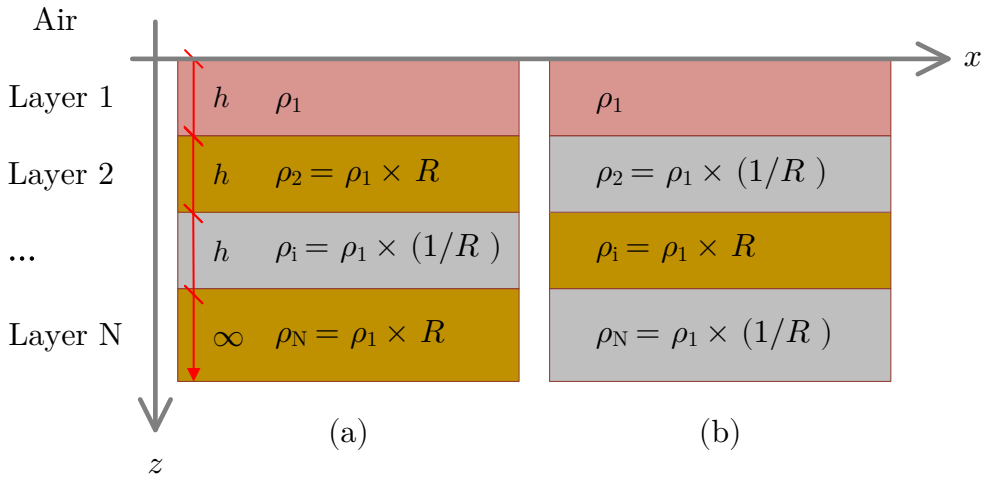

Source: own authorship.

Figure 4.10. Approximation error as function of the resistivity contrast ratio R. Relative error is kept below 1% for $R < 3$ and below 5% for $R < 10$.

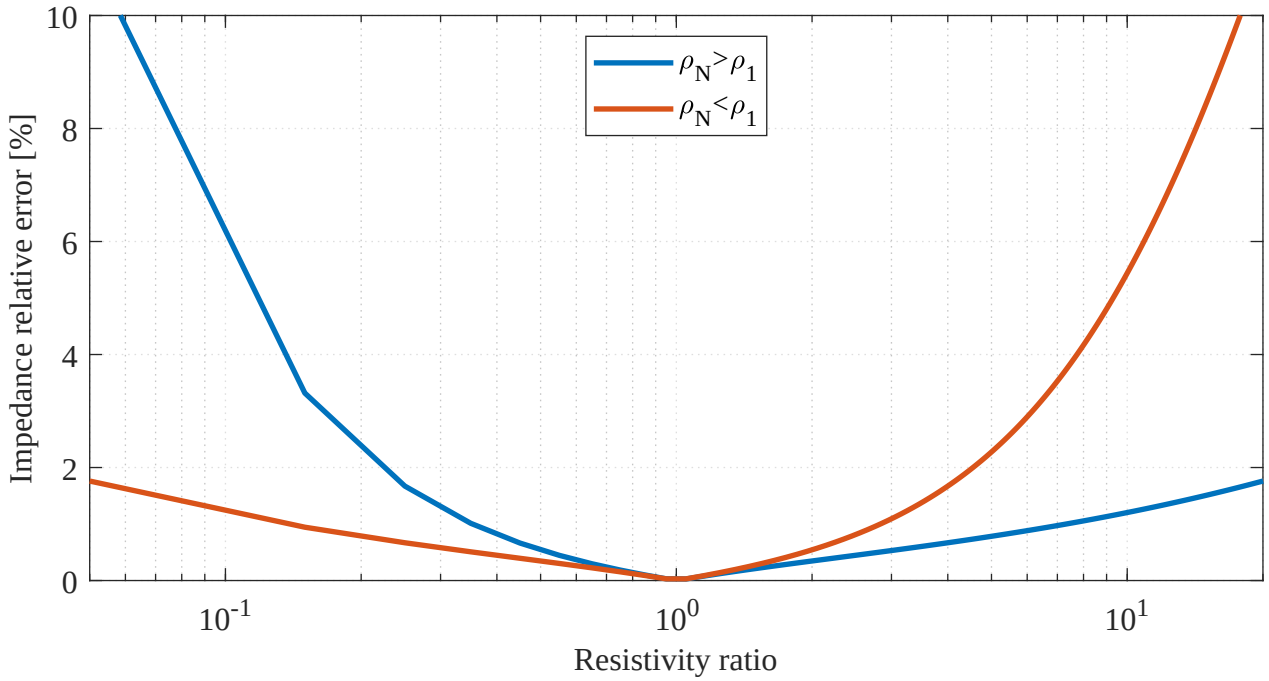

Source: own authorship.

range reach the order of 20%, results are consistent with what is reported in the literature (PAPAGIANNIS *et al.*, 2005; TSIAMITROS *et al.*, 2007).

Table 4.9 presents the computational load imposed by each approach, measured in floating-point operations (flops). Values correspond to the average number of operations to compute the

Figure 4.11. Approximation error as function of the layer thickness and contrast ratio, for top layer resistivities equal to, respectively, 10000, 1000, 100 and 10 Ω.m. Thickness axis is normalized with respect to the skin depth δ. Maximum error is less than 5.45% for depths shallower than 5% of the skin depth δ.

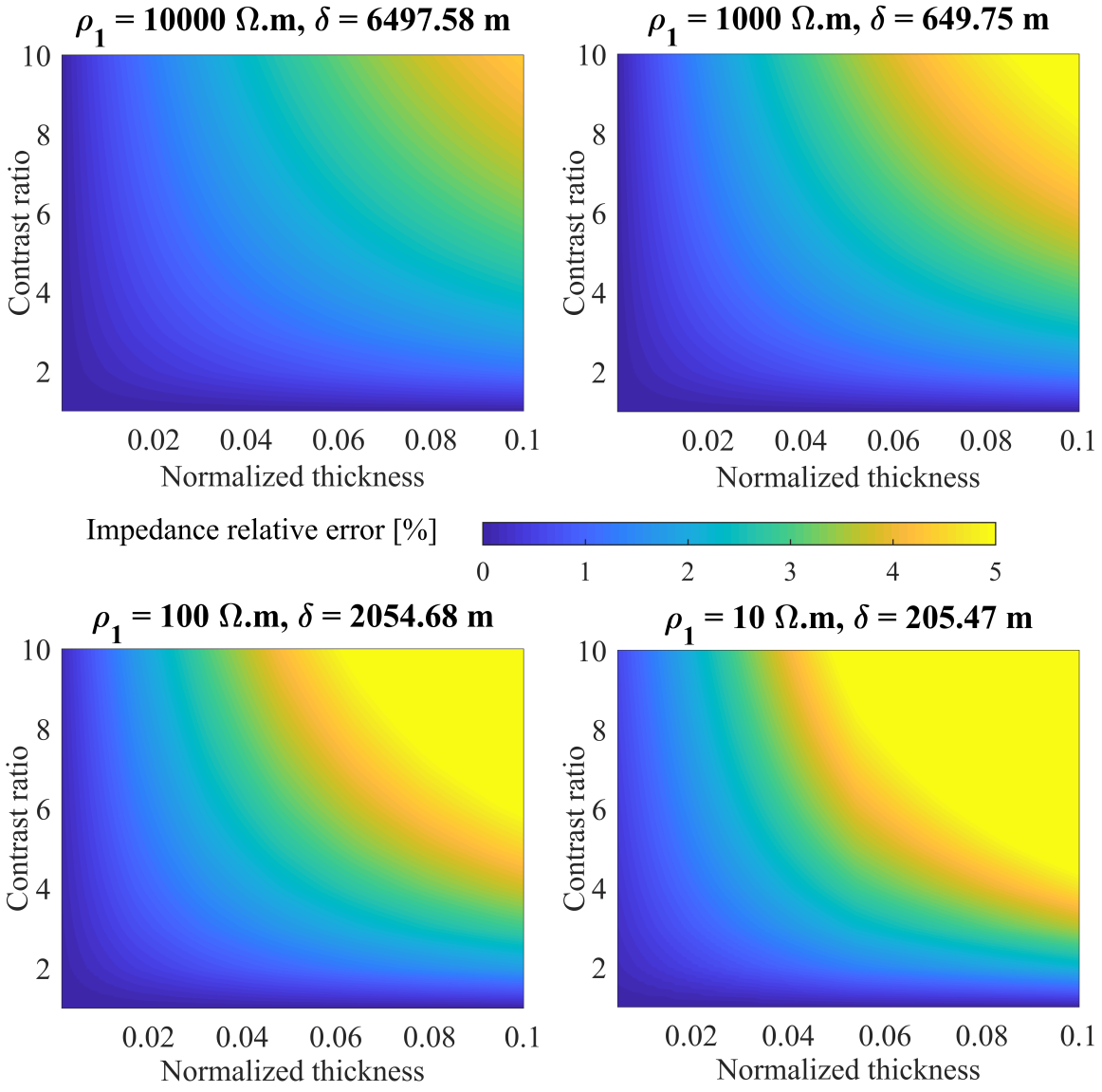

Source: own authorship.

mutual impedance between conductors, evaluated for each soil model presented in Tables 4.2 to 4.6. Results show that the proposed technique reduces the number of necessary floating-point operations in 98% compared with the exact analytical solution, which is mainly explained by the absence of need to perform numerical integrations.

In order to illustrate how this performance gain affects practical applications, computational times are evaluated. Computations shown in Table 4.9 took, respectively, 28.5729 ms and 0.4941 ms, to run on an Intel® Core i9-7900X CPU @ 3.3 GHz with 64 GB RAM and 10 cores.

Table 4.8. Maximum errors, contrast ratios and frequencies.

Model	Maximum Δ [%]	Maximum R	Frequency [MHz]
1	4.31	2.5	0.89
2	8.03	4.3	0.7
3	2.34	1.68	0.2
4	12.75	15.01	0.5
7	16.48	10.77	0.003
8	10.68	14.81	0.05
9	7.6	0.5	3.42
10	9.61	14.44	0.19
11	11.11	2.5	0.12
12	19.06	12.55	0.1
13	6.49	7.37	0.003
15	4.55	0.6	39.01
16	18.48	2.4	2
17	13.33	9.47	0.62
18	14.95	85.75	0.006
19	13.88	16.36	0.04
20	7.57	39.11	0.002

Source: own authorship.

Although computational times of the order of milliseconds may seem quite acceptable for most power systems applications, there are situations, such as low-frequency interference studies, where large systems are involved and require self and mutual impedances to be calculated several thousand times, as well as in transient studies where translations from time-domain to frequency-domain are performed for a very high number of frequencies, in processes that often take hours to run (CIGRÉ WG-36.02, 1995; MARTINS-BRITTO, 2017b; DAWALIBI *et al.*, 1987; MARTINEZ-VELASCO, 2015). In such cases, the achieved performance gain is not to be neglected.

Table 4.9. Average computational load.

Approach	Computational load [flops]	Time [ms]
Analytical	34.4477×10^6	28.5729
Proposed	0.7158×10^6	0.4941

Source: own authorship.

Figure 4.12. Frequency response of two-layered soil models 1, 2 and 3. Errors are under 2% from the 1 Hz range up to the 10 kHz band.

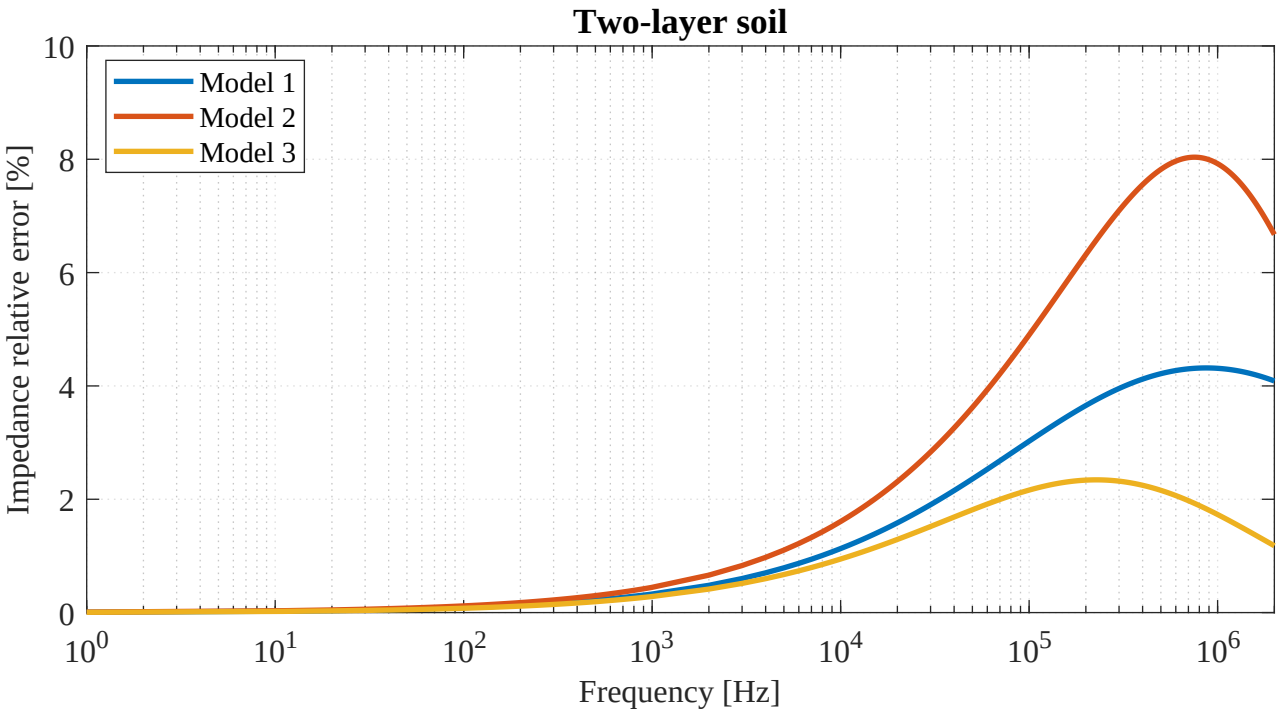

Source: own authorship.

Figure 4.13. Frequency response of three-layered soil models 4, 7, 8 and 9. Models 4 and 9 perform under 2% error from 1 Hz up to the 10 kHz band.

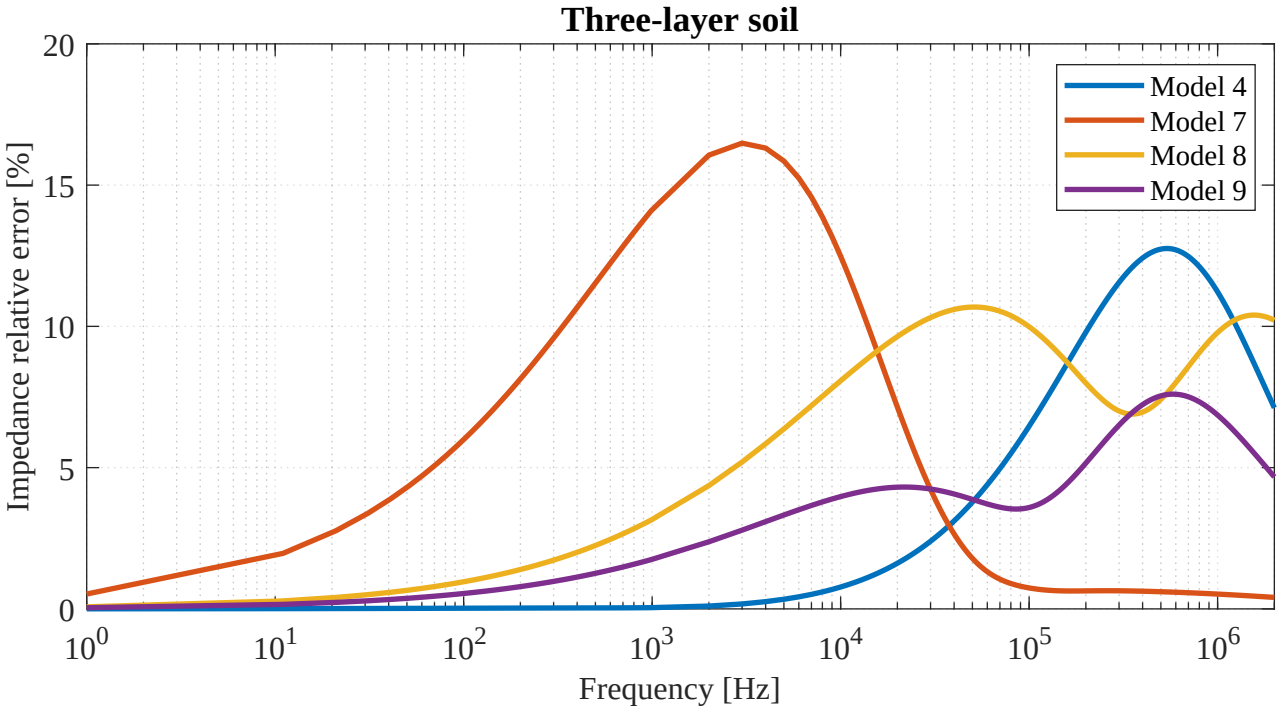

Source: own authorship.

Figure 4.14. Frequency response of four-layered soil models 10, 11, 12 and 13. Errors are below 2% in the range from 1 Hz to 100 Hz.

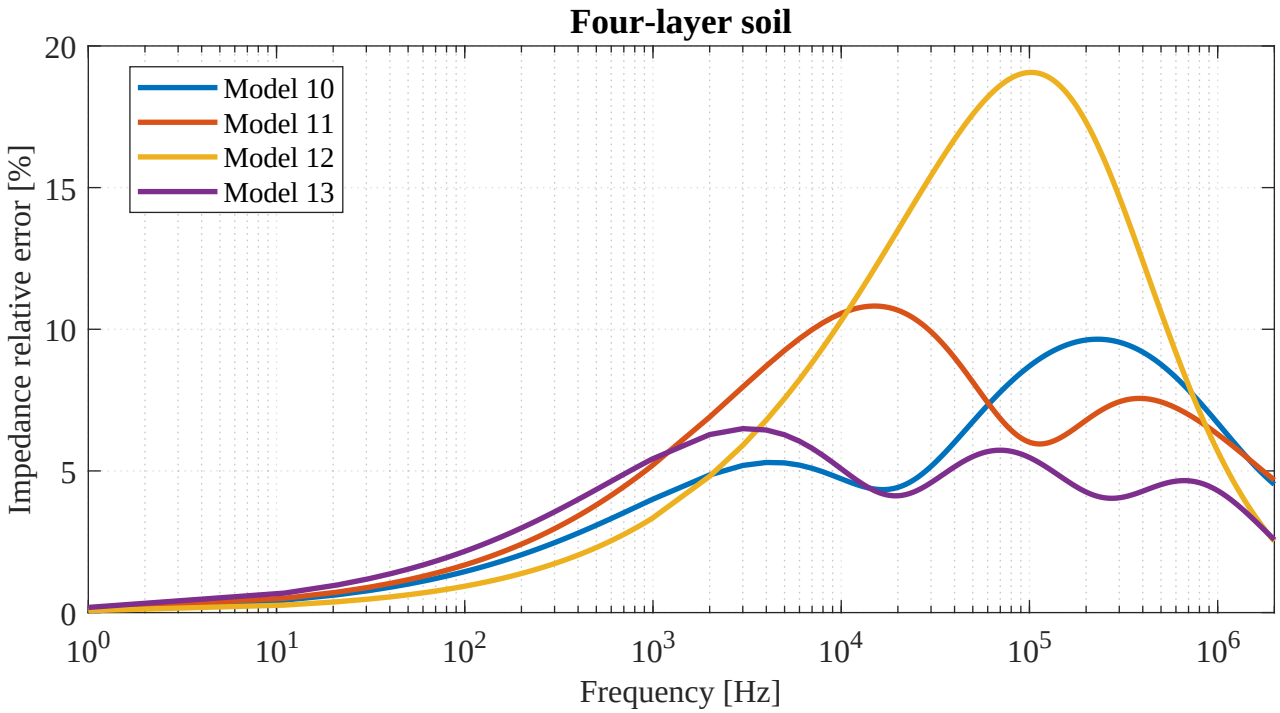

Source: own authorship.

Figure 4.15. Frequency response of five-layered soil models 15, 16 and 17. Errors are below 2% in the range from 1 Hz up to the 10 kHz band.

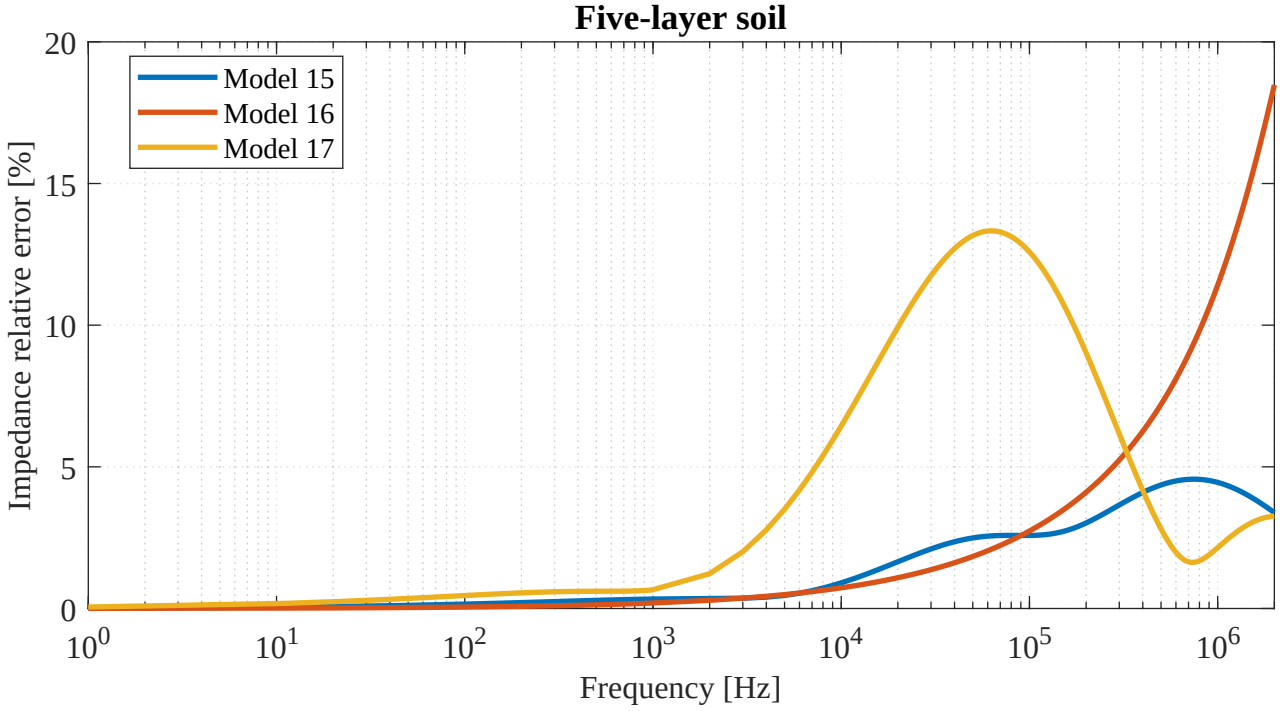

Source: own authorship.

Figure 4.16. Frequency response of six-layered soil models 18, 19 and 20. Errors are below 3% from 1 Hz up to 100 Hz.

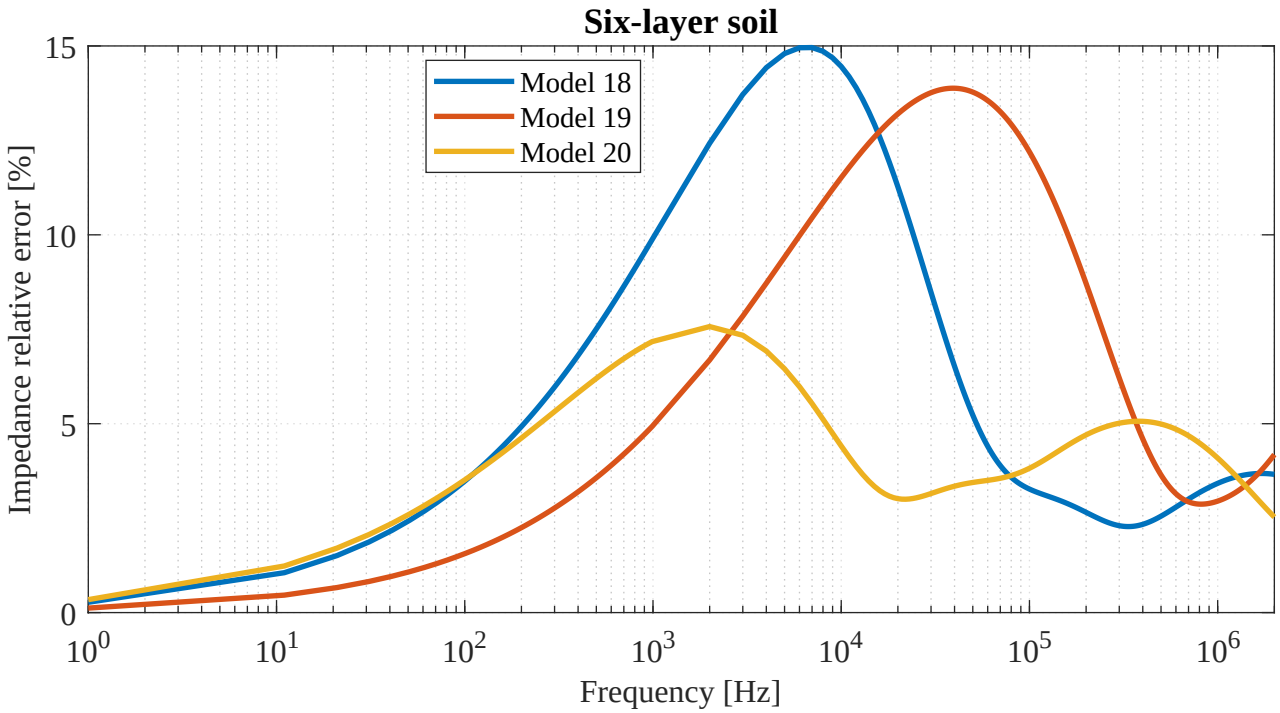

Source: own authorship.

4.3.5 Validity of the new expression

The idea of representing a multilayer soil by its uniform equivalent, proposed in this work, agrees with the very nature of the techniques currently available for measuring and modeling soil parameters, as they describe the equivalent, or apparent, values measured from the earth surface.

The discussed formula efficiently accounts for the multilayered characteristic of real soils and the effect of the deep soil layer on ground return impedances, rather than merely defining a uniform soil structure as the average of apparent resistivities, as it has become a common industry practice (IEEE, 2000).

However, there is a limitation related to the frequency, as approximation errors rise considerably within the high-frequency spectrum. This is due to the fact that under such circumstances, the uniform equivalent formula no longer describes the effectively conductive portion of the soil, determined by the skin depth δ, nor accounts for the effects of displacement currents, expressed by the imaginary parts of the complex-valued parameters conductivity and permit-

tivity originally present in the formulation by Nakagawa *et al.* (1973). For very fast transients with frequencies close to 1 MHz and above, earth may be regarded as a homogeneous structure having the properties of the surface layer, as reported by Papagiannis *et al.* (2005).

Conditions for validity of the proposed formula are: power system frequencies, shallow earth models and low contrast ratios between layer resistivities. As a rule of thumb, accurate results are expected for frequencies up to the kHz band, contrast ratios lower than 10 and depths lower than 5% of the skin depth δ.

Still, the proposed technique is a useful approach that has been proved to be accurate for a variety of power systems applications, in special, but not restricted, to those which rely on the computation of self and mutual impedances between conductors at 50 and 60 Hz.

The main advantages of the presented method are: (a) the same expression is valid independently of the soil model, avoiding a kernel function whose form and complexity grows with the number of layers; (b) no numerical integrations are necessary, without concerns with stability and convergence issues; and (c) a substantial gain of performance is obtained, with a computational load reduction of 98%.

4.4 CASE STUDIES

4.4.1 Applications of the equivalent resistivity formula

There is a wide range of problems relevant to the industry that may potentially benefit from the proposed equivalent resistivity formula. To illustrate the usefulness, accuracy and performance aspects of the proposed technique, two of such problems are presented and discussed.

First, in Section 4.4.1.1, the transient response of a transmission line subject to an asymmetrical fault is evaluated using ATP. Then, in Section 4.4.1.2, induced voltages on a pipeline due to a nearby energized conductor are computed using software FEMM and SESTLC, which are based on the methods described respectively in (CROZIER; MUELLER, 2016; DAWALIBI, 1998). Both cases emphasize the importance of properly taking into account the multilayered nature of actual soils.

4.4.1.1 Line-to-ground fault response of a transmission line

Figures 4.17, 4.18 and Table 4.10 describe the 150 kV single-circuit test system studied in (TSIAMITROS *et al.*, 2007; PAPAGIANNIS *et al.*, 2005). The transmission line is considered to be 200 km long. A line-to-ground fault through a resistance of 2 Ω is applied at the open end of phase c at $t = 10$ ms.

Figure 4.17. Single-circuit 150 kV transmission system.

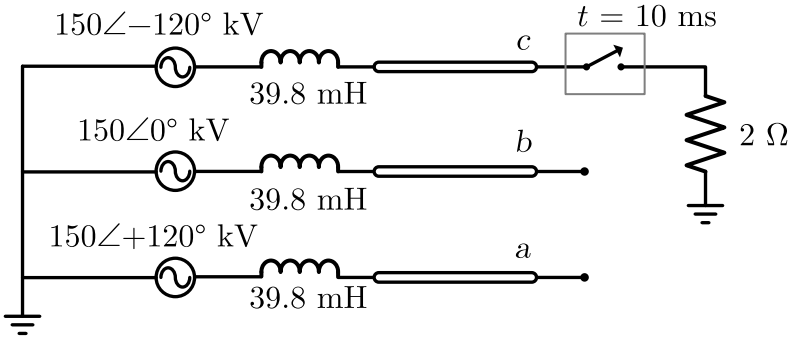

Source: adapted from (TSIAMITROS *et al.*, 2007; PAPAGIANNIS *et al.*, 2005).

Figure 4.18. Transmission line cross-section. Dimensions in meters.

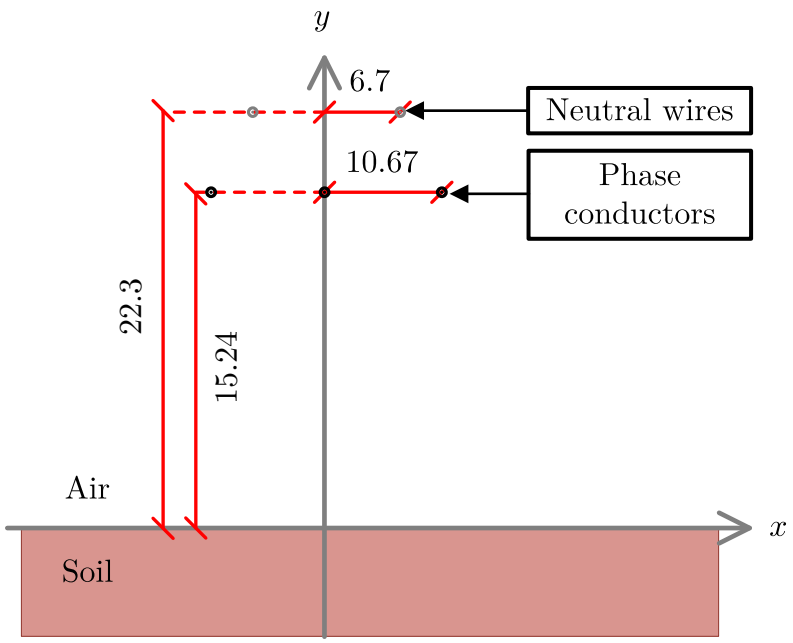

Source: own authorship.

A time-domain simulation is carried out using the ATP software and two scenarios are considered: (a) the soil is assumed to be homogeneous with a resistivity equal to the value of the first layer; and (b) the soil stratification is included in the model by using the uniform

equivalent approach. Since in previous studies two and three-layered soil models were already analyzed, the four-layered soil model number 12 from Table 4.4 is chosen for this case study. The choice is justified by the fact that this model results in the most visible differences and does not represent any loss of generality. Transmission line parameters are computed using the Line/Cable Constants ATP routine. Transient voltages are calculated using a time-step $\Delta t = 1$ μs, which is enough to provide the desired accuracy.

Table 4.10. Specifications of transmission line conductors in Figure 4.18.

Conductor	Diameter [cm]	Resistance [Ω/km]	Reactance [Ω/km]
Phases	2.5141	0.0924806	0.0156758
Neutral	0.9144	3.42313	0.261225

Source: own authorship.

Figure 4.19 shows the phase b open-end voltages. There is a difference of 9.4 kV, or 5.44%, between the overvoltage peak values of each soil model.

This discrepancy in results caused by using different soil models may be enough to require modifications in the design of the tower insulating supports with the addition of more disks, in order to avoid operating too closely to the safety limits or, in the worst case, insulation breakdown. Results show that the earth stratification has significant impacts in transient currents and voltages caused by asymmetrical faults. Furthermore, the proposed technique allows to accurately consider the soil structure in calculations using standard electromagnetic transients software.

4.4.1.2 Inductive interference between a power line and a pipeline

Figure 4.20 represents a case study adapted from (FURLAN, 2015), described by the following design parameters: a single phase transmission line sharing the right-of-way with an 8″ diameter underground carbon steel pipeline installed at 1.2 m depth. The pipeline runs parallel to the transmission line axis for 5 km, with a lateral separation of 100 m. The transmission line operates with a nominal current of 1000 A. The phase conductor is a ACSR 636 MCM 27/7 (Peacock), positioned at 17.2 m above the soil surface. Pipeline parameters are shown in Table 4.11. Soil is assumed to be the same as in the previous section, i.e., the four-layered structure

Figure 4.19. Phase *b* open-end voltages. Peak value is 172.7 kV for the four-layered earth and 163.3 kV for the homogeneous soil model. Difference between both models is 9.4 kV.

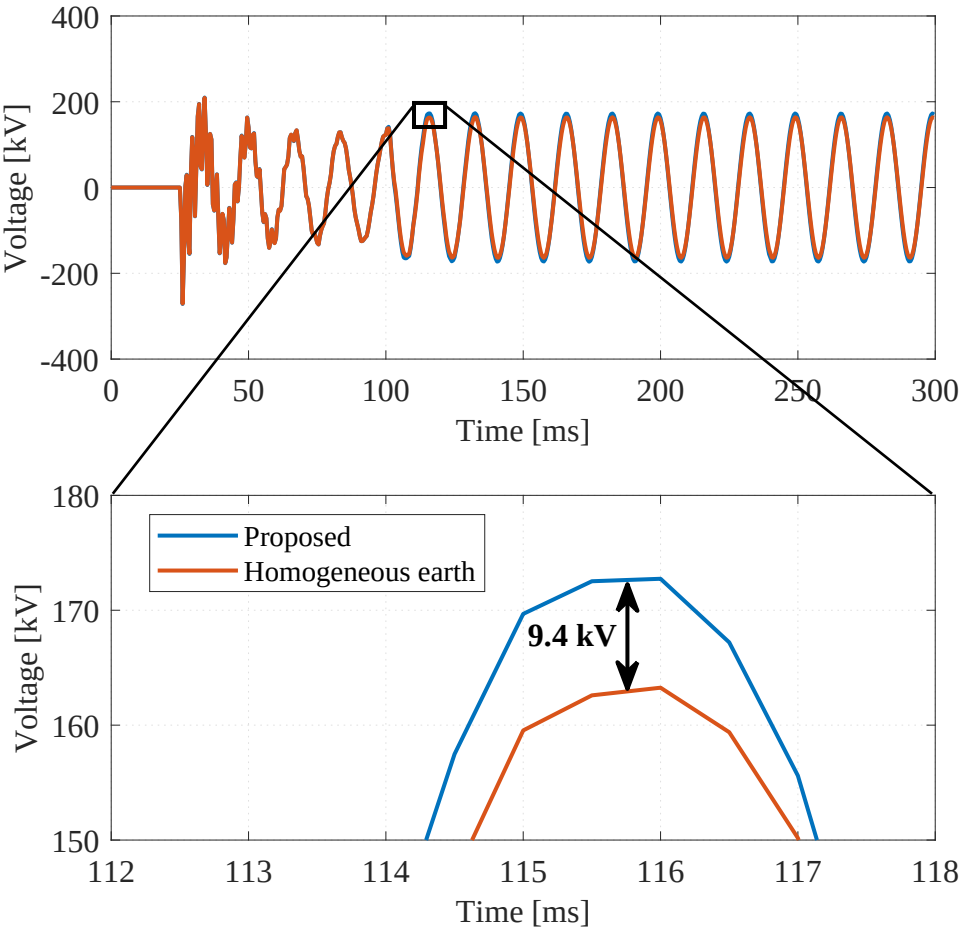

Source: own authorship.

described by model number 12 from Table 4.4, without loss of generality.

Table 4.11. Pipeline characteristics for the system shown in Figure 4.20.

Parameter	Value
Internal radius	0.1014 m
External radius	0.1095 m
Electrical resistivity	1.720×10^{-7} Ω.m
Magnetic permeability	3.771×10^{-4} H/m

Source: own authorship.

Simulations are carried out to determine the voltages induced on the pipeline by the energized phase conductor due to magnetic coupling. First, the finite element method is employed to compute voltages considering the actual four-layered soil structure, using the FEMM package, which is a popular open-source finite element modeling and analysis tool that computes

Figure 4.20. Single phase line and pipeline cross-section. Dimensions in meters. Parallel length is 5 km.

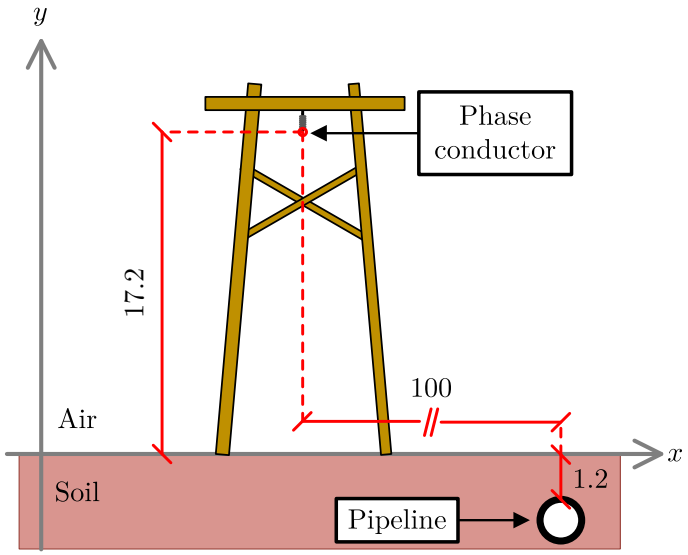

Source: own authorship.

electromagnetic fields distribution over a discretized domain (CROZIER; MUELLER, 2016). Then, calculations are performed using the classic circuit model described in Section 4.1, under two premises: (a) the soil is considered to be homogeneous with a resistivity equal to the value of the first layer; and (b) the soil stratification is accounted by using the uniform equivalent approach. The SESTLC package is employed for this purpose, which is a specialized software designed to predict induced voltages and currents from a transmission line on a target conductor. It assumes the earth to be a uniform medium and uses a circuit theory approach, along with the complex ground return plane proposed in (DERI *et al.*, 1981; DAWALIBI, 1998).

Figure 4.21 shows the pipeline induced voltages due to the parallel exposure. There is a good agreement between results produced by FEMM and the proposed technique, with a maximum error of 2%. On the other hand, errors as high as 50% arise when the soil structure is not properly represented.

It is also relevant to observe the computational times involved: for this simple parallelism case, FEMM needed around half an hour to run calculations, whereas SESTLC took less than one minute to process the model. Thus, the proposed formula combined with a circuit theory approach provides a performance gain of the order of 98% in comparison with the finite element method, which is known to be a computationally demanding technique. This performance improvement not only benefits the simulation of complex geometries, where self and mutual

Figure 4.21. Pipeline induced voltages due to magnetic coupling with the phase conductor. Maximum error between FEMM and the proposed technique is 2%. Maximum error between the four-layered model and homogeneous earth is 50%.

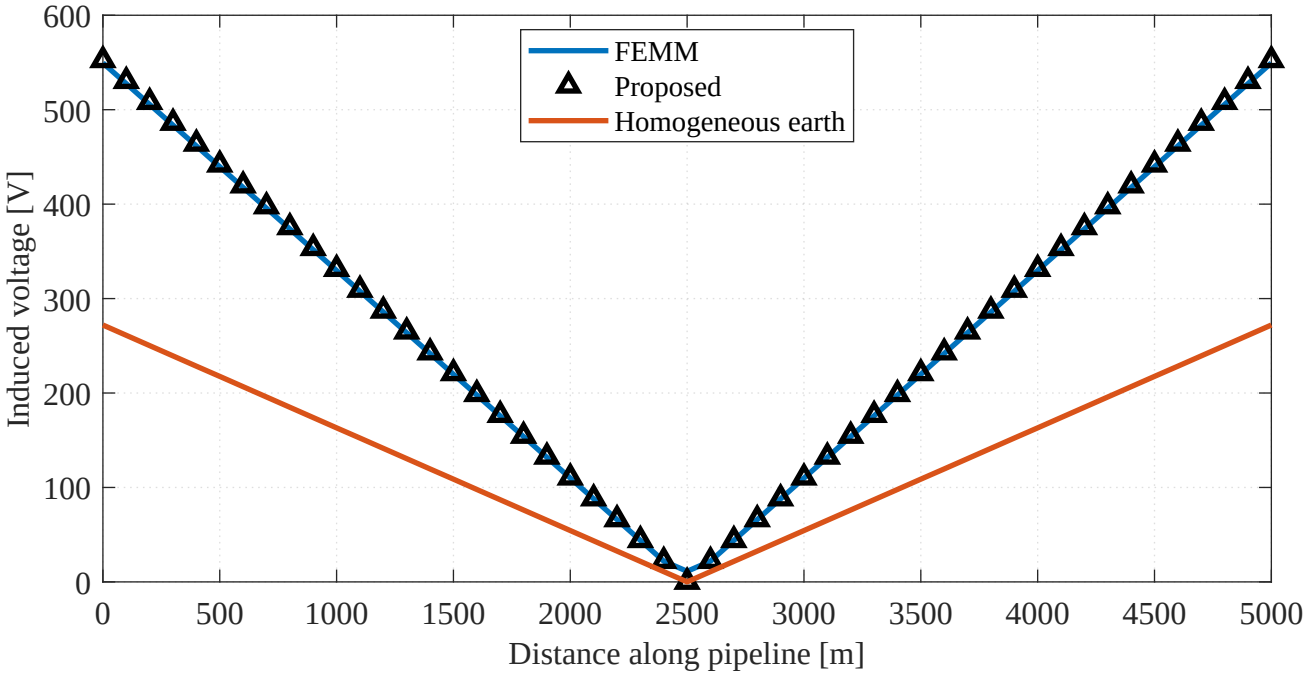

Source: own authorship.

conductor impedances have to be computed several times, but allows for the execution of optimization studies as well.

4.4.2 Validation of the ATP circuit implementation

This section is intended to evaluate the viability of using ATP as an EMI simulation tool and the validity of the circuit model synthesized in Figure 4.7. A simple topology is first studied, and more complex cases are progressively introduced, with adding more conductors and different geometries, such as crossings and obliquities. Results are compared with simulations from specialized commercial software, such as the SESTLC, already described in the previous case study.

4.4.2.1 Inductive interference between a traction system and a pipeline

Figure 4.22 represents a system adapted from (MILESEVIC *et al.*, 2011), consisting of a single-phase overhead electric traction line (contact conductor) in the vicinity of a buried pipeline.

Figure 4.22. Geometry of the approximation between an electric traction system (railway) and a pipeline. Coordinates given in meters with reference to the railway axis.

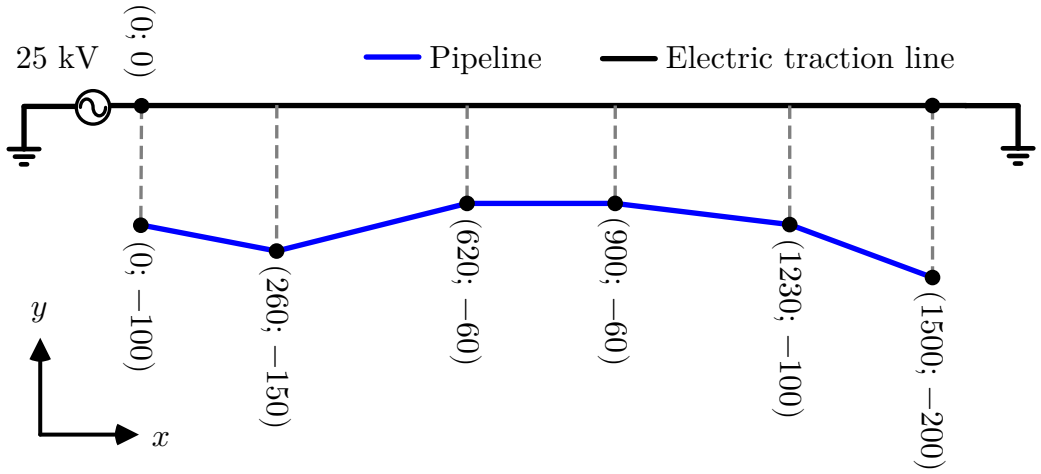

Source: adapted from (MILESEVIC *et al.*, 2011).

The electromagnetic interference zone extends to a total length of 1500 m and the pipeline approximation is comprised of obliquities and one parallel section, as described by the vertex coordinates shown in Figure 4.22. The height of the energized conductor is 5.5 m and the pipeline is buried at depth 1.5 m.

Parameters of the conductors are given in Table 4.12. Since the objective now is not to evaluate the effects of the soil structure, earth resistivity is assumed to be uniform and equal to 500 Ω.m.

Table 4.12. Parameters of the electric traction system and pipeline conductors.

Conductor	Inner radius [m]	Outer radius [m]	Resistivity [Ω.m]	μ_r
Contact conductor	0.004039	0.0121	3.9393×10^{-8}	1.073
Pipeline	0.1014	0.1095	1.724×10^{-7}	300

Source: own authorship.

Using the subdivision scheme described in Section 4.2, the circuit shown in Figure 4.23 is constructed, composed of six nodes and five sections of equivalent parallelisms. Power system

frequency is 60 Hz and the excitation current is 5 kA, representing a short-circuit in the traction line, with a fault resistance of 1 Ω. The pipeline is considered to be grounded at both extremities through a grounding resistance of also 1 Ω.

Figure 4.23. ATPDraw representation of the equivalent circuit of the electric traction system and the pipeline.

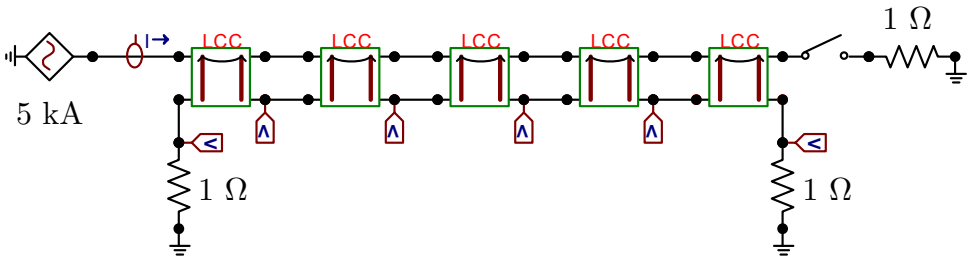

Source: own authorship.

First, the steady-state response of the interfered system is evaluated, so that comparisons can be made with similar programs. This is accomplished by closing the switch in Figure 4.23 at any given time, then letting $t \to \infty$ and extracting the peak value of the resulting sinusoidal voltage waveforms. Figure 4.24 shows the resulting induced voltages as a function of the pipeline distance, as well as the results obtained using the SESTLC software. It is clear that there is an excellent agreement between both models, with errors inferior to 1%. Discrepancies are mainly explained by the different numerical methods adopted in each program to compute mutual impedances.

With the validity of the ATP model having been verified, the proposed implementation is leveraged to investigate the transient behavior of the induced voltages in the target line. The switch in Figure 4.23 is closed at $t = 0.05$ s and the simulation is carried out until $T_{max} = 0.15$ s is reached. Figures 4.25 to 4.30 show the induced voltages as a function of time at fixed points located along the pipeline, corresponding to distances: 0, 260, 620, 900, 1230 and 1500 m. Two time windows are presented in each picture, so that a clear view of the transient and steady-state regimes is provided.

Figure 4.24. Steady-state induced voltages due to inductive coupling with the electric traction system conductor. Errors between the proposed ATP model and SESTLC are below 1%.

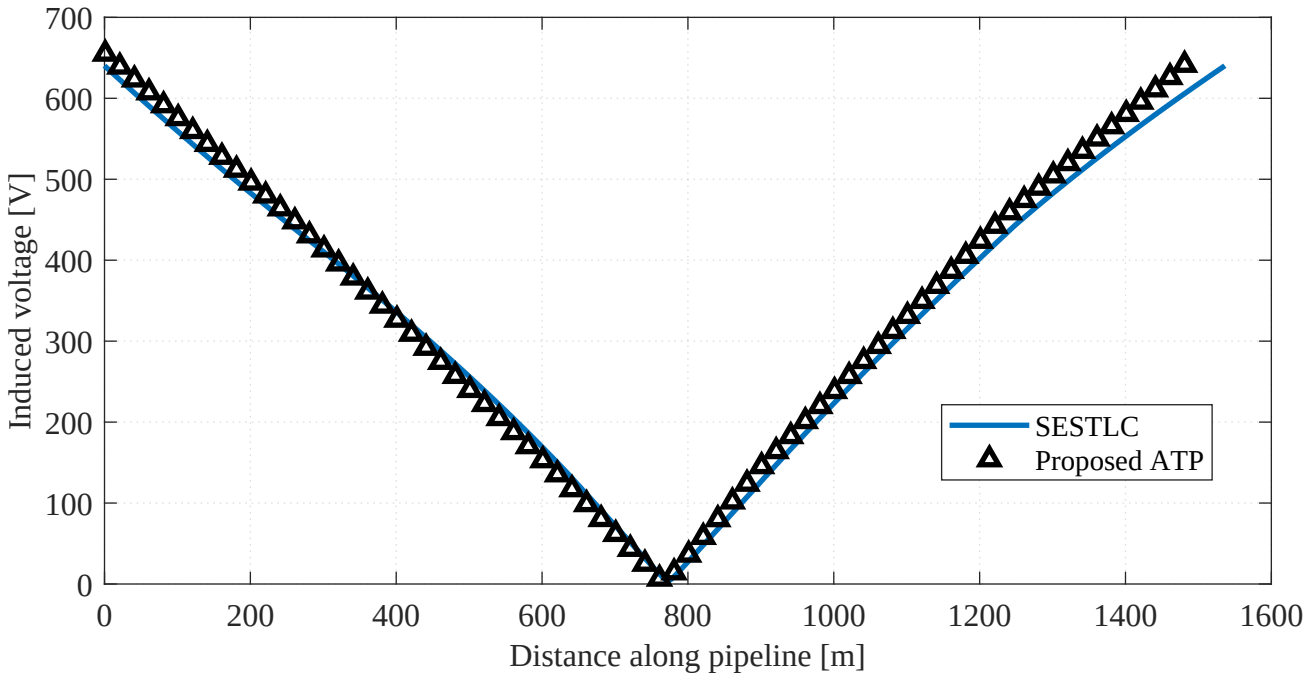

Source: own authorship.

Figure 4.25. Pipeline induced voltages versus time at distance: 0 m.

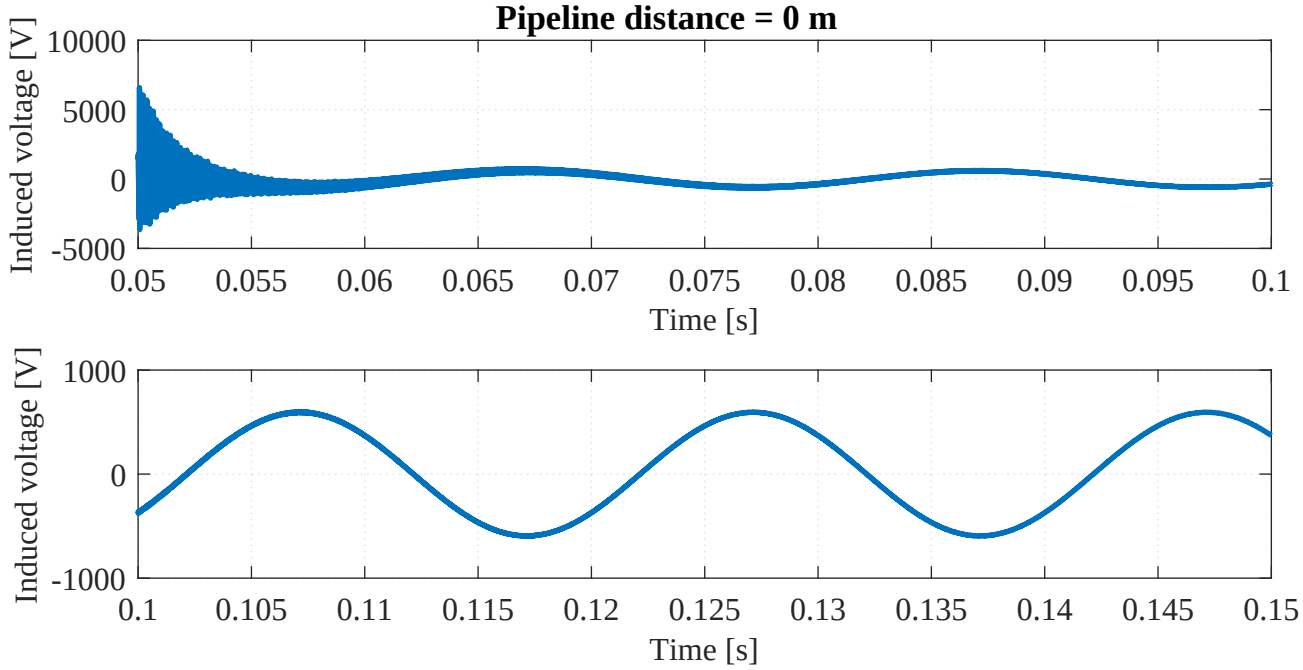

Source: own authorship.

Figure 4.26. Pipeline induced voltages versus time at distance: 260 m.

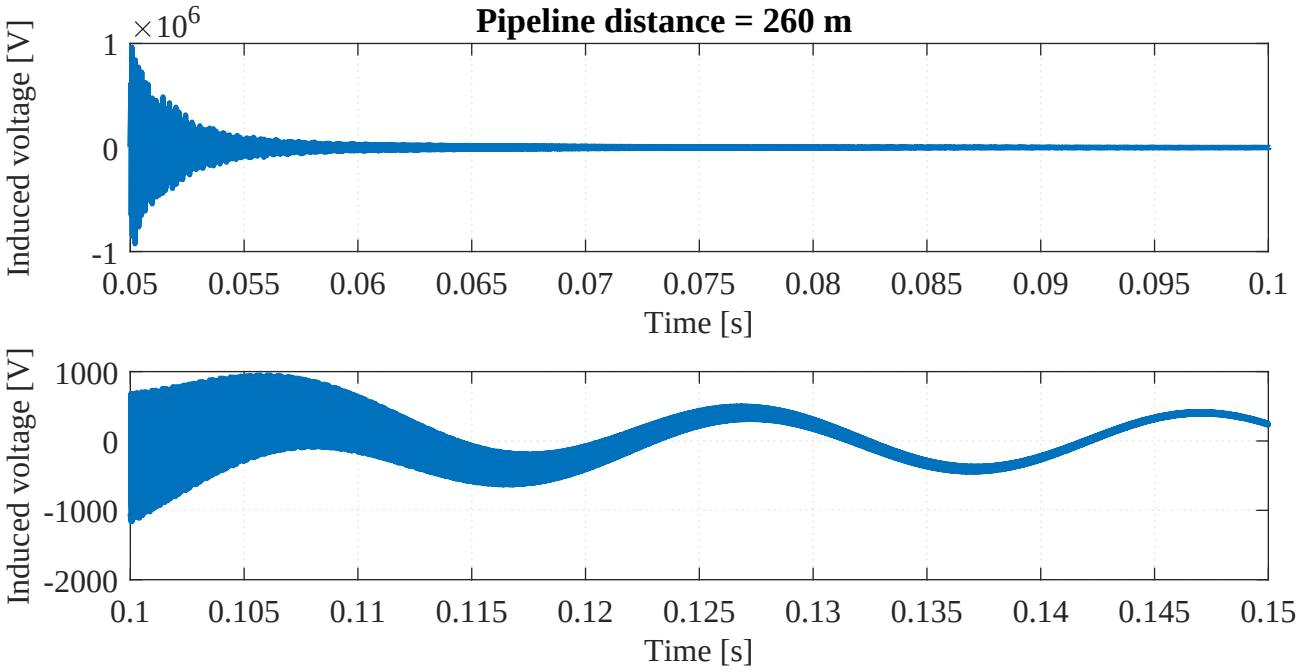

Source: own authorship.

Figure 4.27. Pipeline induced voltages versus time at distance: 620 m.

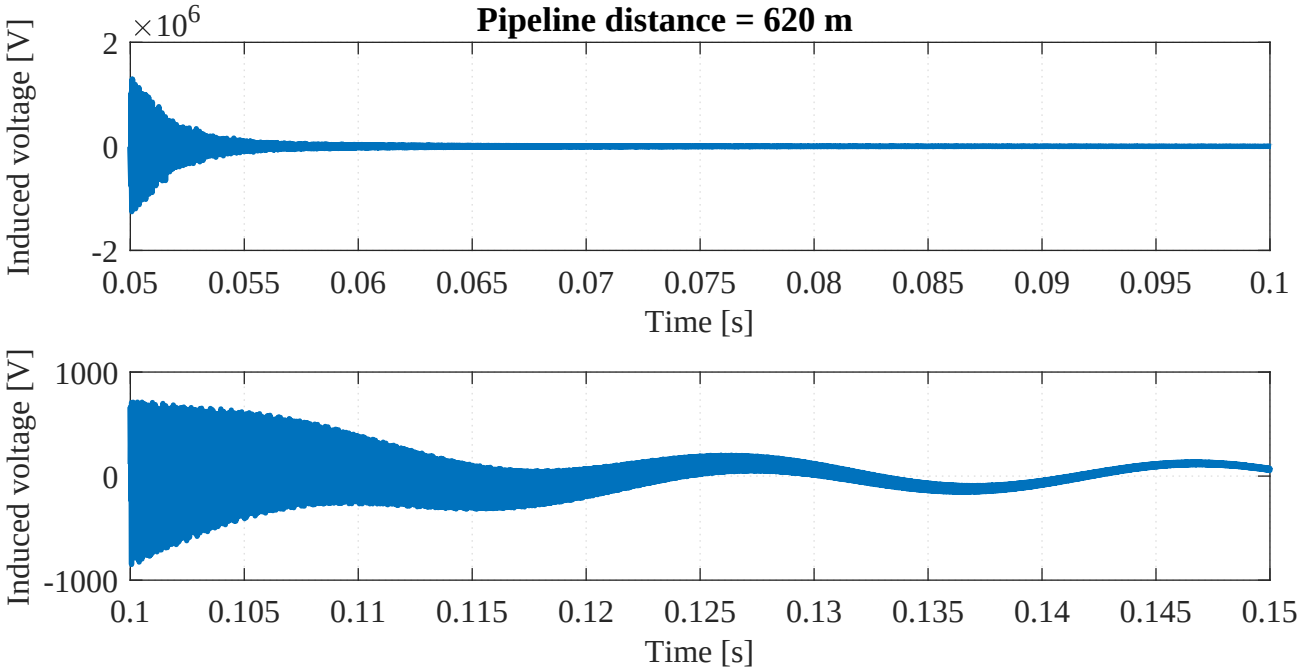

Source: own authorship.

Figure 4.28. Pipeline induced voltages versus time at distance: 900 m.

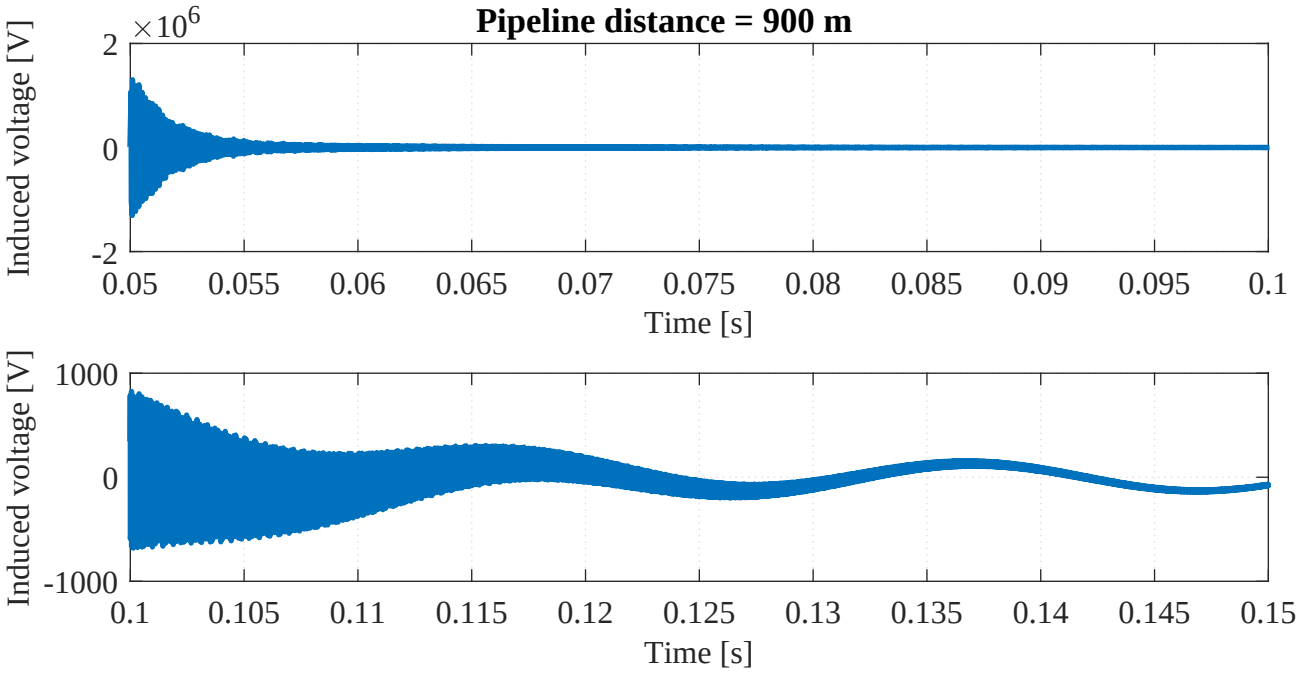

Source: own authorship.

Figure 4.29. Pipeline induced voltages versus time at distance: 1230 m.

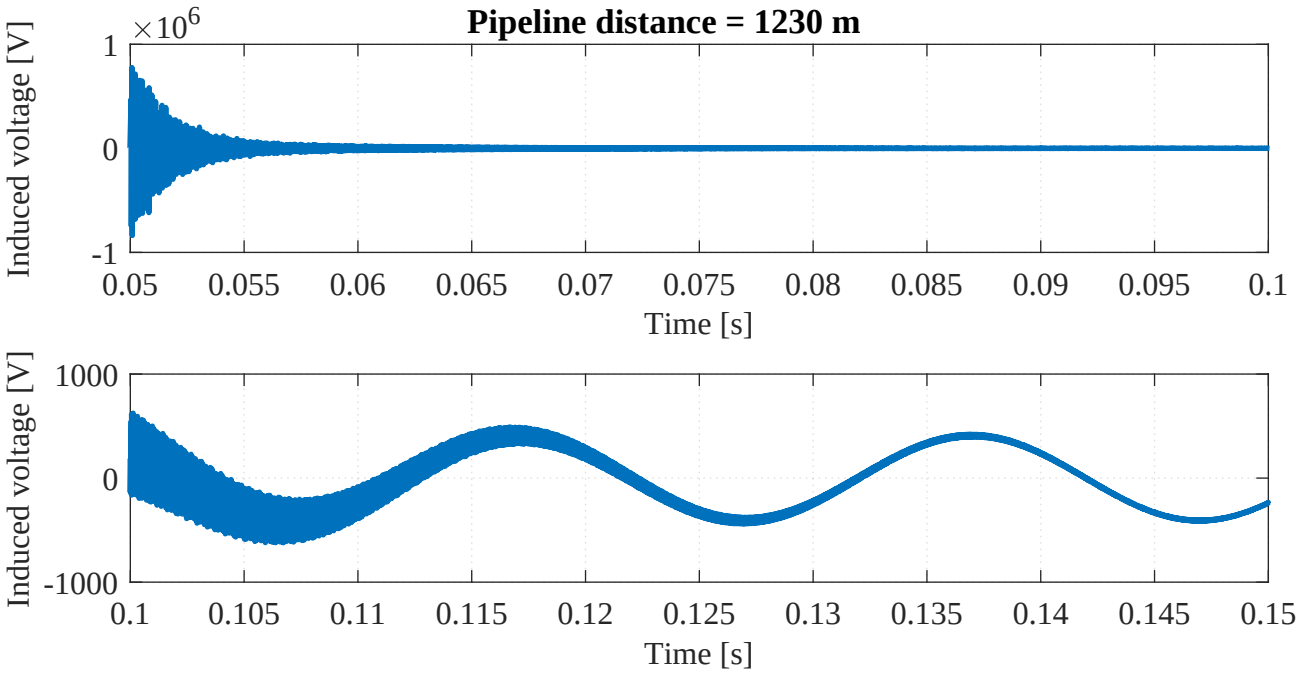

Source: own authorship.

Figure 4.30. Pipeline induced voltages versus time at distance: 1500 m.

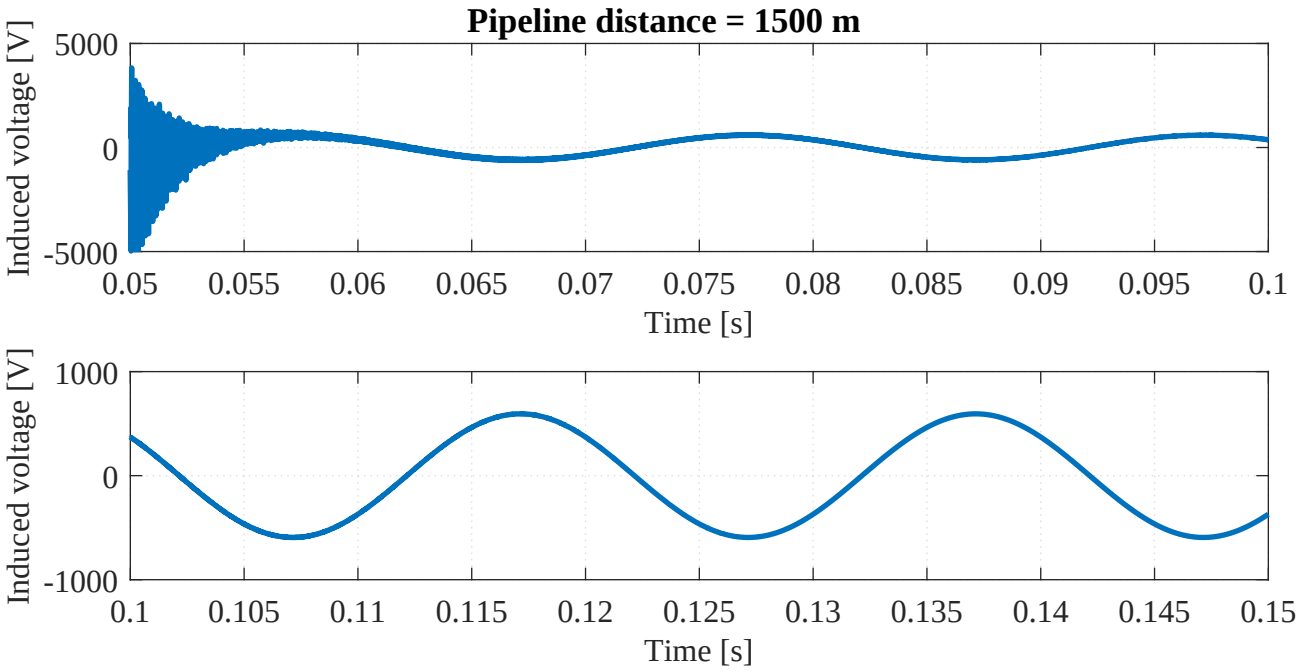

Source: own authorship.

Results show that although the steady-state induced voltages along the pipeline, shown in Figure 4.24, are kept within the nominal safety limits described in Table 2.3, considerably higher values may occur in transient conditions, due to the interaction of the line capacitances and inductances.

Maximum transient values at intermediate pipeline points, corresponding to 260 m, 620 m, 900 m and 1230 m, shown, respectively, in Figures 4.26 to 4.29, draw attention due to their magnitude being several orders larger than typical tolerable values, in such way that one may question the physical significance of the obtained results. In this case, two aspects should be considered, both related to the purely theoretical nature of the system represented in Figure 4.22. First, the proposed configuration is composed of only two conductors, which implies that the target line is exposed to the effects of the energized conductor in its entirety, without the mitigation naturally provided by the presence of shield wires typically employed in real installations. Second, the system is energized by an ideal current source, characterized by an infinite impedance and an infinite short-circuit capacity, which, again, does not happen in practical situations. On the other hand, transient solutions in the target line are numerically

stable, converge to the expected steady-sate values and show the characteristics of capacitive switching transients. This shows that the model provides results which are consistent with the simulation assumptions, even if they are strictly theoretical. A realistic system is discussed in Section 4.4.2.2, where it is shown that relevant transient effects still affect the target line, but within fairly reasonable ranges of values.

Figure 4.31 shows the currents at the receiving end of the transmission line in the presence of the interfered pipeline (regular circuit shown in 4.23) and a variation where the pipeline is removed. It is clear that the presence of the interfered pipeline not only affects current amplitudes during transients, but the angular lagging as well.

Figure 4.31. Currents at the receiving end of the transmission line in the presence of the target pipeline and neglecting the interference, in the period between $t = 0.01$ s and $t = 0.02$ s. Source current waveform is included to establish a baseline.

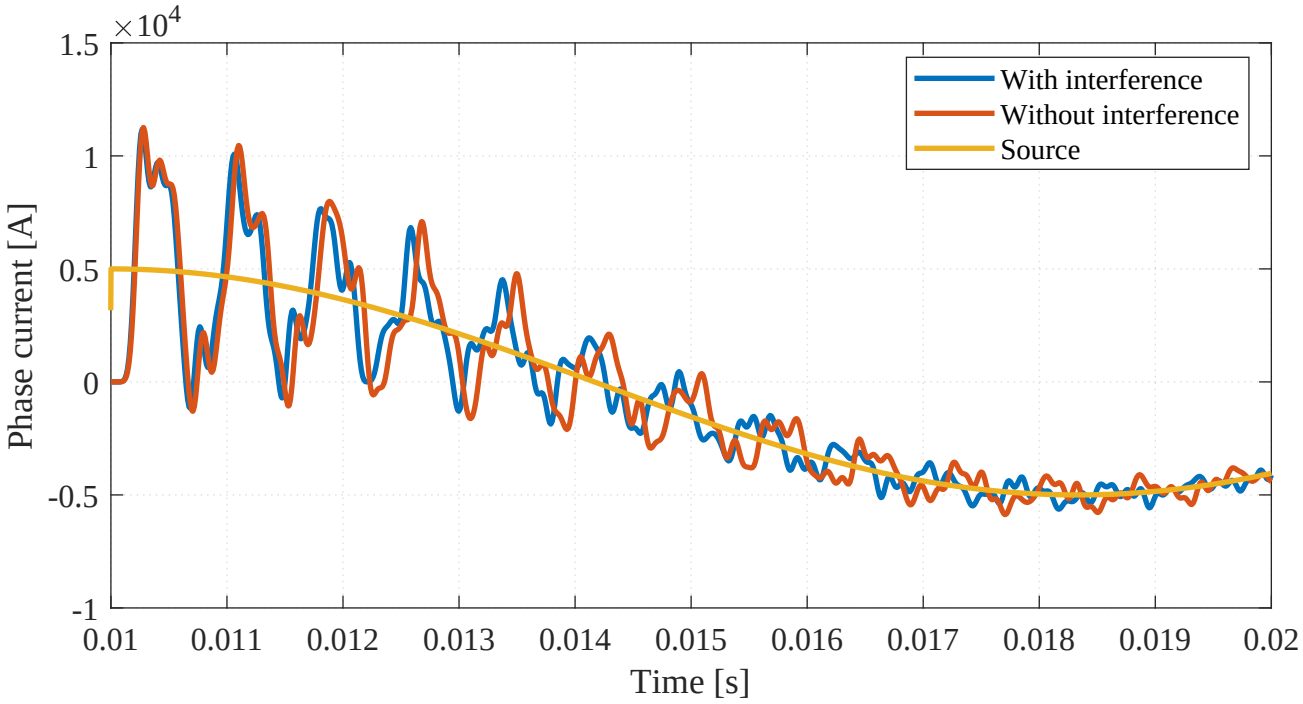

Source: own authorship.

4.4.2.2 Total interference between an 88 kV distribution system and a pipeline

In this section, all the techniques proposed along this chapter are applied to a case study based on real design data and field measurements.

The power system under study, summarized in the single-line diagram shown in Figure 4.32, consists of an 88 kV transmission line branch, designed to supply an industrial customer with a Y-connected load, power factor of 0.95 (inductive), rated current 100 A. The transmission line extends for 3.5 km, from the branch connection to the terminal substation. Specifications of the transmission line conductors are provided in Table 4.13.

Short-circuit levels at the transmission line terminals are represented by two Thèvenin equivalents, whose parameters come from the ONS (Operador Nacional do Sistema Elétrico[1]) database and are considered design premises.

Figure 4.32. Single-line diagram of the power system.

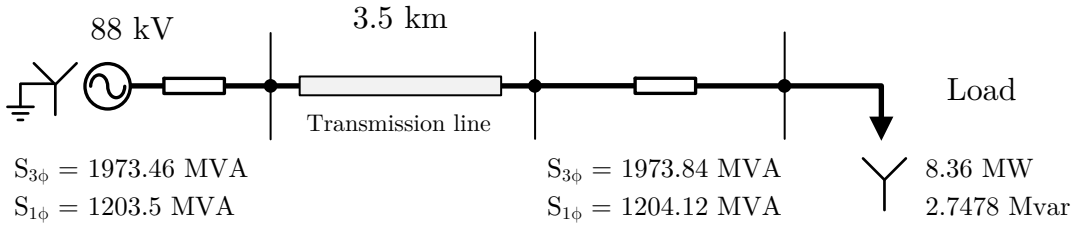

Source: own authorship.

Table 4.13. Parameters of the 88 kV distribution system and pipeline conductors.

Conductor	Inner radius [m]	Outer radius [m]	Resistivity [Ω.m]	μ_r
Phases	0.004635	0.01257	3.9342×10^{-8}	1.064
Shield wire	0.001524	0.004572	2.4446×10^{-7}	63.29
Pipeline	0.1014	0.1095	1.724×10^{-7}	300

Source: own authorship.

The transmission line, whose typical cross-section is given in Figure 4.33, shares the right-of-way with an 8″ natural gas underground pipeline over an extension of 1.5 km, as illustrated in Figure 4.34. The approximation geometry consists of oblique segments, one parallel section and one crossing, according to the coordinates given in the figure. Towers are spaced with an

[1]Brazil's Operator of the National Electricity System.

average span length of 250 m. The towers within the EMI zone are numbered from 1 to 7. The transmission line extends outwards the electromagnetic coupling region for 1 km, or four spans, before and after the shared right-of-way.

Figure 4.33. Cross-section of a 88 kV distribution line tower. Dimensions in meters.

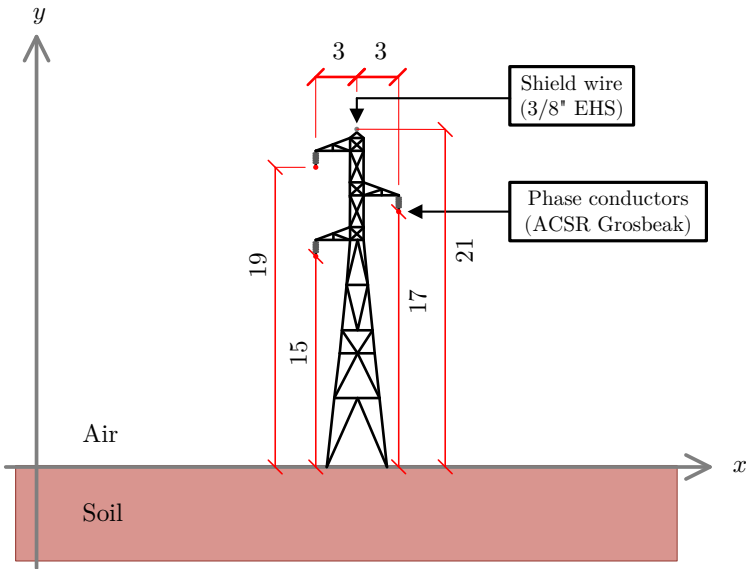

Source: own authorship.

Figure 4.34. Geometry of the approximation between a 88 kV distribution line and a pipeline. Coordinates given in meters with respect to the transmission line axis.

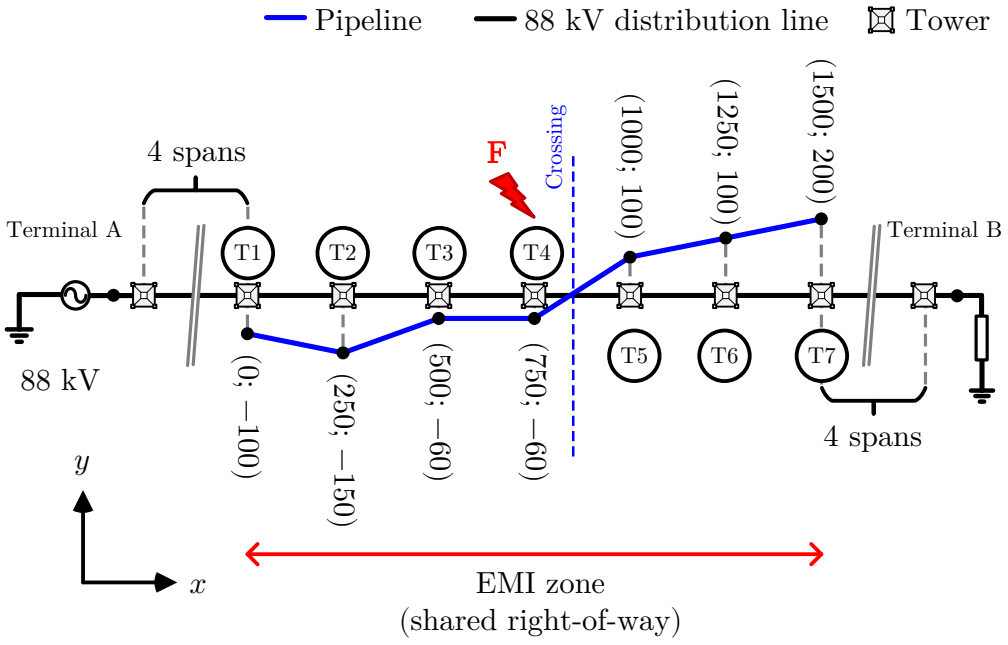

Source: own authorship.

Using the procedures described in Section 4.2, the circuit shown in Figure 4.35 is constructed, in which the EMI zone is composed of 15 equivalent parallelism sections. Each LCC block is parameterized according the tower geometry, shown in Figure 4.33, and the appropriate resistivity values. Shunt resistors labeled [T1, T2, ..., T7] are the tower grounding resistances connected to the shield wire. Shunt voltage sources connected to the pipeline bus, labeled [S1, S2, ..., S16], are controlled by the currents flowing through resistors [T1, T2, ..., T7] and by the Green's functions corresponding to each soil model described in Table 4.15, which are computed using the routines given in Appendix A.

Tables 4.14 and 4.15 contain, respectively, soil apparent resistivity measurements and resulting soil models at the tower locations. Table 4.15 shows that the soil models within the EMI zone are composed of two and three layers.

Table 4.14. Apparent resistivity measurements along the 88 kV transmission line.

Location	$a = 1$ **[m]**	$a = 2$ **[m]**	$a = 4$ **[m]**	$a = 8$ **[m]**	$a = 16$ **[m]**	$a = 32$ **[m]**
	Apparent resistivity ρ_a [Ω.m]					
Tower 1	201.35	254.64	383.68	510.50	609.38	578.08
Tower 2	334.52	365.59	463.20	507.48	592.29	549.94
Tower 3	285.97	330.12	384.06	424.70	433.91	338.81
Tower 4	116.35	135.24	162.31	213.86	192.07	144.10
Tower 5	286.30	362.39	445.53	603.84	623.46	532.85
Tower 6	313.09	533.69	653.77	800.09	1050.84	929.95
Tower 7	399.15	612.94	743.38	996.34	1221.79	884.73

Source: own authorship.

Table 4.15. Soil stratification data along the 88 kV transmission line.

Location	**Layers**	ρ_1 **[Ω.m]**	ρ_2 **[Ω.m]**	ρ_3 **[Ω.m]**	h_1 **[m]**	h_2 **[m]**
Tower 1	2	175.74	636.52	–	1.32	–
Tower 2	2	318.98	581.48	–	1.73	–
Tower 3	3	263.89	491.24	280.04	1.38	11.34
Tower 4	3	114.42	361.61	116.87	2.37	5.39
Tower 5	3	282.70	1083.60	475.78	2.17	4.69
Tower 6	2	202.79	1068.91	–	0.72	–
Tower 7	3	292.25	1273.55	466.26	0.91	19.88

Source: own authorship.

Figure 4.35. ATPDraw representation of the equivalent circuit of the 88 kV distribution system and the pipeline.

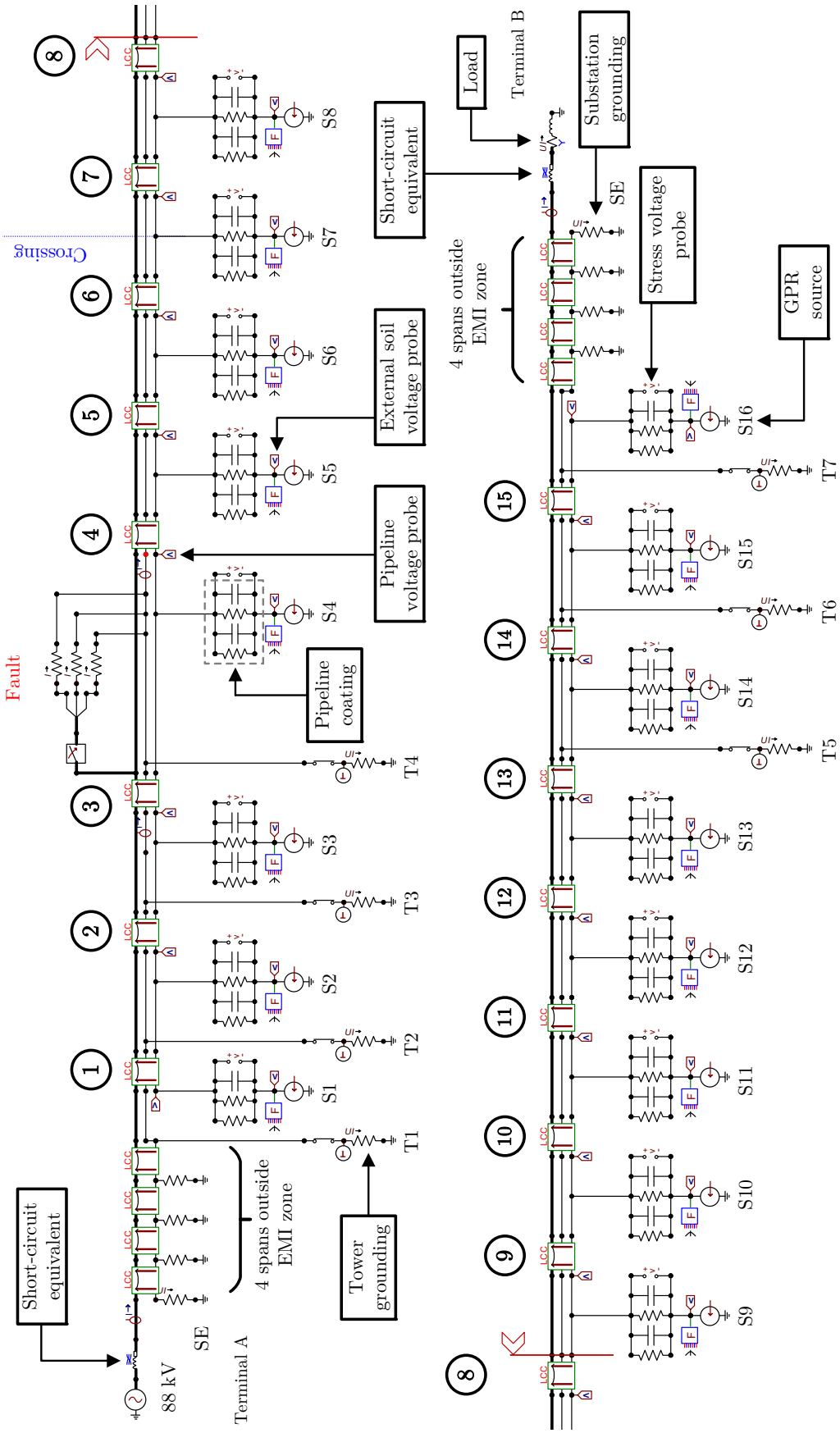

Source: own authorship.

Table 4.16 presents the equivalent resistivity values, calculated according to the method proposed in Section 4.3.3, as well as the uniform model values, determined as the simple arithmetic mean of the apparent resistivities.

Table 4.16. Soil resistivity equivalent and uniform models along the 88 kV transmission line.

Location	Top layer ρ_1 [Ω.m]	Bottom layer ρ_N [Ω.m]	Equivalent model ρ_{eq} [Ω.m]	Uniform model ρ [Ω.m]
Tower 1	175.74	636.52	633.8381	445.1014
Tower 2	318.98	581.48	580.4287	468.8367
Tower 3	263.89	280.04	282.4957	366.2617
Tower 4	114.42	116.87	118.0623	160.6550
Tower 5	282.70	475.78	476.5476	475.7283
Tower 6	202.79	1068.91	1065.8011	744.4843
Tower 7	292.25	466.26	474.2594	809.7217

Source: own authorship.

First, a simple verification is performed in order to validate the circuit model, the same as in the preceding sections. Assuming nominal load conditions and a uniform soil model, pipeline induced voltages are evaluated and compared with results from the SESTLC program. For this purpose, the power system is energized by a current source with amplitude equal to 100 A per phase, and the soil resistivity is assumed equal to the average uniform value of 500.33 Ω.m for all LCC blocks.

Figure 4.36. Pipeline voltages due to inductive coupling with the 88 kV distribution line under nominal load conditions. Error between the proposed ATP model and SESTLC is below 5% in the worst point.

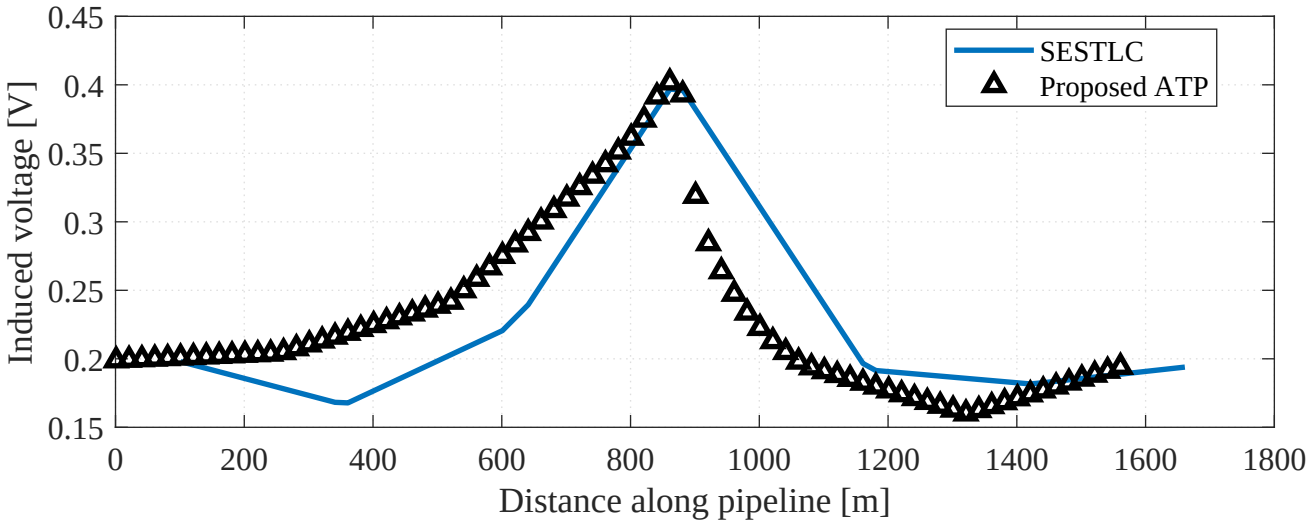

Source: own authorship.

Results agree with the reference software within a margin of less than 5%, with an excellent fit at the crossing location, where the pipeline induced voltage reaches its maximum value. There is a slight difference in the shapes of the curves, which is explained by the subdivision scheme adopted in the proposed implementation. If the target line is subdivided into smaller segments, a smoother profile is expected, with a better adherence to the reference results. This is planned to be addressed in the future development of this work.

Having proved its validity, the proposed model is explored to its full potential to analyze the transient voltages induced in the target pipeline under fault conditions. Soil resistivity variations along the transmission line route are modeled using the equivalent resistivity values given in Table 4.16. Grounding resistances at the tower locations inside the EMI zone are computed using the methods described in Section 2.4.3, considering the same counterpoise configuration employed in Figure 3.16, i.e., four horizontal conductors, with 25 m each, buried 50 cm beneath the soil surface. Grounding parameters are calculated using the multilayered soil models presented in Table 4.15, and are summarized in Table 4.17. Typical values of 0.10 Ω are assumed at the terminal substations A and B.

Table 4.17. Grounding resistances along the 88 kV transmission line.

Location	**Grounding resistance [Ω]**
Tower 1	10.45
Tower 2	11.63
Tower 3	8.86
Tower 4	3.92
Tower 5	11.69
Tower 6	23.15
Tower 7	23.69
Outside EMI zone	12.80

Source: own authorship.

The fault is simulated at the location corresponding to Tower 4 due to its proximity with the pipeline at the crossing point, as shown in Figure 4.34. This is expected to produce the worst-case scenario for faults involving the ground, in which a significant part of the fault current is discharged directly into the soil at the closest pipeline vicinity. In the electrical equivalent, given in Figure 4.35, the fault is represented by a time-controlled switch at the end of the third section, connecting the respective phases to the shield wire through fault resistances equal to 1 mΩ.

A single-phase-to-ground (AG) fault is applied by closing the phase a switch at $t = 0.03$ s, and the simulation is executed until $T_{max} = 0.15$ s is reached. Figure 4.37 contains the phase currents flowing from Terminal A. Figure 4.38 presents the currents in the fault branch and the portion discharged to the soil at the fault location.

Figure 4.37. Phase currents flowing from the grid connection (Terminal A). Maximum transient current in the faulted phase is 13.64 kA and decays to 8.98 kA in steady-state.

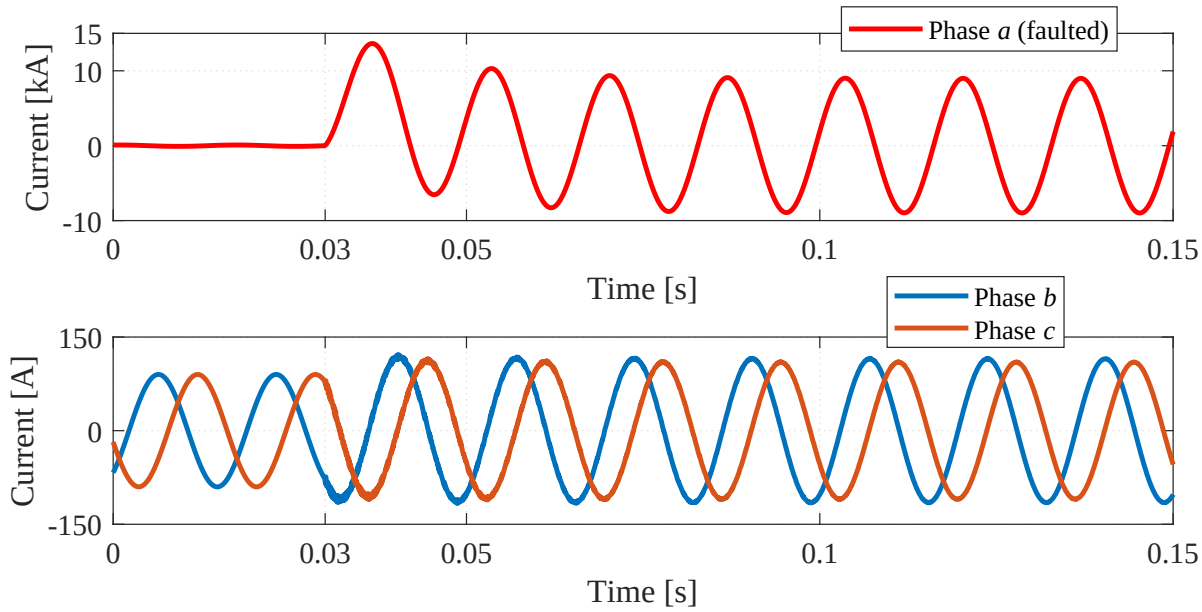

Source: own authorship.

Figure 4.38. Currents through the fault branch and the grounding system of the faulted tower. Maximum values are, respectively, 13.64 kA and 4.61 kA. Steady-state values are 8.99 kA and 3.03 kA.

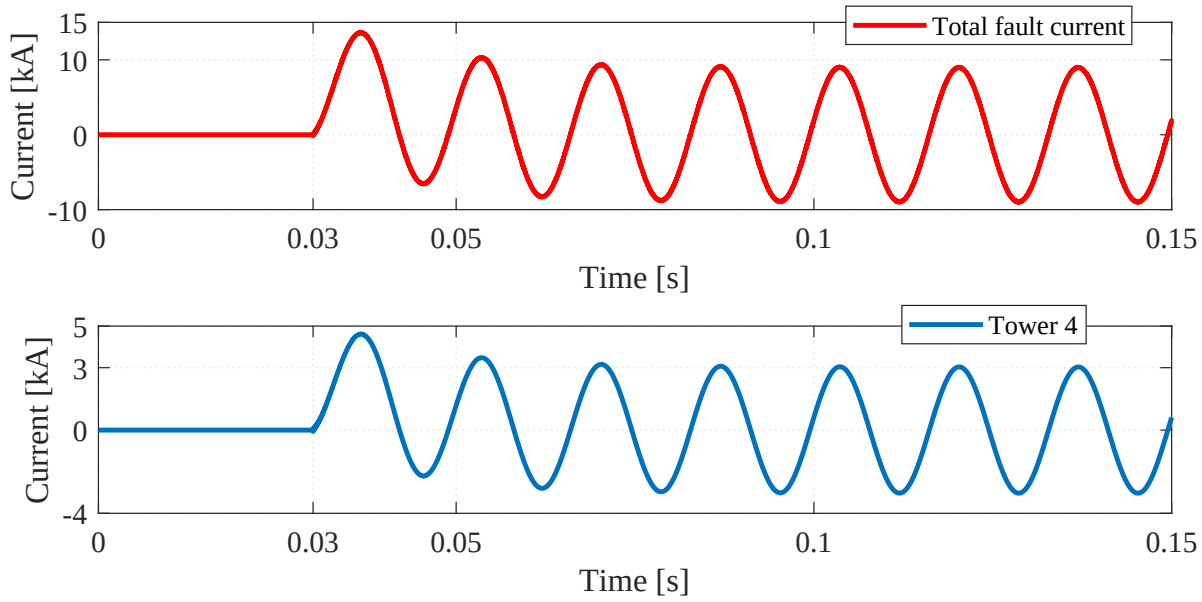

Source: own authorship.

Figure 4.39 shows the currents returning from the fault branch to the terminal substations through the shield wires.

Figure 4.39. Currents returning from the fault branch through the shield wires to Terminals A and B. Maximum absolute values are, respectively, 5.1 kA and 3.93 kA. Steady-state values are 3.41 kA and 2.56 kA.

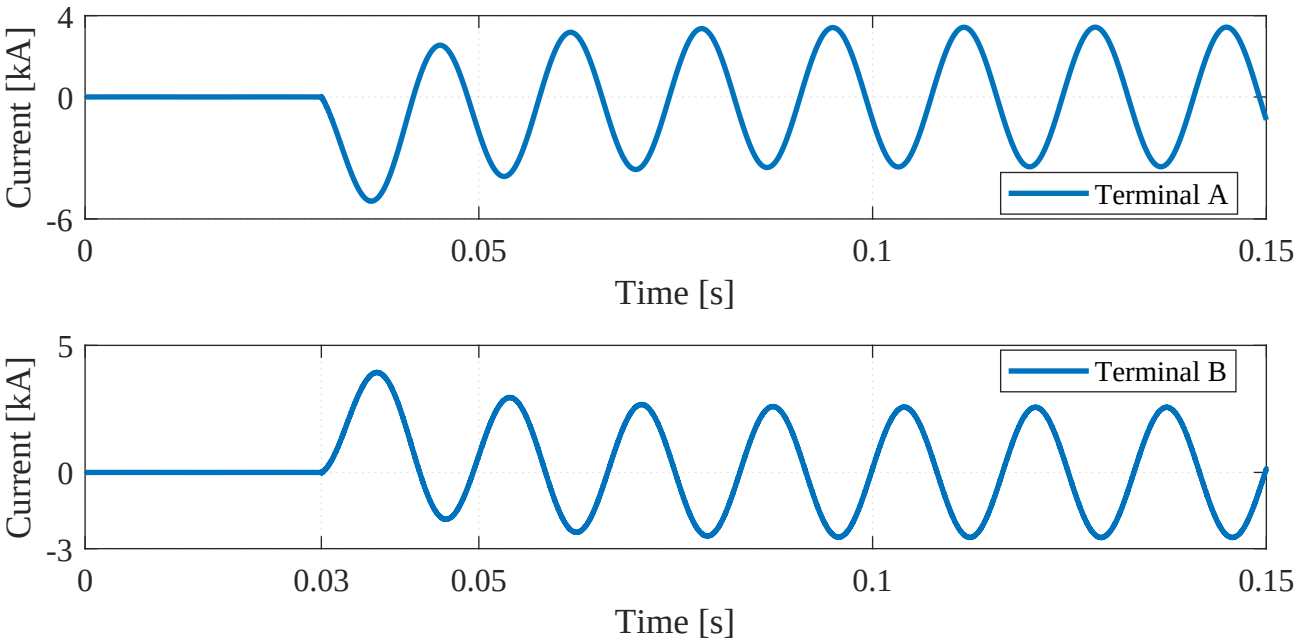

Source: own authorship.

Despite the fact that the fault occurs approximately at the center of the transmission line, there is a clear unbalance between the current components returning to each terminal through the shield conductors. This is explained by the larger grounding resistances at the towers located after the fault point, as Table 4.17 shows. This effect can also be observed in Figure 4.40, which summarizes the ground currents distribution along the transmission line.

Figure 4.40. Currents discharged into the soil through the grounding conductors. Terminal substations are represented by A and B. Towers inside the EMI zone are numbered from 1 to 7.

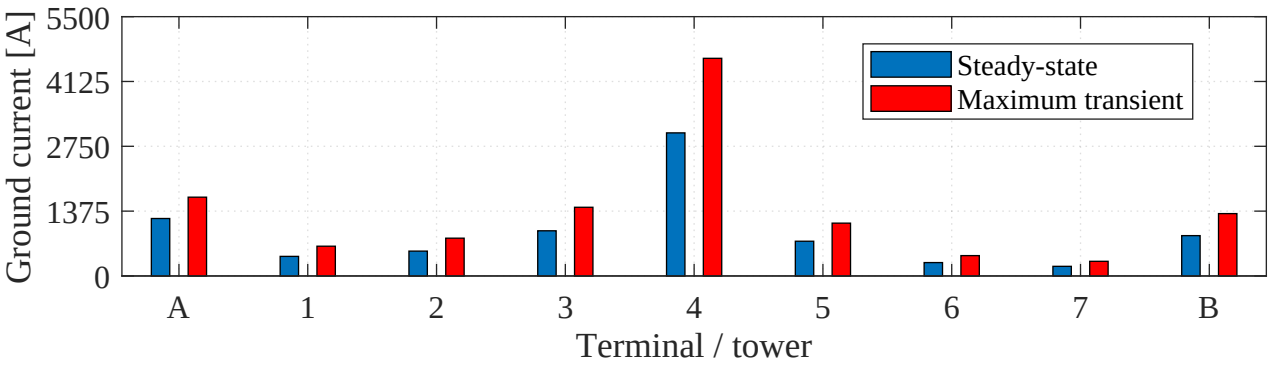

Source: own authorship.

Phase and shield wire currents (Figures 4.37 and 4.39) cause a potential rise in the pipeline metal due to inductive coupling. Ground currents (Figure 4.40) elevate the soil potential outside the pipeline, which results in the stress voltages shown in Figure 4.41. During the first cycle after the fault occurs, transient currents reach peak amplitudes of the order of 50% higher than the steady-state values, which affects the target pipeline in the form of a maximum stress voltage of 1671 V, as opposed to the steady-state value of 1015 V. This difference could determine the need for mitigation measures, depending on the pipeline characteristics and equipment present in the its vicinities.

Figure 4.41. Pipeline potentials, GPR and stress voltages along the interfered pipeline. Maximum stress voltages of 1671 V (transient) and 1015 V (steady-state) occur at the crossing point (811 m along the target pipeline).

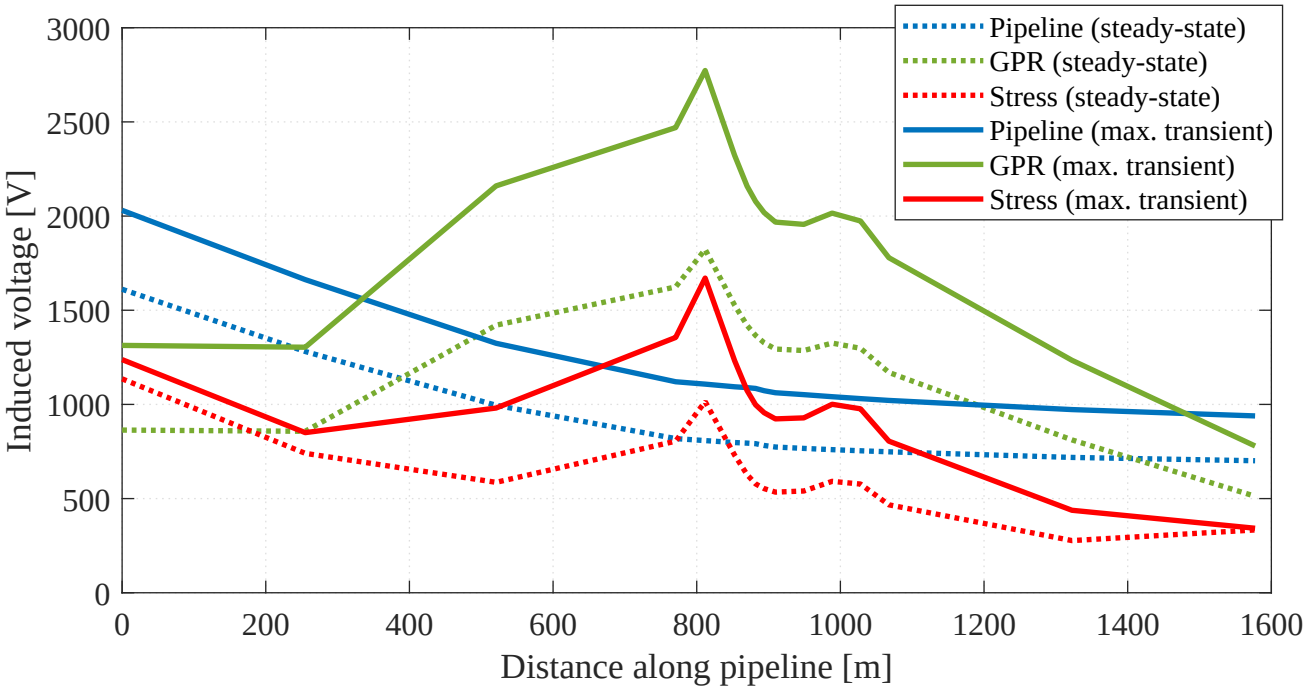

Source: own authorship.

It is relevant to observe that soil potentials reach significant values, but due to the simultaneous rise of the pipeline potentials, the resulting stress is reduced. This effect can be observed by analyzing the time-domain potentials at a fixed observation point. Figure 4.42 presents the evolution of voltages over time at the pipeline section closest to the crossing point, which is the point where the maximum stress voltages in Figure 4.41 occur. It can be clearly seen that the pipeline potential and GPR waveforms follow the behavior of currents in the phases and grounding conductors, which is expected, due to the linear dependency with the source current, expressed in the equations that describe the inductive and conductive coupling mechanisms,

respectively, (2.10) and (2.36). This reinforces the consistency with the theoretical foundations and, therefore, the reliability of the proposed modeling approach.

Figure 4.42. Pipeline potentials, GPR and stress voltages at the crossing point (811 m along the target pipeline).

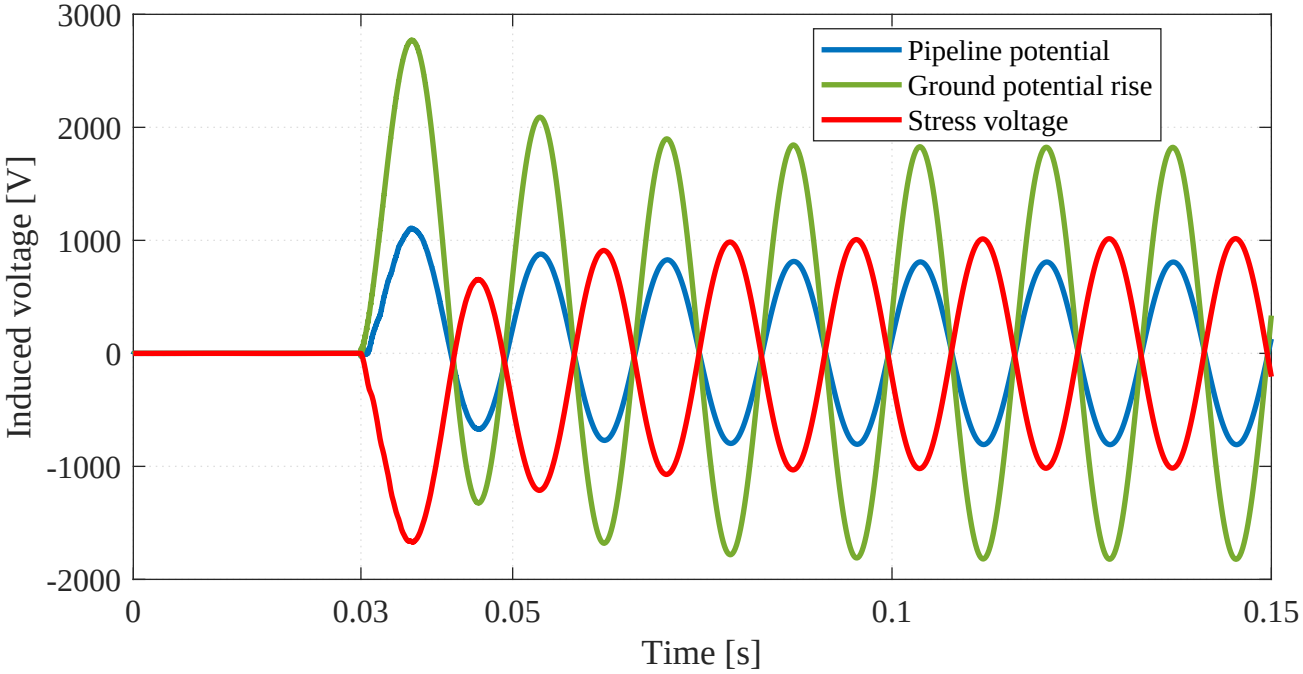

Source: own authorship.

Other types of faults may be evaluated using the proposed circuit model, by appropriately setting the time-controlled switch in Figure 4.35. Figures 4.43 and 4.44 contain the potentials distribution along the pipeline in the events of, respectively, double-phase-to-ground (ABG) and three-phase-to-ground faults (ABCG). Faults are assumed to occur at the same location as in the previous simulation, i.e., Tower 4.

Results may seem unintuitive at first. It is a well known fact that double and three-phase fault types result in larger current magnitudes flowing through the phase conductors, therefore causing more severe impacts on the power system (KHANDELWAL, 2016). On the other hand, Figures 4.43 and 4.44 indicate that the exposed pipeline induced voltages are reduced, as more phases are considered in the fault analysis.

What the simulations demonstrate is that with more phases involved, there is a canceling effect at the fault point, resulting in less current returning through the shield wires, which reduces the electromagnetically induced voltages in the pipeline metal. With the reduction in the shield wire currents, lower current magnitudes are discharged into the earth as well,

decreasing the ground potential rise due to conductive coupling. This behavior is observed in both cases shown in Figures 4.43 and 4.44.

Figure 4.43. Pipeline potentials, GPR and stress voltages along the interfered pipeline for a double-phase-to-ground (ABG) fault.

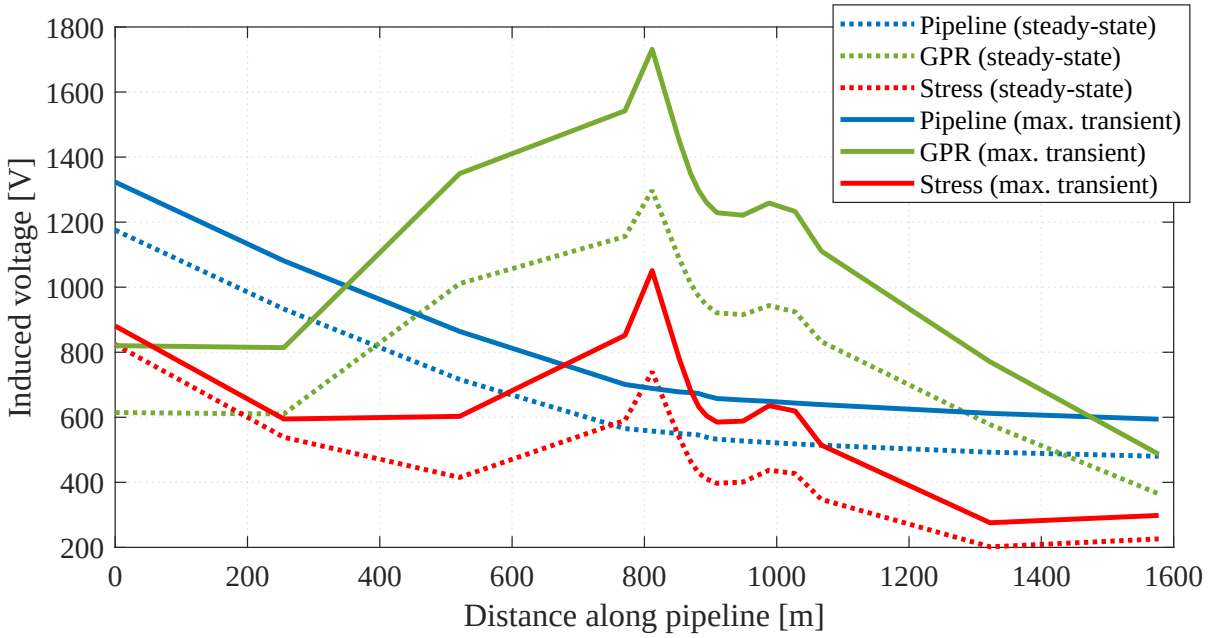

Source: own authorship.

Figure 4.44. Pipeline potentials, GPR and stress voltages along the interfered pipeline for a thee-phase-to-ground (ABCG) fault.

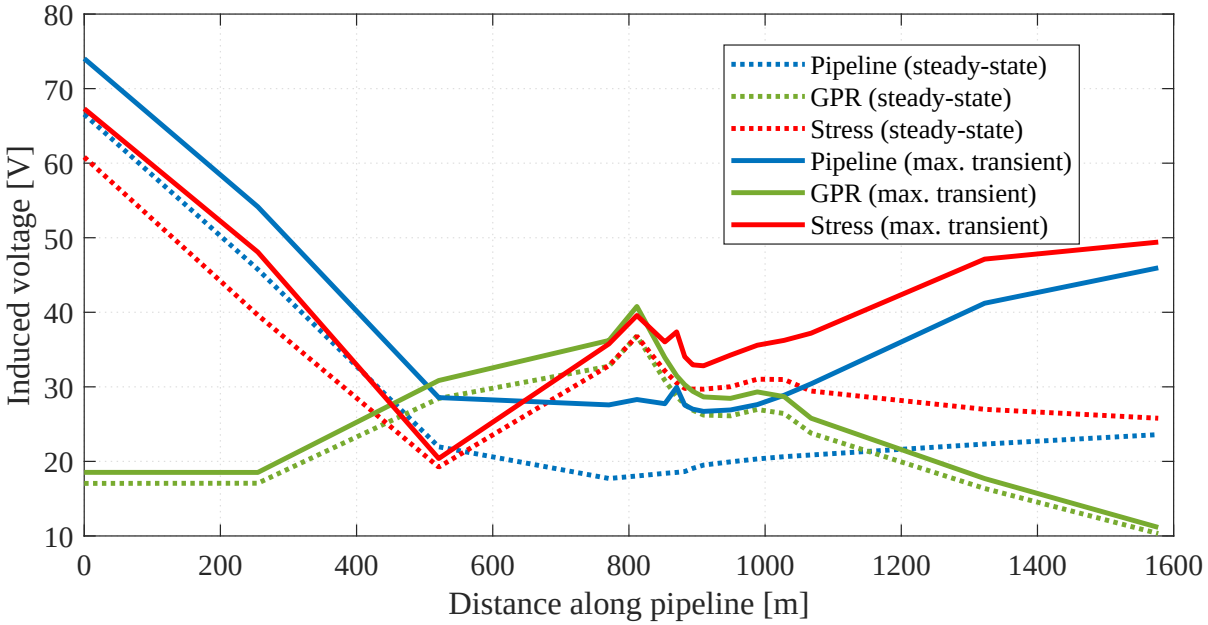

Source: own authorship.

From the discussion, one important observation is that single-phase-to-ground faults not only occur most frequently, but also correspond to the worst-case scenario when the safety of the interfered system is concerned, despite the fact of being the least severe type of fault from the perspective of the power system (KHANDELWAL, 2016; PRASAD *et al.*, 2018). This happens because of the highest unbalance condition between the phase and shield wire currents, which increases both the inductive and conductive voltage components in the target line. This justifies a common practice among engineers in charge of such interference studies, which is to work with single-phase-to-ground faults only (CIGRÉ WG-36.02, 1995).

One last test is performed in order to illustrate how the modeling paradigm affects the transmission line response. The system shown in Figure 4.35 takes into account significant aspects present in practical situations, in special the existence of an interfered conductor and the variations of the soil resistivity along the transmission line route.

Figure 4.45 shows the currents flowing through the faulted phase, considering the single-phase-to-ground case, when these characteristics are ignored, i.e., the interfered pipeline is removed and the soil is accounted as a uniform medium represented by the average apparent resistivity. Discrepancies between models become even more evident when ground currents at the fault location (Tower 4) are observed, as presented in Figure 4.46.

Figure 4.45. Fault currents flowing from Terminal A comparing the realistic model with the case where interferences and soil resistivity variations are ignored. Maximum discrepancy between results is 898 A.

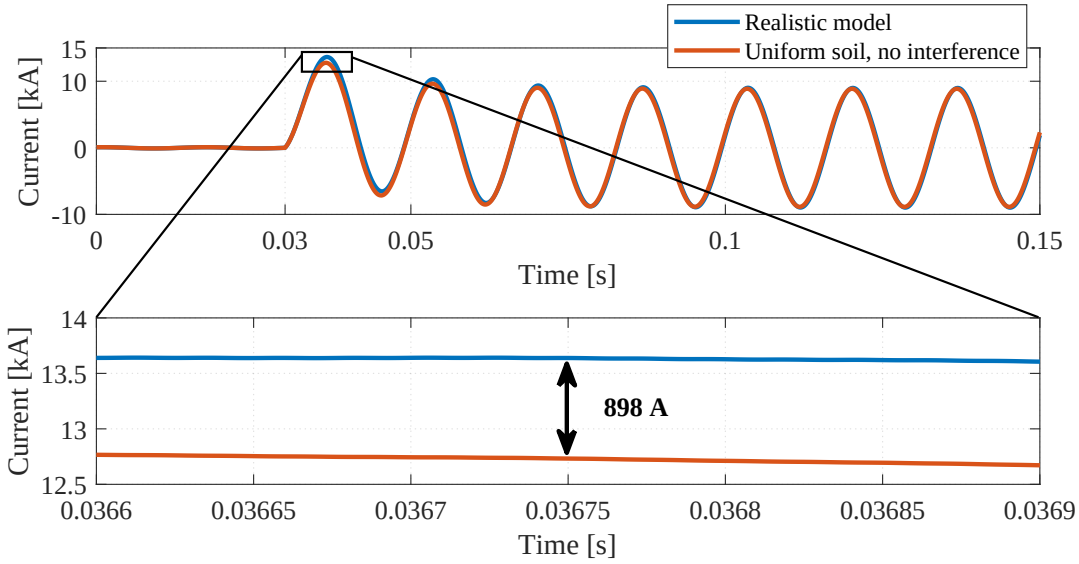

Source: own authorship.

Figure 4.46. Fault currents through the faulted tower grounding comparing the realistic model with the case where interferences and soil resistivity variations are ignored. Maximum discrepancy between both models is 2836 A.

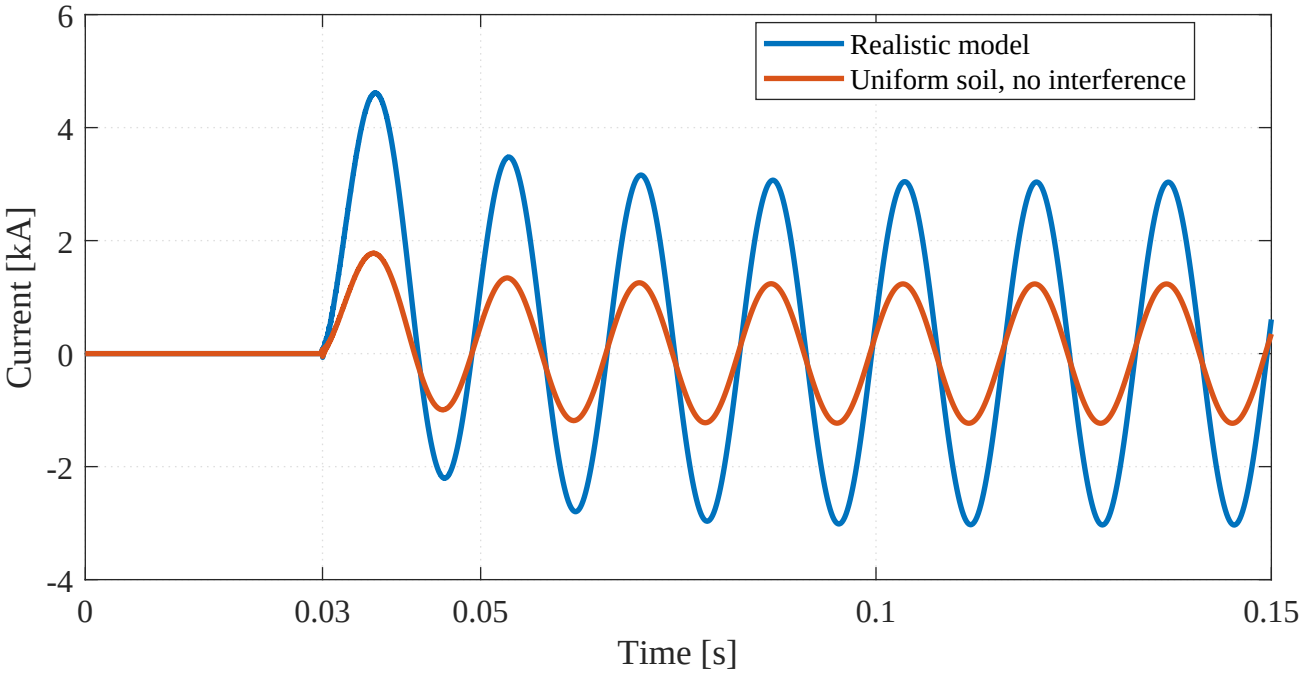

Source: own authorship.

These results emphasize the relevance of employing accurate simulation methods based on consistent field data when carrying out studies involving power lines. The verified discrepancies are sufficient to impact the performance of protective devices, as well as mitigation designs related to touch and step voltages.

Besides, it should be noticed that the case at hand consists of a relatively small system, with only 3.5 km extension. For larger transmission lines, with lengths of the order of hundreds of kilometers, more soil variations are likely to occur, and the influence of the interfered conductor on the transmission line impedances is expected to become more pronounced.

On a final note related to computational performance, the ATP model discussed in this section, composed of 3.5 km of transmission line conductors, 1.5 km of pipelines and seven towers explicitly modeled, required 6 seconds to run in the same computer that took 5 days to execute the FDTD model described in Section 3.3.3, with satisfactory agreement between both models.

4.5 CHAPTER SUMMARY

The present chapter described an ATP-based implementation destined to run realistic EMI simulations of arbitrary systems, both in steady-state and transient conditions.

A review of the classic interference circuit model was performed, as well as the time-domain behavior of the basic components necessary to build the equivalent circuit representative of the inductive, capacitive and conductive coupling mechanisms between power lines and interfered conductors.

In order to introduce the multilayered property of real soils into the native ATP routines that handle ground return impedances, a uniform equivalent resistivity formula was proposed and validated. Tests were performed on twenty soil models based on real measurements, from 2 to 6 layers, with computations of the mutual impedances between two overhead conductors over the frequency range between 1 Hz to 2 MHz. Approximation errors are of the order of 1% at power system frequencies to the kHz band, proving the uniform equivalent approach to be accurate for steady-state conditions and surges commonly verified in electrical systems. By means of a relatively simple equivalence formula, complex soil structures are introduced into practical applications using tools already available, tested and well-documented.

With the necessary methods and supporting routines available, additional case studies were executed. First, an imperfect parallel approximation between an electric traction line and a pipeline was analyzed to evaluate the viability of using ATP as an EMI simulation tool. Then, an interference study based on real design data involving an 88 kV distribution line and a gas pipeline was performed. Induced voltages agreed with the reference steady-state values, with the advantage that it was possible to observe important transient effects, not only in the target line, but also on how the presence of an interfered conductor and soil variations affect the transmission line currents.

Finally, the proposed circuit model allows the execution of sophisticated simulations, involving the three relevant coupling mechanisms (inductive, capacitive, conductive), in which heterogeneities are handled with excellent accuracy for all practical purposes, with a remarkable performance gain. This may not only benefit the user interested in EMI analysis, but also opens a wide range of possibilities related to EMTP studies involving power lines.

CHAPTER 5

CONCLUSIONS AND FUTURE WORK

This thesis described the problem of the mutual electromagnetic interferences between power lines and neighboring metallic facilities: the causes, underlying mechanisms, relevant parameters and impacts on the affected systems, with emphasis on safety aspects.

Two complete sets of tools, based on distinct approaches, were developed and validated, with the purpose of enabling the user to perform advanced time-domain simulations of interference scenarios involving: (a) power systems comprised of arbitrary numbers of phases, energization sources, shield wires and interfered conductors; (b) complex interference approximations; (c) multilayered soil structures; (d) changes in geometry and soil conditions along the lines; (e) explicit modeling of shield wires and grounding structures; (f) simultaneous evaluation of inductive, capacitive and conductive coupling effects; (g) material heterogeneities; and (h) power system frequencies to very fast transients, such as lightning discharges.

First, a general-purpose FDTD code was developed to carry out investigations of transient electromagnetic interferences on relatively small domains, but with augmented levels of detail, accounting for arbitrary combinations of different materials, and covering the high-frequency spectrum. This provided a clear perspective of how effective the tools and techniques based on the electromagnetic theory can be when applied to power system transients, especially those related to lightning phenomena and electrical grounding. However, due to its intrinsically heavy computational load, which requires very long simulation times, the FDTD method was considered impracticable to be adopted as a systematic solution to work with interference studies involving practical cases, where real installations may extend for several kilometers.

Motivated by these performance concerns, a circuit-based model using the Alternative Transients Program (ATP) was proposed for simulations of large scale systems, horizontally multilayered soil models and frequencies up to the kHz band.

One particularly challenging aspect of the ATP implementation was the introduction of

N-layered soils into its native Line/Cable Constants routine, which is responsible for calculating ground return impedances. To accomplish this task, a new uniform equivalent resistivity formula was proposed and tested, having provided accurate results for steady-state regimes and lower frequency surges commonly verified in power systems, with errors inferior to 1% and a performance gain of 98%, depending on the application.

Simulations were carried out in steady-state conditions, as well as transients due to line energization and phase-to-ground faults. Not only the proposed models were proven valid by comparisons with reports in the literature and results from state-of-the-art software, but also an important progress was achieved: it became possible to obtain the transient response of the interfered systems using a circuit model, as opposed to common approaches that only handle the phasor solution. Indeed, results showed that even though the steady-state response may point to conformity to safety criteria, the target system may still be exposed to potentially harmful transient voltages and currents.

Having executed both the source and the target systems in the same simulation instance provided a fundamental insight on how the modeling procedure affects the transmission line response, especially regarding the presence of external conductors in the vicinities of the phase conductors, soil resistivity variations and multiple connections between the shield wires to the ground, factors that greatly influenced the current distribution in the power line under fault conditions. This reinforces the idea that relying on unrealistic premises when carrying out studies involving transmission line parameters may lead to significant errors.

The proposed methods proved viable to perform complex EMI simulations between transmission lines and arbitrary metallic structures, in which inductive, capacitive and conductive coupling mechanisms on multilayered soil structures are modeled with improved accuracy and remarkable computational performance.

It should be noted, however, that, despite the considerable performance improvement, the proposed time-domain circuit model discussed in this thesis does not invalidate or diminish whatsoever the previous efforts invested to develop the simulation model based on the FDTD method. Both techniques, each one with its own advantages and limitations, are complimentary, such that the long term continuity of this work points towards the construction of a hybrid scheme, in which the ATP circuit model is employed to obtain the macro response of the larger

portions of the transmission system, such as the current distribution along shield wires and grounding conductors, which then, by using lumped components as suggested in Appendix B, Section B.3, are supplied as input parameters to the FDTD model, focusing at regions in the 3D space where increased levels of detail are necessary. This will allow the execution of very sophisticated simulations, giving the user access to the spatial distribution of the transient induced voltages and currents, touch and step voltages, electromagnetic shielding effects etc., which is expected to greatly assist in the development of EMI mitigation designs.

Finally, the proposed circuit model may benefit from several enhancements, to be addressed by the author in the near future:

- Improvement of the subdivision scheme of the source and target lines to increase the accuracy of the inductive coupling model;
- Modifications on the equivalent resistivity model, by using nonlinear fitting techniques, to achieve improved accuracy at high frequencies and for soils with high contrast ratios;
- Replacement of the standard Line/Cable Constants ATP routine by a true multilayered version, using the methods given in Section 2.6, allowing for the simulation of high-frequency phenomena up to 2 MHz;
- Inclusion of underground transmission line models;
- Reformulation of the electrical grounding models, to eliminate the equipotential assumption and include the ohmic losses along grounding conductors, allowing the simulation of large grounding grids with greater accuracy;
- Development of a friendly interface, preferably integrated to the ATPDraw software and using MODELS language, to aid in the construction of complex systems using the proposed circuit models, with a minimum programming effort;
- Validation of the proposed simulation techniques by comparison with real field measurements or tests using scale models;
- Additional application studies related to the effects of the interfered structure and soil variations on the transmission line transients and impacts on protection, fault location algorithms etc.

REFERENCES

AARTS, R. M.; JANSSEN, A. J. E. M. Approximation of the Struve Function H1 Occurring in Impedance Calculations. *The Journal of the Acoustical Society of America*, v. 113, n. 5, p. 2635–2637, 2003. ISSN 00014966. Retrieved from: <http://scitation.aip.org/content/asa/journal/jasa/113/5/10.1121/1.1564019>. Cited in page 18.

ABNT. *NBR 15751 - Sistemas de Aterramento de Subestações - Requisitos*. 2009. 1–53 p. Cited 2 times in pages 37 and 39.

ABNT. *NBR 7117 - Medição da Resistividade e Determinação da Estratificação do Solo*. 2012. 1–72 p. Cited 4 times in pages 9, 10, 11, and 12.

ABRAMOWITZ, M.; STEGUN, I. *Handbook of Mathematical Functions: with Formulas, Graphs, and Mathematical Tables*. 9 revised. ed. Dover Publications, 1965. 1046 p. ISSN 1421-9875. ISBN 0486612724. Retrieved from: <http://www.ncbi.nlm.nih.gov/pubmed/22230940https://www.karger.com/Article/FullText/324520>. Cited in page 18.

ALAMO, J. del. A Comparison Among Eight Different Techniques to Achieve an Optimum Estimation of Electrical Grounding Parameters in Two-Layered Earth. *IEEE Transactions on Power Delivery*, v. 8, n. 4, p. 1890–1899, 1993. Cited in page 14.

AMETANI, A.; MIYAMOTO, Y.; ASADA, T.; BABA, Y.; NAGAOKA, N.; LAFAIA, I.; MAHSEREDJIAN, J.; TANABE, K. A Study on High-Frequency Wave Propagation along Overhead Conductors by Earth-Return Admittance / Impedance and Numerical Electromagnetic Analysis. In: *Proc. IPST 2015*. Cavtat, Croatia: [s.n.], 2015. Cited in page 48.

AMETANI, A.; YONEDA, T.; BABA, Y.; NAGAOKA, N. An Investigation of Earth-Return Impedance Between Overhead and Underground Conductors and Its Approximation. *IEEE Transactions on Electromagnetic Compatibility*, v. 51, n. 3, p. 860–867, 2009. ISSN 0018-9375. Retrieved from: <http://ieeexplore.ieee.org/lpdocs/epic03/wrapper.htm?arnumber=4914803>. Cited 3 times in pages 18, 47, and 79.

ARFKEN, G. B.; WEBER, H. J. *Mathematical Methods for Physicists*. 6. ed. [S.l.]: Elsevier, 2005. 1200 p. ISBN 9780080470696,9780120598762,9780120885848,0080470696,0120598760,0120885840. Cited in page 29.

BARAÚNA, D. M.; LIMA, A. C. S. *Análise da Influência de Linhas de Transmissão Aéreas em Regime Permanente em Tubulações Metálicas Enterradas*. Rio de Janeiro: Universidade Federal do Rio de Janeiro, 2007. 55 p. Cited in page 72.

BARIC, T.; NIKOLOVSKI, S. Influence of Conductor Segmentation in Grounding Resistance Calculation Using Boundary Element Method. *Progress in Electromagnetic Research Symposium*, p. 141–144, 2004. Cited in page 35.

BENSTED, D.; DAWALIBI, F.; WU, A. The Application of Computer Aided Grounding Design Techniques to a Pulp and Paper Mill Grounding System. *IEEE Transactions on Power Apparatus and Systems*, IA-17, n. 1, 1981. Cited in page 34.

BÉRENGER, J.-P. Perfectly Matched Layer (PML) for Computational Electromagnetics. *Synthesis Lectures on Computational Electromagnetics*, v. 2, n. 1, p. 1–117, 2007. Retrieved from: <http://doi.org/10.2200/s00030ed1v01y200605cem008>. Cited in page 152.

BOYCE, W. E.; DIPRIMA, R. C. *Elementary Differential Equations and Boundary Value Problems*. 10th. ed. [S.l.]: John Wiley & Sons, 2012. 833 p. ISBN 0470458313. Cited in page 18.

CARSON, J. R. Wave Propagation in Overhead Wires with Ground Return. *Bell Syst. Tech. J.*, v. 5, p. 539–554, 1926. Cited 5 times in pages 16, 17, 18, 46, and 47.

CAULKER, D.; AHMAD, H.; ALI, M. S. M. Effect of Lightning Induced Voltages on Gas Pipelines using ATP-EMTP Program. In: *2008 IEEE 2nd International Power and Energy Conference*. Johor Bahru, Malaysia: IEEE, 2008. p. 393–398. ISBN 1424424054. Cited in page 72.

CENELEC. *EN 50443-2011 - Effects of Electromagnetic Interference on Pipelines Caused by High Voltage AC Electric Traction Systems and/or High Voltage AC Power Supply Systems*. 2011. 1–32 p. Cited in page 38.

CHEN, J.; ZHAO, F.; ZHOU, S.; TIAN, H. FDTD Simulation of Lightning Current along Vertical Grounding Rod Appended to a Horizontal Grounding grid. In: . [S.l.: s.n.], 2010. p. 1478–1481. ISBN 9781424456239. Cited 5 times in pages 48, 53, 54, 55, and 57.

CHOW, Y. L.; YANG, J. J.; HOWARD, G. E. Complex Images for Electrostatic Field Computation in Multilayered Media. *IEEE Transactions on Microwave Theory and Techniques*, v. 39, n. 7, p. 1120–1125, 1991. ISSN 15579670. Cited in page 79.

CHRISTOFORIDIS, G. C.; LABRIDIS, D. P.; DOKOPOULOS, P. S. Inductive interference calculation on imperfect coated pipelines due to nearby faulted parallel transmission lines. *Electric Power Systems Research*, v. 66, n. 2, p. 139–148, 2003. ISSN 03787796. Cited in page 1.

CHRISTOFORIDIS, G. C.; LABRIDIS, D. P.; DOKOPOULOS, P. S. Inductive Interference Calculation on Imperfect Coated Pipelines Due to Nearby Faulted Parallel Transmission Lines. *Electric Power Systems Research*, v. 66, p. 139–148, 2003. ISSN 03787796. Cited in page 48.

CIGRÉ WG-36.02. *Technical Brochure n. 95 - Guide on the Influence of High Voltage AC Power Systems on Metallic Pipelines*. Paris: CIGRÉ, 1995. 1–135 p. Cited 18 times in pages 1, 2, 8, 14, 15, 16, 18, 21, 22, 23, 24, 29, 47, 69, 70, 71, 89, and 117.

COURANT, R.; FRIEDRICHS, K.; LEWY, H. On the Partial Difference Equations of Mathematical Physics. *IBM Journal of Research and Development*, v. 11, n. 2, p. 215—-234, 1967. Retrieved from: <http://doi.org/10.1147/rd.112.0215>. Cited in page 144.

COUSIN, I.; TABBAGH, A.; BRUAND, A.; RICHARD, G.; SAMOUE, A. Electrical Resistivity Survey in Soil Science: a Review. *Soil & Tillage Research*, v. 83, p. 173–193, 2005. Cited in page 78.

CROZIER, R.; MUELLER, M. A New MATLAB and Octave Interface to a Popular Magnetics Finite Element Code. In: *2016 XXII International Conference on Electrical Machines (ICEM)*. Lausanne, Switzerland: IEEE, 2016. p. 1251–1256. Retrieved from: <https://ieeexplore.ieee.org/document/7732685>. Cited 2 times in pages 93 and 97.

DABKOWSKI, J. I. R. I.; TAFLOVE, A. *Mutual Design Considerations for Overhead AC Transmission Lines and Gas Transmission Pipelines Volume 1: Engineering Analysis*. 1978. 1–511 p. Cited 3 times in pages 2, 23, and 46.

DABKOWSKI, J. I. R. I.; TAFLOVE, A. *Mutual Design Considerations for Overhead AC Transmission Lines And Gas Transmission Pipelines Volume 2: Prediction and Mitigation Procedures*. 1978. 1–186 p. Cited 2 times in pages 2 and 46.

DACONTI, J. R.; BRASIL, D. O. C. Experience of Chesf Concerning Interferences Between EHV Transmission Lines and Pipelines. In: *International Conference on Large High Voltage Electric Systems - Cigré*. Paris: CIGRÉ, 1986. Cited in page 1.

DALZIEL, C. F.; LEE, W. R. Reevaluation of Lethal Electric Currents. *IEEE Transactions on Industry and General Applications*, IGA-4, n. 5, p. 467–476, 1968. ISSN 0018943X. Cited in page 38.

DAS, S.; SANTOSO, S.; GAIKWAD, A.; PATEL, M. Impedance-based Fault Location in Transmission Networks: Theory and Application. *IEEE Access*, v. 2, p. 537–557, 2014. ISSN 21693536. Cited 3 times in pages 2, 49, and 77.

DAWALIBI, F.; BARBEITO, N. Measurements and computations of the performance of grounding systems buried in multilayer soils. *IEEE Transactions on Power Delivery*, v. 6, n. 4, p. 1483–1490, 1991. ISSN 19374208. Cited 3 times in pages 47, 79, and 83.

DAWALIBI, F.; BLATTNER, C. Earth Resistivity Measurement Interpretation Techniques. *IEEE Transactions on Power Apparatus and Systems*, PAS-103, n. 2, p. 374–382, 1984. ISSN 0018-9510. Retrieved from: <http://ieeexplore.ieee.org/lpdocs/epic03/wrapper.htm?arnumber=4112522>. Cited in page 14.

DAWALIBI, F.; MUKHEDKAR, D. Optimum Design of Substation Grounding in a Two Layer Earth Structure: Part II - Comparaison Between Theorical and Experimental Results. *Power Apparatus and Systems, IEEE Transactions on*, v. 94, n. 2, p. 252–261, 1975. ISSN 0018-9510. Cited in page 47.

DAWALIBI, F.; MUKHEDKAR, D. Optimum Design of Substation Grounding in a Two Layer Earth Structure: Part III - Study of Grounding Grids Performance and New Electrode Configuration. *IEEE Transactions on Power Apparatus and Systems*, n. 2, 1975. Cited 3 times in pages 30, 34, and 47.

DAWALIBI, F.; MUKHEDKAR, D.; BENSTED, D. Measured and Computed Current Densities in Buried Ground Conductors. *IEEE Transactions on Power Delivery*, PAS-100, n. 8, p. 4083–4092, 1981. Cited in page 35.

DAWALIBI, F. P. Modern Computational Methods for the Design and Analysis of Power System Grounding. In: *International Conference on Power System Technology*. Beijing: [s.n.], 1998. p. 122–126. ISBN 0780347544. Cited 2 times in pages 93 and 97.

DAWALIBI, F. P.; DONOSO, F. Integrated Analysis Software for Grounding, EMF, and EMI. *IEEE Computer Applications in Power*, v. 6, n. 2, p. 19–24, 1993. Retrieved from: <https://ieeexplore.ieee.org/document/207467>. Cited 3 times in pages 47, 72, and 139.

DAWALIBI, F. P.; MA, J.; SOUTHEY, R. D. Behaviour of grounding systems in multilayer soils: A parametric analysis. *IEEE Transactions on Power Delivery*, v. 9, n. 1, p. 334–342, 1994. ISSN 19374208. Cited in page 47.

DAWALIBI, F. P.; MUKHEDKAR, D. Optimum Design of Substation Grounding in a Two Layer Earth Structure Part I - Analytical Study. *IEEE Transactions on Power Apparatus and Systems*, PAS-94, n. 2, p. 252–261, 1975. Cited in page 47.

DAWALIBI, F. P.; SOUTHEY, R. D.; MALRIC, Y.; TAVCAR, W. *Power Line Fault Current Coupling to Nearby Natural Gas Pipelines: Volume 1, Analytic Methods and Graphical Techniques: Final report. EPRI-EL-5472-Vol.1. [Electromagnetic and Conductive Coupling Analysis of Powerlines and Pipelines (ECCAPP)]*. United States: [s.n.], 1987. Cited 5 times in pages 46, 69, 71, 72, and 89.

DERI, A.; TEVAN, G.; SEMLYEN, A.; CASTANHEIRA, A. The Complex Ground Return Plane a Simplified Model for Homogeneous and Multi-Layer Earth Return. *IEEE Transactions on Power Apparatus and Systems*, PAS-100, n. 8, p. 3686–3693, aug 1981. ISSN 0018-9510. Retrieved from: <http://ieeexplore.ieee.org/document/4111058/>. Cited 4 times in pages 18, 47, 79, and 97.

DOMMEL, H. W. *EMTP Theory Book*. [S.l.]: Microtran Power System Analysis Corporation, 1996. Cited 5 times in pages 43, 45, 46, 74, and 153.

DOMMEL, W. H. Digital Computer Solution of Electromagnetic Transients in Single- and Multiphase Networks. *IEEE Transactions on Power Apparatus and Systems*, n. 4, p. 388–399, 1969. Cited 2 times in pages 141 and 153.

DWIGHT, H. B. Calculation of Resistances To Ground. *Transactions of the American Institute of Electrical Engineers*, v. 55, n. 12, p. 1319–1328, 1983. ISSN 00941492. Cited in page 47.

ELKATEB, T.; CHALATURNYK, R.; ROBERTSON, P. K. An Overview of Soil Heterogeneity: Quantification and Implications on Geotechnical Field Problems. *Canadian Geotechnical Journal*, v. 40, p. 1–15, 2003. Cited in page 9.

ELSHERBENI, A.; DEMIR, V. *The Finite-Difference Time-Domain Method for Electromagnetics with MATLAB® Simulations*. 2nd. ed. [S.l.]: SciTech Publishing, 2015. ISBN 9781891121715. Cited 4 times in pages 52, 140, 142, and 150.

FRAIJI, T. K.; BASTOS, J. P. A. *Interferência Eletromagnética entre Linhas de Transmissão e Dutos, Utilizando o ATP - Uma Análise da LT 525 kV Campos Novos - Blumenau*. Florianópolis: Universidade Federal de Santa Catarina, 2007. 88 p. Cited in page 72.

FURLAN, A. G. L. *Estudo de Interferências Eletromagnéticas entre Linhas de Transmissão e Dutos Enterrados*. 1–132 p. Tese (Dissertação (Mestrado)) — Universidade Federal de Santa Catarina, 2015. Cited 7 times in pages 16, 27, 28, 48, 71, 81, and 95.

FURLAN, A. G. L.; MARTINS-BRITTO, A. G.; KUO-PENG, P.; LUZ, M. V. F. Cálculo da Interferência Indutiva entre Linhas de Transmissão e Dutos Utilizando Método dos Elementos Finitos e Analíticos. In: *COTEQ2015-156*. Cabo de Santo Agostinho / PE: ABENDI, ABRACO, ABCM e IBP, 2015. p. 1–7. Cited in page 85.

GÜEMES, J. A.; HERNANDO, F. E. Method for calculating the ground resistance of grounding grids using FEM. *IEEE Transactions on Power Delivery*, v. 19, n. 2, p. 595–600, 2004. ISSN 08858977. Cited in page 48.

HADDAD, A.; WARNE, D. *Advances in High Voltage Engineering*. [S.l.]: The Institte of Electrical and Electronics Engineers, Inc., 2009. 669 p. ISBN 1849190380,9781849190381,0852961588,9780852961582. Cited in page 8.

HAGINOMORI, E.; KOSHIDUKA, T.; ARAI, J.; IKEDA, H. *Power System Transient Analysis - Theory and Practice Using Simulation Programs (ATP-EMTP)*. 1. ed. [S.l.]: John Wiley & Sons Inc., 2016. 281 p. ISBN 9781118737538. Cited in page 153.

HE, J.; ZENG, R.; ZHANG, B. *Methodology and Technology for Power System Grounding*. Singapore: John Wiley & Sons Singapore Pte. Ltd., 2013. 1–566 p. ISBN 9781118255001. Retrieved from: <http://doi.wiley.com/10.1002/9781118255001>. Cited 13 times in pages 2, 8, 10, 13, 28, 29, 32, 33, 35, 47, 79, 81, and 136.

HEPPE, R. Computation of Potential at Surface Above an Energized Grid or Other Electrode, Allowing for Non-Uniform Current Distribution. *IEEE Transactions on Power Apparatus and Systems*, PAS-98, n. 6, p. 1978–1989, 1979. ISSN 0018-9510. Retrieved from: <http://ieeexplore.ieee.org/lpdocs/epic03/wrapper.htm?arnumber=4113714>. Cited in page 46.

IEC. *Publication 60479-1 - Effects of Current Passing Through the Human Body*. 1984. Cited in page 37.

IEC. *Publication 61312-1: Protection against lightning electromagnetic impulse - Part 1: General principles*. 1995. Cited in page 51.

IEEE. *Guide for Measuring Earth Resistivity, Ground Impedance, and Earth Surface Potentials of a Ground System*. New York, NY: The Institte of Electrical and Electronics Engineers, Inc., 1984. 54 p. Cited in page 79.

IEEE. *Guide for Safety In AC Substation Grounding*. The Institte of Electrical and Electronics Engineers, Inc., 2000. 202 p. Retrieved from: <https://ieeexplore.ieee.org/servlet/opac?punumber=7109076>. Cited 11 times in pages 9, 12, 13, 37, 38, 39, 47, 52, 57, 82, and 92.

International Telecommunication Union. *Directives Concerning the Protection of Telecommunication Lines Against Harmful Effects from Electric Power and Electrified Railway Lines*. Geneva: [s.n.], 1989. Cited in page 70.

ISERHIEN-EMEKEME, R. E. Electrical Resistivity Survey for Predicting Aquifer at Onicha-Ugbo, Delta State, Nigeria. *Journal of Applied Mathematics and Physics*, v. 02, n. 07, p. 520–527, 2014. ISSN 2327-4352. Retrieved from: <http://www.scirp.org/journal/doi.aspx?DOI=10.4236/jamp.2014.27060>. Cited in page 83.

KHANDELWAL, M. A Review on Transmission Line Faults Detection. *International Journal of Electrical Engineering & Technology (IJEET)*, v. 7, n. 2, p. 50–58, 2016. Cited 2 times in pages 115 and 117.

KINDERMANN, G.; CAMPAGNOLO, J. M. *Aterramento Elétrico*. 3ª. ed. Porto Alegre / RS: [s.n.], 1995. 1–113 p. Cited in page 82.

KUROKAWA, S.; DALTIN, R. S.; PRADO, A. J. do; BOVOLATO, L. F.; PISSOLATO, J. Decomposição modal de linhas de transmissão a partir do uso de duas matrizes de transformação. *SBA: Controle & Automação Sociedade Brasileira de Automática*, v. 18, n. 3, p. 372–380, 2007. ISSN 01031759. Cited in page 46.

LEE, J.-b.; ZOU, J.; LI, B.; JU, M. Efficient Evaluation of the Earth Return Mutual Impedance of Overhead Conductors Over a Horizontally Multilayered Soil. *COMPEL: The International Journal for Computation and Mathematics in Electrical and Electronic Engineering*, v. 33, n. 4, p. 1379–1395, 2013. Cited 3 times in pages 47, 78, and 79.

LI, Y. *Materials for Modern Technologies: Selected, peer reviewed papers from the 2015 Spring International Conference on Material Sciences and Technology (MST-S), April 14-16, 2015, Beijing, China*. [S.l.]: Trans Tech Publications, 2015. 168 p. ISBN 3038354635,9783038354635. Cited in page 40.

LI, Z.-x.; FAN, J.-b.; CHEN, W.-j. Numerical Simulation of Substation Grounding Grids Buried in both Horizontal and Vertical Multilayer Earth Model. *International Journal for Numerical Methods in Engineering*, v. 69, n. August 2006, p. 2359–2380, 2007. Cited 2 times in pages 32 and 47.

LOVELOCK, D.; RUND, H. *Tensors, Differential Forms, and Variational Principles*. New York, NY: Dover Publications, 1989. 381 p. ISBN 0486658406. Cited in page 33.

LUCCA, G. Mutual Impedance between an Overhead and a Buried Line with Earth Return. In: *Proc. Int. Electr. Eng. 9th Int. Conf. EMC*. [S.l.: s.n.], 1994. p. 80–86. Cited in page 47.

MARTINEZ-VELASCO, J. A. *Transient Analysis of Power Systems*. [S.l.]: Wiley-IEEE Press, 2015. 648 p. ISBN 9781118352342. Cited in page 89.

MARTINS-BRITTO, A. G. Cálculo de Parâmetros de Linhas Aéreas sob Condições de Interferência e Solo Estratificado: Estudo da Influência sobre Localizadores de Faltas. In: *XI CBQEE - Conferência Brasileira de Qualidade de Energia Elétrica*. Curitiba / PR: SBQEE, 2017. Cited in page 40.

MARTINS-BRITTO, A. G. *Modeling of the Electromagnetic Interferences between Power Lines and Underground Metallic Pipelines and Impact Analysis*. 121 p. Tese (Master's Thesis) — University of Brasília, 2017. Cited 13 times in pages vii, 2, 8, 14, 16, 17, 35, 40, 61, 65, 71, 81, and 89.

MARTINS-BRITTO, A. G.; RONDINEAU, S. R. M. J.; LOPES, F. V. Power Line Transient Interferences on a Nearby Pipeline Due to a Lightning Discharge. In: *International Conference on Power Systems Transients (IPST 2019)*. Perpignan, France: IEEE Xplore, 2019. p. 6. Cited in page 57.

MILESEVIC, B.; FILIPOVIC-GRCIC, B.; RADOSEVIC, T. Analysis of Low Frequency Electromagnetic Fields and Calculation of Induced Voltages to an Underground Pipeline. In: *Proceedings of the 2011 3rd International Youth Conference on Energetics (IYCE)*. Leiria, Portugal: IEEE, 2011. p. 1–7. Cited 2 times in pages 72 and 99.

MOMBELLO, E.; TRAD, O.; RIVERA, J.; ANDREONI, A. Two-layer soil model for power station grounding system calculation considering multilayer soil stratification. *Electric Power Systems Research*, v. 37, n. 1, p. 67–78, 1996. ISSN 03787796. Cited in page 10.

MORGAN, V. T. The Current Distribution, Resistance and Internal Inductance of Linear Power Systems Conductors - A Review of Explicit Equations. *Transactions on Power Delivery*, v. 28, n. 3, p. 1252–1262, 2013. Cited in page 20.

MUALEM, Y. Anisotropy of Unsaturated Soils. *Soil Science Society of America Journal*, v. 48, n. 3, p. 505, 1984. Retrieved from: <https://doi.org/10.2136/sssaj1984.03615995004800030007x>. Cited in page 9.

MUKHEDKAR, D.; DAWALIBI, F. P. Multi Step Analysis of Interconnected Grounding Electrodes. *IEEE Transactions on Power Apparatus and Systems*, v. 95, n. 1, p. 113–119, 1976. ISSN 00189510. Cited in page 35.

NACE. *SP0177-2007 - Mitigation of Alternating Current and Lightning Effects on Metallic Structures and Corrosion Control Systems*. 2007. 1–25 p. Cited 6 times in pages 8, 38, 40, 49, 52, and 65.

NAGAR, R. P.; VELAZQUEZ, R.; LOELOEIAN, M.; MUKHEDKAR, D.; GERVDIS, Y. Review of Analytical Methods for Calculating the Performance of Large Grounding Electrodes - Part 1: Theoretical Considerations. *IEEE Transactions on Power Apparatus and Systems*, PAS-104, n. 11, p. 3123–3133, 1985. Cited 2 times in pages 34 and 35.

NAKAGAWA, M.; AMETANI, A.; IWAMOTO, K. Further Studies on Wave Propagation in Overhead Lines with Earth Return: Impedance of Stratified Earth. *Proceedings of the Institution of Electrical Engineers*, v. 120, n. 12, p. 1521, 1973. ISSN 00203270. Retrieved from: <https://digital-library.theiet.org/content/journals/10.1049/piee.1973.0312>. Cited 9 times in pages 17, 19, 20, 47, 77, 79, 80, 83, and 93.

PAPAGIANNIS, G.; TSIAMITROS, D.; LABRIDIS, D.; DOKOPOULOS, P. A Systematic Approach to the Evaluation of the Influence of Multilayered Earth on Overhead Power Transmission Lines. *IEEE Transactions on Power Delivery*, v. 20, n. 4, p. 2594–2601, oct 2005. ISSN 0885-8977. Retrieved from: <http://ieeexplore.ieee.org/document/1514508/>. Cited 11 times in pages 16, 17, 20, 47, 48, 77, 81, 83, 87, 93, and 94.

PAWAR, S. D.; MURUGAVEL, P.; LAL, D. M. Effect of relative humidity and sea level pressure on electrical conductivity of air over Indian Ocean. *Journal of Geophysical Research*, v. 114, n. D2, 2009. Retrieved from: <https://doi.org/10.1029/2007jd009716>. Cited in page 9.

PEABODY, A. W.; VERHIEL, A. L. The Effects of High-Voltage AC Transmission Lines on Buried Pipelines. *IEEE Transactions on Industry and General Applications*, IGA-7, n. 3, p. 395–402, 1971. Cited in page 1.

PEPPAS, G. D.; PAPAGIANNIS, M.-P.; KOULOURIDIS, S.; PYRGIOTI, E. C. Induced Voltage on an Aboveground Natural Gas/Oil Pipeline Due to Lightning Strike on a Transmission Line. In: *2014 International Conference on Lightning Protection (ICLP)*. Shanghai, China: ICLP, 2014. p. 461–467. ISBN 9781479935444. Cited in page 72.

PERZ, M. C.; RAGHUVEER, M. R. Generalized Derivation of Fields and Impedance Correction Factors of Lossy Transmission Lines. Part II - Lossy Conductors Above Lossy Ground. *IEEE Transactions on Power Apparatus and Systems*, PAS-93, n. 6, p. 1832 – 1841, 1974. Cited in page 80.

POLLACZEK, F. On the Field Produced by an Infinitely Long Wire Carrying Alternating Current. *Electrische Nachrictentechnik*, III, n. 9, p. 339–359, 1926. Cited 2 times in pages 46 and 47.

PORSANI, J. L.; MALAGUTTI, W. *Ground penetrating radar (GPR): Proposta Metodológica de Emprego em Estudos Geológico-geotécnicos nas Regiões de Rio Claro e Descalvado-SP*. 145 p. Tese (Doutorado) — Universidade de São Paulo, 1999. Cited in page 9.

PRASAD, A.; Belwin Edward, J.; RAVI, K. A Review on Fault Classification Methodologies in Power Transmission Systems: Part-I. *Journal of Electrical Systems and Information Technology*, v. 5, n. 1, p. 48–60, 2018. ISSN 23147172. Cited in page 117.

QI, L.; YUAN, H.; LI, L.; CUI, X. Calculation of Interference Voltage on the Nearby Underground Metal Pipeline due to the Grounding Fault on Overhead Transmission Lines. *IEEE Transactions on Electromagnetic Compatibility*, v. 55, n. 5, p. 965–974, 2013. Cited in page 1.

RAKOV, V. A.; UMAN, M. A. *Lightning: Physics and Effects*. [S.l.]: Cambridge University Press, 2003. 706 p. ISBN 9780521583275. Cited 4 times in pages 49, 50, 51, and 67.

RODEN, J. A.; GEDNEY, S. D. Convolution PML (CPML): An Efficient FDTD Implementation of the CFS-PML for Arbitrary Media. *Microwave and Optical Technology Letters*, v. 27, n. 5, p. 334–339, 2000. Cited in page 152.

SAADAT, H. *Power System Analysis*. 2. ed. [S.l.: s.n.], 1999. 720 p. ISBN 0-07-012235-0. Cited in page 41.

SADIKU, M. N. *Numerical Techniques in Electromagnetics*. 2. ed. [S.l.]: CRC Press, 2000. 760 p. ISBN 9781420063097. Cited in page 29.

SEEDHER, H. R.; THAPAR, B. Finite Expressions for Computation of Potential in Two Layer Soil. *IEEE Transactions on Power Apparatus and Systems*, PWRD-2, n. 4, p. 1098–1102, 1987. Cited in page 47.

SENEFF, H. L. Study of the Method of Geometric Mean Distances Used in Inductance Calculations. 1947. Cited in page 22.

SERAN, E.; GODEFROY, M.; PILI, E.; MICHIELSEN, N.; BONDIGUEL, S. What we can learn from measurements of air electric conductivity in 222 Rn-rich atmosphere. *Earth and Space Science*, v. 4, n. 2, p. 91–106, 2017. Retrieved from: <https://doi.org/10.1002/2016ea000241>. Cited in page 9.

SOUTHEY, R.; DAWALIBI, F. Improving the Reliability of Power Systems with More Accurate Grounding System Resistance Estimates. *Proceedings. International Conference on Power System Technology*, v. 4, p. 98–105, 2005. Retrieved from: <http://ieeexplore.ieee.org/lpdocs/epic03/wrapper.htm?arnumber=1053512>. Cited 2 times in pages 80 and 84.

STEINBERG, B. K.; LEVITSKAYA, T. M. Electrical Parameters of Soils in the Frequency Range from 1 kHz to 1 GHz, Using Lumped-circuit Methods. *Radio Science*, v. 36, n. 4, p. 709–719, 2001. Cited 2 times in pages 9 and 79.

STEVENSON, W. D.; GRAINGER, J. J. *Power System Analysis*. Internatio. [S.l.]: McGraw-Hill Education, 1994. 787 p. ISBN 9780071133388. Cited 5 times in pages 2, 21, 41, 42, and 43.

STRATTON, J. A. *Electromagnetic Theory*. Reissued e. Hoboken, New Jersey: John Wiley & Sons, Inc., 2007. 649 p. ISSN 0031-9228. ISBN 0470131535. Retrieved from: <http://scitation.aip.org/content/aip/magazine/physicstoday/article/48/1/10.1063/1.2807887http://physicstoday.scitation.org/doi/10.1063/1.2807887>. Cited in page 78.

SUNDE, E. D. *Earth Conduction Effects in Transmission Systems*. New York, NY: Dover Publications, 1968. Cited 2 times in pages 46 and 47.

TAKAHASHI, T.; KAWASE, T. Analysis of Apparent Resistivity in a Multi-Layer Earth Structure. *IEEE Transactions on Power Delivery*, v. 5, n. 2, p. 604–612, 1990. Cited 2 times in pages 2 and 13.

THEODOULIDIS, T. On the Closed-Form Expression of Carson's Integral. *Periodica Polytechnica Electrical Engineering and Computer Science*, v. 59, n. 1, p. 26–29, 2015. ISSN 20645260. Retrieved from: <https://pp.bme.hu/eecs/article/view/7894>. Cited in page 18.

TINNEY, W. F.; WALKER, J. W. Direct Solutions of Sparse Network Equations by Optimally Ordered Triangular Factorization. *Proceedings of the IEEE*, v. 55, n. 11, p. 1801 – 1809, 1967. Cited in page 157.

TODD, D. K. *Groundwater Hydrology*. 2nd. ed. [S.l.]: Wiley, 2006. 556 p. ISBN 9788126508365. Cited in page 9.

TSIAMITROS, D. A.; PAPAGIANNIS, G. K.; DOKOPOULOS, P. S.; ARRANGEMENT, A. O. L. Homogenous Earth Approximation of Two-Layer Earth Structures: An Equivalent Resistivity Approach. *IEEE Transactions on Power Delivery*, v. 22, n. 1, p. 658–666, 2007. Cited 10 times in pages 13, 16, 77, 79, 80, 81, 83, 84, 87, and 94.

TSIAMITROS, D. A.; PAPAGIANNIS, G. K.; DOKOPOULOS, P. S.; EQUATIONS, A. E. F. Earth Return Impedances of Conductor Arrangements in Multilayer Soils - Part I : Theoretical Model. v. 23, n. 4, p. 2392–2400, 2008. Cited in page 47.

UMASHANKAR, K.; TAFLOVE, A.; BEKER, B. Calculation and Experimental Validation of Induced Currents on Coupled Wires in an Arbitrary Shaped Cavity. *IEEE Transactions on Antennas and Propagation*, v. 35, n. 11, p. 1248—-1257, 1987. Retrieved from: <http://doi.org/10.1109/tap.1987.1144000>. Cited in page 149.

WEDEHPOL, L. M.; WILCOX, D. J. Transient Analysis of Underground Power-Transmission Systems. System-modal and Wave-propagation Characteristics. *Proceedings of the Institution of Electrical Engineers*, v. 120, n. 2, p. 253–260, 1973. Cited 2 times in pages 74 and 76.

WEDEPOHL, L. M. Application of Matrix Methods to the Solution of Travelling-Wave Phenomena in Polyphase Systems. *Proceedings of the Institution of Electrical Engineers*, v. 110, n. 12, p. 2200, 1963. ISSN 00203270. Retrieved from: <http://digital-library.theiet.org/content/journals/10.1049/piee.1963.0314>. Cited in page 45.

WEDEPOHL, L. M.; NGUYEN, H. V. Frequency-dependent Transformation Matrices for Untransposed Transmission Lines Using Newton-Raphson Method. *IEEE Transactions on Power Systems*, v. 11, n. 3, p. 1538–1546, 1996. ISSN 08858950. Cited 2 times in pages 45 and 46.

WENNER, F. A Method for Measuring Earth Resistivity. *Journal of the Washington Academy of Sciences*, v. 5, n. 16, p. 561–563, 1915. Cited 2 times in pages 10 and 11.

WHELAN, J. M.; HANRATTY, B.; MORGAN, E. Earth Resistivity in Ireland. In: *CDEGS Users' Group*. Montreal: Safe Engineering Services - SES, 2010. p. 155–164. Cited 3 times in pages 13, 76, and 81.

YANG, Y.; MA, J.; DAWALIBI, F. P. An Efficient Method for Computing the Magnetic Field Generated by Transmission Lines with Static Wires. In: *Proceedings. International Conference on Power System Technology*. Kunming, China: IEEE, 2002. p. 871–875. ISBN 0780374592. Retrieved from: <https://ieeexplore.ieee.org/document/1047524>. Cited in page 27.

YEE, K. S. Numerical Solution of Initial Boundary Value Problems Involving Maxwell's Equations in Isotropic Media. *IEEE Transactions on Antennas and Propagation*, v. 14, n. 3, p. 302–307, 1966. ISSN 15582221. Cited 3 times in pages 53, 140, and 141.

ZHANG, B.; CUI, X.; LI, L.; HE, J. Parameter Estimation of Horizontal Multilayer Earth by Complex Image Method. *IEEE Transactions on Power Delivery*, v. 20, n. 2 II, p. 1394–1401, 2005. ISSN 08858977. Cited 6 times in pages 10, 12, 13, 47, 79, and 83.

ZIPSE, D. W. Lightning Protection Systems: Advantages and Disadvantages. *IEEE Transactions on Industry Applications*, v. 30, n. 5, p. 1351–1361, 1994. Cited 2 times in pages 51 and 67.

ZOU, J.; ZENG, R.; HE, J. L.; MEMBER, S. S.; GUO, J.; MEMBER, S. S.; GAO, Y. Q.; MEMBER, S. S.; CHEN, S. M.; MEMBER, S. S. Numerical Green ' s Function of a Point Current Source in Horizontal Multilayer Soils by Utilizing the Vector Matrix Pencil Technique. v. 40, n. 2, p. 730–733, 2004. Cited 3 times in pages 29, 32, and 47.

APPENDIX A

CALCULATION OF GREEN'S FUNCTIONS FOR MULTILAYERED SOILS

This appendix contains a computer program written in technical language compatible with free software GNU/Octave to compute Green's functions values for arbitrary multilayered horizontal soils.

The routines leverage modern computational resources to parse the soil stratification data provided by the user and to write symbolic expressions for (2.50)-(2.53), forming a system of linear equations. Solutions to the resulting linear system are the necessary Green's function coefficients $A_{i,j}$ and $B_{i,j}$. Then, by means of direct numerical integrations using quadratures, Green's function (2.49) value is found.

Source codes are provided below.

Listing A.1. Function green_multi_val.m.

```
function [G] = green_multi_val(rho, h, O, P, coeff)
%green_multi Computes Green's function value for a N-layered soil.
%   Author : Amauri G. Martins-Britto (amaurigmartins@gmail.com)
%   Date   : 09 April 2020
%
%   *** Arguments
%   rho : (vector 1 x N) soil resistivities [ohm.m]
%   h   : (vector 1 x N-1) layer thicknesses [m]
%   O   : (vector 1 x 3) (x,y,z) coordinates of the source point [m]
%   P   : (vector 1 x 3) (x,y,z) coordinates of the observation point [m]
%
%   *** Outputs
%   G : (scalar) Green's function value [V]
%
%   External function called: green_multi_sym.m, to compute Green's
%   function coefficients.
%
if nargin == 4
    coeff=[];
end

soil_model = [rho h];
n_layers=(length(soil_model)+1)/2;
n_int=n_layers-1;
```

```
rho=soil_model(1:n_layers);
h=cumsum(soil_model(n_layers+1:end));
x_src=O(1);y_src=O(2);z_src=O(3);
x_obs=P(1);y_obs=P(2);z_obs=P(3);
rr=sqrt((x_obs-x_src)^2+(y_obs-y_src)^2);
zz=z_obs-z_src;
%
src_layer=find(h>z_src);
if isempty(src_layer)
    src_layer=n_layers;
else
    src_layer=src_layer(1);
end
%
obs_layer=find(h>z_obs);
if isempty(obs_layer)
    obs_layer=n_layers;
else
    obs_layer=obs_layer(1);
end
%
syms lambda z D d
assumeAlso(D ≠ 0)
assumeAlso(lambda ≠ 0)
assumeAlso(d ≠ 0)
%
for i=1:n_layers
    eval(['syms rho' num2str(i)]);
    eval(['assumeAlso(rho' num2str(i) ' ≠ 0)']);
    if i<n_layers
        eval(['syms h' num2str(i)]);
        eval(['assumeAlso(h' num2str(i) ' ≠ 0)']);
    end
end
%
if isempty(coeff); [fun,coeff]=green_multi_sym(n_layers, src_layer); end
%
d=z_src;
for i=1:n_layers
    eval(['rho' num2str(i) '=' num2str(rho(i),'%16.16f') ';'])
    if i<n_layers
        eval(['h' num2str(i) '=' num2str(h(i),'%16.16f') ';'])
    end
end
%
T1=eq(obs_layer,src_layer)*exp(-lambda*abs(zz));
T2=eval(['simplify(subs(coeff.A' num2str(src_layer) num2str(obs_layer) ...
    '))']);*exp(-lambda*zz);
T3=eval(['simplify(subs(coeff.B' num2str(src_layer) num2str(obs_layer) ...
    '))']);*exp(lambda*zz);
%
f=(T1+T2+T3)*besselj(0,lambda*rr);
f=matlabFunction(f);
ff=@(lambda) sum([0 f(lambda)],'omitnan');
%
G=rho(src_layer)/(4*pi).* integral(ff,0,Inf,'ArrayValued',true);
%
end
```

Listing A.2. Function green_multi_sym.m.

```
function [fun,coeff] = green_multi_sym(n_layers, src_layer)
%green_multi_sym Computes Green's function symbolic coefficients for a ...
    N-layered soil.
%   Author : Amauri G. Martins-Britto (amaurigmartins@gmail.com)
%   Date   : 09 April 2020
%
%   *** Arguments
%   n_layers  : Number of soil layers
%   src_layer : Layer where the source point is located
%
%   *** Outputs
%   fun   : (struct) Green's function symbolic expressions
%   coeff : (struct) Green's function symbolic coefficients
%
n_int=n_layers-1;
%
syms lambda z D d
assumeAlso(D ≠ 0)
assumeAlso(lambda ≠ 0)
assumeAlso(d ≠ 0)
%
for i=1:n_layers
    eval(['syms rho' num2str(i)]);
    eval(['assumeAlso(rho' num2str(i) ' ≠ 0)']);
    if i<n_layers
        eval(['syms h' num2str(i)]);
        eval(['assumeAlso(h' num2str(i) ' ≠ 0)']);
    end
end
%
solv_param=[];
for j=1:n_layers
    eval(['syms A' num2str(src_layer) num2str(j)]);
    eval(['assumeAlso(A' num2str(src_layer) num2str(j) ' ≠ 0)']);
    eval(['syms B' num2str(src_layer) num2str(j)]);
    solv_param=[solv_param str2sym(['A' num2str(src_layer) num2str(j)]) ...
        str2sym(['B' num2str(src_layer) num2str(j)])];
    if j<n_layers
        eval(['assumeAlso(B' num2str(src_layer) num2str(j) ' ≠ 0)']);
    else
        eval(['B' num2str(src_layer) num2str(j) '=0;']);
    end
    eval(['syms G' num2str(src_layer) num2str(j)]);
    eval(['G' num2str(src_layer) num2str(j) '= ((rho' num2str(src_layer) ...
        '*D)/(2*pi*lambda))*(eq(j,src_layer)*exp(-lambda*abs(z))+A' ...
        num2str(src_layer) num2str(j) '*exp(-lambda*z)+B' ...
            num2str(src_layer) num2str(j) ...
        '*exp(+lambda*z));'])
    eval(['fun.G' num2str(src_layer) num2str(j) '= G' num2str(src_layer) ...
        num2str(j) ';'])
end
%
eqn_count=1;
syseq(eqn_count,1)=subs(diff(eval(['G' num2str(src_layer) ...
    num2str(1)]),z),z,-d)==0;
eqn_count=eqn_count+1;
%
```

```
for i=1:n_int
    syseq(eqn_count,1)=subs(eval(['G' num2str(src_layer) ...
        num2str(i)]),z,eval(['h' num2str(i) '-d']))== ...
         subs(eval(['G' num2str(src_layer) num2str(i+1)]),z,eval(['h' ...
            num2str(i) '-d']));
    eqn_count=eqn_count+1;
    syseq(eqn_count,1)=(1/eval(['rho' num2str(i)]))*subs(diff(eval(['G' ...
        num2str(src_layer) num2str(i)]),z),z,eval(['h' num2str(i) '-d']))==...
         (1/eval(['rho' num2str(i+1)]))*subs(diff(eval(['G' ...
            num2str(src_layer) num2str(i+1)]),z),z,eval(['h' num2str(i) ...
            '-d']));
    eqn_count=eqn_count+1;
end
%
coeff=solve(syseq, solv_param);
eval(['coeff.B' num2str(src_layer) num2str(n_layers) '=0;']);
%
end
```

By using the proposed program, one can systematically obtain the equations that describe soils composed by any number of layers. For instance, it is possible to demonstrate that coefficients $A_{1,1}$ and $B_{1,1}$ of a five-layered soil assume the form given in (A.1)-(A.3), which are troublesome to derive without the aid of a computer (HE *et al.*, 2013).

$$
\begin{aligned}
A_{1,1} = \frac{1}{C_{5,1}} \big[& (\rho_2+\rho_1)(\rho_3+\rho_2)(\rho_4+\rho_3)(\rho_5+\rho_4)\, e^{-\lambda d} \\
& + (\rho_2+\rho_1)(\rho_3+\rho_2)(\rho_4-\rho_3)(\rho_5-\rho_4)\, e^{\lambda(2h_3-2h_4-d)} \\
& + (\rho_2+\rho_1)(\rho_3-\rho_2)(\rho_4-\rho_3)(\rho_5+\rho_4)\, e^{\lambda(2h_2-2h_3-d)} \\
& + (\rho_2+\rho_1)(\rho_3-\rho_2)(\rho_4+\rho_3)(\rho_5-\rho_4)\, e^{\lambda(2h_2-2h_4-d)} \\
& + (\rho_2-\rho_1)(\rho_3-\rho_2)(\rho_4+\rho_3)(\rho_5+\rho_4)\, e^{\lambda(2h_1-2h_2-d)} \\
& + (\rho_2-\rho_1)(\rho_3-\rho_2)(\rho_4-\rho_3)(\rho_5-\rho_4)\, e^{\lambda(2h_1-2h_2+2h_3-2h_4-d)} \\
& + (\rho_2-\rho_1)(\rho_3+\rho_2)(\rho_4-\rho_3)(\rho_5+\rho_4)\, e^{\lambda(2h_1-2h_3-d)} \\
& + (\rho_2-\rho_1)(\rho_3+\rho_2)(\rho_4+\rho_3)(\rho_5-\rho_4)\, e^{\lambda(2h_1-2h_4-d)} \\
& + (\rho_2-\rho_1)(\rho_3+\rho_2)(\rho_4+\rho_3)(\rho_5+\rho_4)\, e^{\lambda(-2h_1+d)} \\
& + (\rho_2-\rho_1)(\rho_3+\rho_2)(\rho_4-\rho_3)(\rho_5-\rho_4)\, e^{\lambda(-2h_1+2h_3-2h_4+d)} \\
& + (\rho_2-\rho_1)(\rho_3-\rho_2)(\rho_4-\rho_3)(\rho_5+\rho_4)\, e^{\lambda(-2h_1+2h_2-2h_3+d)} \\
& + (\rho_2-\rho_1)(\rho_3-\rho_2)(\rho_4+\rho_3)(\rho_5-\rho_4)\, e^{\lambda(-2h_1+2h_2-2h_4+d)} \\
& + (\rho_2+\rho_1)(\rho_3-\rho_2)(\rho_4+\rho_3)(\rho_5+\rho_4)\, e^{\lambda(-2h_2+d)}
\end{aligned}
$$

$$
\begin{aligned}
&+ (\rho_2+\rho_1)(\rho_3-\rho_2)(\rho_4-\rho_3)(\rho_5-\rho_4)\, e^{\lambda(-2h_2+2h_3-2h_4+d)} \\
&+ (\rho_2+\rho_1)(\rho_3+\rho_2)(\rho_4-\rho_3)(\rho_5+\rho_4)\, e^{\lambda(-2h_3+d)} \\
&+ (\rho_2+\rho_1)(\rho_3+\rho_2)(\rho_4+\rho_3)(\rho_5-\rho_4)\, e^{\lambda(-2h_4+d)}\big], \qquad \text{(A.1)}
\end{aligned}
$$

$$
\begin{aligned}
B_{1,1} =& \frac{1}{C_{5,1}}\big[(\rho_2-\rho_1)(\rho_3+\rho_2)(\rho_4+\rho_3)(\rho_5+\rho_4)\, e^{\lambda(-2h_1-d)} \\
&+ (\rho_2-\rho_1)(\rho_3+\rho_2)(\rho_4+\rho_3)(\rho_5+\rho_4)\, e^{\lambda(-2h_1+d)} \\
&+ (\rho_2-\rho_1)(\rho_3+\rho_2)(\rho_4-\rho_3)(\rho_5-\rho_4)\, e^{\lambda(-2h_1+2h_3-2h_4-d)} \\
&+ (\rho_2-\rho_1)(\rho_3+\rho_2)(\rho_4-\rho_3)(\rho_5-\rho_4)\, e^{\lambda(-2h_1+2h_3-2h_4+d)} \\
&+ (\rho_2-\rho_1)(\rho_3-\rho_2)(\rho_4-\rho_3)(\rho_5+\rho_4)\, e^{\lambda(-2h_1+2h_2-2h_3-d)} \\
&+ (\rho_2-\rho_1)(\rho_3-\rho_2)(\rho_4-\rho_3)(\rho_5+\rho_4)\, e^{\lambda(-2h_1+2h_2-2h_3+d)} \\
&+ (\rho_2-\rho_1)(\rho_3-\rho_2)(\rho_4+\rho_3)(\rho_5-\rho_4)\, e^{\lambda(-2h_1+2h_2-2h_4-d)} \\
&+ (\rho_2-\rho_1)(\rho_3-\rho_2)(\rho_4+\rho_3)(\rho_5-\rho_4)\, e^{\lambda(-2h_1+2h_2-2h_4-d)} \\
&+ (\rho_2+\rho_1)(\rho_3-\rho_2)(\rho_4+\rho_3)(\rho_5+\rho_4)\, e^{\lambda(-2h_2-d)} \\
&+ (\rho_2+\rho_1)(\rho_3-\rho_2)(\rho_4+\rho_3)(\rho_5+\rho_4)\, e^{\lambda(-2h_2+d)} \\
&+ (\rho_2+\rho_1)(\rho_3-\rho_2)(\rho_4-\rho_3)(\rho_5-\rho_4)\, e^{\lambda(-2h_2+2h_3-2h_4-d)} \\
&+ (\rho_2+\rho_1)(\rho_3-\rho_2)(\rho_4-\rho_3)(\rho_5-\rho_4)\, e^{\lambda(-2h_2+2h_3-2h_4+d)} \\
&+ (\rho_2+\rho_1)(\rho_3+\rho_2)(\rho_4-\rho_3)(\rho_5+\rho_4)\, e^{\lambda(-2h_3-d)} \\
&+ (\rho_2+\rho_1)(\rho_3+\rho_2)(\rho_4-\rho_3)(\rho_5+\rho_4)\, e^{\lambda(-2h_3+d)} \\
&+ (\rho_2+\rho_1)(\rho_3+\rho_2)(\rho_4+\rho_3)(\rho_5-\rho_4)\, e^{\lambda(-2h_4-d)} \\
&+ (\rho_2+\rho_1)(\rho_3+\rho_2)(\rho_4+\rho_3)(\rho_5-\rho_4)\, e^{\lambda(-2h_4+d)}\big], \qquad \text{(A.2)}
\end{aligned}
$$

$$
\begin{aligned}
C_{5,1} =& \big[(\rho_2+\rho_1)(\rho_3+\rho_2)(\rho_4+\rho_3)(\rho_5+\rho_4) \\
&+ (\rho_2+\rho_1)(\rho_3+\rho_2)(\rho_4-\rho_3)(\rho_5-\rho_4)\, e^{\lambda(2h_3-2h_4)} \\
&+ \rho_2+\rho_1)(\rho_3-\rho_2)(\rho_4-\rho_3)(\rho_5+\rho_4)\, e^{\lambda(2h_2-2h_3)} \\
&+ (\rho_2+\rho_1)(\rho_3-\rho_2)(\rho_4+\rho_3)(\rho_5-\rho_4)\, e^{\lambda(2h_2-2h_4)} \\
&+ (\rho_2-\rho_1)(\rho_3-\rho_2)(\rho_4+\rho_3)(\rho_5+\rho_4)\, e^{\lambda(2h_1-2h_2)}
\end{aligned}
$$

$$
\begin{aligned}
&+ (\rho_2 - \rho_1)(\rho_3 - \rho_2)(\rho_4 - \rho_3)(\rho_5 - \rho_4)\, e^{\lambda(2h_1 - 2h_2 + 2h_3 - 2h_4)} \\
&+ (\rho_2 - \rho_1)(\rho_3 + \rho_2)(\rho_4 - \rho_3)(\rho_5 + \rho_4)\, e^{\lambda(2h_1 - 2h_3)} \\
&+ (\rho_2 - \rho_1)(\rho_3 + \rho_2)(\rho_4 + \rho_3)(\rho_5 - \rho_4)\, e^{\lambda(2h_1 - 2h_4)} \\
&+ (\rho_2 - \rho_1)(\rho_3 + \rho_2)(\rho_4 + \rho_3)(\rho_5 + \rho_4)\, e^{\lambda(-2h_1)} \\
&+ (\rho_2 - \rho_1)(\rho_3 + \rho_2)(\rho_4 - \rho_3)(\rho_5 - \rho_4)\, e^{\lambda(-2h_1 + 2h_3 - 2h_4)} \\
&+ (\rho_2 - \rho_1)(\rho_3 - \rho_2)(\rho_4 - \rho_3)(\rho_5 + \rho_4)\, e^{\lambda(-2h_1 + 2h_2 - 2h_3)} \\
&+ (\rho_2 - \rho_1)(\rho_3 - \rho_2)(\rho_4 + \rho_3)(\rho_5 - \rho_4)\, e^{\lambda(-2h_1 + 2h_2 - 2h_4)} \\
&+ (\rho_2 + \rho_1)(\rho_3 - \rho_2)(\rho_4 + \rho_3)(\rho_5 + \rho_4)\, e^{\lambda(-2h_2)} \\
&+ (\rho_2 + \rho_1)(\rho_3 - \rho_2)(\rho_4 - \rho_3)(\rho_5 - \rho_4)\, e^{\lambda(-2h_2 + 2h_3 - 2h_4)} \\
&+ (\rho_2 + \rho_1)(\rho_3 + \rho_2)(\rho_4 - \rho_3)(\rho_5 + \rho_4)\, e^{\lambda(-2h_3)} \\
&+ (\rho_2 + \rho_1)(\rho_3 + \rho_2)(\rho_4 + \rho_3)(\rho_5 - \rho_4)\, e^{\lambda(-2h_4)} \Big] . \qquad \text{(A.3)}
\end{aligned}
$$

In order to validate the proposed implementation with numerical data, values from soil model 15 of Table 4.5 are chosen. The test layout is illustrated in Figure A.1.

Figure A.1. Source and observation points in a five-layered soil. All dimensions are in meters and not in scale.

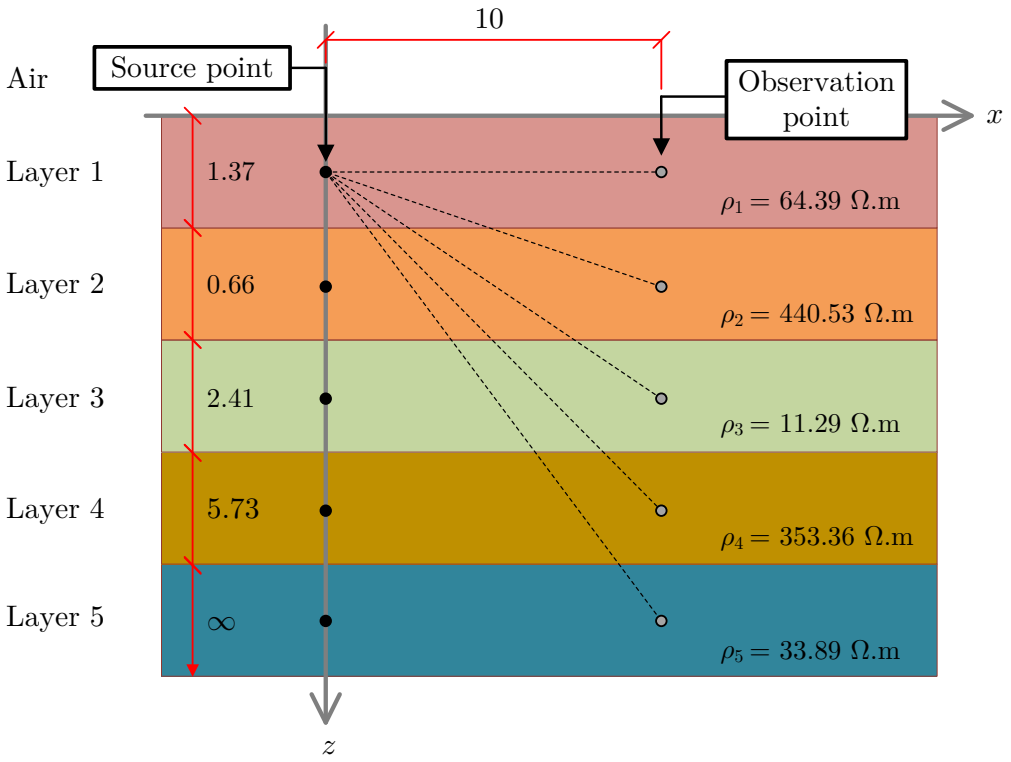

Source: own authorship.

All possible combinations of source and observation layers are evaluated. Regarding the z-coordinate, source and observation points are always placed at the midpoint of the respective layer. The observation point is positioned at a radial distance of 10 m from the source.

Results are compared with the software CDEGS, which is based in the methods reported in (DAWALIBI; DONOSO, 1993). Tables A.1 and A.2 contain the numerical results.

Table A.1. Green's function values calculated in volts using the proposed program.

Source point	**Observation point**				
	Layer 1	Layer 2	Layer 3	Layer 4	Layer 5
Layer 1	0.9115	0.8762	0.8280	0.5318	0.2107
Layer 2	0.8762	0.8006	0.8283	0.5356	0.2123
Layer 3	0.8280	0.8283	0.8245	0.5390	0.2142
Layer 4	0.5318	0.5356	0.5390	0.4048	0.3227
Layer 5	0.2107	0.2123	0.2142	0.3227	0.4308

Source: own authorship.

Table A.2. Green's function values calculated in volts using software CDEGS.

Source point	**Observation point**				
	Layer 1	Layer 2	Layer 3	Layer 4	Layer 5
Layer 1	0.94	0.88	0.839	0.54	0.21
Layer 2	0.878	0.858	0.841	0.542	0.212
Layer 3	0.839	0.841	0.833	0.538	0.217
Layer 4	0.540	0.542	0.538	0.51	0.327
Layer 5	0.21	0.212	0.217	0.327	0.423

Source: own authorship.

It is evident that there is an excellent agreement between results obtained using the proposed computer program and the reference software.

APPENDIX B

DESCRIPTION OF THE FDTD METHOD

This appendix describes the main FDTD equations implemented in this thesis, as given in the original work by Yee (1966). Notation follows (ELSHERBENI; DEMIR, 2015), which contains an in-depth step-by-step explanation of a complete FDTD solution.

The time-domain Maxwell curl equations necessary to specify the electromagnetic field behavior over time and space are:

$$\nabla \times \vec{H} = \varepsilon \frac{\partial \vec{E}}{\partial t} + \sigma^e \vec{E} + \vec{J}_i, \tag{B.1}$$

$$\nabla \times \vec{E} = -\mu \frac{\partial \vec{H}}{\partial t} - \sigma^m \vec{H} - \vec{M}_i, \tag{B.2}$$

in which $\vec{H}$ is the magnetic field vector, in A/m; $\vec{E}$ is the electric field vector, in V/m; $\vec{J}_i$ is the impressed current density vector, in A/m^2; $\vec{M}_i$ is the impressed magnetic current density vector, in V/m^2; ε is the permittivity, in F/m; μ is the permeability of the material, in H/m; σ^e is the electric conductivity, in S/m; and σ^m is the magnetic conductivity, in Ω/m.

The two vector equations (B.1)-(B.2) can be decomposed into six scalar equations in the three-dimensional space. Therefore, in a Cartesian coordinate system (x,y,z):

$$\frac{\partial E_x}{\partial t} = \frac{1}{\varepsilon_x}\left(\frac{\partial H_z}{\partial y} - \frac{\partial H_y}{\partial z} - \sigma_x^e E_x - J_{ix}\right), \tag{B.3}$$

$$\frac{\partial E_y}{\partial t} = \frac{1}{\varepsilon_y}\left(\frac{\partial H_x}{\partial z} - \frac{\partial H_z}{\partial x} - \sigma_y^e E_y - J_{iy}\right), \tag{B.4}$$

$$\frac{\partial E_z}{\partial t} = \frac{1}{\varepsilon_z}\left(\frac{\partial H_y}{\partial x} - \frac{\partial H_x}{\partial y} - \sigma_z^e E_z - J_{iz}\right), \tag{B.5}$$

$$\frac{\partial H_x}{\partial t} = \frac{1}{\mu_x}\left(\frac{\partial E_y}{\partial z} - \frac{\partial E_z}{\partial y} - \sigma_x^m H_x - M_{ix}\right), \tag{B.6}$$

$$\frac{\partial H_y}{\partial t} = \frac{1}{\mu_y}\left(\frac{\partial E_z}{\partial x} - \frac{\partial E_x}{\partial z} - \sigma_y^m H_y - M_{iy}\right), \tag{B.7}$$

$$\frac{\partial H_z}{\partial t} = \frac{1}{\mu_z}\left(\frac{\partial E_x}{\partial y} - \frac{\partial E_y}{\partial x} - \sigma_z^m H_z - M_{iz}\right), \tag{B.8}$$

where subscripts x, y and z denote the components along the respective directions.

B.1 YEE ALGORITHM

The FDTD algorithm proposed by Yee (1966) subdivides the problem geometry into a spatial grid where electric and magnetic field components are placed at discrete positions in space, then it solves (B.3)-(B.8) in time at discrete time-steps. This is performed by approximating the time and space derivatives appearing in (B.3)-(B.8) by finite central differences and solving the resulting set of equations in a manner such that past values are used to calculate the values of fields at future time-steps, thus constructing a time-marching program that simulates the progression of electromagnetic fields over time, in a process analogous in certain aspects with the EMTP algorithm by Dommel (1969), described in Appendix C.

Figure B.1 shows a three-dimensional domain subdivided into $(N_x \times N_y \times N_z)$ cells, forming a grid. Cells are indexed as (i,j,k), with spatial discretization steps $(\Delta x,\Delta y,\Delta z)$ and material parameters (permittivity, permeability, electric, and magnetic conductivities) are distributed over the FDTD grid following the same indexing scheme. Then, electromagnetic field components (B.3)-(B.8) are written using central differences as six FDTD updating equations (B.9a)-(B.14a) with respective coefficient terms.

Electric field components are calculated at time instants $[0, \Delta t, 2\Delta t, ..., n\Delta t, ...]$, whereas magnetic fields are sampled at times $[\frac{1}{2}\Delta t, (1+\frac{1}{2})\Delta t, ..., (n+\frac{1}{2})\Delta t, ...]$. The time-steps at which fields are sampled are denoted by the superscript notation. For instance: $E_x^n(i,j,k)$ represents the electric field component along the x-axis for the node (i,j,k), sampled at time $n\Delta t$.

$$\begin{aligned} E_x^{n+1}(i,j,k) =& C_{exe}(i,j,k) \times E_x^n(i,j,k) \\ &+ C_{exhz}(i,j,k) \times \left[H_z^{n+\frac{1}{2}}(i,j,k) - H_z^{n+\frac{1}{2}}(i,j-1,k)\right] \\ &+ C_{exhy}(i,j,k) \times \left[H_y^{n+\frac{1}{2}}(i,j,k) - H_y^{n+\frac{1}{2}}(i,j,k-1)\right] \\ &+ C_{exj}(i,j,k) \times J_{ix}^{n+\frac{1}{2}}(i,j,k) \end{aligned} \tag{B.9a}$$

with:

$$C_{exe}(i,j,k) = \frac{2\varepsilon_x(i,j,k) - \Delta t\sigma_x^e(i,j,k)}{2\varepsilon_x(i,j,k) + \Delta t\sigma_x^e(i,j,k)}, \tag{B.9b}$$

$$C_{exhz}(i,j,k) = \frac{2\Delta t}{\left[2\varepsilon_x(i,j,k) + \Delta t\sigma_x^e(i,j,k)\right]\Delta y}, \tag{B.9c}$$

$$C_{exhy}(i,j,k) = -\frac{2\Delta t}{\left[2\varepsilon_x(i,j,k) + \Delta t\sigma_x^e(i,j,k)\right]\Delta z}, \tag{B.9d}$$

Figure B.1. Representation of the three-dimensional FDTD domain and of the electromagnetic fields on a Yee cell with modified node numbering.

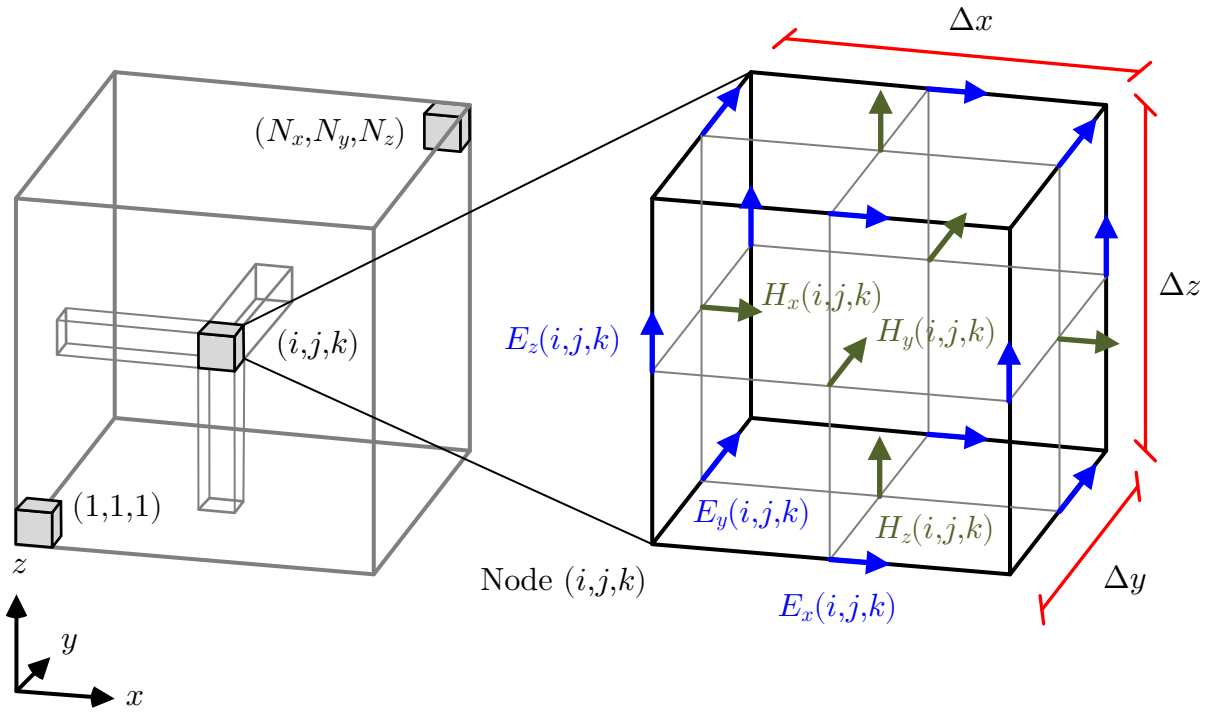

Source: adapted from (ELSHERBENI; DEMIR, 2015).

$$C_{exj}(i,j,k) = -\frac{2\Delta t}{2\varepsilon_x(i,j,k) + \Delta t\sigma_x^e(i,j,k)}. \tag{B.9e}$$

$$\begin{aligned} E_y^{n+1}(i,j,k) =& C_{eye}(i,j,k) \times E_y^n(i,j,k) \\ &+ C_{eyhx}(i,j,k) \times \left[H_x^{n+\frac{1}{2}}(i,j,k) - H_x^{n+\frac{1}{2}}(i,j,k-1)\right] \\ &+ C_{eyhz}(i,j,k) \times \left[H_z^{n+\frac{1}{2}}(i,j,k) - H_z^{n+\frac{1}{2}}(i-1,j,k)\right], \\ &+ C_{eyj}(i,j,k) \times J_{iy}^{n+\frac{1}{2}}(i,j,k) \end{aligned} \tag{B.10a}$$

with:

$$C_{eye}(i,j,k) = \frac{2\varepsilon_y(i,j,k) - \Delta t\sigma_y^e(i,j,k)}{2\varepsilon_y(i,j,k) + \Delta t\sigma_y^e(i,j,k)}, \tag{B.10b}$$

$$C_{eyhx}(i,j,k) = \frac{2\Delta t}{\left[2\varepsilon_y(i,j,k) + \Delta t\sigma_y^e(i,j,k)\right]\Delta z}, \tag{B.10c}$$

$$C_{eyhz}(i,j,k) = -\frac{2\Delta t}{\left[2\varepsilon_y(i,j,k) + \Delta t\sigma_y^e(i,j,k)\right]\Delta x}, \tag{B.10d}$$

$$C_{eyj}(i,j,k) = -\frac{2\Delta t}{2\varepsilon_y(i,j,k) + \Delta t\sigma_y^e(i,j,k)}. \tag{B.10e}$$

$$\begin{aligned} E_z^{n+1}(i,j,k) =& C_{eze}(i,j,k) \times E_z^n(i,j,k) \\ &+ C_{ezhy}(i,j,k) \times \left[H_y^{n+\frac{1}{2}}(i,j,k) - H_y^{n+\frac{1}{2}}(i-1,j,k)\right] \\ &+ C_{ezhx}(i,j,k) \times \left[H_x^{n+\frac{1}{2}}(i,j,k) - H_x^{n+\frac{1}{2}}(i,j-1,k)\right] \\ &+ C_{ezj}(i,j,k) \times J_{iz}^{n+\frac{1}{2}}(i,j,k) \end{aligned}, \tag{B.11a}$$

with:

$$C_{eze}(i,j,k) = \frac{2\varepsilon_z(i,j,k) - \Delta t\sigma_z^e(i,j,k)}{2\varepsilon_z(i,j,k) + \Delta t\sigma_z^e(i,j,k)}, \tag{B.11b}$$

$$C_{ezhy}(i,j,k) = \frac{2\Delta t}{\left[2\varepsilon_z(i,j,k) + \Delta t\sigma_z^e(i,j,k)\right]\Delta x}, \tag{B.11c}$$

$$C_{ezhx}(i,j,k) = -\frac{2\Delta t}{\left[2\varepsilon_z(i,j,k) + \Delta t\sigma_z^e(i,j,k)\right]\Delta y}, \tag{B.11d}$$

$$C_{ezj}(i,j,k) = -\frac{2\Delta t}{2\varepsilon_z(i,j,k) + \Delta t\sigma_z^e(i,j,k)}. \tag{B.11e}$$

$$\begin{aligned} H_x^{n+\frac{1}{2}}(i,j,k) =& C_{hxh}(i,j,k) \times H_x^{n-\frac{1}{2}}(i,j,k) \\ &+ C_{hxey}(i,j,k) \times \left[E_y^n(i,j,k+1) - E_y^n(i,j,k)\right] \\ &+ C_{hxez}(i,j,k) \times \left[E_z^n(i,j+1,k) - E_z^n(i,j,k)\right] \\ &+ C_{hxm}(i,j,k) \times M_{ix}^n(i,j,k) \end{aligned}, \tag{B.12a}$$

with:

$$C_{hxh}(i,j,k) = \frac{2\mu_x(i,j,k) - \Delta t\sigma_x^m(i,j,k)}{2\mu_x(i,j,k) + \Delta t\sigma_x^m(i,j,k)}, \tag{B.12b}$$

$$C_{hxey}(i,j,k) = \frac{2\Delta t}{\left[2\mu_x(i,j,k) + \Delta t\sigma_x^m(i,j,k)\right]\Delta z}, \tag{B.12c}$$

$$C_{hxez}(i,j,k) = -\frac{2\Delta t}{\left[2\mu_x(i,j,k) + \Delta t\sigma_x^m(i,j,k)\right]\Delta y}, \tag{B.12d}$$

$$C_{hxm}(i,j,k) = -\frac{2\Delta t}{2\mu_x(i,j,k) + \Delta t\sigma_x^m(i,j,k)}. \tag{B.12e}$$

$$\begin{aligned} H_y^{n+\frac{1}{2}}(i,j,k) =& C_{hyh}(i,j,k) \times H_y^{n-\frac{1}{2}}(i,j,k) + C_{hyez}(i,j,k) \\ &\times \left[E_z^n(i+1,j,k) - E_z^n(i,j,k)\right] + C_{hyex}(i,j,k) \\ &\times \left[E_x^n(i,j,k+1) - E_x^n(i,j,k)\right] + C_{hym}(i,j,k) \times M_{iy}^n(i,j,k) \end{aligned}, \tag{B.13a}$$

with:

$$C_{hyh}(i,j,k) = \frac{2\mu_y(i,j,k) - \Delta t\sigma_y^m(i,j,k)}{2\mu_y(i,j,k) + \Delta t\sigma_y^m(i,j,k)}, \tag{B.13b}$$

$$C_{hyez}(i,j,k) = \frac{2\Delta t}{\left[2\mu_y(i,j,k) + \Delta t\sigma_y^m(i,j,k)\right]\Delta x}, \tag{B.13c}$$

$$C_{hyex}(i,j,k) = -\frac{2\Delta t}{\left[2\mu_y(i,j,k) + \Delta t\sigma_y^m(i,j,k)\right]\Delta z}, \tag{B.13d}$$

$$C_{hym}(i,j,k) = -\frac{2\Delta t}{2\mu_y(i,j,k) + \Delta t\sigma_y^m(i,j,k)}. \tag{B.13e}$$

$$\begin{aligned} H_z^{n+\frac{1}{2}}(i,j,k) =& C_{hzh}(i,j,k) \times H_z^{n-\frac{1}{2}}(i,j,k) \\ &+ C_{hzex}(i,j,k) \times \left[E_x^n(i,j+1,k) - E_x^n(i,j,k)\right] \\ &+ C_{hzey}(i,j,k) \times \left[E_y^n(i+1,j,k) - E_y^n(i,j,k)\right] \\ &+ C_{hzm}(i,j,k) \times M_{iz}^n(i,j,k) \end{aligned}, \tag{B.14a}$$

with:

$$C_{hzh}(i,j,k) = \frac{2\mu_y(i,j,k) - \Delta t\sigma_z^m(i,j,k)}{2\mu_z(i,j,k) + \Delta t\sigma_z^m(i,j,k)}, \tag{B.14b}$$

$$C_{hzex}(i,j,k) = \frac{2\Delta t}{\left[2\mu_z(i,j,k) + \Delta t\sigma_z^m(i,j,k)\right]\Delta y}, \tag{B.14c}$$

$$C_{hzey}(i,j,k) = -\frac{2\Delta t}{\left[2\mu_z(i,j,k) + \Delta t\sigma_z^m(i,j,k)\right]\Delta x}, \tag{B.14d}$$

$$C_{hzm}(i,j,k) = -\frac{2\Delta t}{2\mu_z(i,j,k) + \Delta t\sigma_z^m(i,j,k)}. \tag{B.14e}$$

B.2 STABILITY CONDITION

The FDTD method requires the choice of the discretization steps (Δt in time, Δx, Δy and Δz in space) to observe a restriction known as Courant-Friedrichs-Lewy (CFL) condition, expressed in (B.15), to guarantee the numerical stability of the solution (COURANT *et al.*, 1967).

$$c_{max}\Delta t = \left[\frac{1}{\Delta x^2} + \frac{1}{\Delta y^2} + \frac{1}{\Delta z^2}\right]^{-\frac{1}{2}}, \tag{B.15}$$

in which c_{max} is the is the maximum wave propagation velocity within the domain.

The physical meaning of the CFL condition in FDTD is that a wave cannot be allowed to travel more than one cell unit in space during one time-step, otherwise divergent spurious fields may occur.

B.3 LUMPED COMPONENTS

Models of lumped components are required to represent energization sources and to properly interface the FDTD model with the circuit-based (ATP) model. They are also necessary for accurate representation of very large systems, in the form of terminations of objects within bounded domains, to account for the equivalent behavior of the portions outside the FDTD space. For example, a conductor that extends for several kilometers outside the FDTD domain can be represented by its equivalent impedance using lumped elements.

In the following discussion, elements are assumed to be oriented along the z direction, therefore only these field components are presented explicitly. Equations for the other two directions are analogous and will be omitted.

B.3.1 Voltage source

Figure B.2 represents a voltage source with magnitude V_S and internal resistance R_S, oriented towards the z-axis, connecting nodes (i, j, k) and $(i, j, k + 1)$.

Figure B.2. Voltage source with magnitude V_S and internal resistance R_S placed between nodes (i, j, k) and $(i, j, k + 1)$.

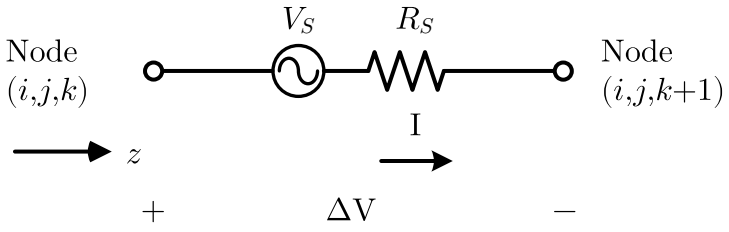

Source: own authorship.

FDTD updating equations for the voltage source are:

$$\begin{aligned} E_z^{n+1}(i,j,k) =& C_{eze}(i,j,k) \times E_z^n(i,j,k) \\ &+ C_{ezhy}(i,j,k) \times \left[H_y^{n+\frac{1}{2}}(i,j,k) - H_y^{n+\frac{1}{2}}(i-1,j,k) \right] \\ &+ C_{ezhx}(i,j,k) \times \left[H_x^{n+\frac{1}{2}}(i,j,k) - H_x^{n+\frac{1}{2}}(i,j-1,k) \right] \\ &+ C_{ezs}(i,j,k) \times V_s^{n+\frac{1}{2}}(i,j,k) \end{aligned}, \tag{B.16a}$$

with:

$$C_{eze}(i,j,k) = \frac{2\varepsilon_z(i,j,k) - \Delta t\sigma_z^e(i,j,k) - \frac{\Delta t\Delta z}{R_s\Delta x\Delta y}}{2\varepsilon_z(i,j,k) + \Delta t\sigma_z^e(i,j,k) + \frac{\Delta t\Delta z}{R_s\Delta x\Delta y}}, \tag{B.16b}$$

$$C_{ezhy}(i,j,k) = \frac{2\Delta t}{\left[2\varepsilon_z(i,j,k) + \Delta t\sigma_z^e(i,j,k) + \frac{\Delta t\Delta z}{R_s\Delta x\Delta y}\right]\Delta x}, \tag{B.16c}$$

$$C_{ezhx}(i,j,k) = -\frac{2\Delta t}{\left[2\varepsilon_z(i,j,k) + \Delta t\sigma_z^e(i,j,k) + \frac{\Delta t\Delta z}{R_s\Delta x\Delta y}\right]\Delta y}, \tag{B.16d}$$

$$C_{ezs}(i,j,k) = -\frac{2\Delta t}{\left[2\varepsilon_z(i,j,k) + \Delta t\sigma_z^e(i,j,k) + \frac{\Delta t\Delta z}{R_S\Delta x\Delta y}\right](R_S\Delta x\Delta y)}. \tag{B.16e}$$

B.3.2 Current source

Figure B.3 represents a current source with magnitude I_S and internal resistance R_S, oriented towards the z-axis, connecting nodes (i,j,k) and $(i,j,k+1)$.

Figure B.3. Current source with magnitude I_S and internal resistance R_S placed between nodes (i,j,k) and $(i,j,k+1)$.

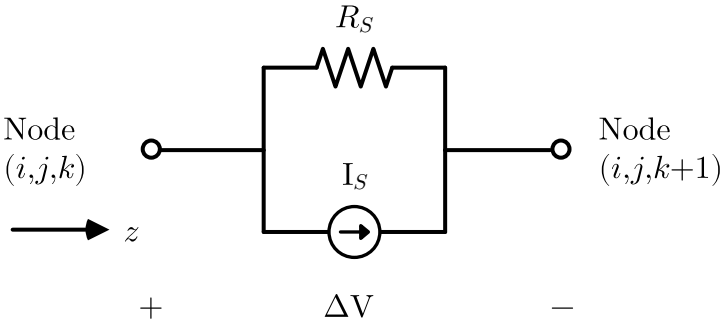

Source: own authorship.

FDTD updating equations for the current source are:

$$\begin{aligned} E_z^{n+1}(i,j,k) =& C_{eze}(i,j,k) \times E_z^n(i,j,k) \\ &+ C_{ezhy}(i,j,k) \times \left[H_y^{n+\frac{1}{2}}(i,j,k) - H_y^{n+\frac{1}{2}}(i-1,j,k)\right] \\ &+ C_{ezhx}(i,j,k) \times \left[H_x^{n+\frac{1}{2}}(i,j,k) - H_x^{n+\frac{1}{2}}(i,j-1,k)\right] \\ &+ C_{ezs}(i,j,k) \times I_s^{n+\frac{1}{2}}(i,j,k) \end{aligned}, \tag{B.17a}$$

with:

$$C_{eze}(i,j,k) = \frac{2\varepsilon_z(i,j,k) - \Delta t\sigma_z^e(i,j,k) - \frac{\Delta t\Delta z}{R_s\Delta x\Delta y}}{2\varepsilon_z(i,j,k) + \Delta t\sigma_z^e(i,j,k) + \frac{\Delta t\Delta z}{R_s\Delta x\Delta y}}, \tag{B.17b}$$

$$C_{ezhy}(i,j,k) = \frac{2\Delta t}{\left[2\varepsilon_z(i,j,k) + \Delta t\sigma_z^e(i,j,k) + \frac{\Delta t\Delta z}{R_s\Delta x\Delta y}\right]\Delta x}, \tag{B.17c}$$

$$C_{ezhx}(i,j,k) = -\frac{2\Delta t}{\left[2\varepsilon_z(i,j,k) + \Delta t\sigma_z^e(i,j,k) + \frac{\Delta t\Delta z}{R_s\Delta x\Delta y}\right]\Delta y}, \tag{B.17d}$$

$$C_{ezs}(i,j,k) = -\frac{2\Delta t}{\left[2\varepsilon_z(i,j,k) + \Delta t\sigma_z^e(i,j,k) + \frac{\Delta t\Delta z}{R_s\Delta x\Delta y}\right]\Delta x\Delta y}. \tag{B.17e}$$

B.3.3 Resistor

Figure B.4 represents a resistor with resistance R, oriented towards the z-axis, connecting nodes (i,j,k) and $(i,j,k+1)$.

Figure B.4. Resistor with resistance R placed between nodes (i,j,k) and $(i,j,k+1)$.

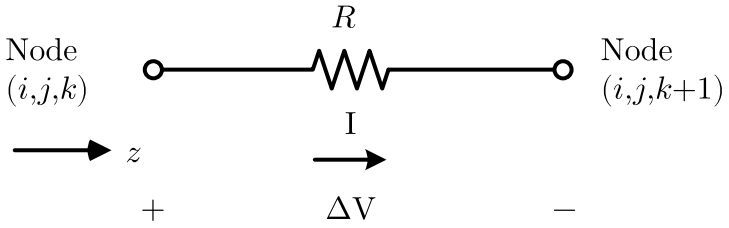

Source: own authorship.

FDTD updating equations for the resistor are:

$$\begin{aligned} E_z^{n+1}(i,j,k) =& C_{eze}(i,j,k) \times E_z^n(i,j,k) \\ &+ C_{ezhy}(i,j,k) \times \left[H_y^{n+\frac{1}{2}}(i,j,k) - H_y^{n+\frac{1}{2}}(i-1,j,k)\right], \\ &+ C_{ezhx}(i,j,k) \times \left[H_x^{n+\frac{1}{2}}(i,j,k) - H_x^{n+\frac{1}{2}}(i,j-1,k)\right] \end{aligned} \tag{B.18a}$$

with:

$$C_{eze}(i,j,k) = \frac{2\varepsilon_z(i,j,k) - \Delta t\sigma_z^e(i,j,k) - \frac{\Delta t\Delta z}{R\Delta x\Delta y}}{2\varepsilon_z(i,j,k) + \Delta t\sigma_z^e(i,j,k) + \frac{\Delta t\Delta z}{R\Delta x\Delta y}}, \tag{B.18b}$$

$$C_{ezhy}(i,j,k) = \frac{2\Delta t}{\left[2\varepsilon_z(i,j,k) + \Delta t\sigma_z^e(i,j,k) + \frac{\Delta t\Delta z}{R\Delta x\Delta y}\right]\Delta x}, \tag{B.18c}$$

$$C_{ezhx}(i,j,k) = -\frac{2\Delta t}{\left[2\varepsilon_z(i,j,k) + \Delta t\sigma_z^e(i,j,k) + \frac{\Delta t\Delta z}{R\Delta x\Delta y}\right]\Delta y}. \tag{B.18d}$$

B.3.4 Inductor

Figure B.5 represents an inductor with inductance L, oriented towards the z-axis, connecting nodes (i, j, k) and $(i, j, k + 1)$.

Figure B.5. Inductor with inductance L placed between nodes (i, j, k) and $(i, j, k + 1)$.

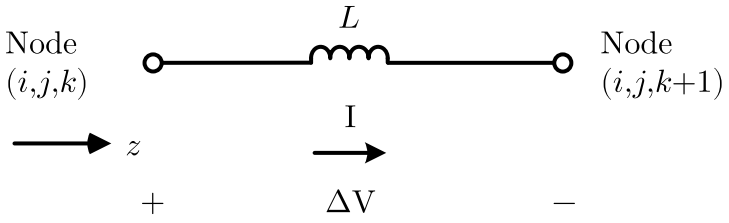

Source: own authorship.

FDTD updating equations for the inductor are:

$$\begin{aligned} E_z^{n+1}(i,j,k) =& C_{eze}(i,j,k) \times E_z^n(i,j,k) \\ &+ C_{ezhy}(i,j,k) \times \left[H_y^{n+\frac{1}{2}}(i,j,k) - H_y^{n+\frac{1}{2}}(i-1,j,k) \right] \\ &+ C_{ezhx}(i,j,k) \times \left[H_x^{n+\frac{1}{2}}(i,j,k) - H_x^{n+\frac{1}{2}}(i,j-1,k) \right] \\ &+ C_{ezj}(i,j,k) \times J_{iz}^{n+\frac{1}{2}}(i,j,k) \end{aligned}, \tag{B.19a}$$

with:

$$C_{eze}(i,j,k) = \frac{2\varepsilon_z(i,j,k) - \Delta t \sigma_z^e(i,j,k)}{2\varepsilon_z(i,j,k) + \Delta t \sigma_z^e(i,j,k)}, \tag{B.19b}$$

$$C_{ezhy}(i,j,k) = \frac{2\Delta t}{\left[2\varepsilon_z(i,j,k) + \Delta t \sigma_z^e(i,j,k)\right] \Delta x}, \tag{B.19c}$$

$$C_{ezhx}(i,j,k) = -\frac{2\Delta t}{\left[2\varepsilon_z(i,j,k) + \Delta t \sigma_z^e(i,j,k)\right] \Delta y}, \tag{B.19d}$$

$$C_{ezj}(i,j,k) = -\frac{2\Delta t}{2\varepsilon_z(i,j,k) + \Delta t \sigma_z^e(i,j,k)}. \tag{B.19e}$$

B.3.5 Capacitor

Figure B.6 represents a capacitor with capacitance C, oriented towards the z-axis, connecting nodes (i, j, k) and $(i, j, k + 1)$.

Figure B.6. Capacitor with capacitance C placed between nodes (i, j, k) and $(i, j, k+1)$.

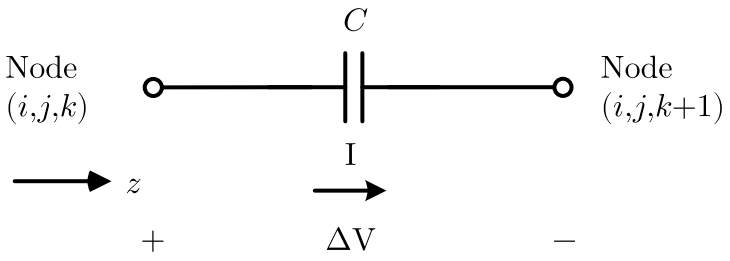

Source: own authorship.

FDTD updating equations for the capacitor are:

$$\begin{aligned} E_z^{n+1}(i,j,k) =& C_{eze}(i,j,k) \times E_z^n(i,j,k) \\ &+ C_{ezhy}(i,j,k) \times \left[H_y^{n+\frac{1}{2}}(i,j,k) - H_y^{n+\frac{1}{2}}(i-1,j,k)\right], \\ &+ C_{ezhx}(i,j,k) \times \left[H_x^{n+\frac{1}{2}}(i,j,k) - H_x^{n+\frac{1}{2}}(i,j-1,k)\right] \end{aligned} \tag{B.20a}$$

with:

$$C_{eze}(i,j,k) = \frac{2\varepsilon_z(i,j,k) - \Delta t\sigma_z^e(i,j,k) + \frac{2C\Delta z}{\Delta x\Delta y}}{2\varepsilon_z(i,j,k) + \Delta t\sigma_z^e(i,j,k) + \frac{2C\Delta z}{\Delta x\Delta y}}, \tag{B.20b}$$

$$C_{ezhy}(i,j,k) = \frac{2\Delta t}{\left[2\varepsilon_z(i,j,k) + \Delta t\sigma_z^e(i,j,k) + \frac{2C\Delta z}{\Delta x\Delta y}\right]\Delta x}, \tag{B.20c}$$

$$C_{ezhx}(i,j,k) = -\frac{2\Delta t}{\left[2\varepsilon_z(i,j,k) + \Delta t\sigma_z^e(i,j,k) + \frac{2C\Delta z}{\Delta x\Delta y}\right]\Delta y}. \tag{B.20d}$$

B.4 THIN-WIRE MODEL

Line conductors are crucial structures in the context of grounding and EMI studies. However, their radii are small (centimeters) in comparison with the domain space dimensions (dozens to hundreds of meters), which would require a very large number of subdivisions in order to be modeled as objects conforming to the FDTD grid, possibly rendering FDTD simulations impracticable due to the amount of memory and computational time required.

To address this issue, it is employed the technique proposed by Umashankar *et al.* (1987) to model a thin wire with a radius inferior than a cell size, which is based on the Faraday's law contour-path formulation. Figure B.7 shows a thin wire with radius a, oriented along the z direction, and the surrounding magnetic field components H_x and H_y.

The thin wire is modeled by setting four magnetic field update equations (B.21a)-(B.24a):

Figure B.7. Thin wire with radius a, oriented towards the z direction, placed between nodes (i,j,k) and $(i+1,j+1,k+1)$, and the surrounding magnetic field components H_x and H_y.

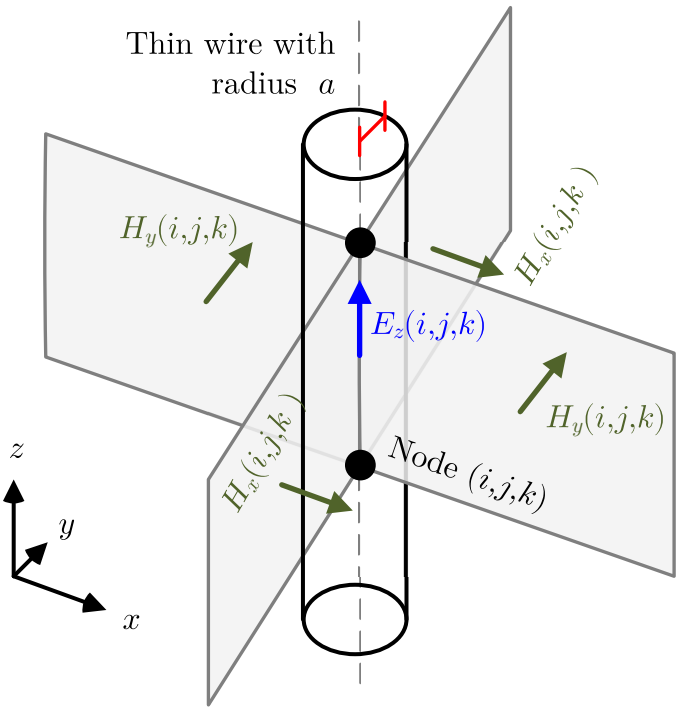

Source: adapted from (ELSHERBENI; DEMIR, 2015).

$$\begin{aligned} H_y^{n+\frac{1}{2}}(i,j,k) =& C_{hyh}(i,j,k) \times H_y^{n-\frac{1}{2}}(i,j,k) \\ &+ C_{hyez}(i,j,k) \times [E_z^n(i+1,j,k) - E_z^n(i,j,k)], \\ &+ C_{hyex}(i,j,k) \times [E_x^n(i,j,k+1) - E_x^n(i,j,k)] \end{aligned} \tag{B.21a}$$

with:

$$C_{hyh}(i,j,k) = 1, \tag{B.21b}$$

$$C_{hyez}(i,j,k) = \frac{2\Delta t}{\mu_y(i,j,k)\Delta x \ln\left(\frac{\Delta x}{a}\right)}, \tag{B.21c}$$

$$C_{hyex}(i,j,k) = -\frac{\Delta t}{\mu_y(i,j,k)\Delta z}. \tag{B.21d}$$

$$\begin{aligned} H_y^{n+\frac{1}{2}}(i-1,j,k) =& C_{hyh}(i-1,j,k) \times H_y^{n-\frac{1}{2}}(i-1,j,k) \\ &+ C_{hyez}(i-1,j,k) \times [E_z^n(i,j,k) - E_z^n(i-1,j,k)] \\ &+ C_{hyex}(i-1,j,k) \times [E_x^n(i-1,j,k+1) - E_x^n(i-1,j,k)] \end{aligned} , \tag{B.22a}$$

with:

$$C_{hyh}(i-1,j,k) = 1, \tag{B.22b}$$

$$C_{hyez}(i-1,j,k) = \frac{2\Delta t}{\mu_y(i-1,j,k)\Delta x \ln\left(\frac{\Delta x}{a}\right)}, \tag{B.22c}$$

$$C_{hyex}(i-1,j,k) = -\frac{\Delta t}{\mu_y(i-1,j,k)\Delta z}. \tag{B.22d}$$

$$\begin{aligned} H_x^{n+\frac{1}{2}}(i,j,k) =& C_{hxh}(i,j,k) \times H_x^{n-\frac{1}{2}}(i,j,k) \\ &+ C_{hxey}(i,j,k) \times \left[E_y^n(i,j,k+1) - E_y^n(i,j,k)\right], \\ &+ C_{hxez}(i,j,k) \times \left[E_z^n(i,j+1,k) - E_z^n(i,j,k)\right] \end{aligned} \tag{B.23a}$$

with:

$$C_{hxh}(i,j,k) = 1, \tag{B.23b}$$

$$C_{hxey}(i,j,k) = \frac{\Delta t}{\mu_x(i,j,k)\Delta z}, \tag{B.23c}$$

$$C_{hxez}(i,j,k) = -\frac{2\Delta t}{\mu_x(i,j,k)\Delta y \ln\left(\frac{\Delta y}{a}\right)}. \tag{B.23d}$$

$$\begin{aligned} H_x^{n+\frac{1}{2}}(i,j-1,k) =& C_{hxh}(i,j-1,k) \times H_x^{n-\frac{1}{2}}(i,j-1,k) \\ &+ C_{hxey}(i,j-1,k) \times \left[E_y^n(i,j-1,k+1) - E_y^n(i,j-1,k)\right], \\ &+ C_{hxez}(i,j-1,k) \times \left[E_z^n(i,j,k) - E_z^n(i,j-1,k)\right] \end{aligned} \tag{B.24a}$$

with:

$$C_{hxh}(i,j-1,k) = 1, \tag{B.24b}$$

$$C_{hxey}(i,j-1,k) = \frac{\Delta t}{\mu_x(i,j-1,k)\Delta z}, \tag{B.24c}$$

$$C_{hxez}(i,j-1,k) = -\frac{2\Delta t}{\mu_x(i,j-1,k)\Delta y \ln\left(\frac{\Delta y}{a}\right)}. \tag{B.24d}$$

B.5 ABSORBING BOUNDARY CONDITIONS

FDTD calculations require the solution domain to be bounded, since no computer can process an unlimited amount of data. Thus, the treatment of the problem space boundaries is an important concept in the FDTD technique, as modeling an open scattering problem requires special techniques to accurately represent the system under study and avoid undesirable reflections due to inadvertent truncation of the simulation space.

Such techniques consist of enforcing the so-called absorbing boundary conditions (ABC), which is performed by surrounding the computational domain with one or more layers of finite-thickness materials made of fictitious constitutive parameters. The effect of such materials is to simulate the continuous propagation of the waves incident at the domain boundaries to beyond the computational space, by creating a wave-impedance matching condition.

The ABC implementation used in this work is the convolutional perfectly matching layer (CPML), introduced by Roden & Gedney (2000). Only the basic mechanisms are given below, without going further into the formalisms. A detailed analysis of the CPML is provided in (BÉRENGER, 2007).

The general form of the updating equation for a non-CPML lossy medium is given in (B.9a) for the E_x component. The respective updating equation for the CPML region is modified to:

$$\begin{aligned} E_x^{n+1}(i,j,k) =& C_{exe}(i,j,k) \times E_x^n(i,j,k) \\ &+ C_{exhz}(i,j,k) \times \left[H_z^{n+\frac{1}{2}}(i,j,k) - H_z^{n+\frac{1}{2}}(i,j-1,k) \right] \\ &+ C_{exhy}(i,j,k) \times \left[H_y^{n+\frac{1}{2}}(i,j,k) - H_y^{n+\frac{1}{2}}(i,j,k-1) \right] \\ &+ C_{\psi exy}(i,j,k) \times \psi_{exy}^{n+\frac{1}{2}}(i,j,k) + C_{\psi exz}(i,j,k) \times \psi_{exz}^{n+\frac{1}{2}}(i,j,k) \end{aligned} , \tag{B.25a}$$

with new coefficients:

$$C_{\psi exy}(i,j,k) \Leftarrow \Delta y C_{exhz}(i,j,k), \tag{B.25b}$$

$$C_{\psi exz}(i,j,k) \Leftarrow \Delta z C_{exhy}(i,j,k), \tag{B.25c}$$

$$\psi_{exy}^{n+\frac{1}{2}}(i,j,k) = b_{ey} \psi_{exy}^{n-\frac{1}{2}}(i,j,k) + a_{ey} \left[H_z^{n+\frac{1}{2}}(i,j,k) - H_z^{n+\frac{1}{2}}(i,j-1,k) \right], \tag{B.25d}$$

in which a_{ey} and b_{ey} are coefficients determined by imposing impedance matching conditions at the interface between the regular domain and the CPML. A similar procedure is valid for updating the other electric and magnetic field components as well, by using their respective updating equations and CPML parameters.

APPENDIX C

BRIEF DESCRIPTION OF THE CALCULATION METHODS USED IN ATP

In order to establish a clear understanding of the actual operations performed during simulations carried out in this thesis, a brief review of the calculation methods employed in ATP is provided.

The ATP has been developed using FORTRAN language specifically to handle problems related to power systems analysis, and is able to provide numerically stable time-domain solutions for a wide range of networks consisting of interconnections of resistances, inductances, capacitances, single and multiphase π-circuits, distributed-parameter lines and nonlinear circuit elements (DOMMEL, 1996). Transient phenomena are simulated at every discrete interval of time Δt, over a period ranging from $t = 0$ to $t = T_{max}$ seconds.

For nonresistive elements, relations between nodal voltages and currents are expressed by differential equations. The trapezoidal rule is employed in ATP for numerical integration, thus converting the differential equations into central difference (algebraic) expressions, in which the element response at time t depends on the values of the preceding time-step $(t - \Delta t)$. Then, the circuit is represented by a nodal conductance equation which is solved iteratively (HAGINOMORI *et al.*, 2016).

The following sections describe the formulation of the main circuit components used in ATP, as originally derived by Dommel (1969).

C.1 RESISTANCE MODEL

Figure C.1 shows a resistance R connecting nodes k and m. The time-domain relation between current $i_{km}(t)$ and voltages $v_k(t)$ and $v_m(t)$ is given by Ohm's law:

$$i_{km}(t) = \frac{v_k(t) - v_m(t)}{R}. \tag{C.1}$$

Figure C.1. Resistance R connecting nodes k and m (a); and time-domain ATP equivalent circuit (b).

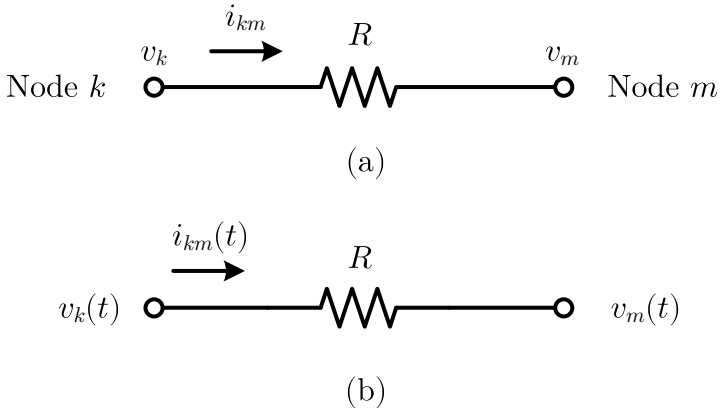

Source: own authorship.

C.2 INDUCTANCE MODEL

Figure C.2 shows an inductance L between nodes k and m and its equivalent ATP circuit. The basic equation for the inductor is:

$$v_k - v_m = L\frac{di_{km}}{dt}, \tag{C.2}$$

and the current is obtained by integration between times $(t - \Delta t)$ and t:

$$i_{km}(t) = i_{km}(t - \Delta t) + \frac{1}{L}\int_{t-\Delta t}^{t} (v_k - v_m)\, dt. \tag{C.3}$$

Using the trapezoidal rule, (C.3) is rewritten in the form of (C.4), which is the same as representing the inductor by the equivalent circuit in Figure C.2 (b):

$$i_{km}(t) = \frac{\Delta t}{2L}\left[v_k(t) - v_m(t)\right] + I_{km}(t - \Delta t), \tag{C.4}$$

$$I_{km}(t - \Delta t) = i_{km}(t - \Delta t) + \frac{\Delta t}{2L}\left[v_k(t - \Delta t) - v_m(t - \Delta t)\right]. \tag{C.5}$$

C.3 CAPACITANCE MODEL

Figure C.3 shows a capacitance C connecting nodes k and m and its equivalent ATP circuit. The basic relation for the capacitor is:

$$i_{km} = C\frac{d\left(v_k - v_m\right)}{dt}, \tag{C.6}$$

Figure C.2. Inductance L connecting nodes k and m (a); and time-domain ATP equivalent circuit (b).

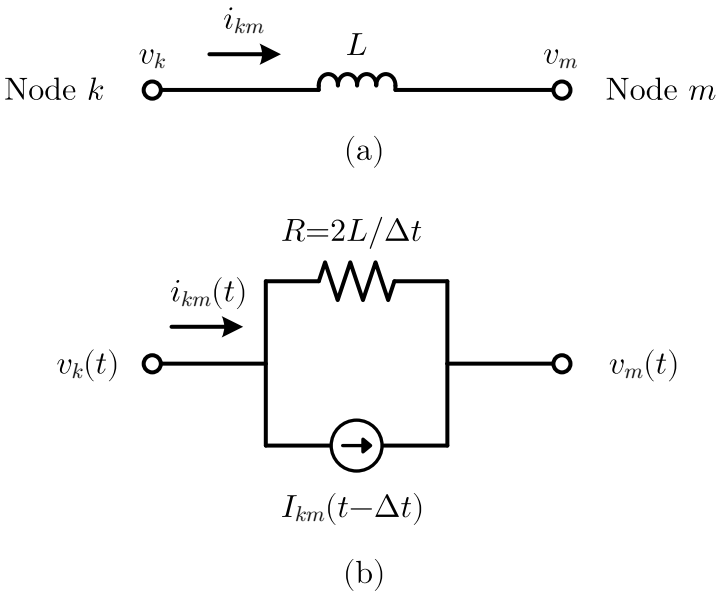

Source: own authorship.

which is rewritten using the trapezoidal rule as:

$$i_{km}(t) = \frac{2C}{\Delta t}\left[v_k(t) - v_m(t)\right] + I_{km}(t - \Delta t), \tag{C.7}$$

in which I_{km} is the current source in the equivalent circuit shown in Figure C.3 (b), determined as:

$$I_{km}(t - \Delta t) = -i_{km}(t - \Delta t) - \frac{2C}{\Delta t}\left[v_k(t - \Delta t) - v_m(t - \Delta t)\right]. \tag{C.8}$$

C.4 DISTRIBUTED-PARAMETER TRANSMISSION LINE MODEL

Figure C.4 shows a distributed-parameter transmission line connecting nodes k and m and its equivalent ATP circuit. The basic equations that describe the relationship between voltage and current are:

$$-\frac{\partial v}{\partial x} = L'\left(\frac{\partial i}{\partial t}\right), \tag{C.9}$$

$$-\frac{\partial i}{\partial x} = C'\left(\frac{\partial v}{\partial t}\right), \tag{C.10}$$

in which L' and C' are, respectively, the inductance and capacitance per unit length. The solution is:

$$v_k(t - \tau) + Z_C \cdot i_{km}(t - \tau) = v_m(t) - Z_C \cdot i_{mk}(t), \tag{C.11}$$

Figure C.3. Capacitance C connecting nodes k and m (a); and time-domain ATP equivalent circuit (b).

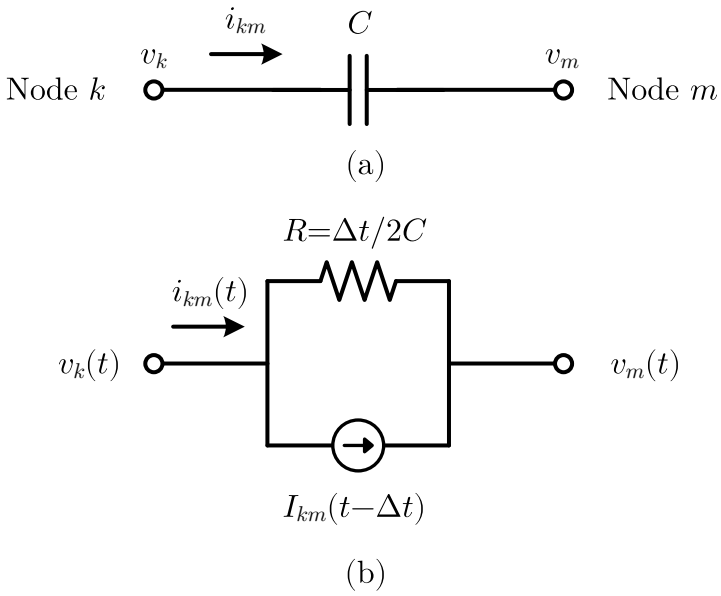

Source: own authorship.

$$v_k(t) - Z_C \cdot i_{km}(t) = v_m(t-\tau) + Z_C \cdot i_{mk}(t-\tau), \tag{C.12}$$

with the surge impedance Z_C and travel time τ determined as:

$$Z_C = \sqrt{\frac{L'}{C'}}, \tag{C.13}$$

$$\tau = \sqrt{L'C'}. \tag{C.14}$$

Current $i_{km}(t)$ can be represented by a voltage at self node k and a known current before travel time τ, and the two nodes can be treated as separated circuits, as shown in Figure C.4 (b), with equivalent parameters given by:

$$i_{km}(t) = \frac{1}{Z_C} v_k(t) + I_k(t-\tau), \tag{C.15}$$

$$I_k(t-\tau) = -\frac{1}{Z_C} v_m(t-\tau) - i_{mk}(t-\tau). \tag{C.16}$$

C.5 FUNDAMENTAL NODAL EQUATIONS

As shown in the preceding sections, circuit components in ATP are treated as resistors in parallel with appropriately chosen current sources. Then, any network composed of n nodes is

Figure C.4. Distributed-parameter transmission line connecting nodes k and m (a); and time-domain ATP equivalent circuit (b).

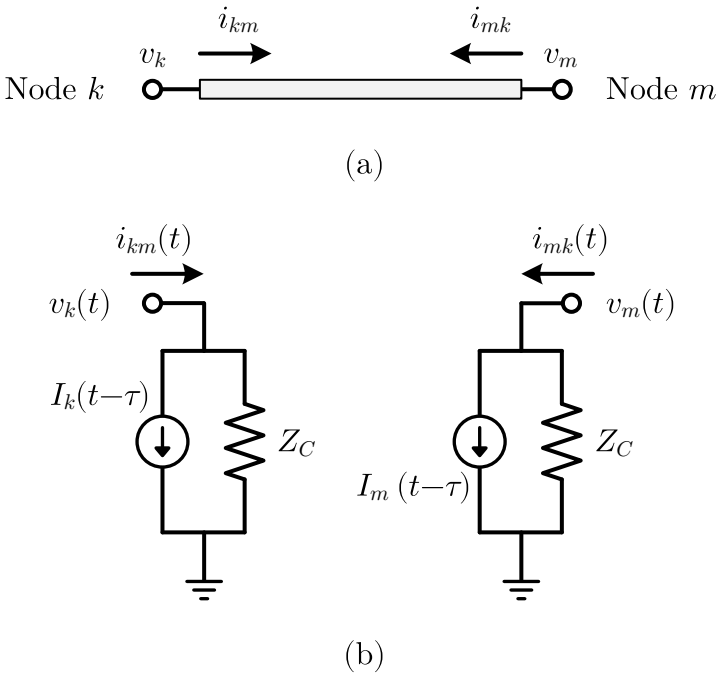

Source: own authorship.

described by the following system of n equations, represented in matrix form as:

$$\boldsymbol{G} \cdot \boldsymbol{v(t)} = \boldsymbol{i(t)} - \boldsymbol{I_H}, \tag{C.17}$$

in which $\boldsymbol{G}$ is the circuit conductance $n \times n$ matrix, $\boldsymbol{v(t)}$ is the vector of n node voltages, $\boldsymbol{i(t)}$ is the vector of n current sources; and $\boldsymbol{I_H}$ is the vector of n current source history terms. Unknown voltages and currents are calculated at each time-step until T_{max} is reached, according to the following procedure: matrix $\boldsymbol{G}$ is built and triangularized with ordered elimination and exploitation of sparsity (TINNEY; WALKER, 1967). For each time-step, the vector on the right-hand side of (C.17) is assembled from known history terms and known current and voltage sources. Then the system of linear equations is solved for $\boldsymbol{v(t)}$, using the information contained in the triangularized conductance matrix. Before proceeding to the next time-step, history terms $\boldsymbol{I_H}$ are updated for use in future time-steps.

View publication stats